UNIVERSITÀ DEGLI STUDI DI TRIESTE

UNIVERSITÀ DEGLI STUDI DI TRIESTE

XXXVII CICLO DEL DOTTORATO DI RICERCA IN FISICA

CHEMICAL EVOLUTION OF SHORT-LIVED RADIOACTIVE ELEMENTS IN GALAXIES

SETTORE SCIENTIFICO-DISCIPLINARE: ASTRONOMIA E ASTROFISICA

DOTTORANDA
ARIANNA VASINI

COORDINATORE
PROF. FRANCESCO LONGO

SUPERVISORE
PROF.SSA FRANCESCA MATTEUCCI

CO-SUPERVISORE
DR. EMANUELE SPITONI

ANNO ACCADEMICO 2023-2024

UNIVERSITÀ DEGLI STUDI DI TRIESTE

XXXVII CICLO DEL DOTTORATO DI RICERCA IN FISICA

CHEMICAL EVOLUTION OF SHORT-LIVED RADIOACTIVE ELEMENTS IN GALAXIES

SETTORE SCIENTIFICO-DISCIPLINARE: ASTRONOMIA E ASTROFISICA

DOTTORANDA
ARIANNA VASINI

COORDINATORE
PROF. FRANCESCO LONGO

SUPERVISORE
PROF.SSA FRANCESCA MATTEUCCI

CO-SUPERVISORE
DR. EMANUELE SPITONI

ANNO ACCADEMICO 2023-2024

Abstract

In this Thesis a chemical evolution study on Short-Lived Radioactive isotopes (SLRs) will be presented, with the purpose of analysing the recent evolution of the Milky Way (MW) and the Local Group (LG), unveiling the nucleosynthesis production sites of these isotopes and constraining the already available and upcoming observations.

The question regarding the origin of the elements first arose with the publication of the periodic table of the elements, in the XIX century, and the interest grew even more after the natural radioactivity was discovered. An element is *radioactive* or *unstable* when it naturally turns, or *decays*, into another element, by the transformation of a proton into a neutron or vice-versa. Each radioactive element decays with a specific decay timescale, which, being a nuclear property, is not influenced by the surrounding environment. The half-life of the radioactive nuclei span an extremely wide range of values, from infinitesimal fractions of a second to times longer than the current age of the Universe.

Only in the mid-20^{th} century, it became clear that the origin of the elements was intrinsically connected to Astronomy. The first nucleosynthesis episode, in fact, occurred during the Big Bang, where Hydrogen, Helium, Lithium and Beryllium were produced. After that phase, with the birth of the first stars, the formation of the heavier elements, commonly referred to as *metals*, started. It is within the stars, in fact, that the metals are synthesised and later ejected into the interstellar medium once the stars have reached the final stages of their evolution and die.

It is in this context that chemical evolution comes in. By adopting as input parameters the nucleosynthesis prescriptions that describe how each star pollutes the interstellar medium, the chemical evolution theory studies how the chemical abundances evolve in time and space in the galaxies. Chemical evolution aims at reproducing the abundances of the elements observed in the MW and in the external structures in order to constrain the unique set of fundamental parameters that drive the evolution of a galaxy and in particular the star formation rate. The study of the present time chemical abundances to reconstruct the histories of galaxies is known as *galactic archaeology*.

Even though chemical evolution, stellar evolution and observations have widely investigated the origin and formation of the elements, the periodic table still holds unanswered questions and, at the same time, conceals tools for studying the Universe that have not been exploited yet. Among these tools, the SLRs have been poorly explored even though, being characterised by half-lives of the order of the *millions of years*, could represent the perfect tracer of the phenomena that the Galaxy experienced in its recent history.

The two most important SLRs are ^{26}Al and ^{60}Fe, believed to be mainly produced by massive stars ($M > 8\,M_{\odot}$) and detected in the MW since 1991 by the γ-ray instruments COMPTEL first, and INTEGRAL later. Given their main supposed production site and their half-life, their role in astrophysics has been that of tracers of the regions of active star formation. However, it is not yet clear if nova systems do also contribute to the present day abundance of ^{26}Al (and in case they do, how much), and on the other side, ^{26}Al observations are poorly constrained. Furthermore, ^{60}Fe represents an equally tough challenge, because although there is consensus on its production sites (massive stars exclusively), the available observations are affected by even larger error bars. Chemical evolution can in principle solve these issues, but a detailed chemical evolution study on ^{26}Al and ^{60}Fe was performed only once and more than twenty-five years ago.

The aim of this Thesis is that of clarifying the nucleosynthesis of ^{26}Al and ^{60}Fe with particular emphases on solving the issue regarding the production of ^{26}Al by nova systems. A better understanding of their production opens the possibility of an improved constraint to the current observations of ^{26}Al and ^{60}Fe in the MW from the theoretical side. Besides, predictions regarding the ^{26}Al and ^{60}Fe content in the LG can also be performed, in view of a new dedicated survey currently under development.

To pursue this scope, the starting point is the testing of the stellar yields for massive stars and nova systems now available for ^{26}Al and ^{60}Fe, by the means of a detailed 1D chemical evolution model of the MW. By changing the stellar yields, the amount of elements ejected in the interstellar medium changes and therefore, the evolution of the abundances in the gas is modified accordingly. The best set of yield is identified as the one that better reproduces the current observations of ^{26}Al and ^{60}Fe. Constraining the yields represents the first step to reduce the uncertainties in the analysis of the chemical abundances. The results of this first study in fact, are used as input parameters in the following steps of this Thesis. What emerges clearly in this first study is the necessity of including novae in the ^{26}Al production to reproduce the observations, since assuming a null nova contribution underestimates by far the masses of ^{26}Al as measured in the MW.

As a second step in the ^{26}Al and ^{60}Fe analysis, the MW model was refined. In

the study above a 1D chemical evolution model was adopted, where only the radial dimension, namely the Galactocentric distance, was considered. Nonetheless, to properly study these isotopes a 2D model, where also a dependency on the azimuth is taken into account, is necessary. In fact, when a SLR isotope is ejected in the interstellar medium, it decays before homogeneously mixing with the preexisting gas. Therefore, the composition of the gas depends not only on the radial distance but also on the azimuth. The effects of this dependency can be studied only when the azimuthal dimension is introduced, hence the necessity of a 2D model. By adopting the yields previously constrained we repeated the MW analysis on ^{26}Al and ^{60}Fe by using a 2D model. This second study confirmed even more the importance of the role played by novae. Not only their production is fundamental to reproduce the ^{26}Al observed but the existence of two different nova populations, bulge and disc, as suggested by observations is confirmed. The only way to reproduce the observations in fact, is by assuming a larger ^{26}Al production from bulge novae relative to disc novae, confirming several previous studies.

Finally, the chemical evolution of the Large Magellanic Cloud (LMC) was performed. A new instrument, COSI-SMEX, designed to detect ^{26}Al and ^{60}Fe in the MW is in its latest phases of development and its launch is scheduled for 2027. The improvements made in the instrumentation relative to the previous satellites could allow us to detect ^{26}Al and ^{60}Fe in the LMC for the first time. Unfortunately, no theoretical estimates regarding these two isotopes are currently available for external galaxies, therefore it is still impossible to know if COSI will or will not be able to detect them. Hence, in this third study, the abundances of ^{26}Al and ^{60}Fe in the LMC were computed, in order to explore the limits of COSI. Considering the sensitivity of COSI, from this study we concluded that ^{26}Al in the LMC will be observable in the near future, whereas ^{60}Fe will be not.

In summary, in this Thesis the chemical evolution of ^{26}Al and ^{60}Fe is presented. By the means of a 1D chemical evolution model the role of novae in the ^{26}Al production has been clarified for the first time: we can state that without their contribution it is impossible to reproduce the ^{26}Al observations. Then, a revision to the MW results was performed, in order to account for the 2D distribution of ^{26}Al and ^{60}Fe. Here a dichotomy in the nova population emerged: the bulge novae should pollute the interstellar medium up to ten times more than the disc novae to reproduce the observations. This assumption is supported by several observations, and therefore this work confirms it. Finally, with the constraints provided by the first work, a theoretical estimate of the ^{26}Al and ^{60}Fe content in the LMC has been performed. According to our results, the ^{26}Al flux from the LMC is within the detection limits of the new upcoming survey, COSI, but the ^{60}Fe flux is not.

At last, a smaller section of this Thesis is dedicated to the investigation of the

[Mg/Mn] versus [^{27}Al/Fe] diagnostic that has been lately used to discriminate between the MW in situ population and the accreted one. The stars accreted from external galaxies and those originally born in the MW should be located in different regions of the [Mg/Mn] vs [^{27}Al/Fe] plane due to the different timescales of productions of these isotopes. However, the nucleosynthesis of some of these elements, in particular ^{27}Al and Mn, is still quite uncertain and therefore it is not clear how reliable this chemical diagnostic actually is. By the means of a 1D chemical evolution model we explored the uncertainties that affect this chemical combination concluding that the yields are still too uncertain and this diagnostic should be used together with other chemical clocks.

Contents

Contents vii

List of Figures xii

List of Tables xxiv

1 Introduction 1
- 1.1 Nucleosynthesis of elements . . . 2
  - 1.1.1 Nuclear burnings: up to the Fe group . . . 3
  - 1.1.2 Neutron capture: beyond the Fe peak . . . 6
- 1.2 Short-Lived Radioisotopes . . . 6
  - 1.2.1 ^{26}Al and ^{60}Fe nuclear properties . . . 8
  - 1.2.2 ^{26}Al and ^{60}Fe nucleosynthesis . . . 11
- 1.3 State of the Art and Thesis aims . . . 22
- 1.4 Structure of the Thesis . . . 25

2 Chemical evolution models 26
- 2.1 Input parameters . . . 27
  - 2.1.1 Initial Conditions . . . 27
  - 2.1.2 Birthrate Function: SFR and IMF . . . 28
  - 2.1.3 Stellar Yields . . . 29
  - 2.1.4 Gas Flows . . . 30
- 2.2 Chemical evolution equations . . . 32
  - 2.2.1 Chemical evolution equations for radioactive isotopes . . . 34

3 Instruments and Observations 36
- 3.1 Telescopes for γ energy band . . . 36
- 3.2 First measurements . . . 39
- 3.3 COMPTEL and INTEGRAL . . . 42
  - 3.3.1 Instrumentation . . . 42

3.3.2 Observations . . . 46
3.4 Future perspectives: COSI-SMEX . . . 54

4 Chemical Evolution of ^{26}Al and ^{60}Fe in the Milky Way 57
4.1 Introduction . . . 57
4.2 The model . . . 59
4.2.1 Main assumptions . . . 59
4.2.2 Nucleosynthesis and yields . . . 62
4.3 Results . . . 64
4.3.1 ^{26}Al mass . . . 64
4.3.2 ^{60}Fe mass . . . 66
4.3.3 Injection rates . . . 68
4.4 Discussion on the model parameters . . . 69
4.5 Discussion on the yields . . . 71
4.6 Conclusions . . . 73

5 ^{26}Al in the Milky Way: the role of novae in a 2D chemical evolution model 75
5.1 Introduction . . . 76
5.2 The reference 1D chemical evolution model . . . 77
5.2.1 Galactic thick and thin discs . . . 78
5.2.2 The bulge . . . 78
5.2.3 Nucleosynthesis prescriptions . . . 79
5.3 The 2D chemical evolution model . . . 79
5.3.1 Multiple spiral patterns of Spitoni et al. (2023) . . . 79
5.3.2 SFR and perturbations . . . 81
5.4 Results . . . 82
5.4.1 Nova systems . . . 82
5.4.2 ^{26}Al mass 2D distribution . . . 83
5.4.3 ^{26}Al mass azimuthal oscillations . . . 84
5.4.4 ^{26}Al: predictions versus observations . . . 85
5.4.5 Galactic observational constraints . . . 86
5.5 Conclusions . . . 87

6 Evolution of SLRs in the LMC: predictions for future γ-ray surveys 96
6.1 Introduction . . . 97
6.2 The Model . . . 98
6.2.1 Chemical Evolution Equation . . . 98
6.2.2 Model assumptions . . . 98

6.2.3 Star Formation History . . . 99
6.2.4 Nucleosynthesis and yields . . . 103
6.3 Results . . . 103
6.3.1 Observational constraints . . . 103
6.3.2 ^{26}Al and ^{60}Fe masses . . . 106
6.4 Discussion . . . 108
6.5 Conclusions . . . 111

7 Galactic archaeology with the [Mg/Mn] vs. [Al/Fe] plane: Uncertainties and caveats 113
7.1 Introduction . . . 114
7.2 Chemical evolution models for the MW and LMC . . . 116
7.2.1 The MW discs . . . 116
7.2.2 The LMC . . . 116
7.2.3 Nucleosynthesis prescriptions . . . 118
7.3 Observational data . . . 119
7.4 Results . . . 120
7.4.1 MW: [Mg/Fe], [Al/Fe], and [Mn/Fe] . . . 120
7.4.2 MW: [Mg/Mn] versus [Al/Fe] . . . 122
7.4.3 LMC: [Mg/Fe], [Al/Fe], and [Mn/Fe] . . . 124
7.4.4 LMC: [Mg/Mn] versus [Al/Fe] . . . 124
7.4.5 Testing different nucleosynthesis and IMF prescriptions . . . 128
7.4.6 The effects of Galactic wind . . . 129
7.5 Conclusions . . . 131

8 Closing remarks 134
8.1 Discussion and conclusions . . . 134
8.1.1 SLRs in the Milky Way . . . 134
8.1.2 SLRs in the Large Magellanic Cloud . . . 138
8.1.3 The [Mg/Mn] versus [Al/Fe] plane . . . 139
8.2 Future perspectives . . . 141

List of Figures

1.1 Evolutionary traces on the temperature-density plane in log-log scale. The position on the plane represent the current nuclear phase of each star. The coloured dots represent the point of ignition of a burning. Taken from Diehl et al. (2022). 4

1.2 Solar System abundances from Lodders (2021) as a function of the mass number A. Different processes are indicated by different colours: the Big Bang nucleosynthesis in yellow, the stellar fusion in green, and the r- and s- processes are highlighted in blue and red, respectively. Taken from Arcones et al. (2023). 5

1.3 Table of isotopes in the neighbourhood of ^{26}Al. Each isotope is identified by its symbol and its number of nucleons and are divided between stable isotopes in black cells and unstable isotopes in coloured cells. The lifetime, as well as the spin and parity, are listed in the second and third row and at the bottom left the main decay channel is indicated. For the stable isotopes, the abundance fraction is reported at the bottom. Taken from Diehl et al. (2021b). 9

1.4 Energetic levels of ^{26}Al and ^{26}Mg. To study ^{26}Al the ground state, $^{26}\mathrm{Al}^{g}$, and the isomeric state, $^{26}\mathrm{Al}^{m}$, have to be considered. $^{26}\mathrm{Al}^{g}$ decays into the first excited state of ^{26}Mg, that than de-excites to the ground state, emitting the characteristic 1808.63 keV line. $^{26}\mathrm{Al}^{m}$ typically decays into the ground state of ^{26}Mg, even though under stellar interior condition it can also decay into its own ground state, $^{26}\mathrm{Al}^{g}$. Taken from Diehl et al. (2021b). 9

1.5 ^{60}Fe and the neighbouring isotopes involved in its production and destruction reactions. In black, the stable isotopes cells, whereas the coloured ones represent the unstable. The information reported in each cell are the symbol of each element with its nucleon number, the half-life, the spin and the parity. In the bottom left corner of the unstable isotopes the decay mechanism is indicated. For the stable ones, the abundance fraction is reported. Taken from Diehl et al. (2021b). 10

1.6 Energy levels involved in the decay chain of ^{60}Fe. Starting from the ground state of ^{60}Fe, a β^- decay to ^{60}Co occurs, that in turns decays into ^{60}Ni. The double de-excitation of ^{60}Ni to its ground state produces the two characteristic γ-ray lines at 1.173 MeV and 1.332 MeV. Taken from Diehl et al. (2021b). 11

1.7 MgAl reaction chain. Taken from Arnould et al. (1999). 12

1.8 Temporal evolution of the ^{26}Al mass fraction in the H convective core for different ZAMS masses. The maximum is reached after few Myr and is followed by a monotonic decrease due to the ^{26}Al β^+ decay into ^{26}Mg. The decline is shallower than the pure β^+ decay (cyan dot-dashed line) because ^{26}Al continues to be produced. It is precisely thanks to this production that a fraction of ^{26}Al is preserved until the end on the central H burning. Taken from Limongi et al. (2006). 14

1.9 Different contributions to the ^{26}Al total yield for different initial stellar masses. The contribution analysed are ascribed to the wind (green diamonds), the C/Ne convective shell (blue triangles) and the explosive nucleosynthesis (red squares). The total yield is depicted by black dots. Taken from Limongi et al. (2006). 16

1.10 Schematic representation of a nova system during the accretion phase. Taken from www.astro.berkeley.edu. 17

1.11 Snapshots of the evolution of Mg-Al group nuclei along the accreted envelope of a ONe nova. The four panels represent four different temperatures and the temporal evolution proceeds from the top panel down to the bottom one. Taken from José et al. (1997). 18

1.12 Different contributions to the ^{60}Fe total yield for different initial stellar masses. The contribution analysed are ascribed to the He convective shell (green diamonds), the C convective shell (blue triangles) and the explosive nucleosynthesis (red squares). The total yield is depicted by black dots. Taken from Limongi et al. (2006). . 21

3.1 Schematic representation of a Compton telescope: by measuring the deposition on the first detector and the final absorption by the second detector, the angle θ can be determined and therefore the direction of the incident γ-photon can be constrained to lie in the Compton cone. 37

3.2 **Left:** Sketch of the spectrometer SPI (Spectrometer on INTEGRAL, mounted on the INTEGRAL telescope. The Germanium detector is stored in the lower part of the instrument (in yellow). Dimensions (height $\times$ diameter) are 2.26 $\times$ 0.78 m^2 (Diehl, 2013b). **Right:** Pictures of the Ge detector composed of 19 sub-units (lower figure), coded mask and photo-multipliers (upper figures, left and right respectively) of SPI (credits to Diehl 2013a). 38

3.3 The instrument was symmetrically designed so that both the upward and downward fluxes could be measured. **Left:** Upward flux at 4 g cm^{-2}. **Right:** Total downward flux at 3.5 g cm^{-2}. Taken from Lockwood et al. (1979). 40

3.4 Spectrum obtained by the summed data collected by the four detectors during the 2 weeks flight in 1979 (Mahoney et al., 1982). The location of the target lines is clearly indicated. The ^{26}Al line at 1.809 MeV is the most prominent one. 41

3.5 **Left:** Sketch of the CGRO. COMPTEL and the three other instruments carried, OSSE (Oriented Scitillation Spectrometer Experiment), EGRET (Energetic Gamma-Ray Experiment Telescope.) and BATSE (Burst and Transient Source Experiment) are pictured. **Right:** Section of COMPTEL. In the upper part the seven liquid scintillators can be recognised, and in the lower part the fourteen cylindrical detectors are represented. The principle of operation is schematically pictured by the incoming photon that interacts with the top detector and scatters towards the bottom, before being absorbed. Pictures from Schoenfelder et al. 1993. 43

3.6 **Left:** sketch of the assembled satellite with the orientation in 3D space. **Rigth:** INTEGRAL exploded view. In the central part the two main instruments, SPI on the left and IBIS (Imager on Board the INTEGRAL Satellite) on the right, are sketched. Taken from https://www.cosmos.esa.int/web/integral/spacecraft-drawings. . 45

3.7 Crab nebula in the γ-ray band. **Left:** γ-ray map before background subtraction. Several off-centre extended structure are detected. **Right:** after background subtraction. All the substructures are removed and only the centre, where the Crab pulsar is located, appears. Taken from Diehl et al. (1992). 47
3.8 First map produced adopting COMPTEL data, after two years of observations. The emission is too smooth to be produced by a point source in the Galactic center with a large yield, but not smooth enough to be produced by novae with low yield. The best fit is obtained assuming emission from massive stars, in particular WR stars, whose distribution almost overlaps with the 1.809 MeV map. 47
3.9 Maps of the Galactic plane provided by COMPTEL. From the top to the bottom panel, the energy bands represented are 1.5 - 1.7 MeV, 1.7 - 1.9 MeV and 1.9 - 2.1 MeV. The relevant aspect here is the difference between the middel panel and the other two. In the middel one, where the ^{26}Al flux is expected, the emission is clearly evident, whereas in the other two panel is almost absent. Taken from Diehl et al. (1995). 48
3.10 All-sky map of the 1.809 MeV MW. The contour lines represent the intensity of the emission. The flux is concentrated within the Galactic latitude $|b| \leq 30°$, excluding the purely local origin of ^{26}Al. Nevertheless, the clumpiness shown by the map indicates that the local contribution is non negligible. Taken from Oberlack et al. (1996). 49
3.11 The final 1.809 MeV map provided by COMPTEL, color coded with the flux intensity. Taken from Plüschke et al. (2001). 49
3.12 Energy shifts (yellow data) of the ^{26}Al decay line centroid measured at three different Galactic longitude bins: from 40° to 10°, from 10° to -10° and from -10° to -40°. The shifts are compatible with the expected Doppler shifts caused by the Galactic rotation. The measurements are compared to a 3D distribution of ^{26}Al convoluted with the MW rotation curve. The match between data and model implies that the bulk of the 1.809 MeV emission comes from the inner Galaxy rather than foreground sources. Taken from Diehl et al. (2006b). 50
3.13 1.809 MeV emission map of the MW as obtained after combining 10 years of data. The colour coding represent the intensity of the flux collected, as represented by the colour bar at the bottom. The outstanding feature is the resemblance to the previous COMPTEL map, reported in Fig. 3.11. Taken from Bouchet et al. (2015). 51

3.14 COSI simulations for the Galactic emission al 1.809 MeV produced by the radioactive decay of ^{26}Al (top panel) and for the 1.173 and 1.332 MeV, ascribed to the decay of ^{60}Fe. Taken from J. Tomsick et al. (2019). 54

3.15 Sketch of the design of COSI. Taken from J. Tomsick et al. (2019). . . 55

4.1 The red line represents the SFR(t) at 8 kpc as a function of time. The SFR in the solar neighbourhood, according to the prescriptions assumed, shows two peaks: the first infall is responsible of the first SFR peak, then the SFR drops until the second infall starts and the SFR increases again. The blue line marks the observed present time SFR according to Prantzos et al. (2018). 60

4.2 SFR(t) at 2 kpc as a function of time in the first 3 Gyr since the beginning of SF. The prescriptions assumed (high SFE, short time scale and single infall episode) produce a SFR extremely high at the beginning of the Galaxy which decreases immediately due to the fast gas consumption. 62

4.3 Integrated mass of ^{26}Al as a function of Galactocentric distance for seven models among the computed ones. Model 1C (dash-dotted red line), Model 2C (solid orange line), Model 3C (dash-dot-dotted green line) and Model 5C (dashed blue line) are the only four compatible models I obtain. The three black lines are Model 2, Model 2A and Model 2B, plotted as examples of non compatible models (they were chosen as the highest model among those which do not fit the observations). I stress that Model 2 without novae is a factor 5 lower than the compatible model. The yellow band represents the observed values and the red dot is the best observation. Although 1C, 2C, 3C and 5C all offer a mass value within $1.8 - 3.6$ M$_\odot$ at 5 kpc, Model 1C is the closest to the best observation, ~ 2 M$_\odot$. 66

4.4 Integrated mass of ^{60}Fe as a function of Galactocentric radius obtained with the five models tested. It is evident that Model 1 (dash-dot-dotted red line) and Model 5 (dotted black line), which are the two metallicity dependent ones, produce the lowest ^{60}Fe masses, whereas Model 2, Model 3 and Model 4 produce higher masses of ^{60}Fe. According to the conversion between flux ratio and abundance ratio, ^{60}Fe should lie in the range $0.9 - 1.8$ M$_\odot$. My best model is Model 3 with 1.05 M$_\odot$ produced within 5 kpc from the Galactic centre. 68

4.5 Present time integrated injection rates computed with Model 2 for ^{26}Al (solid red line) and ^{60}Fe (dashed blue line), compared with those by Timmes et al. (1995) for ^{26}Al (dotted red line) and for ^{60}Fe (dash-dotted blue line) only for the disc (R≥ 4 kpc).
Timmes et al. (1995): the results are computed assuming that the time scale of the second infall τ_D is constant (no "inside-out"scenario assumed) and that the IMF is that by Salpeter (1955).
This study: in this case I assumed the "inside-out"scenario for the disc and a Salpeter (1955) IMF. The results I get show that the highest contribution comes from the 6−8 kpc region. The differences between the two studies do not lay in the IMF but in other model prescriptions such as the inside-out scenario. 70

4.6 SFR at the present time as a function of Galactocentric distance I assume in the model. The maximum is located at 4 kpc from the Galactic centre, whereas in the bulge and in the outer Galaxy it decreases. 71

5.1 Spiral pattern speeds $\Omega_{s,1}(R)$, $\Omega_{s,2}(R)$ and $\Omega_{s,3}(R)$ of the multiple spiral modes moving at different pattern speeds of Model A in Spitoni et al. (2023) are indicated by the three coloured horizontal lines. Inner and outer spiral structures (moving with the above-mentioned pattern speeds) are also indicated by the thicker grey and light-blue, respectively. The disc angular velocity $\Omega_d(R)$ computed by Roca-Fàbrega et al. (2014) is indicated with the dotted line. The 2:1 and 4:1 outer and inner Lindblad resonances (OLR and ILR) occur along the solid and dashed black curves, respectively. Resonances have been computed as $\Omega_{p2}(R) = \Omega_d(R) \pm \kappa/2$ and $\Omega_{p4}(R) = \Omega_d(R) \pm \kappa/4$, respectively where κ is the local radial epicyclic frequency. The long vertical dashed lines show the positions of the co-rotation radii assuming the three different Ω_S values. 90

5.2 2D SFR from the bulge to the outskirts of the MW. Six snapshots at different time steps: T_1=0.066 Gyr, T_2=2.25 Gyr, T_3=3.2 Gyr, two recent times T_4=13.5 Gyr and T_5=13.6 Gyr, and the present day time, T_6=13.7 Gyr. The position of the sun is represented by the white-edge star. 91

5.3 2D map of nova outburst rate in the MW at four different times, T_3, T_4, T_5 and T_6. 92

5.4 2D distribution of ^{26}Al mass at the six time steps where I have previously analysed the SFR. The ^{26}Al producers here are massive stars and novae. Each cell is colour coded according to the ^{26}Al mass contained as in Fig. 5.2 the sun is indicated by the white-edge star. 93

5.5 Same as Fig. 5.4 but without any contribution from nova systems. . 94

5.6 *Panel* ***a***: SFR as a function of the azimuth at the present time and the solar neighbourhood. The black dashed lines, in this plot and in those below, mark the peaks of the SFR. *Panel* ***b***: ^{26}Al distribution in the solar ring and present time. In pink, ^{26}Al predicted by Model 1 and in green that from Model 2. *Panel* ***c***: difference between the ^{26}Al production in the two cases. *Panel* ***c***: novae distribution in the solar ring at the present time. 95

6.1 The four SFHs tested in this study. *Top right panel*: Model 1 with a Schmidt-Kennicutt law taken from Kennicutt (1998) with constant SFE ν. The red point is the present time observed SFR, 0.38 $M_\odot$ yr^{-1}, taken from Harris et al. (2009). The dashed red line is the average SFR in the last 4.5 Gyrs, again by Harris et al. (2009) and the dashed black line is the average SFR in the last 4.5 Gyrs that I obtain. *Top left panel*: Model 2 with Hasselquist-like SFH inspired by Hasselquist et al. (2021). *Bottom left*: SFH by Harris et al. (2009) used for Model 3. The authors propose a SFH very low for the first 10 Gyr followed by four bursts, whereas I adopt just three bursts, since the two most recent ones are very close in time and the SF in between is not too low. With this SFH I reproduce the observed value. *Bottom right panel*: SFH by Calura et al. (2003) tested in Model 4. This SFH is inspired by Bradamante et al. (1998) and is derived on purely theoretical basis but it is suitable to fit the data available at the time. Notice that only Model 3 can reproduce the present time value and also the average SFR is consistent with the observation, given the uncertainties. 101

6.2 Abundances of four α-elements, namely, O, Mg, Si and Ca. The models shown are Model 3 with Harris et al. (2009) SFH (green solid line) and Model 4 with Calura et al. (2003) SFH (orange solid line). The data taken from Asa'd et al. (2022) (black circles), Mucciarelli et al. (2008) (dark grey squares) and Hill et al. (2000) (white triangles) refer to LMC globular clusters whereas those by Van der Swaelmen et al. (2013) (light grey circles) regard the LMC bar stars. Since, by means of Tab. 6.2 I already excluded Model 1 and Model 2, here I show just the two remaining ones to clarify if I can rule out another one. It can be seen that Model 4 predicts too much Fe abundance, therefore I select Model 3 as my best model. 107

7.1 SFHs predicted in Chaps. 4 and 6 and used in the paper. For the MW (red line), the Kennicutt (1998) law with exponent $k = 1.5$ is adopted, and the temporal evolution of the SF at the solar ring (8 kpc) is compared with the present-day observed SFR (vertical yellow line, data taken from Prantzos et al. 2018). For the LMC (blue line) I assume a linear Kennicutt (1998) law with a variable SFE to reproduce the Harris et al. (2009) SFR. I compare it with the observation at the present time by Harris et al. (2009) itself (vertical cyan line). 117

7.2 Abundance ratios of the three elements involved. The data are from APOGEE DR17 and are binned and colour-coded according to the data density in each bin. The blue line represents the running median, computed assuming a bin size of 0.1 dex and an overlap of 0.025 dex, and the blue shaded area represents the related standard deviation. *Left panel*: [Mg/Fe] in the MW as predicted by REF MW model (black line) and by NEW MW model (white line) compared to APOGEE data. *Middle panel*: [Al/Fe] MW abundance for both models (same colour-coding as left panel). *Right panel*: [Mn/Fe] abundance for REF MW and NEW MW models (same colour-coding).121

7.3 Data compared to models (REF MW and NEW MW models in the upper panel, REF MW and MIX MW models in the lower panel) and previous results from the literature. The colour-coding shows the [Fe/H] content (see the colour bar). The data are binned so as to show the mean value of [Fe/H] in each bin. The three circles plotted on the models mark the ages 0.3 Gyr, 1 Gyr, and 5 Gyr. The horizontal and diagonal black lines separate three different plane regions as denoted by Fernandes et al. (2023); the unevolved populations lie in the upper left region, the MW high-α in situ population lies in the upper right region; and the MW low-α in situ population lies in the lower region. 123

7.4 LMC abundance ratios of Mg, Al, and Mn. The data are from APOGEE DR17 and are binned and colour-coded as in Fig. 7.2. Again, the blue line represents the running median computed with the same bin size and overlap, and the blue area is the standard deviation. The black and the white lines are the REF LMC model and the NEW LMC model, respectively. 125

7.5 LMC in [Mg/Mn] versus [Fe/H] plane. My models are plotted against the APOGEE DR17 data and the model from Fernandes et al. (2023). As in Fig. 7.3 the colour-coding represents the [Fe/H] content. Again, the circles on the models mark three ages, 0.3 Gyr, 1 Gyr, and 5 Gyr. Here, unlike Fig. 7.3, the data are not binned. *Left panel*: REF LMC model (colour-coded black-edge line) and NEW LMC (with yields corrections, colour-coded white-edge line) are compared to data and to the results of Fernandes et al. (2023). *Right panel*: REF LMC model (colour-coded black-edge line) and MIX LMC model (colour-coded grey-edge line) together with the data and the results of Fernandes et al. (2023). 127

7.6 [Mg/Mn] versus [Al/Fe] for CL04 MW model (colour-coded line, black edge) and K01 MW model (colour-coded line, white edge) compared to APOGEE DR17 data and REF MW model (black line). The colour-coding of the data, the CL04 MW model, and the K01 MW model is the same as Fig. 7.3, as are the binning of the data and the three circles plotted on the model. 129

7.7 SFHs for MW models without wind contribution (red line) and for WIND MW model (pink line) at 8 kpc from Galactic centre, compared to observed data (see reference in Fig. 7.1). 130

7.8 [Mg/Mn] versus [Al/Fe] for WIND MW model (colour-coded line, black edge) and NEW MW model (colour-coded line, white edge) compared to APOGEE DR17 data. The colour-coding is the same as Fig. 7.3, as are the binning of the data and the circles plotted on the model. 131

List of Tables

4.1 Models for different massive star yields. The first column reports the model identification, the second column contains the reference and the third column is used for the details of the models, to distinguish those taken from the same reference. For nova yields (only for ^{26}Al), in the third column the adopted values are listed. These values are the production during one outburst. I then assume 10^4 outbursts in total during the life of a nova system. 64

4.2 Final models, combining massive stars and nova yields, for ^{26}Al. The first column reports the label given to the models with combined yields. The second and third columns contains the prescriptions adopted for massive star yields and nova yields, respectively. "Model 4" is missing because for ^{26}Al it is equivalent to "Model 3". These two models are different only for ^{60}Fe. 65

4.3 Integrated mass of ^{26}Al within three different Galactocentric radii: 5 kpc, 8 kpc and 18 kpc. I compare the mass within 5 kpc with that observed by INTEGRAL, which lies in the range $1.8 - 3.6$ $M_\odot$. Only four models are in agreement with the observed interval: Model 1C, Model 2C, Model 3C and Model 5C. 67

4.4 Integrated mass of ^{60}Fe within 5 kpc, 8 kpc and 18 kpc for the five massive star models tested. It is not possible to perform a comparison with the γ observations because no mass estimates are available for ^{60}Fe. The results listed here are a prediction of the ^{60}Fe mass at different Galactocentric distances, and can be used as constraints for future γ-ray surveys. 69

4.5 Values of the most important observational constraint predicted by my model. Some quantities refer to the solar vicinity (surface density of gas, alive stars, total surface mass density and SF rate) and others are averaged over the whole disc (SNIa rate, SNII rate, nova rate and gas infall rate). The first column specifies the physical quantity considered, the second contains the prediction given by my model, the third contains the observed present day value and the last one lists the reference of the observation. 72

5.1 Descriptions of the nucleosynthesis of the two models tested. The check-marks mark the ^{26}Al sources included in the models. For the reference to the yields adopted for each astrophysical source see Sec. 5.2.3. 79

5.2 ^{26}Al integrated over the five innermost annuli (0 - 5 kpc) at the present time for both models. Columns 2-6 report the ^{26}Al for every single ring (each 1 kpc wide) and column 7 show the total ^{26}Al within 5 kpc. 85

5.3 MW disc (R>2 kpc) constraints: in column 2 the observed quantities, in column 3 the predictions from my models. Models 1 and 2 predict the same observables since they differ only on the nucleosynthesis side. **References:** (1) Prantzos et al. (2011), Chomiuk et al. (2011), (2) Kubryk et al. (2015a), (3) Chris Flynn et al. (2006), (4) Marasco et al. (2012), Lehner et al. (2011), (5) Cappellaro et al. (1997). 86

6.1 List of parameters adopted for the four models tested. The first column contains the parameters and each of the following four columns is representative of a specific model. Notice that the differences among the models lay in the SFR adopted (first row) which is obtained fine tuning the SFE ν, which is variable as well (last row). In the first and second row the short version of the references are reported: Ken98 for Kennicutt (1998), Has21 for Hasselquist et al. (2021), HZ09 for Harris et al. (2009), Cal03 for Calura et al. (2003), Kro93 for Kroupa et al. (1993), Kro01 for Kroupa (2001) and Sal55 for Salpeter (1955). 100

6.2 Observational quantities used to constrain the chemical evolution model. The columns from 1 to 5 indicate, in order, the observable quantity considered, the model, the theoretical prediction from that model, the observation and the reference. It is highlighted that Model 3 and Model 4 reproduce these observables better than Model 1 and Model 2 do, but, relying only on this table, is not possible to prefer one over the other. 105
6.3 In the first two rows the references to the yields are listed, whereas from the third to the sixth row I show the results for all my models, with the best one being Model 3. The first column shows the mass of ^{26}Al produced by massive stars, the second one lists the total mass of ^{26}Al produced by massive stars together with nova systems and the third column contains the results about ^{60}Fe. 108
6.4 Fluxes of ^{26}Al and ^{60}Fe for all the models computed using Eq. 6.1. In the first column I present the flux of ^{26}Al in the case of production only by massive stars, in the second the flux of ^{26}Al considering also the contribution by novae, in the third I list the flux of ^{60}Fe. In the fourth i show the flux ratio ^{60}Fe/^{26}Al using the the values from columns 3 and 2. 109

7.1 Parameters of the five MW and two LMC models tested (indicated in the first column). The following columns list, in order, the SFE (time dependent in both cases), the IMF adopted, the timescale of the infall, the wind efficiency (if included in the model) and the fraction of SNIa. In column three the short reference is reported: Kro93 for Kroupa et al. (1993), Kro91 for Kroupa (2001) and Sal55 for Salpeter (1955). 115
7.2 Modified nucleosynthesis yields. Correction factors adopted in the NEW MW and NEW LMC models for Fe, Mg, Al, and Mn considering the same stellar sources as in Vasini et al. (2022) and Vasini et al. (2023). These same prescriptions are also used in the WIND MW model. 118
7.3 Yield correction adopted in MIX MW model and MIX LMC model. In these two models, I adopt the corrections already introduced in Tab. 7.2 for Mg, Fe, and Al. Regarding Mn, I adopt the original prescriptions since, as displayed in the right panel of Fig. **??**, they are the best at reproducing the observed abundance ratio. 118

Acronyms

AGB **A**symptotic **G**iant **B**ranch. *(p. 19, 59, 62, 63, 73, 74, 79, 84, 103, 106, 118, 122, 142)*

AGN **A**ctive **G**alactic **N**uclei. *(p. 44, 55)*

APOGEE **A**pache **P**oint **O**bservatory **G**alactic **E**volution **E**xperiment. *(p. xix–xxi, 114, 119–122, 124, 125, 127–129, 131, 132)*

BATSE **B**urst **a**nd **T**ransient **S**ource **E**xperiment. *(p. xiv, 43)*

BH **B**lack **H**ole. *(p. 17, 30)*

CCSN **C**ore-**C**ollapse **S**uper**n**ova. *(p. 51, 54, 60, 78, 103, 105, 114, 122)*

CGRO **C**ompton **G**amma **R**ay **O**bservatory. *(p. xiv, 42–44)*

CMD **C**olour-**M**agnitude **D**iagram. *(p. 102)*

COMPTEL **Comp**ton **Tel**escope. *(p. xiv, xv, 18, 42–44, 46–55, 57, 58, 64, 73, 77, 85, 135, 136)*

COSI **Co**mpton **I**mager and **S**pectrometer. *(p. xvi, 24, 54–56, 96, 97, 110–112, 138, 139)*

DR **D**ata **R**elease. *(p. xix–xxi, 114, 119–122, 124, 125, 127–129, 131, 132)*

dSph **d**warf **Sph**eroidal galaxy. *(p. 114)*

ECSN **E**lectron-**C**apture **S**uper**n**ova. *(p. 30, 109, 110)*

EGRET **E**nergetic **G**amma **R**ay **E**xperiment **T**elescope. *(p. xiv, 43)*

ESA **E**uropean **S**pace **A**gency. *(p. 44, 97)*

FWHM **F**ull **W**idth at **H**alf **M**aximum. *(p. 40, 45)*

GRB **G**amma-**R**ay **B**urst. *(p. 44, 55)*

GRIS **G**amma-**R**ay **I**maging **S**pectrometer. *(p. 42)*

HEAO 3 **H**igh **E**nergy **A**stronomy **O**bservatory **3**. *(p. 41, 42)*

HEAO C-1 **H**igh **E**nergy **A**stronomy **O**bservatory **C-1**. *(p. 41)*

IBIS **I**mager on **B**oard the **I**NTEGRAL **S**atellite. *(p. xiv, 45, 46)*

IMF **I**nitial **M**ass **F**unction. *(p. ix, xvii, xxvi, 28, 29, 51, 59, 61, 68–70, 74, 78, 96, 98–100, 102, 108, 109, 111–113, 115, 116, 119, 122, 128, 129, 132, 135, 138–140, 143, 144)*

INTEGRAL **Inte**rnational **G**amma **Ra**y **L**aboratory. *(p. xiv, xxiv, 38, 39, 44, 45, 50, 52–55, 57, 58, 64, 67, 73, 77, 85, 97, 135, 136, 138)*

IRA **I**nstantaneous **R**ecycling **A**pproximation. *(p. 23)*

IREM **I**NTEGRAL **R**adiation **E**nvironment **M**onitor. *(p. 45)*

ISM **I**nter **S**tellar **M**edium. *(p. 4, 5, 23–27, 29, 30, 32, 36, 48, 50, 51, 53, 58, 60, 68, 70, 75, 76, 78, 97, 104)*

LB **L**ocal **B**ubble. *(p. 22)*

LG **L**ocal **G**roup. *(p. i, ii, 86)*

lGRB **l**ong **G**amma **R**ay **B**urst. *(p. 30)*

LIMS **L**ow-**I**ntermediate **M**ass **S**tars. *(p. 29, 118–120, 132)*

LMC **L**arge **M**agellanic **C**loud. *(p. ix, xix, xx, xxvi, 24, 25, 31, 35, 96–99, 102–104, 106–117, 119, 120, 122, 124–127, 131, 132, 134, 138–140, 143)*

LSST **L**arge **S**ynoptic **S**urvey **T**elescope. *(p. 86)*

MS **M**ain **S**equence. *(p. 3, 5, 13, 16, 17)*

MW **M**ilky **W**ay. *(p. i, ix, xv, xvii, xix, xx, xxv, xxvi, 8, 18, 22–29, 31, 35, 39, 40, 46, 49–55, 57–59, 69, 73, 76, 77, 79, 81–83, 85–88, 91, 92, 97, 106–109, 111–117, 119–124, 126, 128–132, 134–140, 143)*

NASA **N**ational **A**eronautics and **S**pace **A**dministration. *(p. 42, 44, 54, 56, 97)*

NS **N**eutron **S**tar. *(p. 17, 30)*

OMC **O**ptical **M**onitoring **C**amera. *(p. 45)*

OSSE **O**riented **S**cintillation **S**pectrometer **E**xperiment. *(p. xiv, 43)*

RGB **R**ed **G**iant **B**ranch. *(p. 119)*

SF **S**tar **F**ormation. *(p. xvi, xviii, xix, xxv, 22–24, 47, 58, 61, 62, 72, 76, 87, 97, 99, 101, 104, 106, 111, 114, 117, 126, 130, 136, 142)*

SFE **S**tar **F**ormation **E**fficiency. *(p. xvi, xviii, xix, xxv, xxvi, 28, 59, 61, 62, 78, 99–102, 106, 115–117)*

SFH **S**tar **F**ormation **H**istory. *(p. xviii–xx, 58, 98, 99, 101–104, 106, 107, 111, 113–117, 126, 128, 130, 131, 139, 142)*

SFR **S**tar **F**ormation **R**ate. *(p. xvi–xix, xxv, 23, 26, 28, 32, 51, 54, 59–62, 69, 71, 75–79, 81–88, 91, 93, 95, 96, 98–106, 108, 110, 111, 114, 116, 117, 126, 128, 130, 132, 135, 137–140)*

SLR **S**hort-**L**ived **R**adioisotope. *(p. i, 7, 8, 22–24, 36, 39, 57, 76, 82, 87, 88, 134)*

SMC **S**mall **M**agellanic **C**loud. *(p. 114)*

SMM **S**olar **M**aximum **M**ission. *(p. 41)*

SN **S**uper**n**ova. *(p. 8, 12, 22, 23, 26, 27, 32, 41–43, 51, 53, 59, 71, 103, 104, 111, 135, 138)*

SNIa Type **Ia** **S**uper**n**ova. *(p. xxv, xxvi, 17, 19, 20, 29, 30, 33, 59, 60, 62, 63, 72–74, 78, 79, 84, 86, 87, 98–100, 103–106, 114–116, 118–120, 122, 132, 135, 140, 141)*

SNIb Type **Ib** **S**uper**n**ova. *(p. 30, 33, 78, 98, 116, 135)*

SNIc Type **Ic** **S**uper**n**ova. *(p. 30, 33, 78, 98, 116, 135)*

SNII Type **II** **S**uper**n**ova. *(p. xxv, 30, 33, 46, 48, 72, 78, 86, 87, 98, 104, 116, 135, 140)*

SPI **Sp**ectrometer on **I**NTEGRAL. *(p. xiv, 38, 45, 46, 50, 51, 97)*

SS **S**olar **S**ystem. *(p. 4, 22, 39, 58, 70)*

Super-AGB **Super-A**symptotic **G**iant **B**ranch. *(p. 59, 62, 63, 73, 74)*

TNR **T**hermo**n**uclear **R**unaway. *(p. 16, 17)*

TOF **t**ime **o**f **f**light. *(p. 37)*

UfD **U**ltra-**f**aint **D**warf. *(p. 114)*

VMS **V**ery **M**assive **S**tar. *(p. 143, 144)*

WD **W**hite **D**warf. *(p. 16, 17, 28, 30, 33, 34, 76, 85, 88, 109, 137, 141, 142)*

WR **W**olf-**R**ayet. *(p. xv, 11, 12, 22, 30, 46–48, 143)*

XMM **X**-ray **M**ulti-**M**irror Mission. *(p. 44)*

ZAMS **Z**ero **A**ge **M**ain **S**equence. *(p. xiii, 13–15)*

1

Introduction

Since the publication of the first version of the periodic table of the elements by Dmitri Mendeleev and Lothar Meyer in the second half of the XIX century, the question regarding the origin of the elements has always been wondered and investigated. It became more and more interesting as soon as other elements were discovered and added to the periodic table in the appropriate location, depending on their properties that the new elements were showing.

Currently, the periodic table counts 118 elements, among which stable and unstable ones can be found, either naturally or artificially produced.

Several branches of science have developed to pursue the exploration of the origin and formation of the elements, and each branch unveiled different aspects of the properties and structure of these nuclei. Nevertheless, after more than a century, the periodic table still holds unanswered questions.

In this context, the role of Astronomy has always been that of investigating the processes and the environments behind the synthesis of the elements. In the XX century, in fact, it became clear that the sites of production of the elements were located inside the stars and therefore, it was within the scopes of Astronomy to discover the mechanisms involved.

In this Thesis the investigation of two specific isotopes, ^{26}Al and ^{60}Fe, from the point of view of chemical evolution is performed. By assuming the prescriptions provided by nucleosynthesis and stellar models, the chemical evolution adopts the abundances of the elements measured in galaxies to unravel the evolution of the galaxy itself, knowing that different elements can highlight different aspects.

In this first Chapter, the fundamental mechanisms of the formation of the elements are explored. Particular attention will be paid to the synthesis of ^{26}Al and ^{60}Fe, explaining their reactions and production sites. Finally, the state of the art and the structure of the Thesis will be presented.

1.1 Nucleosynthesis of elements

After the work of Mendeleev, several decades passed before the link between the origins of atoms and the stars was established. Eddington (1919) analysed one of the most important question of that epoch, namely where the energy continuously radiated by the stars came from. The popular theory at the time was that the gradual shrinkage of the star would convert gravitational energy into heat, necessary to replace the heat radiated away. Unfortunately, this mechanism implied a very strict limit on the lifetime of the stars that was against the theoretical calculation provided by the stellar evolution theory. Anyway, this issue was usually ignored by invoking the plausibility of this hypothesis. Eddington (1919), also mentioning the ideas presented by Russell (1919), proposed a different answer to the problem. The hypothesis was that the energy dissipated as radiation was coming from an unknown but enormous store of energy within the star itself, with some specific requirements:

- it had to generate a huge amount of energy per unit mass under the stellar interior conditions, but almost none under laboratory conditions;
- its rate should not accelerate, since the stars appeared to be quite stable and the transient phenomena appeared to involve only the superficial layers;
- it should die down as time proceeds, so as to allow the star to evolve to the dwarf stages, when the heat radiated is small.

The author did not find the actual explanation regarding the source of the energy sustaining a star, and was not even too confident about this hypothesis. Nevertheless, the features pointed out in Eddington (1919) are precisely those of the nuclear burnings that, now we know, are those sustaining a star.

It was only with the work by Burbidge et al. (1957) that the picture became clearer. At that time, four hypothesis were viable: three of them were predicting a primordial origin of elements requiring matter in a particular state for which there was no evidence, whereas the fourth depicted the stars as the current producers of nuclei. Later, Iben (1967) unravelled the processes occurring in the stellar interior, describing step by step all the nuclear burnings responsible for the production of the chemical elements. The only other environment where the synthesis of elements occurred was the Big Bang. In the very early Universe, in fact, the extreme conditions favoured the production of the lightest elements, Hydrogen (H and its heavier isotope Deuterium ^{2}H), Helium (in two isotopes ^{3,4}He), Lithium (^{7}Li) and

Beryllium (^{7}Be). The absence of stable isotopes with atomic numbers A=5 and A=8, prevented the early epoch synthesis of heavier elements. A three-particle reaction was needed, but the environmental conditions inhibited its occurrence.

At the end of this phase, the Universe was composed of Hydrogen for almost the 75%, Helium for almost the 25% and small traces of Lithium and Beryllium. All the heavier elements were produced later in the stars and still represent a minor fraction of all the matter in the Universe. Hence, for simplicity, the Universe is usually assumed to be chemically composed of three parts, labelled as X, Y and Z. X represents the fraction of Hydrogen, Y represents the fraction of Helium and Z indicates all the elements beyond Helium, usually called *metals*. The metal content in a galaxy is as well indicated by Z and is called *metallicity*.

In the following section the evolution of a star together with the nuclear processes occurring inside and producing metals are presented.

1.1.1 Nuclear burnings: up to the Fe group

As anticipated in the previous section the synthesis of the metals occurs in the stellar interiors and is strictly related to the stellar evolution.

The evolution of a star can be followed on a phase diagram shown in Fig. 1.1 in the temperature-density plane, here represented in log-log scale. The position of a star in this diagram depends on its evolutionary phase, which in turn is strictly related to the nuclear burning occurring in its core. The temporal evolution proceeds from the lowest to the highest temperature and density, therefore every star at its birth is located at the lower left corner and moves towards the upper right one.

The actual birth of a star is marked by the ignition of H in the stellar core. The radiation produced by the H nuclear burning allows the star to balance the gravitational energy, that would lead the star to the gravitational collapse. This phase is called Main Sequence (MS) and is the longest phase that the star will experience. Its duration depends on the initial stellar mass, with lower mass stars experiencing longer MSs. During the H burning, He is synthesised via the *p-p chain* or the *CNO cycle*, depending again on the initial stellar mass. Once the H in the core has been exhausted, no radiation can sustain the star anymore, hence it exits the MS and shrinks under the effect of the gravitational energy. The shrinkage increases the temperature in the core until it reaches the He ignition temperature. At this point, He is ignited in the core and heavier nuclei, namely ^{12}C and ^{16}O, are synthesised. The He burning core is surrounded by a H shell, whose temperature allows the H burning. In this phase therefore, He is synthesised in the shell

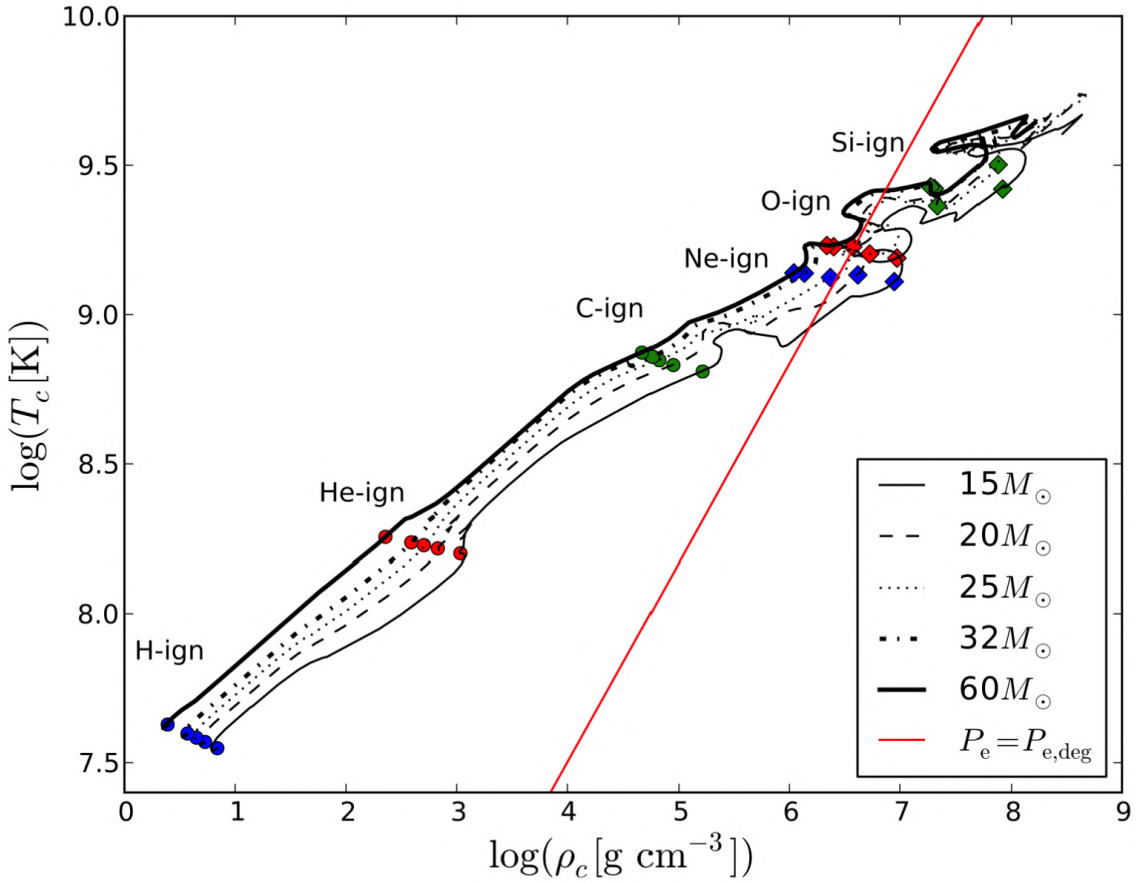

Figure 1.1: *Evolutionary traces on the temperature-density plane in log-log scale. The position on the plane represent the current nuclear phase of each star. The coloured dots represent the point of ignition of a burning. Taken from Diehl et al. (2022).*

and C and O are synthesised in the core. Once all the He in the core has been consumed, the He phase ends and the star again shrinks until the temperature of C ignition is reached. This cycle, where burning phases and contraction phases alternate, proceeds involving different elements in the following sequence: from H to He, from He to C and O, from C to Ne, from Ne to O, from O to Si and last, from Si to Fe. After the synthesis of Fe no other burnings can occur since they would not produce energy but, instead, would consume it. Thus, the star heads towards the latest phases of its life when the products of the nucleosynthesis are ejected in the Inter Stellar Medium (ISM) and the star dies. Fig. 1.2, taken from Arcones et al. (2023), shows the Solar System (SS) abundances (Lodders, 2021) as a function of the mass number A. From left to right the whole periodic table is represented, starting from H up to Pb. Different colours represent the different production mechanisms responsible for the synthesis of those elements. The Big Bang nucleosynthesis is marked in yellow and the nuclear burnings are marked in green. As can be seen, hydrostatic burnings are responsible for the produc-

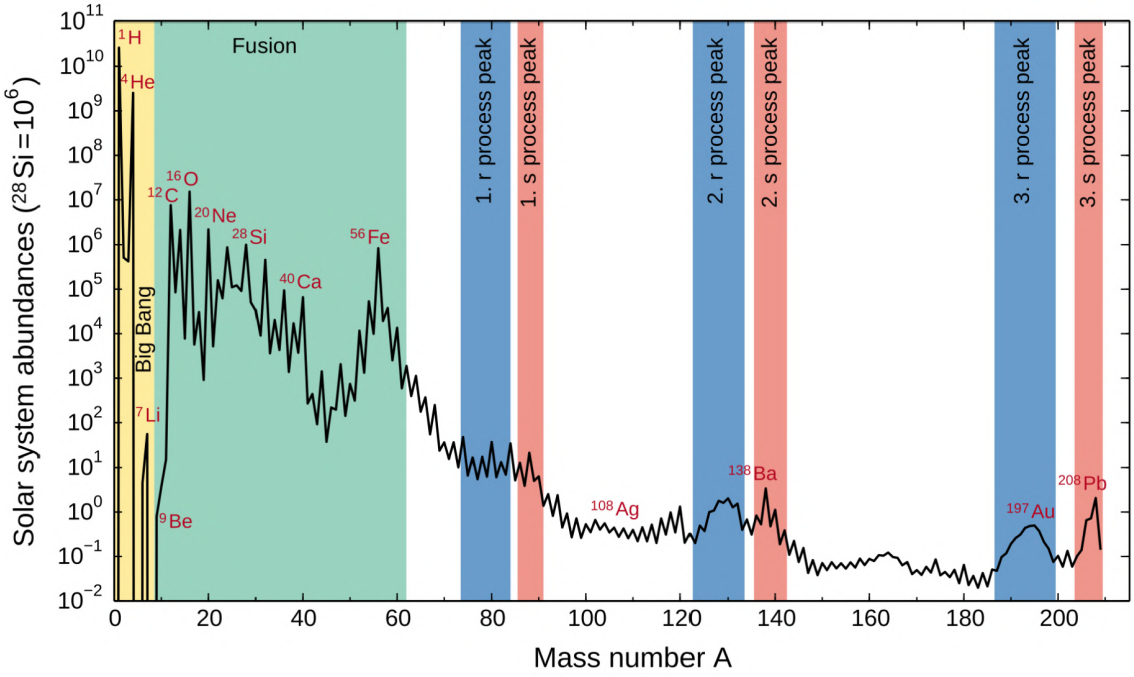

Figure 1.2: *Solar System abundances from Lodders (2021) as a function of the mass number A. Different processes are indicated by different colours: the Big Bang nucleosynthesis in yellow, the stellar fusion in green, and the r- and s- processes are highlighted in blue and red, respectively. Taken from Arcones et al. (2023).*

tion up to the Fe peak, and all the heavier nuclei are produced by different reactions.

The initial mass of the star plays a crucial role in determining the products of the nucleosynthesis, since not all the stars experience the whole sequence of nuclear burnings. The mass not only determines the duration of the MS, the nuclear path followed to synthesise He and the final fate of the star, but it determines which is the burning stage that the star can actually reach. The more massive a star is, the more advanced will be the burning stage that can occur in its core. The mass in fact puts an upper limit on the temperature that the core can reach during the shrinking phase. If a star is not massive enough, it will not reach the Si burning, but it will stop earlier and will pollute the ISM with lighter elements. What is described above is the complete sequence of burnings, which, however, only the most massive stars can experience.

Even though nuclear burnings occur both in the core and in the surrounding shells, the atmosphere of a star never reaches the ignition temperatures, thus maintaining its original chemical composition throughout its whole lifetime. Hence, the chemistry of the stellar interior evolves while the superficial one does not, and rather reflects the chemistry of the gas out of which the star formed.

1.1.2 Neutron capture: beyond the Fe peak

Some of the reactions occurring during the hydrostatic burnings provide a large abundance of free neutrons. During the quiescent He burning neutrons are produced by the reaction chain that, starting from ^{14}N, synthesises ^{25}Mg and, in even larger amount, by the reaction ^{13}C(α,n)^{16}O (Matteucci, 2003). This creates a free neutron rich environment, where neutron capture processes on seed nuclei (mainly ^{56}Fe) can occur. Two types of processes arise from the neutron capture mechanism, the *r-* (*rapid*) and *s-* (*slow*) *process*. The nucleus resulting from a neutron capture process will be a heavier isotope of the original seed, since the proton number does not change. A neutron rich nucleus is, typically, unstable and becomes increasingly unstable the more neutrons it captures, thus increasing the probability of a β decay. If the environment is extremely neutron rich, then the heavy isotope has a higher probability of capturing another neutron rather then β decaying. The characteristic timescale of this phenomenon is of the order of the second (Cowan et al., 2021), hence a r-process. On the contrary, if there are only few neutrons available then the opposite scenario occurs, where the β decay is more probable than a neutron capture. The timescale ranges from hundreds to thousands of years, hence a s-process (see Diehl et al. 2022; Arcones et al. 2023; Holmbeck et al. 2023 for further explanation regarding the astrophysical and nuclear aspects).

The sequence of neutron captures and β decays proceeds, giving rise to heavier and heavier nuclei. The nuclei up to Pb and Bi can be explained by the s-process, whereas to reach U and Th the r-process in an extremely neutron rich environment (created during explosive events) is necessary. In the end, these processes populate the whole periodic table, including the entire range of isotopes existing.

In Fig. 1.2 three local abundance maxima produced by the r-process and the s-process are highlighted in blue and red, respectively. The maxima can be explained considering the nuclear shell model. According to this theory, the nucleons occupy orbitals at specific energies and when an orbital is completed, or *closed*, that nucleus is more tightly bound than the others, and therefore is more stable. This happens at well defined mass numbers, usually called *magic quantum numbers*, namely A=82,126 and 184.

1.2 Short-Lived Radioisotopes

At the end of the XIX century, the periodic table was enriched with new elements, with characteristics that those known until that moment did not show. The discovery of natural radioactivity dates back to those years, when the works of

Henry Becquerel and Pierre and Marie Curie showed clearly that some isotopes could naturally turn into others, emitting radiation. Even though at a first glance this could be considered an exception, where the norm was represented by the stable isotopes, the point of view of Maria Goeppert-Mayer (see Mayer 1952) was opposite: "*It begins to look as if the Universe contained a very large number of metastable, 'fundamental' particles of which we are able to observe only those which, by some accident, have a low probability of decay*". Hence, stable isotopes are the exception, being nuclei with a null probability of decay.

The mathematical form of the radioactive decay can be derived considering that the variation of the number of nuclei $dN(t)$ in a time interval dt should be proportional to the initial number of atoms N and the length of the interval:

$$dN(t) = -\lambda N dt. \tag{1.1}$$

This results in a differential equation:

$$\dot{N}(t) = -\lambda N \tag{1.2}$$

that, when solved, gives the radioactive decay law:

$$N(t) = N_0 e^{-\lambda t}. \tag{1.3}$$

The factor λ represents the probability of decay, and physically, it is the inverse of the decay timescale $\tau = 1/\lambda$. τ has an extremely wide range of possible values that can span from the fraction of seconds, as in the case of ^{6}Be with a mean lifetime of the order of 10^{-21} seconds, to several billion years, such as in the case of ^{130}Te with a mean lifetime of around 10^{25} years.

The advantage of adopting radioactive nuclei as instruments is the possibility to use the intrinsic clock that they carry. Therefore, by measuring their abundance in the Galaxy, not only its nucleosynthesis history can be reconstructed, but it can also be dated without relying on indirect time proxies. Furthermore, by simultaneously analysing more radioactive isotopes with different decay timescales, an even more detailed history can be unveiled.

Some radioactive isotopes in particular have been playing a central role in Astrophysics, given their half-life which is the same as that of several Galactic phenomena. Among these ^{59}Ni (τ_{59} = 76 000 yr), ^{36}Cl (τ_{36} = 300 000 yr), ^{26}Al (τ_{26} = 0.717 Myr), ^{60}Fe (τ_{60} = 2.62 Myr), ^{53}Mn (τ_{53} = 3.7 Myr), ^{129}I ($\tau_{129} \sim$ 10 Myr), ^{244}Pu (τ_{244} = 15.7 Myr), ^{247}Cm (τ_{247} = 80.6 Myr) and ^{146}Sm ($\tau_{146} \sim$ 100 Myr) are usually referred to as *Short-Lived Radioisotopes* (SLRs). Their half-lives, indeed, can be

considered "short" in the astrophysical context, where the typical timescale is the Universe lifetime.

From the 60^{ies} on, SLRs have been used to develop the so called multimessenger astronomy, where astrophysical information is not collected only through radiation, but also through neutrinos, meteorites, and gravitational waves. In addition to the investigation of the radiation emitted during the radioactive decay (see Chapter 3), that allows the study of the recent Milky Way (MW) history by the tracing of the latest supernova (SN) ejecta, different types of investigation have been performed. In the case of ^{244}Pu and ^{247}Cm, for example, the study of the lunar soil was proposed, in order to look for imprints of nearby SN explosions (Fields et al., 1970). Later, also the analysis of the ice cores and deep-sea sediments on Earth was suggested. The idea is that meteorites can embed tiny dust grains that where formed after the condensation of nucleosynthesis products in a region around the solar system. Once they interact with the terrestrial atmosphere they get disrupted and the chemical elements that they carry can be released onto the Earth surface, and from there, they can get captured in ice or in the ocean floor (Ellis et al., 1996; Paul et al., 2001). These structures, considered often as archives, grow over a long time and the material accumulates into layers. The presence of radionuclides in these layers such as ^{10}Be, ^{26}Al, ^{36}Cl, ^{53}Mn, ^{60}Fe and ^{59}Ni allows to date the layers as well as the recent nucleosynthesis events in the solar vicinity (Diehl et al., 2022). A deeper insight in the different uses of SLRs will be given in Section 1.3.

The focus of this Thesis is studying the behaviour over the Galactic scale of two of them in particular, ^{26}Al and ^{60}Fe, being those than more than the others have been investigated in the last decades. For this reason, in the next subsections their nuclear features and nucleosynthesis will be explored.

1.2.1 ^{26}Al and ^{60}Fe nuclear properties

Fig. 1.3 shows ^{26}Al together with the neighbouring nuclides, with ^{27}Al as the only stable Al isotope. Different quantum levels of ^{26}Al are represented in Fig. 1.4. The ground state of ^{26}Al (^{26}Al^{g} for simplicity) has a half-life of 0.717 Myr that decays via electron capture or β^+ decay into the first excited state of ^{26}Mg, that, in turn, γ-decays into its ground state, emitting the characteristic 1808.63 keV line. The first excited ^{26}Al state (^{26}Al^{m}) is an isomeric state at 228 keV. Even though it is connected to the ^{26}Al^{g} state, the decay is highly suppressed (Alain Coc et al., 1999; Banerjee et al., 2018), and the main decay channel is the β^+ decay (half-life of $\sim$ 6 s) into the ground state of ^{26}Mg.

The correct treatment of the ^{26}Al^{g} and ^{26}Al^{m} states is crucial in the reaction

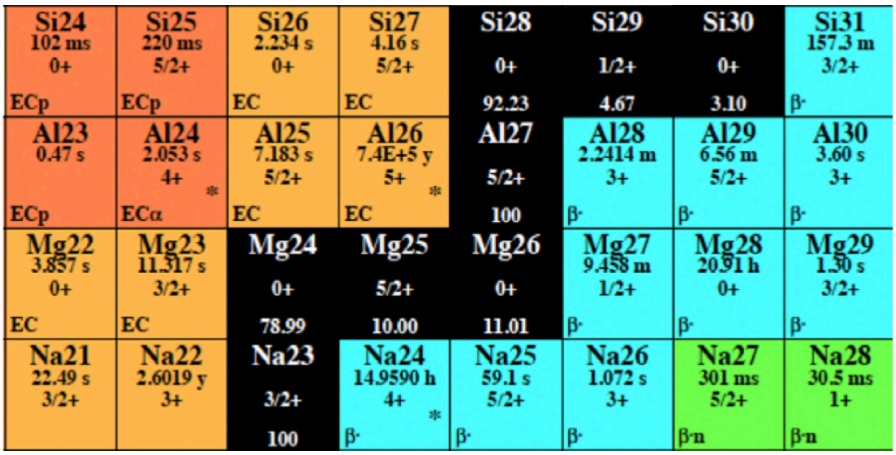

Figure 1.3: *Table of isotopes in the neighbourhood of ^{26}Al. Each isotope is identified by its symbol and its number of nucleons and are divided between stable isotopes in black cells and unstable isotopes in coloured cells. The lifetime, as well as the spin and parity, are listed in the second and third row and at the bottom left the main decay channel is indicated. For the stable isotopes, the abundance fraction is reported at the bottom. Taken from Diehl et al. (2021b).*

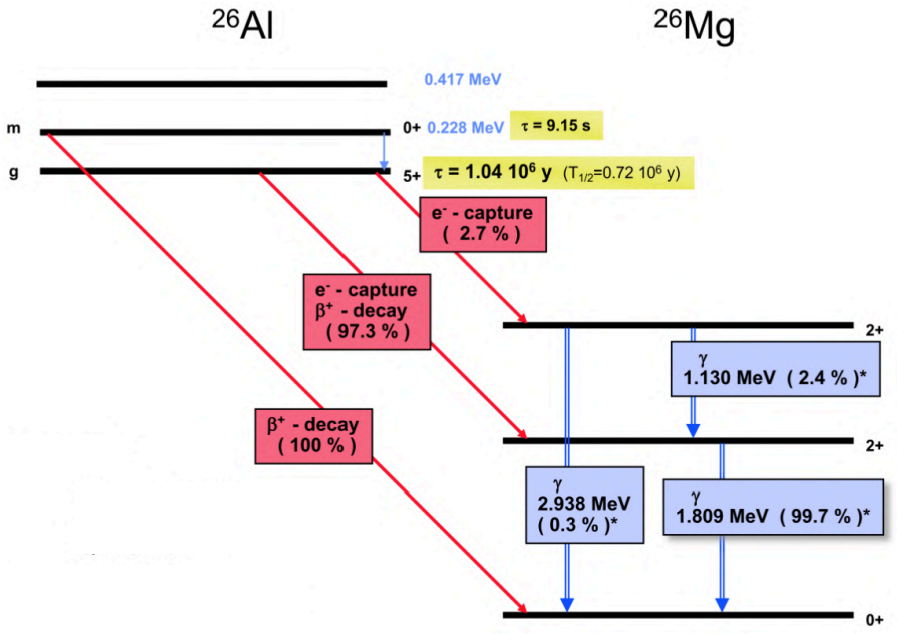

Figure 1.4: *Energetic levels of ^{26}Al and ^{26}Mg. To study ^{26}Al the ground state, $^{26}Al^g$, and the isomeric state, $^{26}Al^m$, have to be considered. $^{26}Al^g$ decays into the first excited state of ^{26}Mg, that than de-excites to the ground state, emitting the characteristic 1808.63 keV line. $^{26}Al^m$ typically decays into the ground state of ^{26}Mg, even though under stellar interior condition it can also decay into its own ground state, $^{26}Al^g$. Taken from Diehl et al. (2021b).*

network calculations (Runkle et al., 2001; Gupta et al., 2001). Three different temperature regimes can be identified:

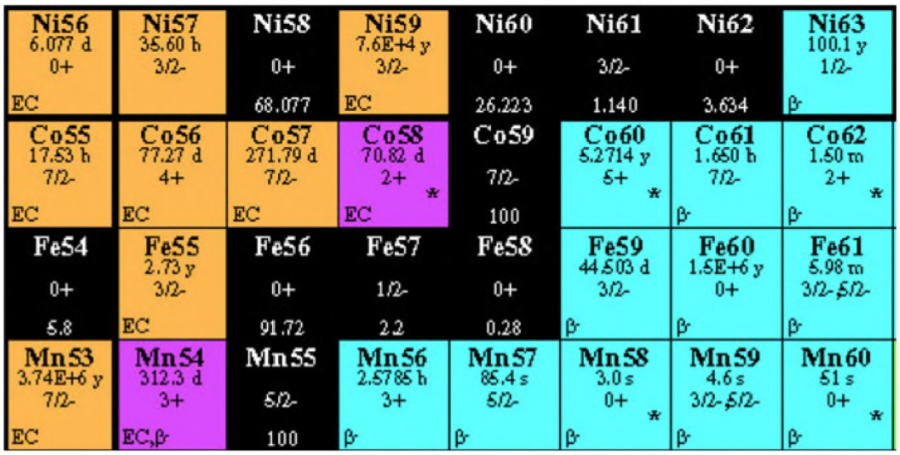

Figure 1.5: *^{60}Fe and the neighbouring isotopes involved in its production and destruction reactions. In black, the stable isotopes cells, whereas the coloured ones represent the unstable. The information reported in each cell are the symbol of each element with its nucleon number, the half-life, the spin and the parity. In the bottom left corner of the unstable isotopes the decay mechanism is indicated. For the stable ones, the abundance fraction is reported. Taken from Diehl et al. (2021b).*

- T $\lesssim$ 0.15 GK: the decay from ^{26}Al^{m} to ^{26}Al^{g}, that works as a communication channel between the two states, is almost completely suppressed, hence can be neglected. The two states can be treated as two different species with their separate production and destruction rates;

- T $\gtrsim$ 0.4 GK: even more energetic states can be populated on very short timescales, resulting in a thermal equilibrium that can be described by the Boltzmann equation. In this case one ^{26}Al species only (^{26}Al^{t}, defined at the thermal equilibrium) is sufficient to correctly treat this species;

- 0.15 GK $\lesssim$ T $\lesssim$ 0.4 GK: the two states can communicate but the timescale required to achieve the thermal equilibrium is comparable or even longer than the timescale of the β^{+} decay of ^{26}Al^{m}. Therefore, none of the two previous treatments is correct and at least the lowest four excited states of ^{26}Al have to be treated. However, this regime is rarely encountered, and the majority of the ^{26}Al production occurs at lower or higher temperatures.

In Fig. 1.5 ^{60}Fe is represented, together with the neighbouring nuclei that take part to its production and destruction reactions. Its half-life, 2.62 Myr, has recently been re-determined (Wallner et al., 2015; Ostdiek et al., 2017) after Rugel et al. (2009) questioned the 75% longer estimate performed by Kutschera et al. (1984).

Fig. 1.6 represents the decay chain of ^{60}Fe with multiple energetic levels involved. The chain starts from the ground state of ^{60}Fe that at first β^{-} decays to

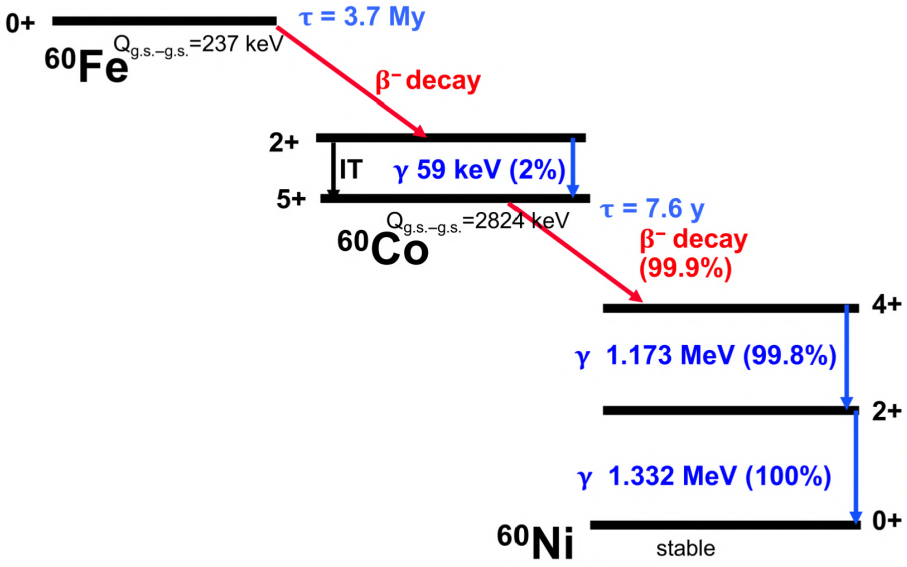

Figure 1.6: *Energy levels involved in the decay chain of ^{60}Fe. Starting from the ground state of ^{60}Fe, a β^- decay to ^{60}Co occurs, that in turns decays into ^{60}Ni. The double de-excitation of ^{60}Ni to its ground state produces the two characteristic γ-ray lines at 1.173 MeV and 1.332 MeV. Taken from Diehl et al. (2021b).*

an excited state of ^{60}Co, and then, to the ground state. ^{60}Co is itself unstable and decays to ^{60}Ni with a half-life of 5.27 yr. To reach its ground state, ^{60}Ni de-excites twice emitting photons at the characteristic wavelengths 1173 keV and 1332 keV (for longer discussion I refer to Diehl et al. 2021b).

1.2.2 ^{26}Al and ^{60}Fe nucleosynthesis

For the sake of this work the nucleosynthesis of ^{26}Al and ^{60}Fe needs to be explored deeper.

The nuclear processes responsible for the ^{26}Al production have been investigated for several decades and the most promising astrophysical sites were easily identified. Arnould et al. (1979), in fact, was already proposing the H burning shell in massive stars as the most likely location for the synthesis of ^{26}Al and also proposed novae as a secondary source, so as to reproduce the ^{26}Al/^{27}Al ratio measured in the Allende meteorite. This hypothesis was reinforced when a year later a new model for the explosive nucleosynthesis of hydrogen rich layers was proposed by Arnould et al. (1980).

At that time the observational side was also developing, and the first measurements provided the first ^{26}Al flux observation. After that, several works examined the production from different sources using those constraints on the nucleosynthesis. For example, Prantzos et al. (1986a) analysed the role of Wolf-Rayet (WR)

stars (M>50 $M_\odot$), that in the most optimistic scenario, according to their results, could account for the entire observed flux. This led to the calculation in Prantzos et al. (1986b) of a whole new set of yields for numerous isotopes for the same mass range. By the end of the nineties, as Walter et al. (1989) stated, SNe, novae, massive stars, WR, red giants and super massive stars had already been proposed and investigated as ^{26}Al and ^{60}Fe sources.

Later on, with the development of the nucleosynthesis calculations other additional degrees of freedom were considered. For example Diehl et al. (1998) opened the question regarding the rotation, stating that it could largely influence the results. It, in fact, would increase the mixing in the hydrogen envelope, whose global effect in the end would be that of increasing the ^{26}Al ejected. This was explored only several years later by Palacios et al. (2005), that found that rotation could double the ^{26}Al production.

On the other side, the investigation on ^{60}Fe had been more insidious, at least at the very beginning, mainly due to the lack of observations, which arrived with several years of delay relative to those of ^{26}Al. A complete treatment of the nuclear network that leads to the synthesis of ^{60}Fe was presented in Woosley et al. (1995) and after that, the discussion on its production was focused on refining those prescriptions.

In the next paragraphs, the state of the art of the nucleosynthesis in different sources of ^{26}Al and ^{60}Fe is analysed. The nuclear reactions involved in the production are presented, together with the main uncertainties still affecting the models.

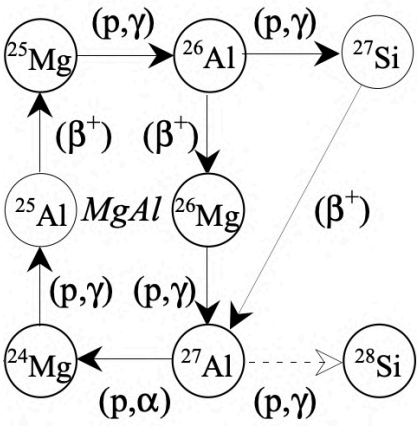

Figure 1.7: *MgAl reaction chain. Taken from Arnould et al. (1999).*

^{26}Al: massive stars

As explained in Arcones et al. (2023) most of the ^{26}Al is synthesised in massive stars in three different evolutionary stages:

- wind ejecta during the evolution;
- hydrostatic burning products ejected during the explosion;

- explosive Ne/C burning.

One of the most recent description of the ^{26}Al nucleosynthesis in massive stars was proposed by Limongi et al. (2006), even though the nuclear processes were known well before (see Walter et al. 1989). Limongi et al. (2006) reported all the conditions under which ^{26}Al is produced during the three already mentioned phases.

Starting from the MS, during the central H burning ^{26}Al is synthesised via the NaMgAl-cycle (see Thielemann et al. 2011) by the ^{25}Mg(p,γ)^{26}Al reaction and is destroyed by the β^+ decay into ^{26}Mg, since the temperature is still too low for the ^{26}Al(p,γ)^{27}Si to occur (see Fig. 1.7). The conversion of ^{25}Mg into ^{26}Al starts as soon as the star enters the MS and comes to completion after few million years. The ^{26}Al mass fraction in the H core depends on the amount of ^{26}Al synthesised and the amount that undergoes the β^+ decay into ^{26}Mg, and the balance between the two reactions changes over time. As pictured in Fig. 1.8 during the very first million years the ^{26}Al mass fraction increases and reaches a peak, after which it monotonically decreases. Nevertheless, the ^{26}Al production continues also after the maximum, which justifies why the decline is shallower than that of a pure β^+ decay (cyan dot-dashed line). It is only thank to that production that ^{26}Al is not completely destroyed but is rather partly preserved until the end of the central H burning. The different lines represent the scenario at different Zero Age Main Sequence (ZAMS) masses, namely the initial stellar masses.

Regarding the dependence of the ^{26}Al produced on the ZAMS stellar mass, an inverse behaviour would be expected. The efficiency of the ^{25}Mg(p,γ)^{26}Al scales directly with the initial mass, therefore the larger the mass the higher the efficiency, the faster the ^{25}Mg consumption, the faster the ^{26}Al decline. Notwithstanding this, the nucleosynthesis models show a strong direct correlation. The reason is that the larger the initial mass, the shorter the MS, and therefore the larger the ^{26}Al left at the end of the MS. This behaviour is also evident in Fig. 1.8, where the traces for different initial masses stop when the MS ends. Going to larger masses the ^{26}Al at the end of the MS is clearly larger.

The following evolutionary phase, the central He burning, is quite efficient in destroying the pre-existing ^{26}Al via the (n,α) and (n,p) reactions. Therefore, the only ^{26}Al preserved is the one locked in the H rich layers or that stored in the regions of the He core that will not be affected by the He burning. At this evolutionary point, the initial stellar mass starts to play a fundamental role in the amount of ^{26}Al ejected during the wind phase:

- masses from 11 to 30 $M_\odot$ eject only a tiny amount of ^{26}Al because their dredge up episodes do not involve the He core and the mass loss is weak. Hence,

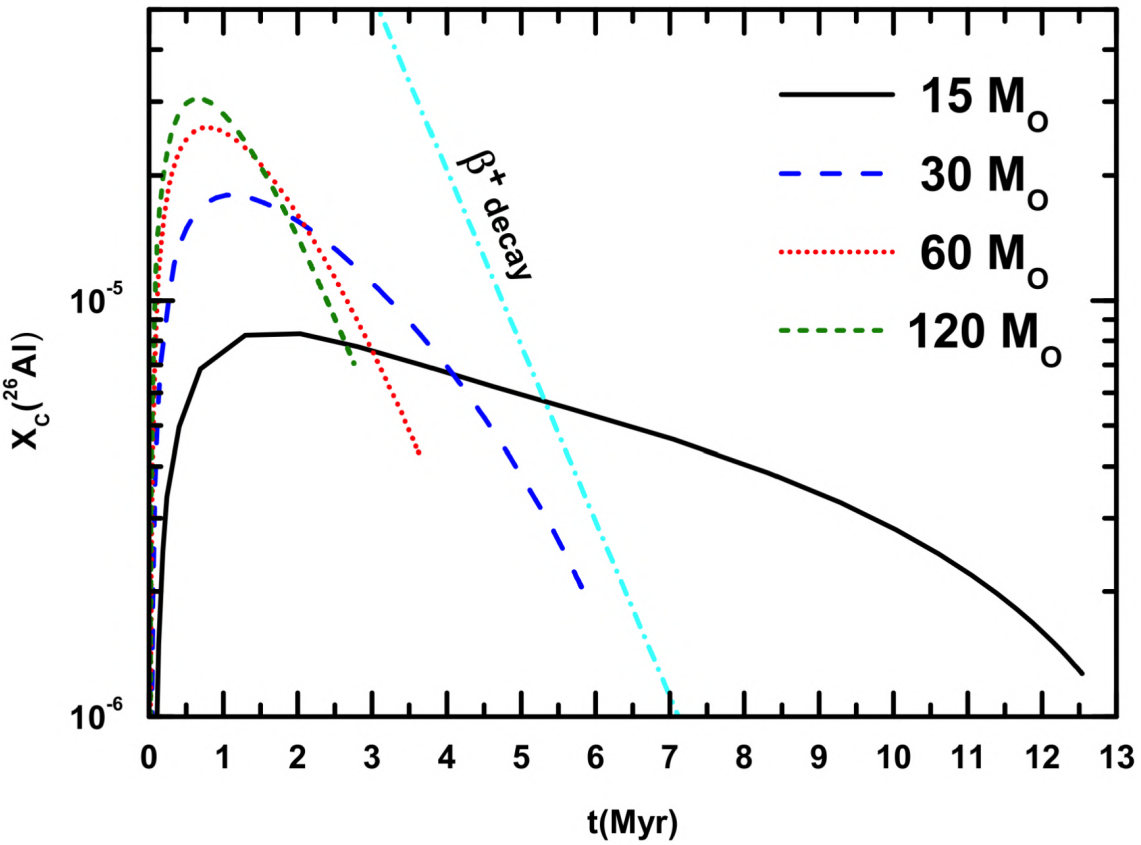

Figure 1.8: *Temporal evolution of the ^{26}Al mass fraction in the H convective core for different ZAMS masses. The maximum is reached after few Myr and is followed by a monotonic decrease due to the ^{26}Al β^+ decay into ^{26}Mg. The decline is shallower than the pure β^+ decay (cyan dot-dashed line) because ^{26}Al continues to be produced. It is precisely thanks to this production that a fraction of ^{26}Al is preserved until the end on the central H burning. Taken from Limongi et al. (2006).*

only a small fraction of the ^{26}Al located in the H-rich envelope is ejected;

- masses from 35 to 40 $M_\odot$ eject a larger amount of ^{26}Al because even though the dredge up does not involve the He core, as for the smaller masses, the mass loss is strong enough to eject part of the He core;

- masses larger than 40 $M_\odot$ eject an even larger quantity of ^{26}Al because, in spite of the absence of the dredge up, the wind strips a substantial portion of the He core.

During later evolutionary stages, the temperature becomes more and more important for the synthesis of ^{26}Al. The production of ^{26}Al can take place in the C shell only after the gravitational collapse following the central Si burning. This collapse in fact, increases the temperature of the C shell up to Log(T)~9.255, triggering the production of ^{26}Al.

At variance with the C burning, ^{26}Al is always produced during Ne burning (both in the core and in the shell). Nonetheless, at the temperatures of Ne burning, the ^{26}Al destruction is quite quick and only the presence of an efficient convective shell could preserve at least part of the ^{26}Al recently produced. Unfortunately the presence of such a shell is predicted only by the stellar models with ZAMS masses 14 and 15 $M_\odot$, that manage to eject a large amount of ^{26}Al.

Regarding the explosive nucleosynthesis, the temperature that the C convective shell experiences (~2.3 billion degrees) is adequate for the ^{26}Al production. The ^{25}Mg(p,γ)^{26}Al reaction is again the main source of ^{26}Al and the (n,p) and (n,α) reactions lead its destruction. It must also be remembered that the shock wave itself, while triggering the production of ^{26}Al, it also destroys part of it when the shock front propagates inside the star. Despite this, as Fig. 1.9 pictures, the explosive nucleosynthesis represents the main ^{26}Al production channel for all the masses from 11 to 120 $M_\odot$ except for the 15 $M_\odot$ where the hydrostatic burning dominates. In this Figure is also evident that the wind contribution is minor up to 60 $M_\odot$, after which it contributes to around ~1/3 of the total ^{26}Al synthesised.

As Thielemann et al. (2011) underlines, the amount of ^{26}Al ejected is, in general, strongly dependent on several factors such as metallicity, initial stellar mass, rotation and mass loss. Many other issues come from the nuclear side, that provides many different input for the nucleosynthesis while carrying large uncertainties. According to Limongi et al. (2006) the prescriptions that may significantly alter the ^{26}Al production are:

- the adopted initial ^{25}Mg abundance. The ^{26}Al ejected during the wind phase scales directly to the initial ^{25}Mg. By doubling it, a doubling of the ^{26}Al ejected is observed;

- the size of the H convective core. The direct effect is that of determining the abundance and the distribution of ^{26}Al inside the stars, whereas the indirect effect is the constrain on the He core size, that drives the following evolution of the star;

- the ^{25}Mg(p,γ)^{26}Al reaction cross section. The amount of ^{26}Al ejected by the wind does not scale monotonically with this cross section and depends on it only mildly.

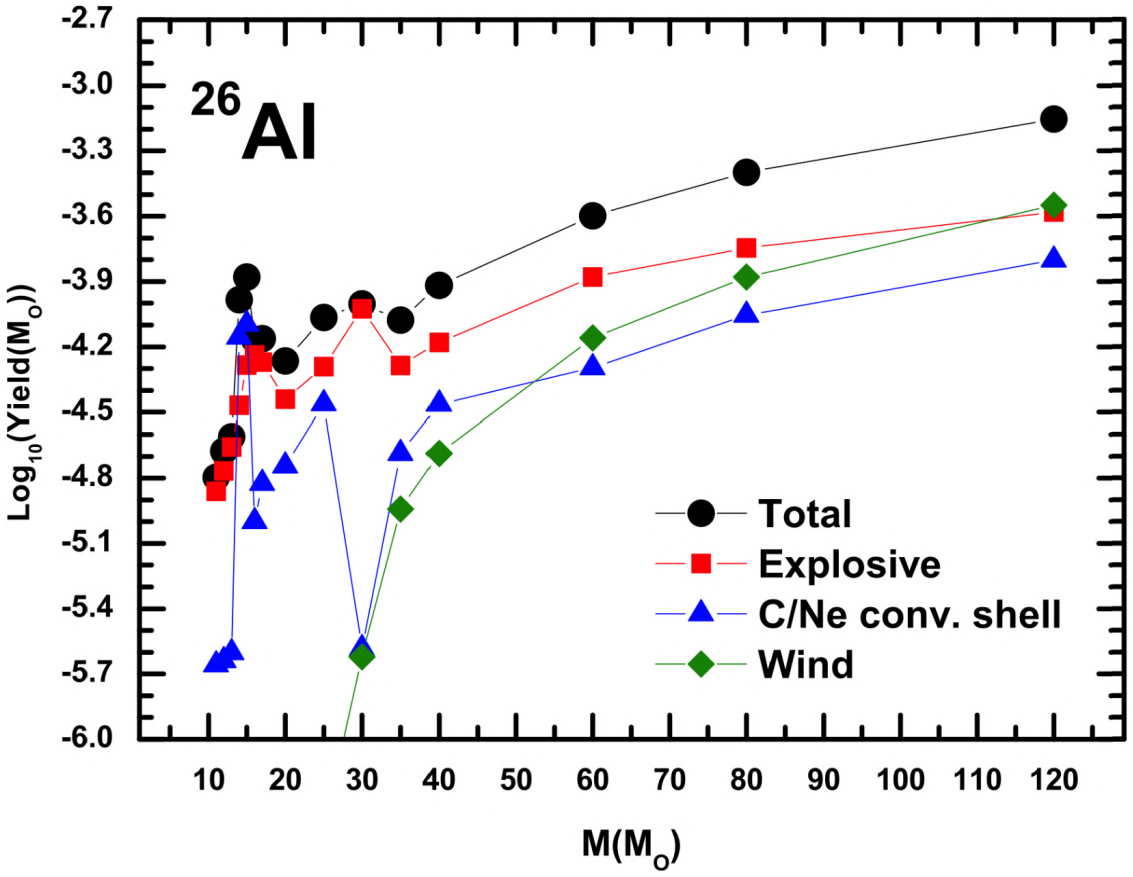

Figure 1.9: *Different contributions to the ^{26}Al total yield for different initial stellar masses. The contribution analysed are ascribed to the wind (green diamonds), the C/Ne convective shell (blue triangles) and the explosive nucleosynthesis (red squares). The total yield is depicted by black dots. Taken from Limongi et al. (2006).*

^{26}Al: nova systems

In the modern scenario (whose beginning for nova theories is set by the work of Schatzman 1951) a Classical Nova is generated when an explosive event is triggered by the ignition of the thermonuclear runaway (TNR) on the surface of a white dwarf (WD) while it accretes material from a low MS companion (Gallagher et al., 1978). Typically, as represented in Fig. 1.10, a nova originates from a semi-detached binary system, where the photosphere of the late-type MS star completely fills its Roche lobe. In this configuration, this MS star transfers H-rich material through the inner L_1 Lagrangian point to the WD companion. Since the accreting material has an angular momentum with respect to the WD, the gas does not fall directly on the WD, but will rather start orbiting around it. Friction and viscosity processes quickly circularize the bulk motion of the accreting gas, forming an accretion disc around the WD. If the accretion rate is low enough, the gas can become degenerate

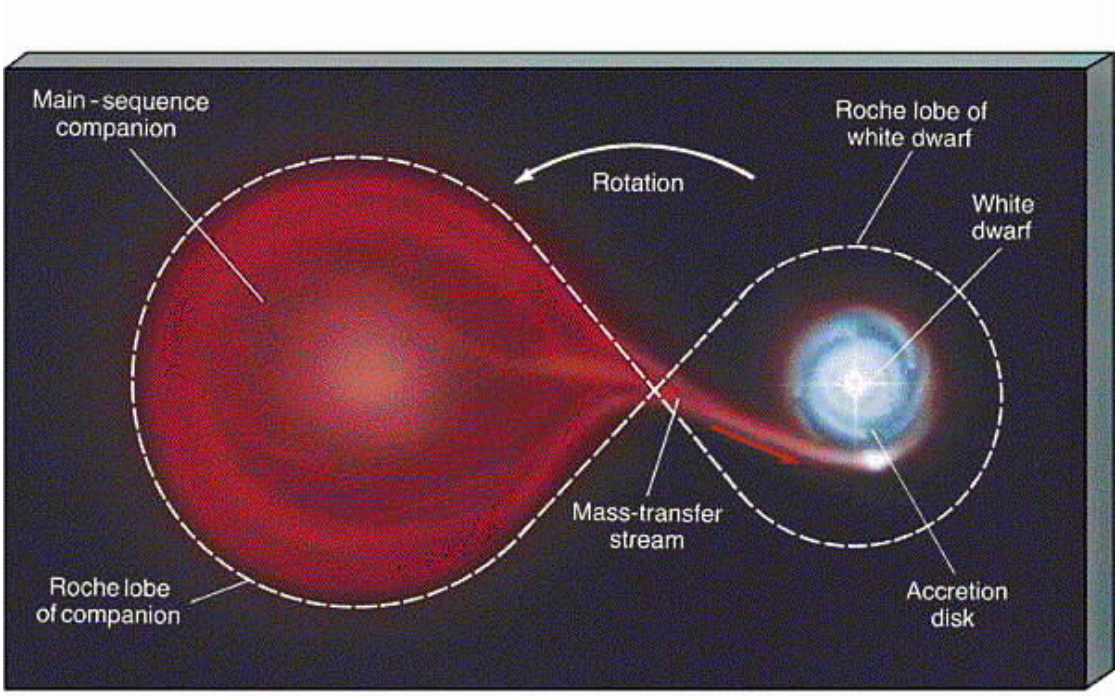

Figure 1.10: *Schematic representation of a nova system during the accretion phase. Taken from www.astro.berkeley.edu.*

before reaching the Chandrasekhar mass (M_{Ch} = 1.44 $M_\odot$) thus triggering the TNR at the base of the accreted envelope which leads to a nova explosion. This event does not disrupt the WD which will experience periodical eruptions (~10^4 during the average lifetime of a nova, 10^8 yr, see Ford 1978) at intervals that may range from a few months ("Recurrent Novae") to 10^5 yr ("Classical Novae") (for further description we refer to Della Valle et al. 2020).

Nova systems can differ for the characteristics of the accreting component as well as for those of the donor star. The accreting component can be a WD with initial mass in the range 0.7 - 1.3 $M_\odot$, and therefore it can be a carbon-oxygen (CO) nova if its mass is in the lower side of the interval or a oxygen-neon (ONe) nova, if its in the more massive end. If the WD mass exceeds the 1.3 $M_\odot$ the system will reach the Chandrasekhar mass and generate a Type Ia SN (SNIa). A nova system will be generated also if the accreting component is a neutron star (NS) or a black hole (BH). On the other side, the donor star can be a low/high mass MS star or a star in a later evolutionary phase. The result is that every combination of accretor + donor produces a nova with different characteristics (interval between two consecutive eruptions, explosion energy, delay-time distribution and nucleosynthesis) thus creating a plethora of possible scenarios.

Novae were largely discussed as a source of ^{26}Al after Compton Telescope (COMPTEL) provided the first 1.809 MeV image of the MW (see Sec. 3.3.2). Nevertheless, novae started being investigated way earlier. For example, Clayton (1984a) proposed novae as the main source of ^{26}Al when the HEAO-3 satellite (see Section 3.2) performed the firsts ^{26}Al flux measurements. The ^{26}Al mass detected in the Galaxy, if produced by massive stars, implied a concentration of ^{27}Al around thirty times higher than the solar one and a flux of ^{44}Ti ~150 times larger than that detected. Novae represented instead the most reasonable option assuming a 40 novae yr^{-1} events and considering that due to obscuration the rate could be even larger. Later, Higdon et al. (1989) tried to discriminate between different nova source models, even though the measurements were still too rough to distinguish between CO and ONe novae. Nofar et al. (1991) instead managed to identify ONe novae as those contributing most to ^{26}Al and after that, works such as A. Coc et al. (1995) and Politano et al. (1995) confirmed that result.

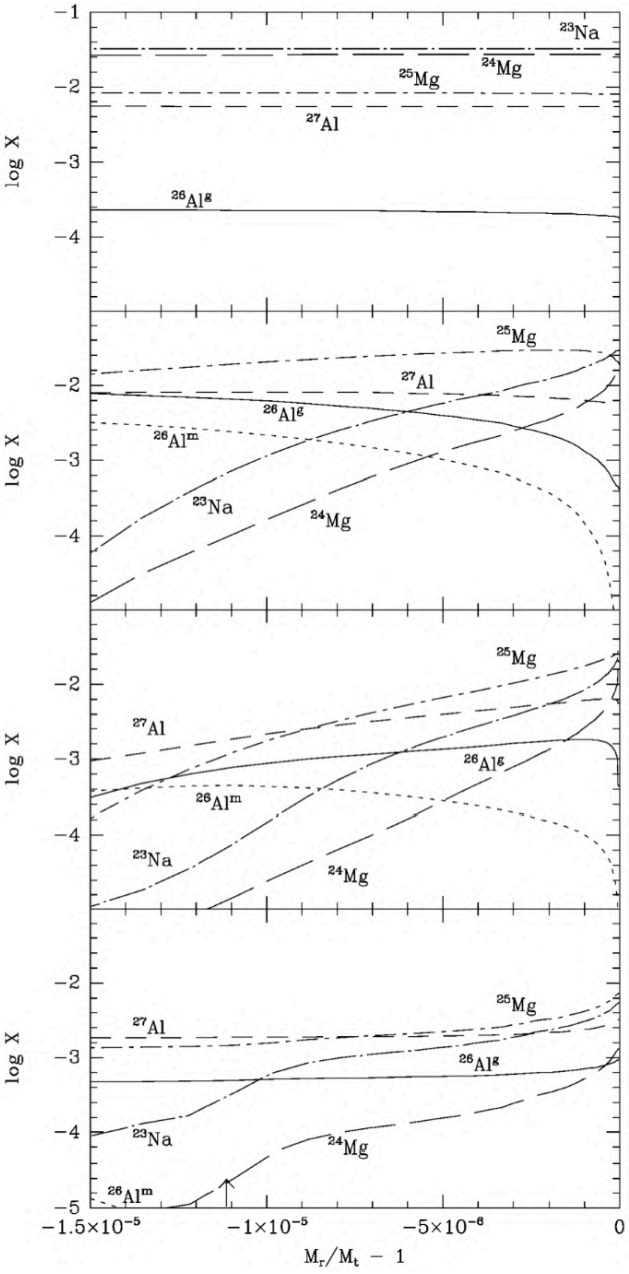

Figure 1.11: *Snapshots of the evolution of Mg-Al group nuclei along the accreted envelope of a ONe nova. The four panels represent four different temperatures and the temporal evolution proceeds from the top panel down to the bottom one. Taken from José et al. (1997).*

José et al. (1997) provided a detailed description of the ^{26}Al production by

novae. In Fig. 1.11 four snapshots of the evolution of the Mg-Al group element at different temperatures are reported. In the first panel, when the temperature at the burning shell has reached ~10^8 K, the profiles along the accreted envelope of the Mg-Al group elements are flat because the convective timescale is similar to the timescale of most of the nuclear reactions. When the temperature rises up to ~2.1×10^8 K, in the second panel, the nuclear timescale becomes shorter, thus allowing mixing only between adjacent regions, and the profiles do not look flat anymore. This is the phase when the abundance of ^{26}Al reaches its maximum value. In the third panel, ^{26}Al is destroyed near the burning shell because of proton capture reactions and the lack of seed nuclei. The fourth panel shows the ejecta when the envelope reaches the size R_{WD} ~10^{12} cm. The amount of ^{26}Al ejected is dependent on the efficiency of the convection which carries ^{26}Al towards the outer and cooler layers, avoiding the destruction via proton capture. The arrow indicates the beginning of the ejected envelope.

^{26}Al: minor contributions

Among the minor contributors to the ^{26}Al Galactic abundance Asymptotic Giant Branch (AGB) stars, ($1.5 \leq M/M_\odot \leq 6.0$) SNIa and cosmic rays can be included.

AGBs started to be explored as candidates for the ^{26}Al production in Norgaard (1980), in an attempt to search for other sites other than massive stars that could contribute to the Galactic ^{26}Al. The production by AGBs was later confirmed by Forestini et al. (1991), that found that low mass AGB stars could be responsible of ~ 0.1 $M_\odot$ of the total 2-3 $M_\odot$ observed at that time. Further calculations were provided by Forestini et al. (1997) and Arnould et al. (1999).

Mowlavi et al. (2000) described the ^{26}Al nucleosynthesis in AGBs in a quite detailed way. The production of ^{26}Al takes place mainly in the hydrogen burning shell (HBS) via the Mg-Al chain of reactions (see Fig. 1.7). The synthesis becomes efficient at temperatures above 35×10^6 K when almost all the ^{25}Mg available is transformed into ^{26}Al. When the temperature of the HBS exceeds ~ 55×10^6 K, ^{26}Al destruction kicks in but this effect is counterbalanced by the synthesis of ^{25}Mg, that replenishes the Mg-Al cycle. The β^+ decay does not play a significant role since its timescale is longer than the interpulse durations. The final ^{26}Al abundance depends strongly on the efficiency of the third dredge up (3DUP): the lower limit is obtained when no material is dredged-up before the 3DUP, and the upper limit is found when the maximum efficiency is reached from the very first pulse. These scenario supports the conclusion by Forestini et al. (1991), confirming that these mechanisms can be responsible for ~0.1 $M_\odot$ of ^{26}Al.

Regarding SNIa, very little attention has been dedicated to their contribution to ^{26}Al. Overall, their distribution does not match at all the ^{26}Al distribution observed and, even though the SNIa yields have been computed (see Nomoto et al. 1984), from a chemical evolution point of view they are almost negligible.

Cosmic rays as a source of ^{26}Al were proposed by Clayton (1994) in order to explain the de-excitation of $^{12}C^*$ and $^{16}O^*$ observed in the direction of the Orion molecular cloud. The excitations were believed to occur when heavy cosmic rays interacted with H- and He-rich environments. Among these interactions one reaction is the ^{26}Mg(H,n)^{26}Al, whose rate was quite similar to the de-excitation of $^{12}C^*$ and which, therefore, was considered to be the trigger of the de-excitation itself. However, this scenario was alternative to the Type II SN production, that was later confirmed to be the best one to reproduce the ^{26}Al flux features, thus excluding the cosmic-ray production.

^{60}Fe in massive stars

The nucleosynthesis of ^{60}Fe, even though it has been less investigated than that of ^{26}Al, is in some ways more simple. The reason is that almost all the ^{60}Fe is produced by massive stars, without notable contribution from other sources.

Limongi et al. (2006) described the nucleosynthesis of ^{60}Fe that occurs during three different phases of a massive star evolution. The parameter that most constrains the production of ^{60}Fe is the temperature, which allows its efficient synthesis in only a few production locations. The synthesis of ^{60}Fe occurs via the ^{59}Fe(n,γ)^{60}Fe reaction that competes with the ^{59}Fe(β^-) decay. In order to cross the ^{59}Fe bottleneck, at a temperature of Log(T)=8.7 a neutron density of 3×10^9 n cm^{-3} is required. The second constrain on the temperature is related to the photodisintegration of both ^{60}Fe and ^{59}Fe, that becomes extremely efficient at temperatures above 2 billion degrees. These conditions reduce the ^{60}Fe production sites to:

- He shell burning;
- C shell burning;
- Ne shell burning.

In the He, C and Ne core burnings the temperature never verifies the required conditions, whereas in the shell burnings it does. On the other side, the upper limit on the temperature prevents ^{60}Fe to be synthesised in more advanced burning stages.

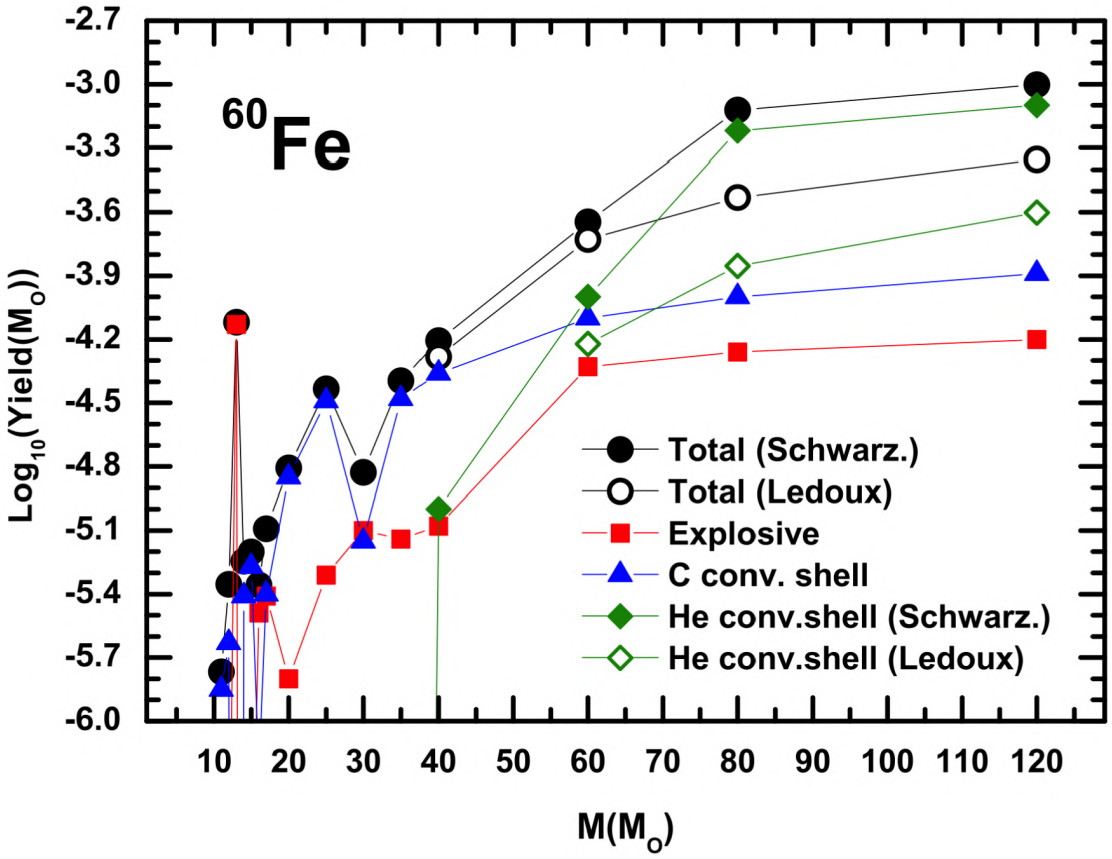

Figure 1.12: *Different contributions to the ^{60}Fe total yield for different initial stellar masses. The contribution analysed are ascribed to the He convective shell (green diamonds), the C convective shell (blue triangles) and the explosive nucleosynthesis (red squares). The total yield is depicted by black dots. Taken from Limongi et al. (2006).*

As explained above, during He core burning the neutron density never exceeds 10^7 n cm^{-3}, therefore no appreciable production of ^{60}Fe occurs. During the He shell burning the temperature as well as the neutron density increases, thus triggering a substantial production of ^{60}Fe.

Similarly, during the C central burning the low concentration of α particles results in an equally low concentration of neutrons so that the situation is analogous to that in the He central burning. The neutron density increases enough during the C shell burning, hence favouring the ^{60}Fe production. As for ^{26}Al, the role of the convective shell is crucial: bringing new fuel (α particles and ^{22}Ne) to the region where the actual burning occurs as well as bringing the freshly made ^{60}Fe outward, where it can be preserved longer. The 30 M$_\odot$ model is the example of the importance of the convective shell: the lack of an efficient convective shell lasting throughout the advanced burnings causes this mass to host the minimum production of ^{60}Fe (see Fig. 1.12).

Lastly, the Ne burning is not a particularly efficient site since the the lack of an

extended and stable convective shell prevents the accumulation of a substantial amount of ^{60}Fe. Not even the Ne convective shell that forms in the 14 $M_\odot$ and 15 $M_\odot$ that was responsible for the strong peak in ^{26}Al yield (see Sec. 1.2.2 and Fig. 1.9) is effective: the neutron density, in fact, remains too low to cross the ^{59}Fe bottleneck.

Fig. 1.12 shows the relative contribution of different processes to the ^{60}Fe yield, such as the production in the shells and that during the explosion. The ^{60}Fe in lower masses ($\lesssim$ 40 $M_\odot$) is dominated by the C convective shell, whereas in the higher masses it is dominated by the He shell. The explosive nucleosynthesis contribution never dominates over the other processes except in the 13 $M_\odot$ model. This happens because in the 13 $M_\odot$ model the temperature necessary to trigger the explosive ^{60}Fe nucleosynthesis occurs in a region where the seed nuclei ^{12}C and ^{22}Ne are more abundant with respect to the location where this temperature occurs in the other stellar models.

As is evident from Fig. 1.12 the wind does not play any role in the ^{60}Fe production since in the stellar models the He convective shell is never lost through the wind in the advanced WR phase.

1.3 State of the Art and Thesis aims

As anticipated in Section 1.2, SLRs have been used in a variety of ways, both observational and theoretical, being the perfect clocks to reconstruct the recent history of the SS and the MW. I leave to Chapter 3 the analysis of the current observational Galactic-scale scenario regarding ^{26}Al and ^{60}Fe, and I treat here only the theoretical models developed to investigate SLRs.

On the theoretical side, the recent literature witnesses how SLRs can actually be the link among different branches of Astrophysics. For example, the study of the Local Bubble (LB) where the SS is located, has been recently refined by Schulreich et al. (2023). Here, the simulation of fourteen SN explosions, all located in the Scorpius-Centaurus OB association, is presented and the evolution of the LB after the explosions is followed (via a hydrodynamical simulation). Among the different phenomena included in the model, also the behaviour of several radioisotopes is analysed. ^{60}Fe is followed in detail, being the only one that was detected in the Antarctic snow, mainly originating from the LB SN explosions. Making use of this isotope they are able to confirm that the LB triggered Star Formation (SF) in the solar vicinity through its expansion, but moreover, they can also suggest the passage of the SS through a neighbouring superbubble before entering the LB.

Population Synthesis models have also been adopted when investigating SLRs.

Siegert et al. (2023) combines together the radioisotope nucleosynthesis maps of several massive star groups obtained through a population synthesis model, in order to obtain a MW global map. In this way, it is possible to simulate the appearance of the sky in γ-ray emission. A good agreement with the γ-ray sky observed is found, even though the model fails at reproducing quantitatively the γ-ray flux. The hypothesis of the author is that the cause could be the underestimation of the yields.

SLRs can also be studied in the context of chemical evolution. This allows the deeper investigation of their astrophysical sources, with the possibility of a better constraining of the yields. In particular, the role played by the SLRs in chemical evolution is that of tracers of the regions of active SF. In fact, considering the short lifetime of their progenitors (as explained in Sec. 1.2.2) and their short half-life (see Sec. 1.2.1), the detection of a SLR is a proof of a recent SF episode occurred in that region. This can help in the study of the material ejected by a SN event, and in particular, in its interaction with the surrounding ISM. Moreover, other fields as well would benefit of a clarification of the astrophysical production sites, as the population synthesis models mentioned above and the observations (as will be explained in Chap. 3).

In the work by Clayton (1984b) the first treatment of radioactive isotopes in the context of chemical evolution is presented. However, the approximations adopted by the author, such as the Instantaneous Recycling Approximation (IRA) and linear dependence of the Star Formation Rate (SFR) on the gas density, are quite restrictive and, according to the author itself, this model is more useful to obtain an analytic relation, even though quite rough, rather than to have quantitative solid results.

The first proper chemical evolution study focusing on ^{26}Al and ^{60}Fe is presented in Timmes et al. (1995), where the theoretical abundances of these two isotopes are estimated by the means of an analytical chemical evolution model. As will be explained in Chap. 2, such a model has intrinsic limitations due to the approximation needed to analytically solve the equations. This limitation has been removed in the context of radioactive isotopes for the first time by Côté et al. (2019a) and Côté et al. (2019b) where the analysis of several radioactive species, from the shorter- to the longer-lived ones, is presented. The authors adopt a stochastic chemical evolution model to describe the evolution of SLRs in the Galaxy using the ratio between the half-life of the isotopes and the time interval between the formation of two subsequent progenitor stars. These results were then used in the work presented by Trueman et al. (2022), where the isotopic abundance ratios in primitive meteorites are compared to the predicted ones to infer the timescales relevant for the birth of the Sun. The same investigation was also applied to a

larger set of isotopes by Lugaro et al. (2022) and the scenario was expanded even more by the Monte Carlo investigation presented in Yagüe López et al. (2021).

In this context, a piece of the puzzle is still missing. Even though in the latest years the interest in SLRs increased and their treatment improved consistently, the comparison with the observational data has not been explored completely yet. The satellites dedicated to the survey of the γ-ray sky provided the abundances and fluxes of ^{26}Al and ^{60}Fe but several uncertainties are still affecting those observations (as will be shown in Chap. 3), and therefore the error bars are still large. Therefore, this Thesis main aim is that of offering a theoretical constraint to the observations of ^{26}Al and ^{60}Fe by the means of a chemical evolution model. By testing the ISM pollution from different sources, an update to the stellar production from different progenitors can also be performed.

As anticipated, the SLRs are tracers of the active regions of SF. In this Thesis, this aspect will also be inspected. The same chemical evolution model will be expanded from the original 1D structure, to a more complex 2D structure that includes the impact of surface mass density variations caused by spiral arms, following the prescriptions presented in the last years. This updated version can account not only for the radial structure of the Galaxy, but can also follow the dishomogeneities along the azimuthal dimension. Hence, the MW spiral arm structure can be reproduced and the SLRs ability to trace the SF can be tested in detail.

Beside the MW, the future perspectives of the γ-ray missions are aiming at the detection of extra-Galactic structures through the upcoming Compton Spectrometer and Imager (COSI), planned to be launched in 2027 (see Sec. 3.4). Given its improved sensitivity, it will hopefully be able to detect the flux from external galaxies, such as the Large Magellanic Cloud (LMC). In this Thesis, a chemical evolution model will be adopted to estimate the ^{26}Al and ^{60}Fe fluxes from the LMC, starting from the constraints obtained to reproduce the MW abundances. This theoretical estimate can give a first answer to the question: *Will COSI be able to detect the LMC?*

By investigating these aspects, this Thesis can contribute to the SLRs present day scenario in a way that has not been explored in the literature yet.

In addition to the SLRs investigation, also a study of some stable isotopes will be presented. In particular, by adopting the same tools and techniques already applied to the SLRs, it will be shown an analysis of the [Mg/Mn] vs. [^{27}Al/Fe] plane, which has been adopted in the last decade as a tool to distinguish accreted from *in-situ* formed populations. In this case, the limitations of this diagnostic will be emphasised in order to highlight the limits within which the [Mg/Mn] vs.

[Al/Fe] plane is reliable.

1.4 Structure of the Thesis

In this Thesis the aims aforementioned will be pursued by presenting four works already published or under peer-review process, after an introduction related to the tools adopted and the observations considered for comparison.

The Thesis is organized as follows. In Chap. 2 the chemical evolution model adopted is presented, with particular emphasis on the fundamental parameters building the model and the chemical evolution equation regulating the ISM enrichment by several different sources, whose detailed modelling is also explained. In Chap. 3 the observations of ^{26}Al and ^{60}Fe are presented, starting from the first results provided up to the most recent updates. The interpretation of those data is also reported, focusing specifically on the astrophysical sites proposed as ^{26}Al and ^{60}Fe sources. In Chap. 4 the chemical evolution of ^{26}Al and ^{60}Fe in the MW is described recalling the parameters and the nucleosynthesis adopted. in Chap. 5 a revision of the previous Chapter results is performed adopting a more complex chemical evolution model. In Chap. 6 the prediction of the ^{26}Al and ^{60}Fe fluxes expected from the LMC is proposed in view of the future γ-ray missions planned. In Chap. 7 the analysis of the [Mg/Mn] vs. [^{27}Al/Fe] diagram recently adopted to constrain the evolution of the local group galaxies is reported, with particular focus on highlighting the main limitations related to the state-of-the-art nucleosynthesis of the isotopes involved. Finally, in Chap. 8 the main conclusions of this Thesis are summarized and future prospects related to further development of the model presented are shown.

2

Chemical evolution models

To provide a theoretical estimate of the ^{26}Al and ^{60}Fe abundances and pursue the main aim of this Thesis, as presented in Section 1.3, a chemical evolution model is needed.

Chemical evolution of galaxies is the study of the abundances of the chemical species and related quantities (such as SN rates and metallicity distribution function) as a function of time and space in the galaxies. Up to now, this studies have been mainly performed focusing on the MW, being the structure for which we have the largest data sets available and therefore, the possibility to better constrain the models. The idea behind chemical evolution is that by adopting the abundance patterns observed as constraints, it is possible to identify a set of parameters that can describe the evolution of the Galaxy up to the present day.

The Big Bang is responsible for the formation of H, He and some isotopes of Li and Be. All the other chemical elements are synthesised in the stellar interiors (see Section 1.1) and are re-injected into the ISM during stellar wind phases or explosive episodes, such as SNe or novae. These elements build up in the ISM and, as time passes, they will get incorporated into new stellar generations, thus creating a cycle where the products of the nucleosynthesis of a stellar generation become the fuel for the following generation. Chemical evolution can follow this cycle by modelling the phenomena that regulate it, such as the SFR, the initial masses of the stars newly formed and the gas flows.

In this Chapter I will describe the chemical evolution models that have been adopted throughout this Thesis focusing on the input parameters and the chemical evolution equation that mathematically describes the composition of the gas. For a deeper discussion on chemical evolution I refer to Matteucci (2003) and Matteucci (2012).

2.1 Input parameters

Chemical evolution models are based on a set of fundamental input hypothesis that regulate the evolution of the chemical composition of the gas:

- initial conditions;
- stellar birthrate function;
- stellar yields;
- gas flows.

Once these quantities are defined, a set of chemical evolution equations can be written and solved: each equation describes mathematically the interplay between the basic physical phenomena that have a direct impact in the ISM chemistry. The solution of each equation is the evolution in time and space of the abundance of a single element. Hence, the set of equations counts as many equations as the elements whose evolution wants to be analysed.

More complex scenarios can be depicted by including additional galactic phenomena. This described here is the smallest set of initial parameters necessary to properly describe the chemical evolution of a galaxy.

2.1.1 Initial Conditions

Initial conditions include assumptions regarding the initial chemical composition of the gas adopted to form the first stellar generation as well as the physical boundaries of the structure in exam.

Regarding the chemical composition, it can either be primordial or pre-enriched. By primordial chemical composition is meant the composition of the Universe at the end of the Big Bang nucleosynthesis, namely H and He in a ratio 3:1 (as already mentioned in Section 1.1). When adopting this initial composition, the first stellar generation does not contain any metal, and only with the firsts SN explosions heavier elements will start polluting the ISM. This is the composition adopted throughout this Thesis to model the evolution of the MW.

On the other side, a pre-enriched composition implies a gas that has already been polluted by one or more stellar generations.

Regarding the boundaries of the structure analysed, a closed box or an open box model can be chosen. A closed box model implies that the galaxy in exam does not exchange matter with the external environment, whereas in an open box model the galaxy experiences ingoing or outgoing fluxes. In this Thesis an open box model is adopted.

2.1.2 Birthrate Function: SFR and IMF

The stellar birthrate function, usually indicated as $B(m,t)$, is an analytical function that represents the number of stars formed in the time interval $(t, t+dt)$ and in the mass range $(m, m+dm)$. The time t and the mass m can be treated as independent variables, therefore $B(m,t)$ can be expressed as the product of two independent functions:

$$B(m,t) = \varphi(m)\psi(t) \tag{2.1}$$

where $\psi(t)$ is the SFR and $\varphi(m)$ is the Initial Mass Function (IMF).

The SFR describes the rate at which the gas is included into new stars. According to Schmidt (1959) and Kennicutt (1998) it can be written as:

$$\psi(t) = \nu\sigma_{gas}^{k} \tag{2.2}$$

expressed in $M_{\odot}\, pc^{-2}\, Gyr^{-1}$. ν is the Star Formation Efficiency (SFE, expressed as the inverse of a time) and σ_{gas} is the surface gas mass density. The value of k was determined for the first time by Schmidt (1959) by a comparison with different sets of observational data such as the distribution of young objects perpendicular to the Galactic plane, the distribution of luminosities in open clusters and the number of WD observed. Since that moment it has been revised (Quirk, 1972; Larson, 1992; Kennicutt, 1989) until Kennicutt (1998) finalised its value to $k = 1.4$.

In this Thesis Eq. 2.2 was adopted when dealing with the MW. On the other side, when external structures were analysed, the SFR adopted was:

$$\psi(t) = \nu M_{gas}^{k}. \tag{2.3}$$

This is almost equivalent to Eq. 2.2, given that in structures where the scaleheights are roughly constant, the surface density can easily be converted in volume density (see Romano et al. 2015).

The IMF represents the spectrum in mass of the stars formed. Several different analytical forms have been proposed, either one-slope or multi-slope power laws. The most simple parametrization of an IMF was proposed by Salpeter (1955):

$$\varphi(m) = Am^{-(1+x)} \tag{2.4}$$

with $x = 1.35$ and A being the normalisation constant derived assuming masses in the range 0.1-100 $M_{\odot}$:

$$\int_{0.1}^{100} m\varphi(m)dm = 1. \tag{2.5}$$

The IMF is typically derived by stellar counts in the solar vicinity, and the most reliable results by Kroupa et al. (1993) imply a three-slope power law:

$$\varphi_{\rm K93}(M) \propto \begin{cases} M^{-1.3} & M < 0.5M_\odot \\ M^{-2.2} & 0.5 < M/M_\odot < 1 \\ M^{-2.7} & M > 1M_\odot. \end{cases} \tag{2.6}$$

Since this relation cannot be tested outside the solar vicinity, a universal IMF, derived from the stellar clusters, was also proposed by Kroupa (2001):

$$\varphi_{\rm K01}(M) \propto \begin{cases} M^{-1.3} & M < 0.5M_\odot \\ M^{-2.3} & M > 0.5M_\odot \end{cases} \tag{2.7}$$

In this Thesis different IMFs were chosen, depending on the structure in analysis and the aim behind the analysis. When treating the MW in order to model it and propose a scenario, Eq. 2.6 was adopted. In case the purpose in analysing the Galaxy was to perform a comparison with previous results taken from the literature, then the IMF was chosen to match that adopted in the literature. The same is valid for external structures: when proposing a model Eq. 2.4 was assumed, whereas for the sake of comparison an IMF matching with that of the reference paper was adopted.

2.1.3 Stellar Yields

A fundamental part of the scenario is represented by the amount of elements produced by the stars. To account for the ISM pollution, chemical evolution makes use of the stellar yields, that represent the amount of chemical elements, both pre-existing and newly formed, re-injected into the ISM by the stars at their death.

As already explained in Chapter 1, stars with different masses and initial metallicity pollute the ISM differently because they follow different evolutionary paths. Therefore, a typical stellar yield set does not cover the whole mass range (0.1-100 $M_\odot$) but rather focuses on smaller mass intervals to treat stars with a similar evolution. In particular stars are usually grouped as follows:

- stars with initial mass < 0.1 $M_\odot$: also called *brown dwarfs*, their lifetime is longer than that of the Universe, hence they have not polluted the ISM yet. These stars influence the ISM chemical composition only by subtracting gas at the moment of their formation;

- stars with initial mass in the range 0.1-8 $M_\odot$: also indicated as *Low-Intermediate Mass Stars* (LIMSs), can follow different evolutionary paths, as single stars, SNIa or novae.

The single stars eject mainly ^{4}He, ^{12}C and ^{14}N, some CNO isotopes and s-process elements (see Section 1.1.2).
SNIa, that originate when a C-O WD accretes material from a red giant or from another WD thus triggering an explosion, produce mostly Fe. Other elements, such as C, Ne, Ca and Mg are synthesised in smaller amounts.
The same systems that give rise to a SNIa, can also generate a nova (see Sec. 1.2.2). A WD that accretes material from the companion fast enough, experiences a nova event before reaching M_{Ch}, that would trigger a SNIa. The nova explosion ejects the outermost layers into the ISM, without destroying the progenitor. Every nova experiences around 10^4 outbursts (see Ford 1978) during its lifetime ($\sim 10^8$ yr);

- stars with initial mass > 8 $M_\odot$: massive stars have short lifetimes and can be divided in subgroups.
  In the range 8-10 $M_\odot$ the stars die as Electron-Capture Supernovae (ECSN), where the explosion is triggered by the the ignition of O in the ONe degenerate core.
  From 10 $M_\odot$ to M_{WR}, the minimum mass to form a WR star, the stars die as Type II SNe (SNII) and explode by core-collapse. After the explosion, the material that falls back onto the core form a NS or a BH, depending on the initial stellar mass. SNIIe mainly produce α-elements, some N, some Fe and Fe-peak elements, s- and r-process elements.
  From M_{WR} to 100 $M_\odot$ the stars die as Type Ib SNe (SNIb) or Type Ic SNe (SNIc) which can be more energetic than a SNII and are typically connected to the long Gamma-Ray Bursts (lGRBs).

In this Thesis several sets of yields have been adopted and in the following Chapters the main characteristics of each set will be presented.

2.1.4 Gas Flows

Since, as anticipated in Section 2.1.1, the galaxies are treated as open boxes the flows of gas inward and outward also have to be modelled.

When treating an infall of gas, the parametrisation by Chiosi (1980) is usually adopted:

$$\dot{\sigma}_{gas,inf}(R,t) = a(R)e^{-t/\tau_{inf}} \tag{2.8}$$

where τ_{inf} is the timescale of formation of the structure in analysis, and is defined as the time needed to accumulate half of the total mass of the galaxy. τ_{inf} is a free parameter, since the formation mechanisms of the galaxy discs are not known a

priori. The chemical composition of the infalling gas is an input condition and can either be primordial (when studying the infall out of which a galaxy formed) or pre-enriched (when dealing with the merger of small external structures with a bigger one).

More complicated formulation of Eq. 2.8 can be adopted. For example, a better description of the chemical features of the MW can be obtained when a second infall episode is included. Chiappini et al. (1997) in fact, showed that a first fast infall episode could explain the formation of the halo and thick disc, whereas a second slower but longer infall could have formed the thin disc. This formulation was later revised by Chiappini et al. (2001), Romano et al. (2003), and Romano et al. (2010) and more recently by Grisoni et al. (2017), Spitoni et al. (2019b), and Romano et al. (2020):

$$\dot{\sigma}_{gas,inf}(R,t) = a(R)e^{-t/\tau_T} + b(R)e^{-(t-t_{max})/\tau_D(R)} \tag{2.9}$$

Here, $a(R)$ and $b(R)$ are two free parameters tuned to reproduce the present time total surface mass density of the thick and thin disc, respectively. In this Thesis the adopted values are 17 $M_\odot$ pc^{-2} and 54 $M_\odot$ pc^{-2}, respectively (see Romano et al. 2000; Chiappini et al. 2001). t_{max} is the delay after the first infall episode (that in this Thesis is fixed to the value of 1 Gyr), and $\tau_D(R)$ is the timescale of the second infall. The dependency on the Galactocentric distance R was included into $\tau_D(R)$ to reproduce the *inside-out* scenario originally proposed by Matteucci et al. (1989). According to that, the thin disc formed out of gas that accumulated slower in the outer part of the Galaxy and faster in the inner part, hence $\tau_D(R)$ is usually parameterised as:

$$\tau_D(R) = 1.033(R/\mathrm{kpc}) + 1.267 \tag{2.10}$$

expressed in Gyr, as proposed by Chiappini et al. (2001).

In this Thesis, the formation of the MW disc was parametrised according to Eq. 2.9 and Eq. 2.10. For the formation of the Galactic bulge, on the other side, a one-infall law as that in Eq. 2.8 was assumed. In the same way, also when modelling the chemical evolution of the LMC Eq. 2.8 was adopted.

Regarding the outflows, they are not a mandatory ingredient for a chemical evolution model since not all the galaxies experience them. The galactic wind is typically observed in dwarf galaxies where the potential well hosting the gas is not deep enough to keep all the material inside the galaxy and part of it can flow outside. This is not the case of the MW, where the Galactic wind contribution is negligible. On the contrary, for external structures such as the LMC (see Chaps. 6 and 7), it is usually written as

$$\dot{\sigma}_{out}(t) = -\omega\psi(t) \tag{2.11}$$

where ω is the wind efficiency expressed in Gyr^{-1}, that is treated as a free parameter and whose value changes from galaxy to galaxy, and $\psi(t)$ is the SFR, since the galactic wind is triggered by the energy released from SN explosions.

Regarding the gas flows, other more complicated scenarios exist. A possibility, for example, is that of an outflowing gas that falls back onto the galaxy, generating the so called *galactic fountains* (see Spitoni et al. 2008; Spitoni et al. 2009). Furthermore, also *radial flows* within the galaxy itself can exist (see Spitoni et al. 2011). Nevertheless, these phenomena were not taken into account in the analysis of the galaxies performed in this Thesis, therefore no mathematical treatment form them will be shown.

2.2 Chemical evolution equations

Once the fundamental ingredients listed in Section 2.1 are provided, the following step is writing the equation to describe the chemical composition of the ISM. Each element whose chemical evolution wants to be analysed needs its own equation and is treated independently of the others.

In several chemical evolution models, it is customary to adopt quantities normalised to the present day t_G. Commonly, the gas mass $M_i(t)$ and the surface gas mass density $\sigma_i(t)$ are substituted by $G_i(t)$:

$$G_i(t) = \frac{\sigma_i(t)}{\sigma_{tot}(t_G)} = \frac{M_i(t)}{M_{tot}(t_G)}. \tag{2.12}$$

Here, $\sigma_i(t) = X_i \sigma_{gas}(t)$ with X_i being the abundance by mass of the element i ($\Sigma_i X_i = 1$). The same is valid for $M_i(t)$ as well as for $G_i(t)$.

The chemical evolution equation for the element i can therefore be written as:

$$\dot{G}_i(R,t) = -\psi(R,t)X_i(R,t) + R_i(R,t) + \dot{G}_{i,inf}(R,t) - \dot{G}_{i,out}(R,t). \tag{2.13}$$

Here $\psi(R,t)X_i(R,t)$ represents the depletion of element i due to the inclusion of gas into new stars, that is therefore dependent on the SFR. $\dot{G}_{i,inf}(R,t)$ is the enrichment of element i ascribed to the infall of external gas and $\dot{G}_{i,out}(R,t)$ is the rate at which the element i is stripped from the ISM due to the galactic wind. Finally, the term $R_i(R,t)$ accounts for the stellar pollution. Its extended expression

is composed of different terms, one for each stellar type:

$$\begin{aligned} R_i(R,t) = & \int_{M_L}^{M_{Bm}} \psi(t-\tau_m) Q_{mi}(t-\tau_m) \varphi(m) dm + \\ & + A \int_{M_{Bm}}^{M_{BM}} \varphi(m) \left[\int_{\mu_{min}}^{0.5} f(\mu) \psi(t-\tau_2) Q_{mi}(t-\tau_2) d\mu \right] dm + \\ & + (1-A) \int_{M_{Bm}}^{M_{BM}} \psi(t-\tau_m) Q_{mi}(t-\tau_m) \varphi(m) dm + \\ & + \int_{M_{BM}}^{M_U} \psi(t-\tau_m) Q_{mi}(t-\tau_m) \varphi(m) dm. \end{aligned} \tag{2.14}$$

The first term represents the contribution from stars in the range M_L-M_{Bm}, where M_L is the minimum mass dying at the time t. Considering that I assume the lifetime of the Universe to be $\sim$ 14 Gyr, then $M_L \sim 0.8\,M_\odot$. $Q_{mi}(t-\tau_m)$ is calculated as $\Sigma_j Q_{ij}(m) X_j(t-\tau_m)$ where $Q_{ij}(m)$ is the production matrix as defined by Talbot et al. (1973) and $X_j(t-\tau_m)$ is the abundance of an element j at the time of formation of the star. $Q_{mi}(t-\tau_m)$ takes as input the chemical composition of the star at its birth and returns the amount of element i produced starting from that composition. The diagonal term of the matrix represents the amount of element i that was already present at the birth of the star and was not processed during the stellar evolution but was rather ejected as it was.

The second integral accounts for the SNIa, that are included in the model according to Matteucci et al. (1986) and Matteucci et al. (2001). These systems are simulated assuming that only a fraction A of the binary systems with a total mass in the range M_{Bm}-M_{BM} can give rise to a SNIa. The lower limit of this interval is determined considering that both the companions have to be massive enough to allow the WD to reach the Chandrasekhar mass, M_{Ch}, and is therefore set to $M_{Bm} = 3\,M_\odot$. The upper limit is fixed considering that each component cannot be more massive than 8 $M_\odot$ to give rise to a CO WD and therefore $M_{BM} = 16\,M_\odot$. The function $f(\mu)$ is the distribution of μ defined as the ratio between the mass of the secondary star to the total mass of the system. The time τ_2 is the lifetime of the secondary star, that being the less massive one with a longer lifetime, represents the clock of the system.

The third term accounts for the single stars in the range M_{Bm}-M_{BM}, that can die as CO WDs or SNII.

The fourth integral represents the contribution coming from SNIb and SNIc, from masses M_{BM} up to $M_U = 100\,M_\odot$.

Together with these contributions, the model includes also novae systems among the polluters. Novae are defined as initially suggested by D'Antona et al. (1991) and later confirmed by Romano et al. (2003). In particular, the rate of nova

formation at a given time t is computed as the fraction α of the rate of formation of WDs:

$$R_{novae}(t) = \alpha \int_{0.8}^{8} \psi(t - \tau_m - \Delta t)\varphi(m)dm \tag{2.15}$$

α is a free parameter and is fine-tuned to reproduce the current observed nova rate in the Galaxy (see Della Valle et al. 2020 and references therein). The time Δt is an additional delay set to 1 Gyr introduced to wait for the WD to cool down, condition necessary to trigger the explosion conditions. Each nova system experiences 10^4 explosion during its lifetime ($\sim 10^8$ yr), therefore the nova outburst rate is obtained as:

$$R_{novae}(t) = 10^4 \cdot \alpha \int_{0.8}^{8} \psi(t - \tau_m - \Delta t)\varphi(m)dm. \tag{2.16}$$

In this approximation it is assumed that all the novae outbursts occur together at the formation of the system, and are not spread out during the whole nova system lifetime ($\sim 10^8$ yr). This aspect has already been analysed by Cescutti et al. (2019) that improved the scenario by adopting multiple explosions, but did not find significant differences for the abundances of the stable isotopes. Concentrating all the outbursts of a nova in one episode is a valid approximation in the case of unstable isotopes too, provided that the rate of formation of nova systems does not vary dramatically over a timescale comparable to the lifetime of a nova ($\sim 10^8$ yr). This condition is verified by the nova formation rate adopted in my model which varies slowly enough in the last $\sim$ 10 Gyr.

2.2.1 Chemical evolution equations for radioactive isotopes

When dealing with radioactive isotopes the interplay between the phenomena listed above is not sufficient to properly describe the evolution of their abundances. The reason is that an additional term to model the depletion caused by the decay has to be introduced in the equation.

To define this contribution it is necessary to recall Eq. 1.3, that describes the decay of radioactive atoms with an exponential law. Given that the number of atoms of the unstable element i, $N_i(t)$, is linearly proportional to its abundance X_i, then it can also be written:

$$\dot{X_i}(t) = X_i(t_0)e^{-t/\tau_i} \tag{2.17}$$

where τ_i is the mean lifetime of the isotope, also equivalent to the inverse of the decay constant $\lambda_i = 1/\tau_i$. If Eq. 2.17 is transposed to the normalised notation adopting $G_i(t)$ it becomes:

$$\dot{G_i}(t) = G_i(t_0)e^{-t/\tau_i} \tag{2.18}$$

that can easily be included into Eq. 2.13:

$$\dot{G}_i(R,t) = -\psi(R,t)X_i(R,t) + R_i(R,t) + \dot{G}_{i,inf}(R,t) - \dot{G}_{i,out}(R,t) - G_i(R,t)e^{-t/\tau_i}. \tag{2.19}$$

It is interesting to note that, as stable isotopes are an exception to the general case represented by the unstable ones, in the same way Eq. 2.13 is a particular case of Eq. 2.19. A stable isotope in fact, since it never decays, has an infinite mean life-time $\tau_i \rightarrow \infty$. Adopting this limit for τ_i in Eq. 2.19 the radioactive decay term $G_i(R,t)e^{-t/\tau_i}$ tends to zero, and Eq. 2.13 can be recovered.

To study the chemical evolution of the MW and the LMC Eq. 2.19 was adopted, excluding the galactic wind term in the case of the MW.

3

Instruments and Observations

Even though the chemical evolution of radioactive isotopes is quite similar to that of stable isotopes, both being based on the same principles and equations, on the observational side some differences arise. Actually, the strategy followed to reveal the presence of SLRs in the Galaxy is completely different and so are also the instruments and the quantity measured. In this Section the instruments adopted to observe the SLRs and the observations obtained with those, are presented.

One of the key points of chemical evolution is that the abundances predicted adopting the chemical evolution equations describe the chemistry of the ISM, whereas the data available refer to the chemical abundances of the stellar atmospheres, obtained by collecting the spectra of the single stars. Under the assumptions presented in Sec. 2.2, these two quantities are comparable to each other.

In the case of SLRs the data are collected by investigating the ISM itself, without any observation involving stars. In particular, the radioactive decay is exploited, being based on nuclear properties that are not dependent on the astrophysical environment. As already presented in Sec. 1.2.1, both ^{26}Al and ^{60}Fe show decay lines with energy falling in the γ-ray region of the spectrum (1.809 MeV for ^{26}Al and 1.172 and 1.332 MeV for ^{60}Fe). By adopting suitable instruments, sensitive to the γ-ray energy band, the photons emitted during the decay can be detected.

3.1 Telescopes for γ energy band

The γ-ray energy band is the high end of the energy spectrum, therefore the main characteristic of a γ-ray photon is the extremely high penetration depth. Therefore, any mirror or lens usually adopted when investigating all the other energetic bands becomes transparent to the γ-ray photons. To overcome this issue, the strategy

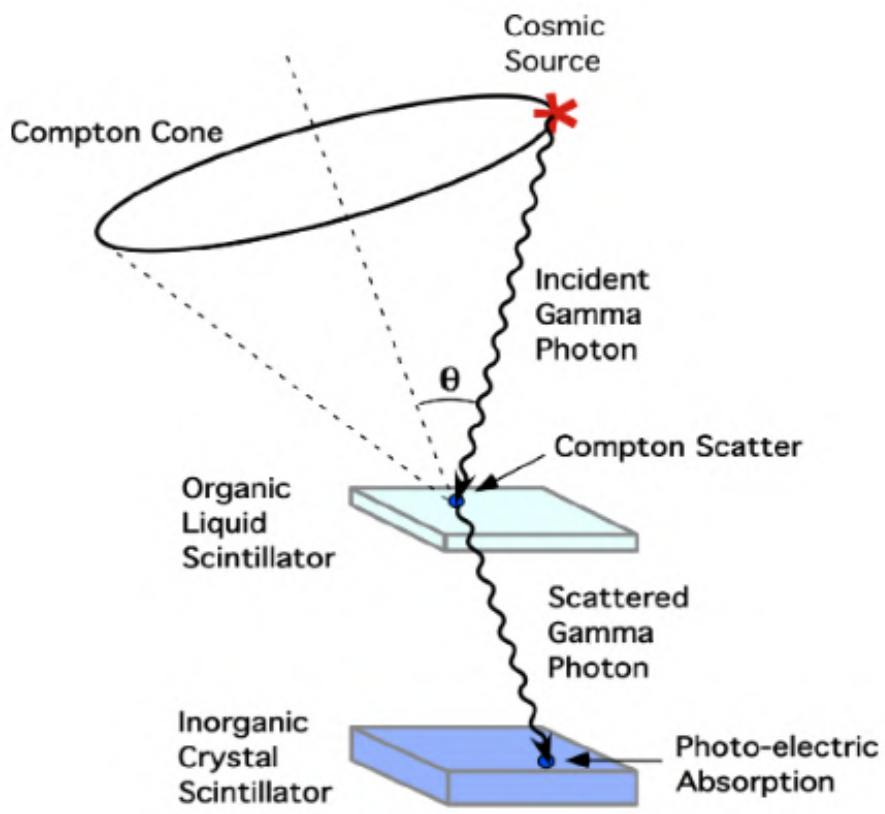

Figure 3.1: *Schematic representation of a Compton telescope: by measuring the deposition on the first detector and the final absorption by the second detector, the angle θ can be determined and therefore the direction of the incident γ-photon can be constrained to lie in the Compton cone.*

adopted to detect high energy photons makes use of the Compton scattering, through the Compton telescopes.

The principle behind a Compton telescope is well summarised in Fig. 3.1. The instrument is composed of two layers each of which is a detector itself, and the geometry and the materials involved are chosen to maximise the efficiency of the detection. When an incoming γ-ray photon produced by a cosmic source interacts with the upper layer it deposits some of its energy. At the same time a scattered γ-ray photon is produced towards the bottom layer, along a direction which, in general, is not the same as that of the original photon. After the specific time of flight (TOF) that depends on the distance between the two layers only, the bottom detector will absorb the scattered photon. By measuring the energy deposited in the first detector and that absorbed by the second one, the Compton angle θ can be determined. This aperture represent the uncertainty in the incoming direction of the original photon and it is typically referred to as Compton cone. By repeating this analysis for all the photons coming from the same source, a set of angles θ will be obtained. The location of the cosmic source is identified by the intersection of

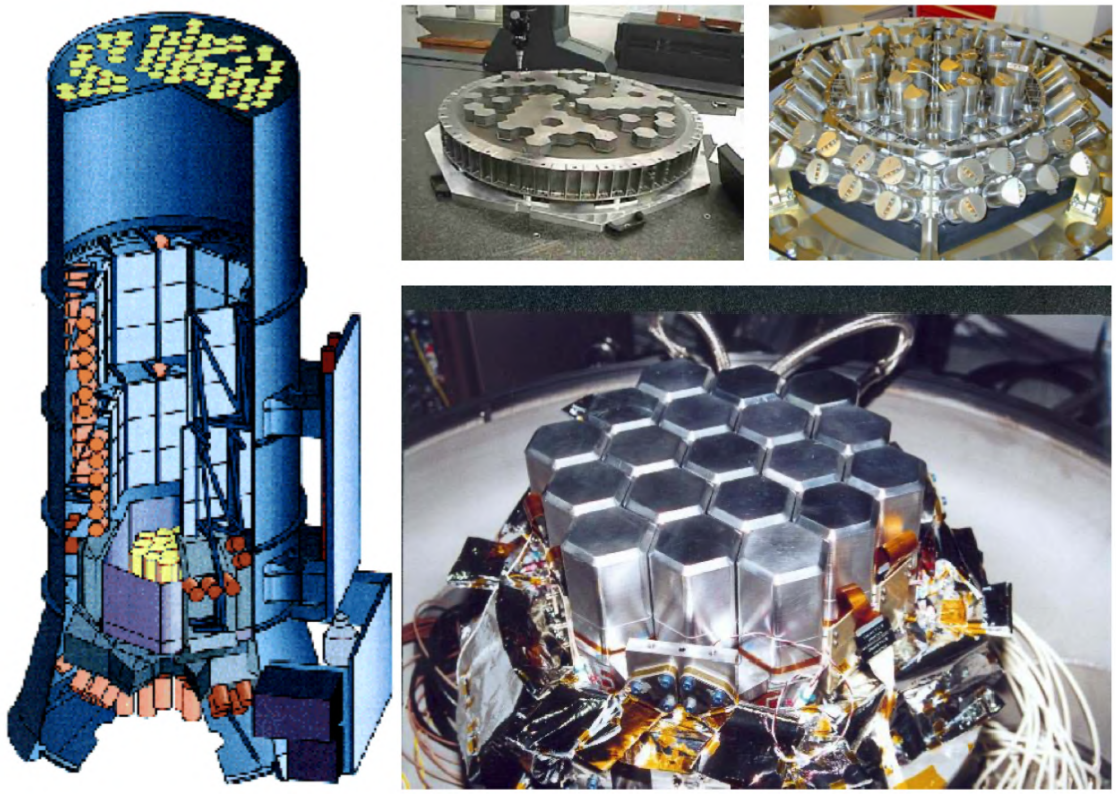

Figure 3.2: ***Left:*** *Sketch of the spectrometer SPI (Spectrometer on INTEGRAL, mounted on the INTEGRAL telescope. The Germanium detector is stored in the lower part of the instrument (in yellow). Dimensions (height × diameter) are 2.26 × 0.78 m^2 (Diehl, 2013b).* ***Right:*** *Pictures of the Ge detector composed of 19 sub-units (lower figure), coded mask and photo-multipliers (upper figures, left and right respectively) of SPI (credits to Diehl 2013a).*

all the Compton cones. This is valid only in the case when the scattered photon is completely absorbed by the second detector. In case of partial absorption a larger and incorrect Compton cone is obtained. It will not contain the location of the source, but it will just produce a broad halo around the source position. Therefore, all the determinations of the point sources locations are based on totally absorbed events only.

The theoretical limitation in using the Compton scattering effect is related to the fluctuations in the energy of the scattered photon. During the interaction with the first layer the detector electrons that participate in the scattering have different energies according to their atomic structure. Hence, also the scattered photon energy will statistically fluctuates (order of tens of eV) which is reflected into a fluctuation in the determination θ. To limit this effect, the detectors typically operate at cryogenic temperatures ($\sim$ 80 K) to ensure that the electrons all occupy the lowest energy orbitals.

On a more practical side, a relevant issue in γ-ray telescopes is the background,

that is particularly difficult to suppress because is generated by the same processes that create the cosmic photons of interest. The telescopes in orbit are exposed to a bombardment of cosmic-rays that, interacting with the instruments, produce a continuum as well as emission lines in the same energy band as the targets of the detectors. Moreover, the estimation of the background cannot be neglected since it dominates the signal to the point that the cosmic photons only contribute at the percentage level or below. To determine the background an empirical fitting is usually adopted, since mathematical modelling fails in accounting correctly for the geometry of the instrumentation and the support structure.

Regarding the nature of the detector, the best choice is solid-state detectors, typically Germanium-based, since they are the only ones able to reach the spectral resolution required to identify γ-ray lines. This is the case for both the γ-ray instruments that detected SLRs in the Galaxy (see Sec. 3.3.1). A typical detector is usually composed of smaller units assembled together. In Fig. 3.2 the Germanium detector of the gamma-ray telescope INTEGRAL is pictured (bottom right figure). The detector itself carries its own systematics that are mainly related to the degradation of the crystalline structure, that prevents the charges to be properly collected. The degradation is repaired through an annealing process: the detector is heated from 80 K to 340 K for 10-14 days, thus curing the defects and restoring the original state of the crystalline structure.

3.2 First measurements

The first evidences of the presence of SLRs in the MW was collected by balloon experiments during campaigns that started in the seventies. The interest of the astrophysical community into SLRs and in particular into ^{26}Al grew after the publication of several theoretical studies. A decade earlier already, Arnett (1969) discussed the nucleosynthesis of ^{26}Al taking place in the carbon burning phase of massive stars (see Sec. **??**). Slightly later, Lee et al. (1977) showed evidence of overabundance of ^{26}Mg originating from the decay of ^{26}Al in the Allende meteorite, concluding that ^{26}Al should have been present in the meteorite itself (and therefore in the SS) at the time of its formation. With the rising interest in SLRs and especially in ^{26}Al, more and more efforts were dedicated to the observational side, in particular to the estimation of the expected flux of their decay lines in preparation to the upcoming generation of instruments for the detection. According to Leising et al. (1985), the lack of information regarding the distribution of the ^{26}Al in the Galaxy was severely limiting the theoretical studies, and the building of dedicated instruments was becoming increasingly necessary.

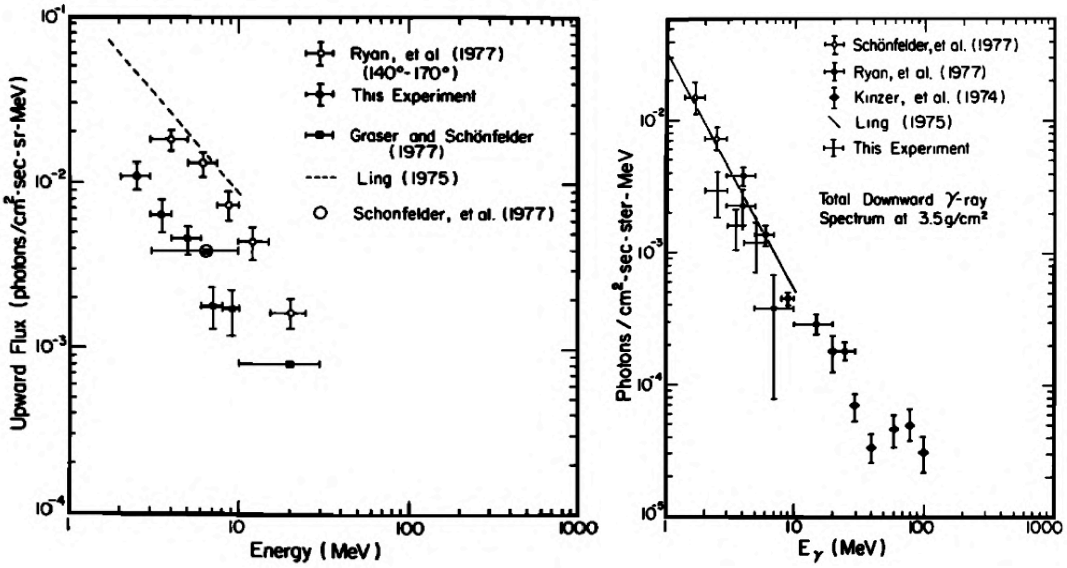

Figure 3.3: *The instrument was symmetrically designed so that both the upward and downward fluxes could be measured.* ***Left:*** *Upward flux at 4 g cm^{-2}.* ***Right:*** *Total downward flux at 3.5 g cm^{-2}. Taken from Lockwood et al. (1979).*

Ramaty et al. (1977) performed the theoretical estimate of the flux from the decay lines of ^{56}Ni, ^{44}Ti, ^{60}Fe and ^{26}Al. The latter represented the most promising candidate for a possible detection because of its intensity ($\sim$ 10 photon cm^{-2} s^{-1} rad^{-1}) and narrow width (FWHM < 3 keV). Successively, Woosley et al. (1980) explored deeper the nucleosynthesis of ^{26}Al in the neon burning phase and the resulting flux of the ^{26}Al decay line at 1.809 MeV. Nonetheless, the very fundamental aspect treated by Woosley et al. (1980) is actually related to the implications of the two possible outcomes of the γ-ray experiments planned to detect the 1.809 MeV line. The two possible results of the surveys were the detection of the line or the non detection. What they highlighted is that in both cases, the result would have been a turning point. Following the calculations to compute the estimated flux, a detection would have implied that the Galactic nucleosynthesis of ^{26}Al has continued at a near constant rate since the beginning of the Galaxy. On the other side a non detection would have been the proof of a non constant production rate, with consequences on the synthesis of most of the heavy elements in the MW.

In the mean time, the first balloon experiments were developed. Lockwood et al. (1979) presented the results of a small Compton telescope mounted on a balloon experiment that made use of organic liquid scintillators. The data were collected during two flights of $\sim$ 5 hours each in 1975 and 1977 over Texas. Unfortunately,

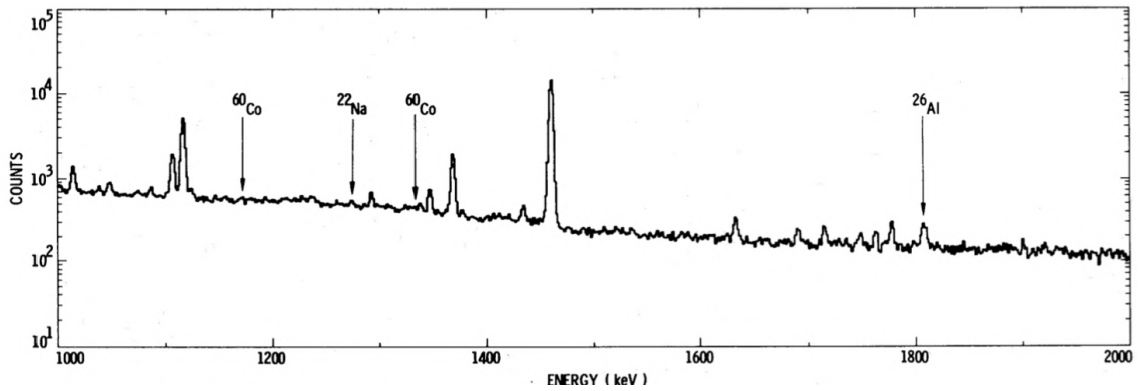

Figure 3.4: *Spectrum obtained by the summed data collected by the four detectors during the 2 weeks flight in 1979 (Mahoney et al., 1982). The location of the target lines is clearly indicated. The ^{26}Al line at 1.809 MeV is the most prominent one.*

the flights were not long enough to determine the γ-ray extraterrestrial flux but only the downward and upward fluxes were constrained. In Fig. 3.3 the results relative to the γ-ray flux both upward (left panel) and downward (right panel) are represented. In both plots theoretical predictions are reported as comparison. On the right, the data are compared to Graser et al. (1977) and to Ling (1975). On the left, the theoretical calculations of Ling (1975) are reported.

Longer observations were taken in 1979 by the HEAO C-1 spectrograph on the HEAO 3 (High Energy Astronomy Observatory 3), which targeted the decay lines of ^{60}Fe (1.173 and 1.332 MeV), ^{26}Al (1.809 MeV) and ^{22}Na (1.275 MeV). The experiment performed a complete sky survey investigating the energy range from 50 keV to 10 MeV to a sensitivity level of 10^{-4} photons cm^{-2} s^{-1}. As presented in Mahoney et al. (1982) the survey obtained a positive detection only for the ^{26}Al line with a significance of 2.6 σ when adopting a point source model. The spectrum obtained is represented in Fig. 3.4. where the 1.809 MeV ^{26}Al decay line is indicated. This detection constrained the ratio of ^{26}Al to ^{27}Al produced by explosive nucleosynthesis in SNe to be $(^{26}\mathrm{Al}/^{27}\mathrm{Al})_{\mathrm{SN}} \sim (5.2\pm2.0)\times10^{-3}$ close to the theoretical value of $\leq 2\times10^{-3}$ for SNe.

Two years later Mahoney et al. (1984) revised the analysis of HEAO 3 data proposed in Mahoney et al. (1982). Remarkably, they found that by adopting a distributed source of γ-rays, the significance of the ^{26}Al line detection increased to 4.7 σ, ruling out the hypothesis of a point source. Moreover, they also provided a first estimate of the ^{26}Al mass, that resulted to be ~ 3 M$_\odot$.

At the same time also the SMM (Solar Maximum Mission) was operating (Forrest et al., 1980). Share et al. (1985) presented γ-ray data in agreement with

the HEAO 3 results. Even though the instrument was not designed for Galactic studies, it was anyway able to detect the ^{26}Al line at a significance of 10 σ. This confirmed the nucleosynthesis of ^{26}Al in the last 10^6 yr and opened the discussion about possible contributions from different sources other than SNe. In particular, the Galactic longitude distribution of novae was known to be strongly peaked towards the Galactic centre, and this could help explaining the flux observed.

The transition to the following generation of instruments was represented by GRIS (Gamma-Ray Imaging Spectrometer) that performed two flights during 1988. In this instrument the old technology adopted in the previous balloon-experiment was substituted with the new frontier one, that will be adopted from that moment on by the next generation of long-term space missions. For the first time high resolution Germanium spectrometer were adopted to achieve significantly greater sensitivity. These flights confirmed an emission from the Galactic Center at 511 keV and also a Galactic diffuse emission of γ-rays and hard X-rays (Tueller et al., 1991).

3.3 COMPTEL and INTEGRAL

3.3.1 Instrumentation

After the several small-size experiments developed in the eighties, the first big-scale γ-ray observatory was proposed. Compton Gamma-Ray Observatory (CGRO) was designed and funded by NASA as one of the four missions in the Great Observatory program, together with Hubble Space Telescope, Chandra X-ray Observatory and Spitzer Space Telescope. It was launched on April 5, 1991 and re-entered the Earth's atmosphere on June 4, 2000.

It carried four instruments among which COMPTEL (Compton Telescope) was the one dedicated to the imaging of the Galaxy in the energy band 0.8-30 MeV. To be an efficient Compton telescope COMPTEL needed to detect efficiently, identify unambiguously and record the direction and energy of the incoming photons (Schönfelder et al., 1984). To fulfil these requirements the instrument counted two detectors and four shielding domes, all represented in Fig. 3.5 (right sketch).

A detailed technical description can be found in Schoenfelder et al. (1993). The first detector was composed of seven cells with 28 cm of diameter and 8.5 cm deep, each of them connected to eight photomultiplier tubes. The second one was instead composed of 14 cylindrical NaI detectors with 28.2 cm of diameter and 7.5 cm deep. Two of the four domes shielded the top detector, whereas the

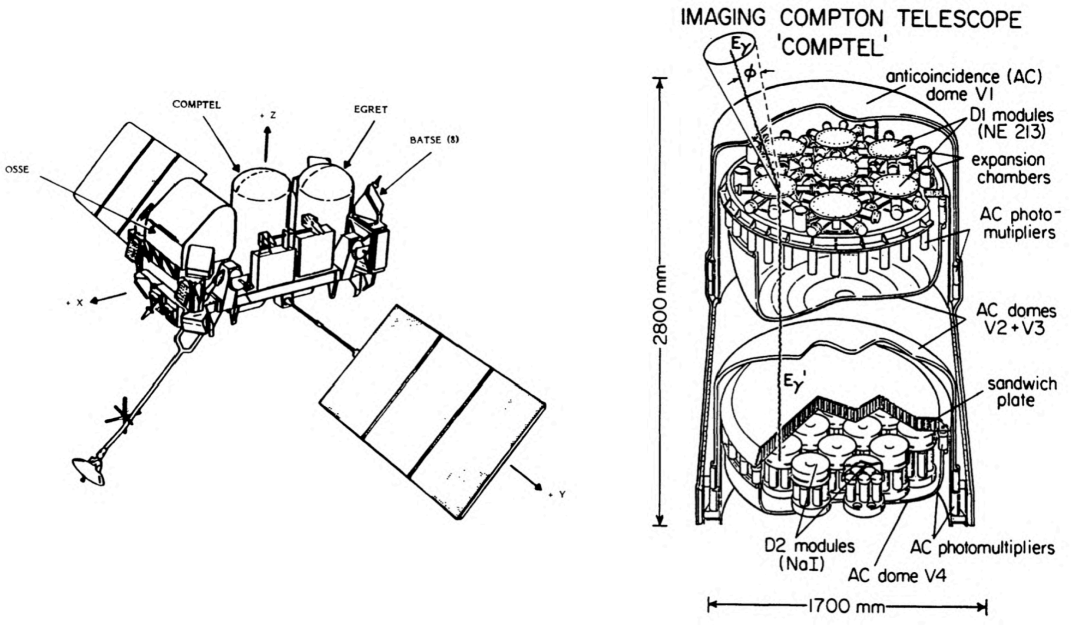

Figure 3.5: ***Left:*** *Sketch of the CGRO. COMPTEL and the three other instruments carried, OSSE (Oriented Scitillation Spectrometer Experiment), EGRET (Energetic Gamma-Ray Experiment Telescope.) and BATSE (Burst and Transient Source Experiment) are pictured.* ***Right:*** *Section of COMPTEL. In the upper part the seven liquid scintillators can be recognised, and in the lower part the fourteen cylindrical detectors are represented. The principle of operation is schematically pictured by the incoming photon that interacts with the top detector and scatters towards the bottom, before being absorbed. Pictures from Schoenfelder et al. 1993.*

other two shielded the bottom one. Through the domes it was possible to reject all those photons that were not coming from the forward direction, assuring an anti-coincidence system.

As explained in Sec. 3.1 one of the main limitations in γ-ray telescopes is the background. To limit the issues on that side COMPTEL was equipped with a system able to image the source, the sky background and the instrumental background simultaneously to improve the signal to noise ratio.

The scientific purpose behind the planning and design of COMPTEL was manifold. As clearly shown on the official COMPTEL website they could be grouped following these headings:

- study of discrete Galactic γ-ray sources such as pulsars, SN remnants, molecular clouds, hard X-ray sources, and higher-energy γ-ray sources;
- study of extra-galactic γ-ray sources such as nearby normal galaxies, active galaxies, quasars, and clusters of galaxies;
- study of the diffuse emission from the Galaxy;

- study of the cosmic diffuse γ-ray emission;
- γ-ray line spectroscopy;
- study of the time history and energy spectra of cosmic GRBs;
- study of solar-flare γ-rays and neutrons;
- search for linear polarisation from sources of medium-energy γ-rays.

In the years following the launch of COMPTEL several of these science objective were pursued and accomplished. Among these, Morris et al. (1993) and Ryan et al. (1993) measured the neutron flux in near-Earth orbits that allowed to determine the COMPTEL sensitivity when used as a neutron telescope. K. Bennett et al. (1993) reported the detection of a blazar with unusual low energy that could explain the bump observed at that same energy in the γ-ray spectrum. In the Active Galactic Nuclei (AGN) community COMPTEL contributed with the discovery of the two first quasars in the MeV regime, as shown by Hermsen et al. (1993). On the stellar side, the Crab nebula was observed by de Jager et al. (1996) and the globular cluster 47 Tucanae was also investigated by O'Flaherty et al. (1995), to prove the presence of a millisecond pulsar.

In the spring of 1999 one of the three gyroscopes on board started deteriorating until showing complete failure by the end of the same year. Therefore, NASA opted for the decommissioning of the satellite until the damages were still small enough to ensure a safe re-enter. The orbit of CGRO was gradually lowered until on June 4, 2000 it landed in the Pacific Ocean.

INTEGRAL is the second medium-sized mission of ESA's Horizon 2000 Science Programme dedicated to the fine spectroscopy and fine imaging of γ-ray sources in the range 15 keV - 10 MeV (C. Winkler et al., 2003). Russia and NASA are also involved providing a Proton launcher from Baikonur, Kazakhstan and the Deep Space Network ground station, respectively. It has been operating since 17 October 2002 even though it was originally planned for a 3 years duration only, with possible extension by 2 additional years. After its success it was further extended every two years until 2022 when the last extension was approved. INTEGRAL will be finally dismissed by the end of 2024, for a total duration of 22 years.

Even though INTEGRAL was ESA's heaviest scientific satellite at the time of launch it could be implemented as a low cost mission by re-using the XMM-Newton Service Module design. Among the different nominal orbits allowed by the launcher, an inclined, highly eccentric geo-synchronous orbit with the apogee in the northern hemisphere was selected. The reasons behind this choice are:

- an easier injection can be performed when adopting an eccentric orbit rather than a circular one;

- it is less demanding on the spacecraft thermal and power subsystems;
- it maximises the time (84% of the 72 hours of orbital period) spent outside the Earth's radiation belts (above 60 00 km of altitude).

During the 5 year operational lifetime the orbit was supposed to slowly shift from the initial one to a more favourable one (higher inclination and perigee) due to the disturbances of the Sun, Earth and Moon (Jensen et al., 2003).

The two main γ-ray instruments carried by INTEGRAL, the spectrometer SPI (Vedrenne et al., 2003) and the imager IBIS (Ubertini et al., 2003) cover the energy range 15 keV-10 MeV. Complementary, it carries two monitor instruments, one in the X-ray energy range 3-35 keV that partially overlaps with the γ-ray instruments sensitivity, and an optical V-band one, OMC. To properly monitor the instrumental background a charged-particle monitor, IREM, is also mounted on the payload (Diehl, 2013b). Fig. 3.6 represents two technical sketches of INTEGRAL. On the left

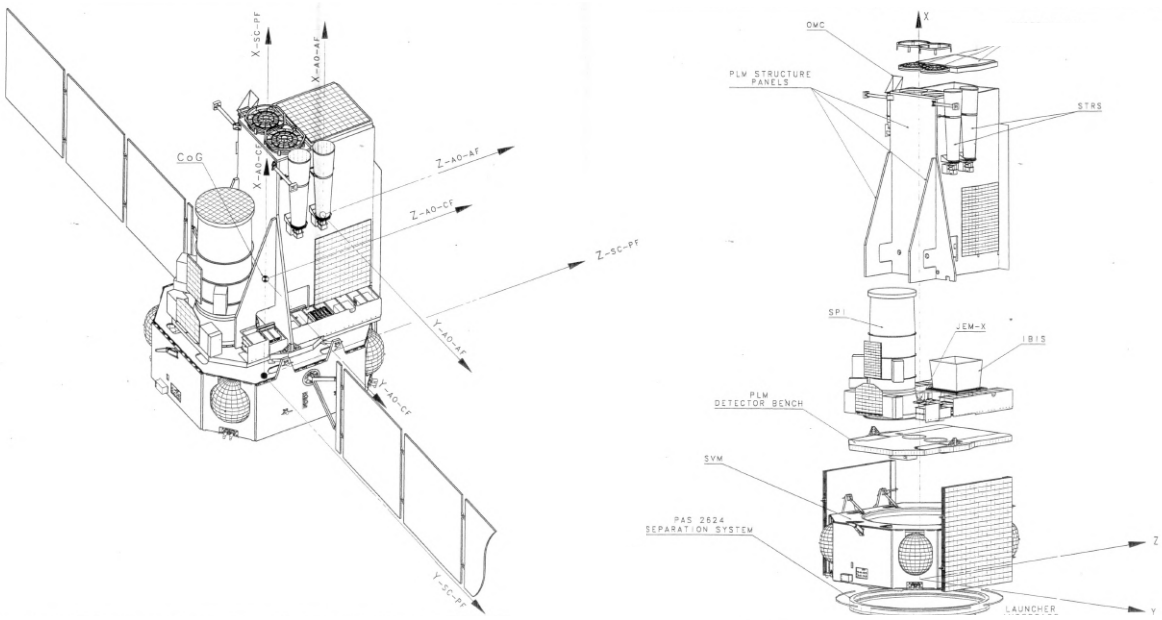

Figure 3.6: ***Left:*** *sketch of the assembled satellite with the orientation in 3D space.* ***Rigth:*** *INTEGRAL exploded view. In the central part the two main instruments, SPI on the left and IBIS (Imager on Board the INTEGRAL Satellite) on the right, are sketched. Taken from https://www.cosmos.esa.int/web/integral/spacecraft-drawings.*

side, a sketch of the complete assembly of the instrument with the orientation in 3D space is shown, whereas on the right side the single components are separated. In particular, IREM and SPI are visible in the central part of the exploded sketch, on the right and left sides respectively.

SPI can perform the spectral analysis of point and extended sources in the energy range 18 keV - 8 MeV. With a resolution of 2.2 keV (FWHM) at 1.33 MeV,

SPI is able to collect fine spectra of the cosmic targets, in order to identify useful spectral lines for the physical study of the source. The detector is composed of 19 Germanium units (15 still operational) at the operating temperature of 85 K. As was previously done with COMPTEL the detector is shielded with an anticoincidence system so as to reduce the background radiation. The performances of SPI, when combined to the immediate location determination of IBIS, can provide a detailed map of the γ-ray MW, thus accomplishing the main scientific goal of the mission.

3.3.2 Observations

COMPTEL data analysis was composed of three phases (Diehl et al., 1992):

- the calibration of raw data;
- the background and response determination;
- the scientific analysis.

As explained in Sec. 3.1, the main issue in this energy band is the background, as shown in Fig. 3.7. On the left, the imaging of the Crab nebula sky region before the instrumental background subtraction is represented. The presence of the background creates the extended and irregular structures highlighted by the darker shade. On the right, the same region of the sky after background subtraction is plotted. The extended features disappear and only the central region where the Crab pulsar is located is left. This analysis provided in 1993 the first preliminary imaging of the Galactic plane in the 1.809 MeV γ-ray line, signature of ^{26}Al recent decay. Diehl et al. (1993) presented the map in Fig. 3.8 and analysed different source models to explain the emission. The point source hypothesis was excluded after the comparison with their emission simulations. Indeed, a point source responsible of a large fraction of the emission would have produced a clumpy image. Nevertheless, the nova distribution hypothesis was also excluded, since in that case an even smoother image was expected. The best fit was obtained assuming production by a population of SNII. In particular the WR stars, that were already proposed as a production site of ^{26}Al by Dearborn et al. (1985), follow a spatial distribution that overlaps almost perfectly with the COMPTEL map, supporting even more this hypothesis.

Further confirmation of the production from SNII was provided by Diehl et al. (1995), by the means of new emission maps along the Galactic plane (Fig. 3.9). The three maps refer to three different energy bands, namely, from the top to the bottom panel, 1.5 - 1.7 MeV, 1.7 - 1.9 MeV and 1.9 - 2.1 MeV. With respect to the previous map (see Fig. 3.8) the degree of detail shows a large improvement but the most stunning feature in this case is how much the middle panel (1.7 - 1.9 MeV),

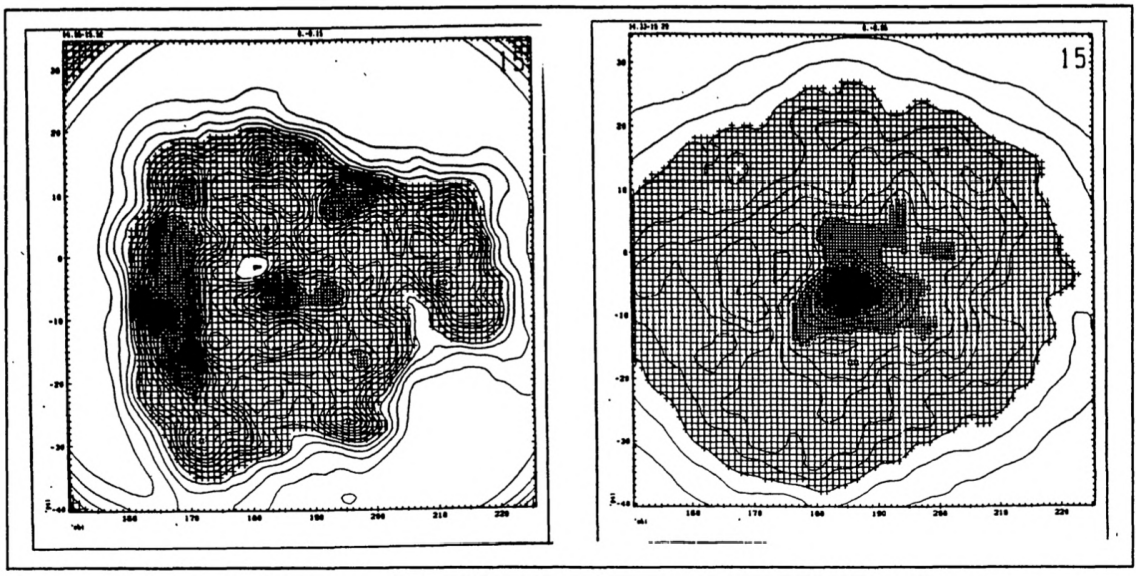

Figure 3.7: *Crab nebula in the γ-ray band.* ***Left:*** *γ-ray map before background subtraction. Several off-centre extended structure are detected.* ***Right:*** *after background subtraction. All the substructures are removed and only the centre, where the Crab pulsar is located, appears. Taken from Diehl et al. (1992).*

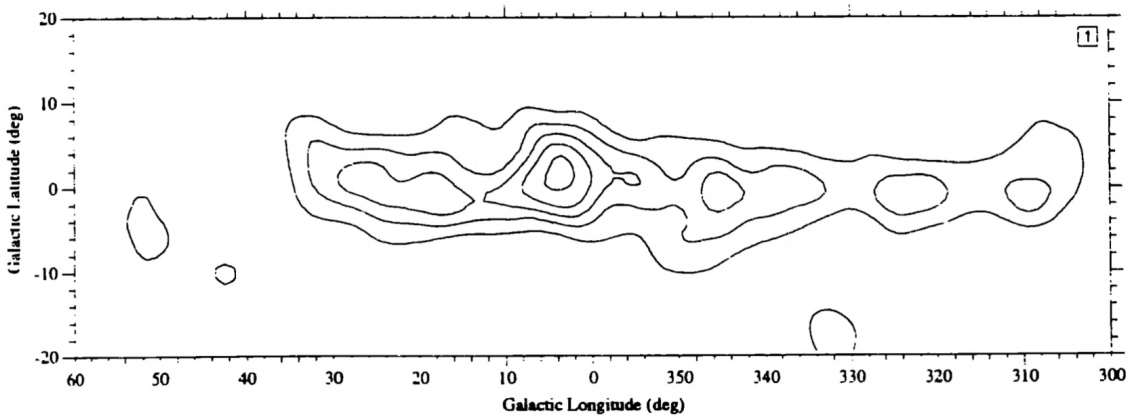

Figure 3.8: *First map produced adopting COMPTEL data, after two years of observations. The emission is too smooth to be produced by a point source in the Galactic center with a large yield, but not smooth enough to be produced by novae with low yield. The best fit is obtained assuming emission from massive stars, in particular WR stars, whose distribution almost overlaps with the 1.809 MeV map.*

where the signature of the ^{26}Al decay is expected, differs from the other two. It indeed shows a prominent emission on the Galactic plane, whereas the others are nearly empty. Part of the clumpy structure is ascribed to active SF regions as Vela, Carina and Cygnus.

Figure 3.10 by Oberlack et al. (1996) provides the 1.809 MeV map of the whole Galaxy from 3.5 yr of observation. The contour levels of the emission indicate the

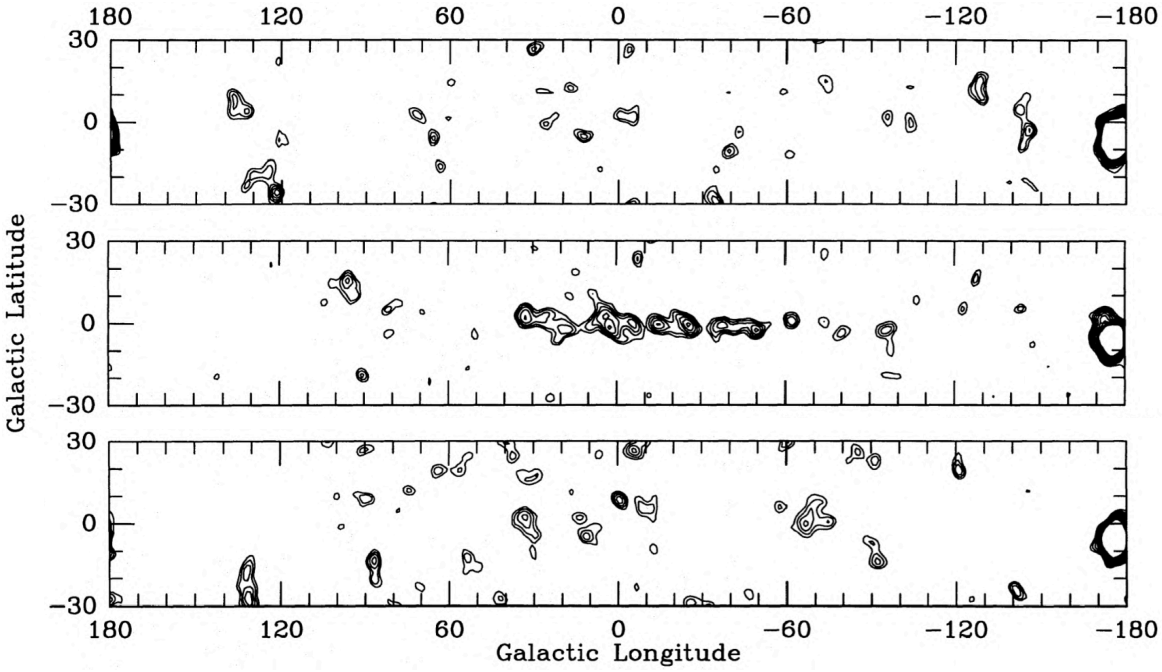

Figure 3.9: *Maps of the Galactic plane provided by COMPTEL. From the top to the bottom panel, the energy bands represented are 1.5 - 1.7 MeV, 1.7 - 1.9 MeV and 1.9 - 2.1 MeV. The relevant aspect here is the difference between the middel panel and the other two. In the middel one, where the ^{26}Al flux is expected, the emission is clearly evident, whereas in the other two panel is almost absent. Taken from Diehl et al. (1995).*

flux intensity and the author also indicate the regions responsible for the emission. The distribution, concentrated in the Galactic latitude $|b| \leq 30°$, rules out the purely local origin of ^{26}Al. Nevertheless, the clumpiness in the map indicates that the local contribution is non negligible, as emphasised also by Schoenfelder et al. (1996).

Once all the data from the nine years exposure were collected, some more general and firm conclusions could be drawn and the final 1.809 MeV map in Fig. 3.11 was released (Plüschke et al., 2001).

First of all, the 1.809 MeV map allowed to exclude the purely local origin of ^{26}Al. The most likely scenario was that the 1.809 MeV flux was produced by a localised foreground inside the solar circle but within few kpc from the Sun (Diehl et al., 1995) together with a diffuse Galactic emission.

Regarding the stellar progenitors that ejects ^{26}Al back into the ISM, the best hypothesis was that only a combination of different sources could reproduce the maps. In particular, SNII or WR stars could be responsible for most of the ^{26}Al flux. Novae, on the other side, were a promising candidate for a secondary, more diffuse

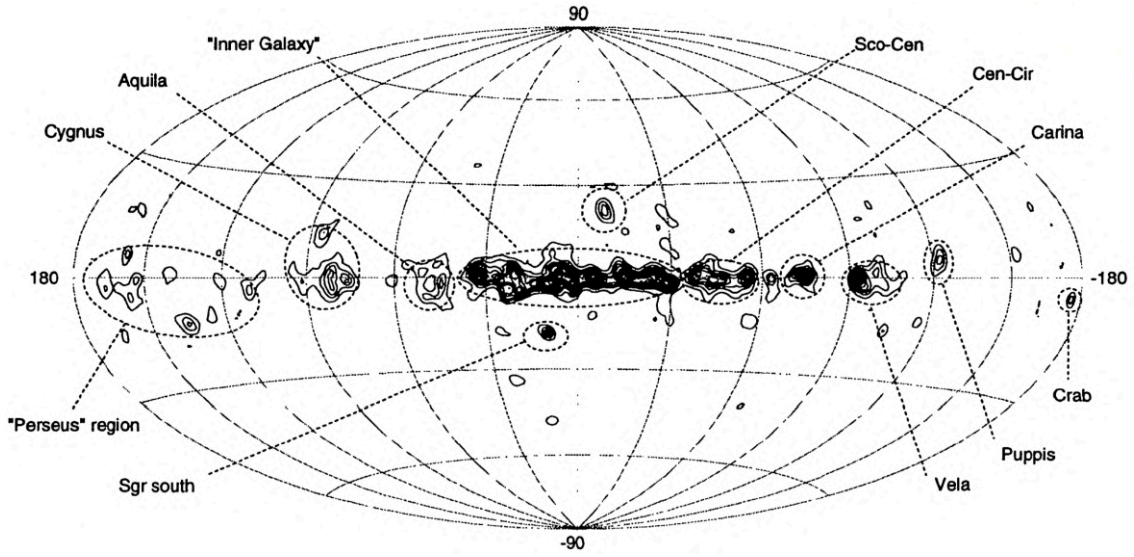

Figure 3.10: *All-sky map of the 1.809 MeV MW. The contour lines represent the intensity of the emission. The flux is concentrated within the Galactic latitude $|b| \leq 30°$, excluding the purely local origin of ^{26}Al. Nevertheless, the clumpiness shown by the map indicates that the local contribution is non negligible. Taken from Oberlack et al. (1996).*

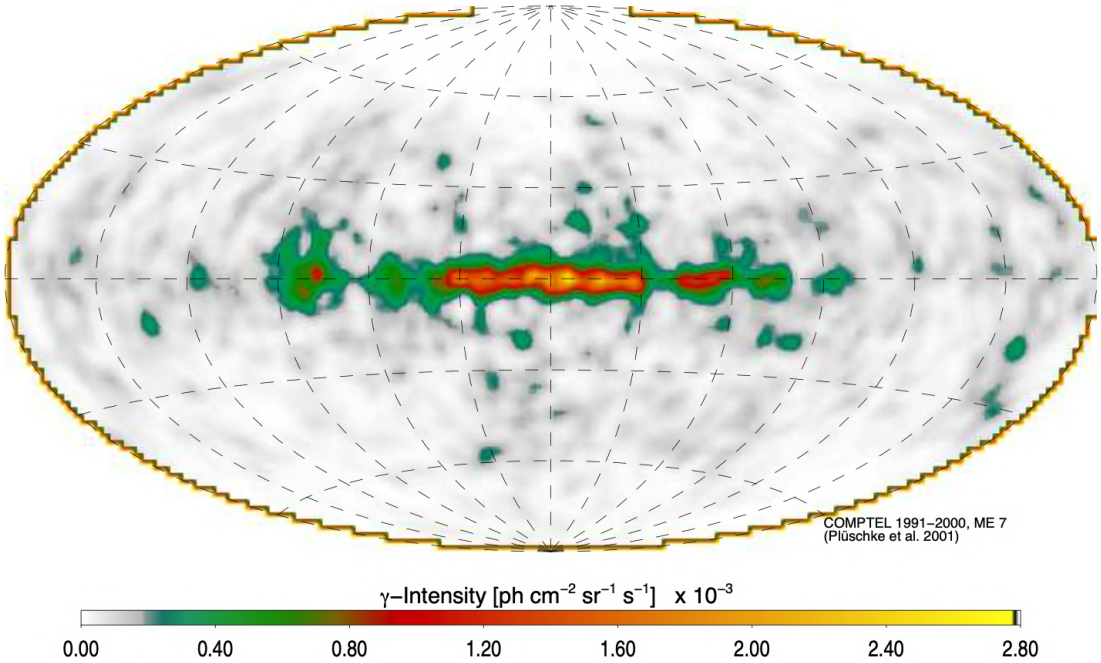

Figure 3.11: *The final 1.809 MeV map provided by COMPTEL, color coded with the flux intensity. Taken from Plüschke et al. (2001).*

source. This scenario also confirmed the hypothesis by Oberlack et al. (1996), according to which ^{26}Al production came mainly from a young stellar population

with an underlying older population.

The observed flux was also converted into a ^{26}Al mass, assuming the distance of the sources. Given that some of the ^{26}Al flux came from local progenitors, the total mass of ^{26}Al should be in the range 1 - 1.5 $M_{\odot}$ (Schoenfelder et al., 1996).

After the dismission of COMPTEL, INTEGRAL was designed to be sensitive to the same radiation so as to collect the legacy of COMPTEL and refine its previous results. The measurements performed, indeed, showed strinking similarities to the COMPTEL ones and several features of the COMPTEL-based ^{26}Al image reappear in the INTEGRAL result (Diehl et al., 2021a). The resolution of the instruments was improved so that SPI could reveal more info about the location of the sources (through the Doppler shifts in the ^{26}Al line centroid) induced from Galactic rotation and from dynamics of the ejected ^{26}Al as it propagates in the ISM (Diehl et al., 2003b; Diehl et al., 2006a).

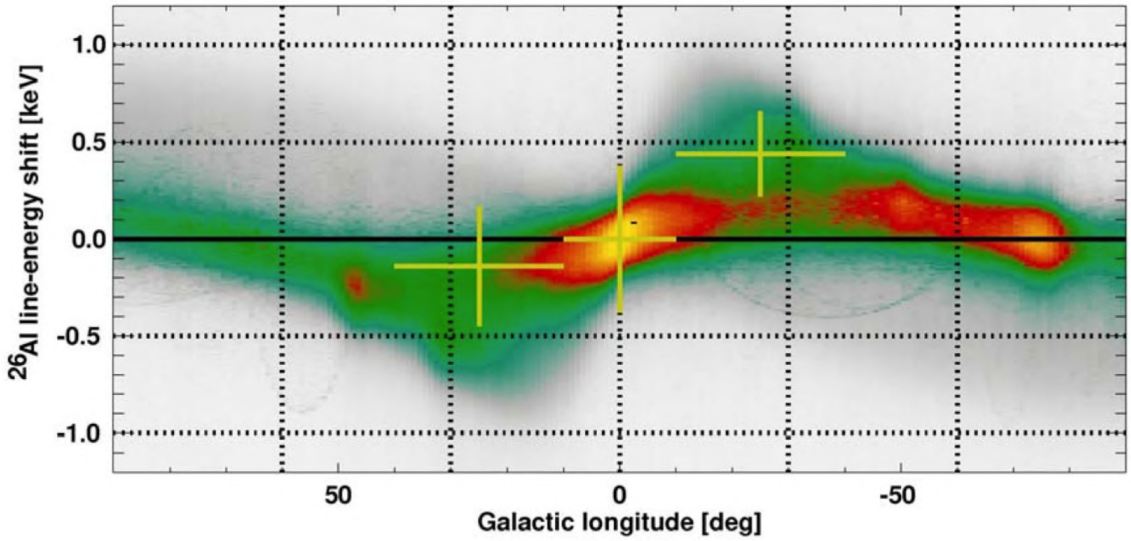

Figure 3.12: *Energy shifts (yellow data) of the ^{26}Al decay line centroid measured at three different Galactic longitude bins: from 40° to 10°, from 10° to -10° and from -10° to -40°. The shifts are compatible with the expected Doppler shifts caused by the Galactic rotation. The measurements are compared to a 3D distribution of ^{26}Al convoluted with the MW rotation curve. The match between data and model implies that the bulk of the 1.809 MeV emission comes from the inner Galaxy rather than foreground sources. Taken from Diehl et al. (2006b).*

The expected Doppler shift in the centroid of the ^{26}Al line was actually detected, as shown in Fig. 3.12 taken from Diehl et al. (2006b). Here, the Doppler shift measured at different Galactic longitudes is plotted (yellow data). In particular three Galactic longitude bins were taken: from 40° to 10°, from 10° to -10° and from -10° to -40°. The positive energy shift on the y axis can be ascribed to a blue shifted source, whereas on the contrary, the negative shifts are produced by red shifted

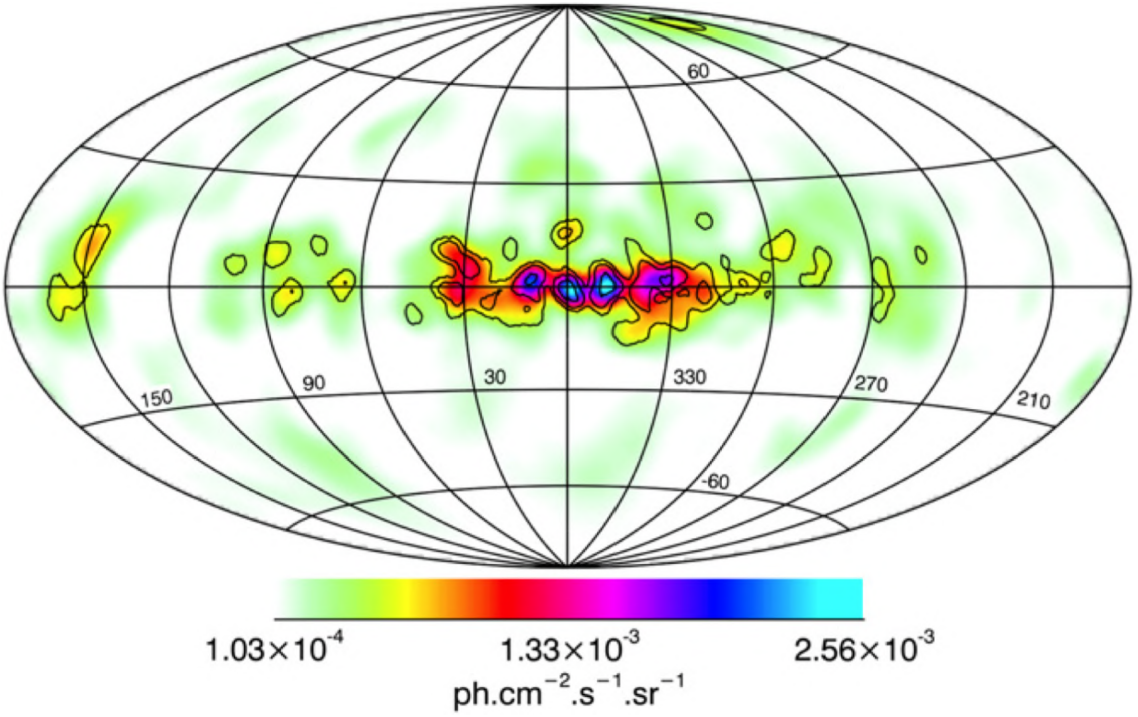

Figure 3.13: *1.809 MeV emission map of the MW as obtained after combining 10 years of data. The colour coding represent the intensity of the flux collected, as represented by the colour bar at the bottom. The outstanding feature is the resemblance to the previous COMPTEL map, reported in Fig. 3.11. Taken from Bouchet et al. (2015).*

sources. The data are then compared to the 3D distribution of ^{26}Al convoluted with the rotation curve of the Galaxy. The perfect match between data and model confirms the Galactic nature of the 1.809 MeV flux: since the ^{26}Al rotates together with the Galactic ISM, the emission comes mainly from the inner Galaxy rather than foreground sources (Diehl et al., 2007).

With the increased precision of SPI the possibility to adopt ^{26}Al as an estimator of the current SFR in the Galaxy opened up. The advantage of using the γ-ray techniques is that a highly penetrating radiation is less sensitive to the occultation by interstellar clouds, whose location is still pretty unsure (Diehl et al., 2006b; Diehl et al., 2021a). Moreover, the γ-ray flux collected is the average over a time scale (~1 Myr) associated with one current generation of massive stars.

From the spectrum obtained by SPI, Diehl et al. (2006b) measured a 1.809 MeV flux of (3.3±0.4) × 10^{-4} ph cm^{-2} s^{-1}. From this value, the ^{26}Al mass could also be derived, that resulted in 2.8±0.8 M$_\odot$. Adopting the same data and assuming an IMF for the Galaxy, the current core-collapse SN rate could be estimated. The measurements imply 1.9±1.1 CCSNe per century, which in turn corresponds to a SFR of ~4 M$_\odot$ yr^{-1} (Diehl et al., 2006b).

After ten years of data the updated 1.809 MeV map of the MW in Fig. 3.13

was presented by Bouchet et al. (2015). As anticipated, it strongly resembles the COMPTEL one in Fig. 3.11. The whole MW is colour coded following the 1.809 MeV flux, according to the colour bar represented at the bottom.

The improved sensitivity of INTEGRAL allowed the satellite to investigate also ^{60}Fe for the first time. ^{60}Fe, as already anticipate in Sect. 1.2.1, differs from ^{26}Al in few aspects, that, even though could seem minor, actually increase the uncertainty in the measurements. As previously explained in Sect. 1.2.1, ^{60}Fe decays in ^{60}Co that in turn decays into ^{60}Ni with τ_{60Co} ~7.6 yr. The biggest issue when dealing with ^{60}Fe is related to the interaction between cosmic rays and the spacecraft: the irradiation by cosmic rays produces spurious ^{60}Co nuclei inside the instrumentation which are not related to any ^{60}Fe from cosmic sources. This spurious ^{60}Co population should reach a steady state within few lifetimes τ_{60Co} and therefore, during the first ≈10 years it shows a quasi-linear growth. This prevents fine measurements of ^{60}Fe.

Due to these limitation the conclusions drawn regarding ^{60}Fe are less firm. Several authors analysed the data and estimated independently the ^{60}Fe flux in the Galaxy. Martin et al. (2009) found $9.1\pm2.6 \times 10^{-5}$ ph cm^{-2} s^{-1}, whereas Wang et al. (2007) obtained $4.4\pm0.9 \times 10^{-5}$ ph cm^{-2} s^{-1} rad^{-1}. Additionally, Wang et al. (2020) also estimated a flux of ^{60}Fe of $0.31\pm0.06 \times 10^{-3}$ ph cm^{-2} s^{-1} when the two decay lines are combined together.

Adopting these measurements for the ^{60}Fe flux, also the flux ratio ^{60}Fe/^{26}Al was explored. This quantity is indeed relevant as a test for stellar evolution and nucleosynthesis models because, if the sources of the two isotopes are the same, their actual number and distances cancel out in such a ratio (Wang et al., 2020). Wang et al. (2007) found a ^{60}Fe/^{26}Al flux ratio of (14.8±6.0)% and later, Wang et al. (2020) revised this value obtaining a ratio of (18.4±4.2)%, compatible within the errors with the previous one. These results are consistent with the theoretical predictions by Timmes et al. (1995) (^{60}Fe/^{26}Al~16.0%±12.0%), Limongi et al. (2006) (^{60}Fe/^{26}Al~18.5%±6.25%) and with those by Limongi et al. (2013) (^{60}Fe/^{26}Al~11.0%±4.0%).

What all the authors agree on is the fact that the emission is in any case too weak to determine a ^{60}Fe Galactic distribution, therefore maps as those reported in Fig. 3.11 and Fig. 3.13 are not yet available.

INTEGRAL was also able to investigate nearby localised regions of the Galaxy identified as stellar associations. The most interesting results were obtained for the Cygnus (Knödlseder et al., 2004; Martin et al., 2009), Orion (Siegert et al., 2017a), Vela (Maurin et al., 2004), Carina (Voss et al., 2012) and Scorpius-Centaurus (Diehl

et al., 2010) groups of massive stars.

Among those listed, the most interesting regions are Cygnus and Orion. The Cygnus region was already addressed by COMPTEL, as reported in Diehl (1995) and del Rio et al. (1996). After the INTEGRAL data were collected several works focused on that region, such as Diehl et al. (2003a) and Reipurth et al. (2008). Cygnus appeared quite bright in the 1.809 MeV emission, with indications of a slightly broadening of the line, consistent with the typical motion of the ISM (Martin et al., 2009). What in general emerged was that due to the small statistic on the astrophysical fluxes and the poor angular resolution of the instrument its 1.809 MeV morphology could not be determined accurately. Nevertheless, the location of the centre was determined to be (l,b)=(81°,-1°) and the bulk motion of the emitting medium was almost negligible. The total 1.809 MeV flux measured was (6±1) $\times 10^{-5}$ ph cm^{-2} s^{-1} that includes the Cygnus emission, together with the background and foreground contribution. Modelling the latter two, the emission from the Cygnus region only was reduced to (3.9±1.1) $\times 10^{-5}$ ph cm^{-2} s^{-1} (Martin et al., 2009).

Regarding the ^{60}Fe emission at 1.173 and 1.332 MeV in the Cygnus region, it was expected to be quite weaker relative to the ^{26}Al one. Indeed, no 1.173/1.332 MeV signal was detected. The reason could be related to the age of the region: since Cygnus is pretty young (~3 Myr) no or very few SNe occurred up to now. This hypothesis is actually confirmed by the lack of SN remnants and radio pulsars (Martin et al., 2009). Only an upper limit for the ^{60}Fe flux in the Cygnus region was derived, resulting 1.6×10^{-5} ph cm^{-2} s^{-1}.

The Orion region is located towards the outer Galaxy and hosts one of the most nearby massive star cluster, Orion OB1 (≈450 pc). It is characterised by a a large spread in the age of the stars, from 1.5 Myr to 15 Myr, that allows to derive a history of the ^{26}Al emission, by adopting population synthesis models. Voss et al. (2010) derived a flat time profile of the 1.809 MeV emission in Orion, and predicted that it will increase in time. Moreover, Diehl (2002) found a 1.809 MeV emission of 7.5×10^{-5} ph cm−2 s^{-1}.

In conclusion, COMPTEL first and INTEGRAL later, derived the 1.809 morphology of the MW, finding consistent results. ^{26}Al appears to be distributed in the Galactic plane with a higher concentration towards the Galactic centre and the nearby sources do not dominate the emission. The production by massive stars is the one that best reproduces the observation due to their distribution in the Galaxy, even though an additional smaller contribution from more diffuse sources, such as novae, could explain even better the smoothness of the 1.809 MeV maps. By analysing the data it was possible to determine the ^{26}Al flux and mass

that resulted to be (3.3±0.4) × 10^{-4} ph cm^{-2} s^{-1} and 2.8±0.8 $M_{\odot}$, respectively. The current CCSN rate and SFR in the MW was also derived, obtaining 1.9±1.1 CCSNe per century and ∼4 $M_{\odot}$ yr^{-1}.

INTEGRAL also detected the 1.173 MeV and 1.332 MeV, corresponding to the decay chain of ^{60}Fe. Due to its nuclear and astrophysical characteristics the measurements are more uncertain. Notwithstanding this, the ^{60}Fe flux was determined to be (9.1±2.6) × 10^{-5} ph cm^{-2} s^{-1} and the flux ratio ^{60}Fe/^{26}Al was constrained to (18.4±4.2)%.

3.4 Future perspectives: COSI-SMEX

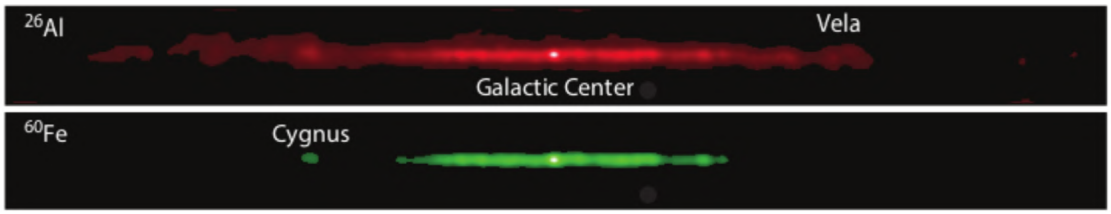

Figure 3.14: *COSI simulations for the Galactic emission al 1.809 MeV produced by the radioactive decay of ^{26}Al (top panel) and for the 1.173 and 1.332 MeV, ascribed to the decay of ^{60}Fe. Taken from J. Tomsick et al. (2019).*

INTEGRAL is currently in its latest phase and no other currently operational instrument is able to perform its same observations, with the same quality and coverage. Therefore, the White Paper by Timmes et al. (2019) advocated for the need of a new instrument covering the γ-ray energy band that has been explored by INTEGRAL until now. The requests made suggest a new γ-ray instruments with a line sensitivity 1-2 orders of magnitude better than the previous ones ($\simeq 1\times10^{-7}$ ph cm^{-2} s^{-1}) angular resolution of 1-2° and energy resolution of 0.1°. Such an instrument could pursue the science already explored by COMPTEL and INTEGRAL but with a new level of detail. These technical requirements will enable to differentiate the emission lines from specific OB associations against the diffuse radioactive afterglow of stellar activity, increasing the number of observed OB associations of a factor between 10 and 35.

With this purpose NASA is working to a new γ-ray instrument, Compton Spectrometer and Imager (COSI), described by J. Tomsick et al. (2019). COSI will cover the energy band often referred to as “MeV Gap", from 0.2 to 5 MeV, given the little attention that has been addressed to it over the last decades. From the technical point of view it matches the requirements laid down by Timmes et al. (2019) as well as the science cases. COSI will hopefully be able to:

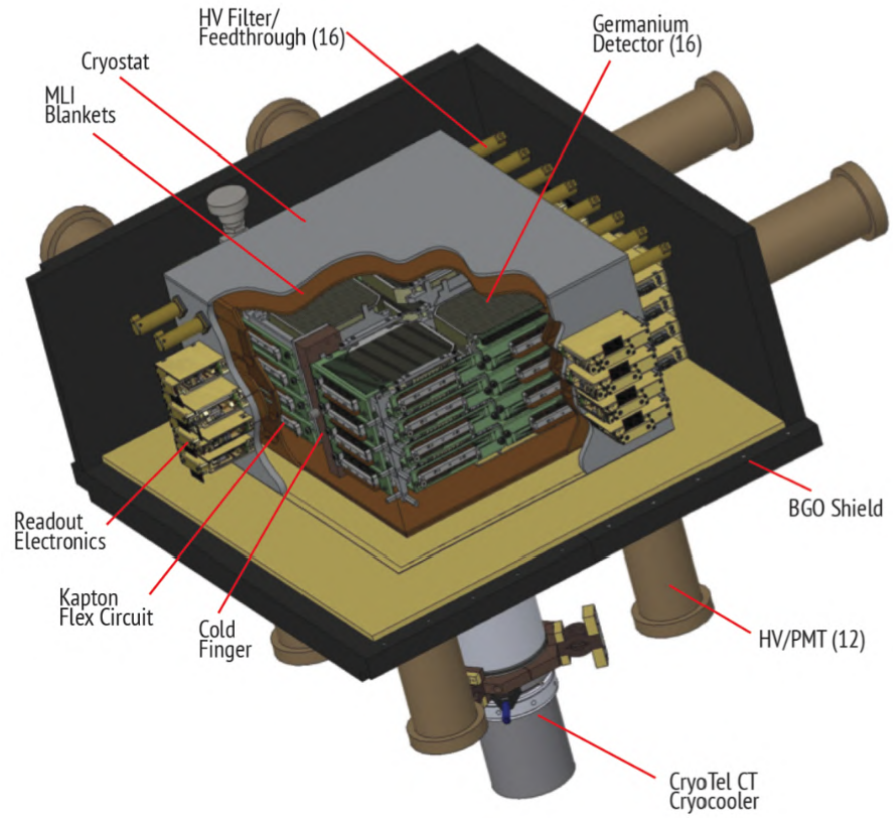

Figure 3.15: *Sketch of the design of COSI. Taken from J. Tomsick et al. (2019).*

- image ^{26}Al with unprecedented sensitivity and perform the first mapping of ^{60}Fe;
- study both compact objects in the Galaxy and external AGNs, together with GRBs;
- search for electromagnetic counterparts to gravitational waves adopting the improved field of view and localisation capabilities.

The simulation of the MW emission as will be detected by COSI have already been performed. Those at 1.809 MeV (^{26}Al decay emission) and 1.173 and 1.332 MeV (^{60}Fe decay emission) are reported in Fig. 3.14. To obtain these maps the flux distribution by COMPTEL and INTEGRAL was assumed.

As its precursors COMPTEL and INTEGRAL, COSI also is a Compton telescope, adopting sixteen Germanium detectors housed in a cryostat and cryogenically cooled at <80 K. This, together with the shielding applied, will contribute to reduce the background. Fig. 3.15 sketches the design of COSI.

The first tests were carried out performing high-altitude balloon flights back in 2005, 2009, 2014 and 2016. This last flight in particular was quite successful, as demonstrated by J. A. Tomsick (2016) that documented the discovery and localisation of the GRB160530A. After the positive results obtained during the test

flights, the launch of COSI was initially planned for 2025 but currently, NASA delayed it to 2027.

4

Chemical Evolution of ^{26}Al and ^{60}Fe in the Milky Way

In this Chapter I show the theoretical mass estimates of ^{26}Al and ^{60}Fe throughout the Galaxy, performed with a numerical chemical evolution model including detailed nucleosynthesis prescriptions for stable and radioactive nuclides. The aim is that of providing a value for the ^{26}Al and ^{60}Fe masses in the Galaxy to be compared with the COMPTEL and INTEGRAL observations and constrain the ^{26}Al and ^{60}Fe nucleosynthesis. The final purpose is that of identifying the best set of yields that can reproduce the ^{26}Al and ^{60}Fe masses which can be adopted in future chemical evolution studies.

The Chapter is organised as follows. In Sect. 4.2 I describe the chemical evolution model, in Sect. 4.3 I show the results obtained, in Sect. 4.4 I compare some theoretical predictions with the observational constraints, in Sect. 4.5 I comment the yields adopted and in Sect. 4.6 I draw the main conclusions.

The results presented in this Chapter are published in the paper Vasini et al. (2022).

4.1 Introduction

As anticipated in Chap. 3, COMPTEL (see Schönfelder et al. 1984) and INTEGRAL (see Christoph Winkler 1994) were both designed to detect the decay emission in the Galaxy of two unstable elements, ^{26}Al and ^{60}Fe. It is recalled from Chap. 1 that ^{26}Al and ^{60}Fe are both SLRs, with decay times τ_{26Al} = 1.05 Myr and τ_{60Fe} = 3.75 Myr, respectively (Diehl, 2013b). Their lifetimes make them suitable for the study of the recent history of the MW, with particular focus on the latest nucleosynthesis

events (see Brinkman et al. 2021), since they can be considered tracers of the active SF regions.
As showed in Chap. 3, COMPTEL and INTEGRAL agreed on the ^{26}Al observed. In particular, COMPTEL estimated around 1.5 – 2 $M_\odot$ of ^{26}Al within 5 kpc from the Galactic centre (Prantzos et al., 1996) and INTEGRAL observations range from 1.7 ± 0.2 $M_\odot$ (Martin et al., 2009) to 2.0 ± 0.3 $M_\odot$ (Diehl et al. 2010; Diehl 2016), depending on the assumed source location.

The information collected on ^{60}Fe are poorer, since, among the two, only INTEGRAL had the sensitivity to observe it and it provided only the ^{60}Fe flux finding that the brightness of its two emission lines, 1.173 MeV and 1.332 MeV, was ~ 15% ± 5% of that of ^{26}Al.

However, the progresses in γ-ray observations were not followed at the same rate by chemical evolution investigations, which could have offered new theoretical constraints independent of the observational ones. One of the main reasons for this lack is the complexity of the treatment of radioactive nuclei within a standard chemical evolution model.

To obtain easy and explicit solutions for the equations, the adopted models were mainly analytical, such as those developed by Clayton (1984b) and Clayton (1988). The limits of analytical models are the assumptions necessary to derive the solution which are typically very restrictive. For example, some models consider only one burst of SF, simulating a stellar population formed at the same time and from the same gas, which represents a very rough hypothesis for the evolution of the MW. Another restrictive hypothesis is IRA (instantaneous recycling approximation): stars with mass < 1 $M_\odot$ never die, whereas stars > 1 $M_\odot$ die instantaneously, thus enriching immediately the ISM with their nucleosynthesis products. In other words, this approximation neglects the stellar lifetimes and is acceptable only for elements produced on timescales negligible relative to the age of the Universe.

The most robust way to study chemical evolution is by using the numerical models introduced in Chap. 2, both for stable and unstable nuclei where it is possible to consider the effect of many stellar generations, different Star Formation Histories (SFHs) and the detailed stellar lifetimes and stellar yields. In the past, detailed numerical models for radioactive nuclides have been computed only by Timmes et al. (1995) and by Côté et al. (2019a), this latter focused on the isotopic ratios at the time of formation of the SS.

This work is aimed at analysing the chemical evolution of ^{26}Al and ^{60}Fe in the MW by means of a very detailed chemical evolution model, already tested for a wide set of data relative to both the solar vicinity and the whole disc (see Romano

et al. 2010; Romano et al. 2020; Palla et al. 2020). The model, accounting for the formation and evolution of the thick and thin discs, is a revised version of the two-infall model of Chiappini et al. (1997) (see Chap. 2). For the bulge I adopt a separate model taken from Matteucci et al. (2019). Both models (for the discs and the bulge) take into account detailed stellar lifetimes, SN progenitors and detailed stellar yields. Moreover, they assume that the two discs and the bulge formed by different episodes of extra-galactic gas accretion, occurring on different timescales. Here, these models have been improved by including the equations for the radioactive elements ^{26}Al and ^{60}Fe (see Eq. 2.19). The adopted stellar yields are the most recent ones and they include: massive stars, AGB stars, Super-AGB stars, SNIa and, for the first time, the contribution of novae to radioactive nuclide production.

I aim at obtaining new theoretical constraints to the observed mass of ^{26}Al in the Galaxy, as well as providing a clear prediction for the ^{60}Fe mass in the MW that could be used as a reference for future γ observations. I also intend to compare the results to the previous work on ^{26}Al and ^{60}Fe by Timmes et al. (1995).

4.2 The model

In this Section I recall the main assumptions and characteristics of the adopted chemical evolution model for the different galactic components (discs and bulge).

4.2.1 Main assumptions

Thick and thin discs

I aim at studying the evolution of the chemical abundances of ^{26}Al and ^{60}Fe throughout the whole Galaxy, both in the bulge and in the discs. To purse this objective, for the thick and thin discs evolution I consider the two-infall model as described in Eq. 2.9 with the *inside-out* scenario obtained adopting Eq. 2.10. The SFR is the Schmidt-Kennicutt in Eq. 2.2 with SFE $\nu = 1$ Gyr^{-1} for the thin disc and $\nu = 2$ Gyr^{-1} for the thick disc in agreement with previous works (e.g. Grisoni et al. 2017). As IMF the Kroupa et al. (1993) presented in Eq. 2.6 was adopted. The Galactic thin-disc is divided into concentric rings around the Galactic centre, each of them 2 kpc wide, without any exchange of matter among them. The first ring inside 2 kpc contains the bulge. Inside each ring, homogeneous mixing of gas is assumed. The total surface mass density in each ring is tuned to reproduce the observed exponential present time distribution (see later). The

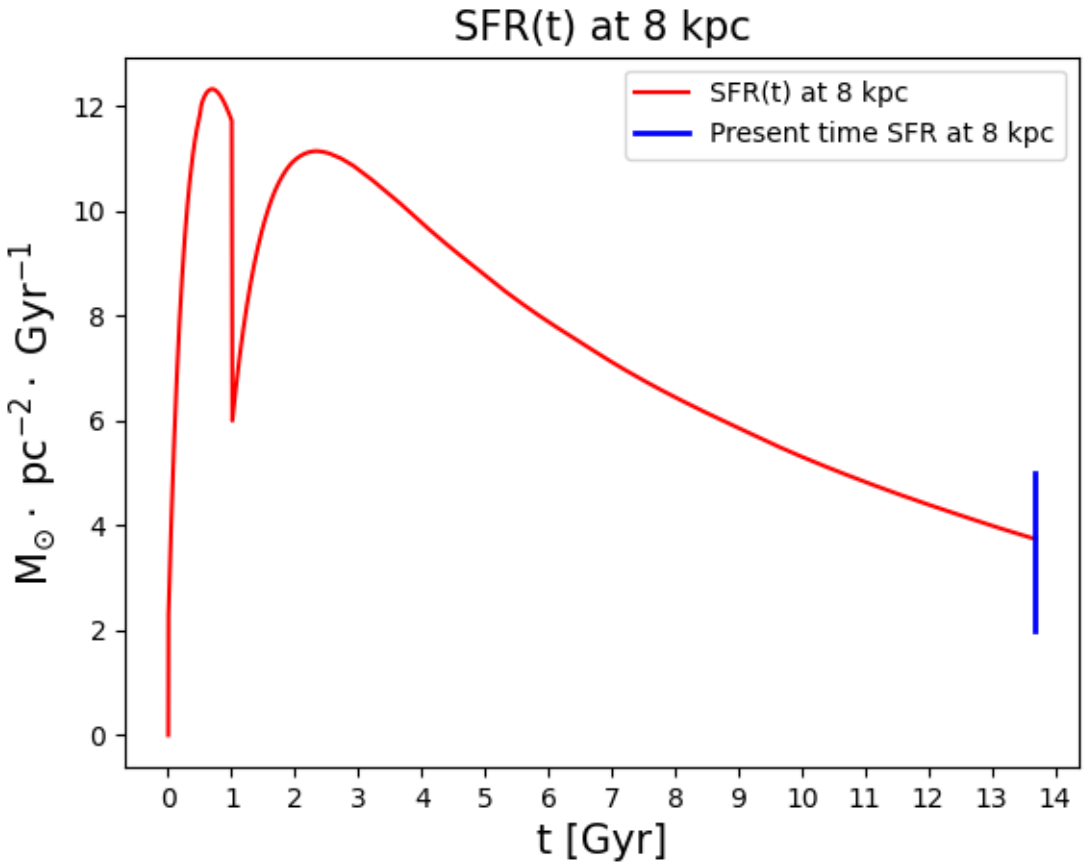

Figure 4.1: *The red line represents the SFR(t) at 8 kpc as a function of time. The SFR in the solar neighbourhood, according to the prescriptions assumed, shows two peaks: the first infall is responsible of the first SFR peak, then the SFR drops until the second infall starts and the SFR increases again. The blue line marks the observed present time SFR according to Prantzos et al. (2018).*

amount of gas and its chemical composition are instead the unknowns of my model.

In Fig. 4.1 I show the SFR as a function of time in the solar neighbourhood. The two peaks are due to the assumed double infall. The first infall, with 1 Gyr of time scale during which the thick-disc formed, is responsible for the first peak whereas the second infall, still ongoing at the present time, forms the thin-disc. The present SFR value at 8 kpc is around $\sim 3\ M_\odot\ pc^{-2}\ Gyr^{-1}$, in agreement with the observations (see Prantzos et al. 2018).

The stars that contribute to the chemical enrichment of the ISM are CCSN, SNIa and novae, that are included in the model as indicated in Eq. 2.14 and Eq. 2.15.

The bulge

As already stated, the previous assumptions are valid only for the Galactic thick and thin discs ($R > 2$ kpc), whereas for the bulge ($R \leq 2$ kpc) the prescriptions are different. I follow the model by Matteucci et al. (2019), which already reproduces the main observational bulge features.
The SFR is again that by Kennicutt (1998) as reported in Eq. 2.2 with a SFE $\nu = 25$ Gyr^{-1}, and the IMF by Salpeter (1955) reported in Eq. 2.4, which is top-heavier than the one for the discs and is in agreement with the IMF derived for the bulge by Calamida et al. (2015).
These choices are required if one wants to reproduce the stellar metallicity distribution function as well as the abundance patterns of the bulge (see Cescutti et al. 2011; Matteucci et al. 2019).

I assume that the bulge formed very quickly during a single infall event according to Eq. 2.8 with timescale $\tau_B = 0.1$ Gyr, shorter than for the thick and thin discs.
This choice of the input parameters outlines a bulge with an intense SF at the beginning of its history, which leads to a quick consumption of gas with the consequence of almost no SF at the present time. The SFR in the bulge during the first 3 Gyr is shown in Fig. 4.2. Here, one can see that the gas in the bulge is very quickly consumed and the SF becomes very low already within 0.5 Gyr, and it stays flat at ~ 0.2 M$_\odot$ pc^{-2} Gyr^{-1} up to the present time, in agreement with the observations. In fact, the observed number of stars with ages lower than 5 Gyr should be not higher than $\sim 10\%$ of the total Bernard et al. (2018) and the youngest ones could have been accreted from the inner thin disc (see Matteucci et al. 2019). Therefore, the contribution of the bulge to the present time observed masses of ^{26}Al and ^{60}Fe, which have decay timescales of the order of few million years, is negligible. On the contrary, the disc is still forming stars at the present time and therefore it contributes to the observed masses of these two radionuclides. In my model, the SFR is, in fact, now active in the thin disc and in agreement with the present time observed values (see later).

The chemical evolution equation adopted to compute the ^{26}Al and ^{60}Fe masses is the one presented in Eq. 2.19. In the term accounting for the radioactive decay, the decay timescales τ are imposed to $\tau_{26Al} = 1.05$ Myr and $\tau_{60Fe} = 3.75$ Myr, as in the discs (see Sec. 1.2.1).

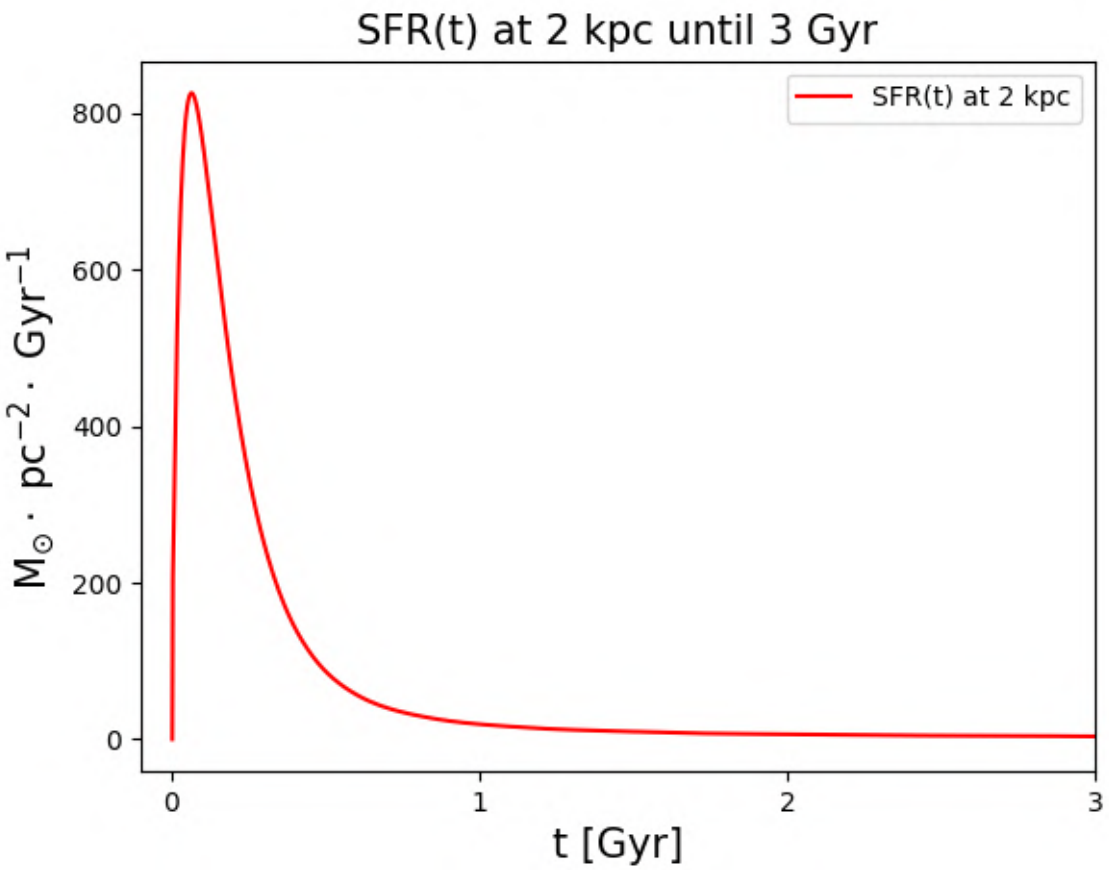

Figure 4.2: *SFR(t) at 2 kpc as a function of time in the first 3 Gyr since the beginning of SF. The prescriptions assumed (high SFE, short time scale and single infall episode) produce a SFR extremely high at the beginning of the Galaxy which decreases immediately due to the fast gas consumption.*

4.2.2 Nucleosynthesis and yields

Among the input parameters, the nucleosynthesis plays a major role in this study. To account for the production of ^{26}Al and ^{60}Fe I consider the contribution by massive stars (M≥ 13$M_\odot$), AGB stars (M≤ 6$M_\odot$), Super-AGB stars (6 $M_\odot$ <M< 13 $M_\odot$), SNIa and, only for ^{26}Al, nova systems (see Chap. 1).
For massive stars (M≥ 13$M_\odot$), which are the main producers of the two studied nuclides, I test four different yield sets: Woosley et al. (1995) with initial metallicity dependence (from now on WW95Zdep), Woosley et al. (1995) at the solar metallicity only (WW95$Z_\odot$), Limongi et al. (2006) (LC06), and Limongi et al. (2018) (LC18), which is also dependent on stellar rotation (three different initial rotational velocities, 0 km s^{-1}, 150 km s^{-1} and 300 km s^{-1} are provided). I implement the LC18 set in my model assuming that all stars with [Fe/H]≤ −1 dex are fast rotators (300 km s^{-1}) whereas those with [Fe/H]> −1 dex are non-rotating, as suggested

by Romano et al. (2019). For ^{60}Fe, LC06 offers two different models depending on the convection criterion adopted, namely Schwarzschild or Ledoux criterion. In this study I test both of them, for a total of five sets of massive star yields for ^{60}Fe and only four sets for ^{26}Al.
For AGB stars (M$\leq$ 6 M$_\odot$) I adopt the yields by Karakas (2010) and for Super-AGB stars (6M$_\odot$ <M< 13M$_\odot$) those by Doherty et al. (2014a) and Doherty et al. (2014b). I underline that for stars within the mass interval 10-13 M$_\odot$ I assume constant yields because Doherty et al. (2014a) and Doherty et al. (2014b) do not provide values for this mass range.
To account for the contribution by SNIa I assume the yields by Nomoto et al. (1984). Finally, I consider three different sets of yields for the nova system production of ^{26}Al: one by José et al. (1998) (Model B) and two by José et al. (2007) (Model A and Model C). In particular, in José et al. (1998) seven models for CO novae and seven models for ONe novae are listed. I select the best one following the suggestion by Romano et al. (2003). I assume that the 30% of the nova systems are ONe novae and the remaining 70% are CO novae, and the best model for each kind of novae is the average among the seven available:

$$\langle X_{^{26}Al} \rangle = 0.7 \langle X_{^{26}Al} \rangle_{CO} + 0.3 \langle X_{^{26}Al} \rangle_{ONe} \tag{4.1}$$

In addition, I also compute a fourth model without nova production. Being the nova nucleosynthesis independent of that by massive stars, for ^{26}Al I test the four massive star yields all combined with the four nova sets of yields, for a total of sixteen yield sets tested. The values of the mass of ^{26}Al produced in a nova outburst are listed in Tab. 4.1. These values are then multiplied by the expected number of outbursts during the lifetime of a nova system, that, as anticipated in Sec. 2.2, I assume to be 10^4 (Ford, 1978).
For ^{60}Fe, as anticipated in Chap. 1, novae do not contribute to this isotope, so I test only the five massive star sets of yields.
The yield sets are shown in Tab. 4.1. In the first column, the models are listed, in the second column is reported the reference and the third column contains details of different models belonging to the same reference.

For ^{26}Al, the combination of massive star yields with nova system yields is labelled as described in Tab. 4.2. The first column refers to the final label, the second to the massive star yields, and in the third column the nova yields are listed. I remind that the models labelled as "Model 3" and "Model 4" are different only for ^{60}Fe due to the different convection criteria adopted, whereas for ^{26}Al they produce the same results. In Tab. 4.2, when combining the massive star production with the nova production of ^{26}Al, "Model 4" has been neglected because no differences exist with "Model 3".

Table 4.1: *Models for different massive star yields. The first column reports the model identification, the second column contains the reference and the third column is used for the details of the models, to distinguish those taken from the same reference. For nova yields (only for ^{26}Al), in the third column the adopted values are listed. These values are the production during one outburst. I then assume 10^4 outbursts in total during the life of a nova system.*

Model	Reference	Characteristics
Massive stars		
Model 1	Woosley et al. (1995)	metallicity dependent (Zdep)
Model 2	Woosley et al. (1995)	solar metallicity ($Z_\odot$)
Model 3	Limongi et al. (2006)	Schwarzschild criterion
Model 4	Limongi et al. (2006)	Ledoux criterion
Model 5	Limongi et al. (2018)	
Nova systems (only for ^{26}Al)		
Model A	José et al. (2007)	low production (1.38E-4 $M_\odot$)
Model B	José et al. (1998)	intermediate production (3.82E-4 $M_\odot$)
Model C	José et al. (2007)	high production (7.69E-4 $M_\odot$)

4.3 Results

Here I show the results obtained with the models described above. For each model I compute the integrated mass and the integrated injection rates of ^{26}Al and ^{60}Fe as a function of Galactocentric radius, and, where possible, I compare these theoretical results with the observations.

4.3.1 ^{26}Al mass

For ^{26}Al the surveys COMPTEL and INTEGRAL observed a mass in the range $1.8 - 3.6\ M_\odot$ within 5 kpc from the Galactic centre, so I consider each model within this interval as an acceptable one. In Tab. 4.3 I list the masses of ^{26}Al computed within three significant Galactocentric radii: 5 kpc (the observations scale radius), 8 kpc (the solar neighbourhood) and 18 kpc (the outer border of the Galaxy). I compare the value at 5 kpc with the observations, in order to highlight the best models. From Tab. 4.3 I notice that the models without nova production, those with low nova production (Model A) and with moderate nova production (Model B) produce too low mass of ^{26}Al, independent of the massive star yields. On the contrary Model C (high nova contribution) always agrees with the observations.

Table 4.2: *Final models, combining massive stars and nova yields, for ^{26}Al. The first column reports the label given to the models with combined yields. The second and third columns contains the prescriptions adopted for massive star yields and nova yields, respectively. "Model 4" is missing because for ^{26}Al it is equivalent to "Model 3". These two models are different only for ^{60}Fe.*

Combined models (only for ^{26}Al)		
Final label	**Massive stars**	**Nova systems**
Model 1	Model 1	no production
Model 1A	Model 1	Model A
Model 1B	Model 1	Model B
Model 1C	Model 1	Model C
Model 2	Model 2	no production
Model 2A	Model 2	Model A
Model 2B	Model 2	Model B
Model 2C	Model 2	Model C
Model 3	Model 3	no production
Model 3A	Model 3	Model A
Model 3B	Model 3	Model B
Model 3C	Model 3	Model C
Model 5	Model 5	no production
Model 5A	Model 5	Model A
Model 5B	Model 5	Model B
Model 5C	Model 5	Model C

The four compatible models are Model 1C, Model 2C, Model 3C and Model 5C and are all shown in Fig. 4.3, together with the observed interval (thick yellow line) and three non-fitting models, Model 2, Model 2A and Model 2B, chosen as representative examples. In addition, the red dot at 2 $M_\odot$ represents the most plausible observation of ^{26}Al at 5 kpc according to Diehl et al. (2010) and Diehl (2016). By means of Fig. 4.3 I can select the best model: among the four compatible ones, Model 1C (dash-dotted red line) is the best, with 2.12 $M_\odot$ of ^{26}Al produced, which is the closest value to the observations. These results suggest that the nova contribution to ^{26}Al cannot be avoided in order to reproduce the observations.

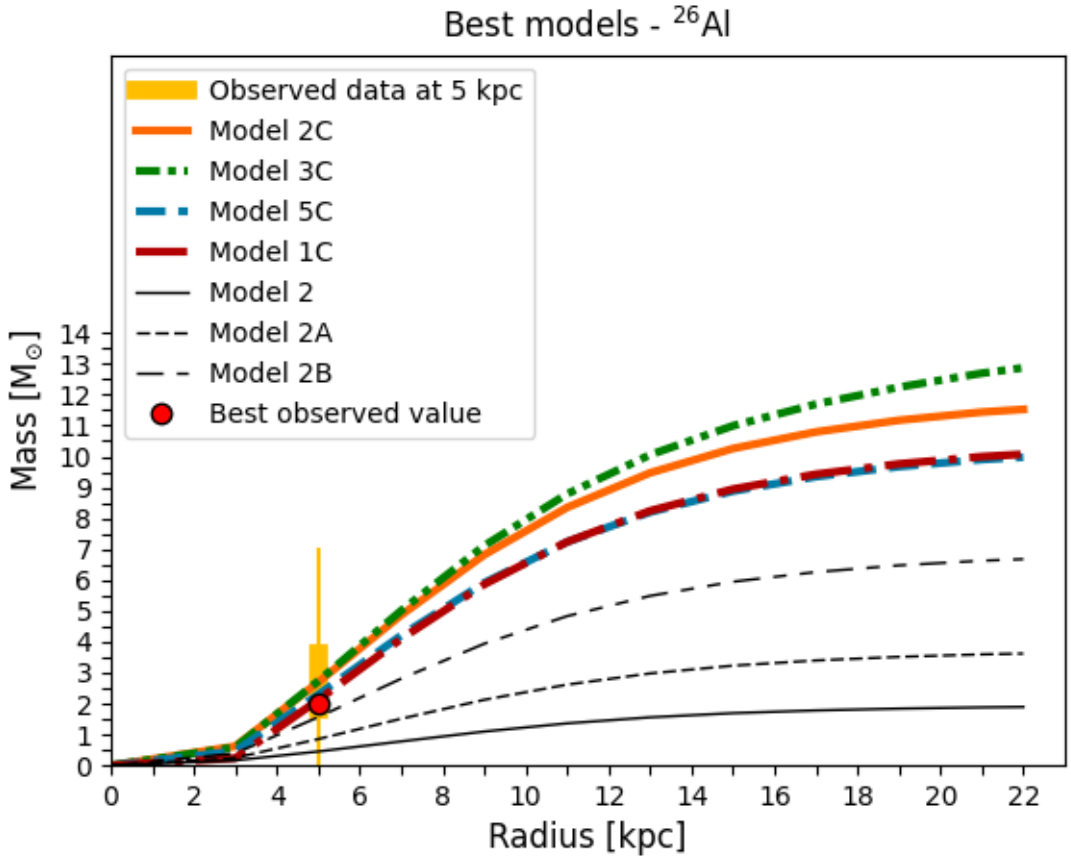

Figure 4.3: *Integrated mass of ^{26}Al as a function of Galactocentric distance for seven models among the computed ones. Model 1C (dash-dotted red line), Model 2C (solid orange line), Model 3C (dash-dot-dotted green line) and Model 5C (dashed blue line) are the only four compatible models I obtain. The three black lines are Model 2, Model 2A and Model 2B, plotted as examples of non compatible models (they were chosen as the highest model among those which do not fit the observations). I stress that Model 2 without novae is a factor 5 lower than the compatible model. The yellow band represents the observed values and the red dot is the best observation. Although 1C, 2C, 3C and 5C all offer a mass value within $1.8 - 3.6\ M_\odot$ at 5 kpc, Model 1C is the closest to the best observation, $\sim 2\ M_\odot$.*

4.3.2 ^{60}Fe mass

Also for ^{60}Fe I compute the integrated mass within 5 kpc, 8 kpc and 18 kpc, that are listed in Tab. 4.4. Nevertheless, I do not perform an observational comparison, due to the absence of a ^{60}Fe mass estimate. The computed values can work as predictions and constraints for future observations. In Fig. 4.4 I show the integrated masses of ^{60}Fe as functions of the Galactocentric distance for all five models, with the yellow stars representing the predicted mass of ^{60}Fe at 5 kpc for each model. Model 1 (dash-dot-dotted red line) and Model 5 (dotted black line) are much lower

Table 4.3: *Integrated mass of ^{26}Al within three different Galactocentric radii: 5 kpc, 8 kpc and 18 kpc. I compare the mass within 5 kpc with that observed by INTEGRAL, which lies in the range 1.8 – 3.6 $M_\odot$. Only four models are in agreement with the observed interval: Model 1C, Model 2C, Model 3C and Model 5C.*

	^{26}Al results			
Radius	**Model 1**	**Model 1A**	**Model 1B**	**Model 1C**
5 kpc	0.10 $M_\odot$	0.50 $M_\odot$	1.22 $M_\odot$	2.12 $M_\odot$
8 kpc	0.36 $M_\odot$	1.38 $M_\odot$	3.20 $M_\odot$	5.86 $M_\odot$
18 kpc	0.65 $M_\odot$	2.32 $M_\odot$	5.29 $M_\odot$	9.76 $M_\odot$
Radius	**Model 2**	**Model 2A**	**Model 2B**	**Model 2C**
5 kpc	0.45 $M_\odot$	0.85 $M_\odot$	1.56 $M_\odot$	2.69 $M_\odot$
8 kpc	1.10 $M_\odot$	2.12 $M_\odot$	3.94 $M_\odot$	6.82 $M_\odot$
18 kpc	1.84 $M_\odot$	3.51 $M_\odot$	6.48 $M_\odot$	11.17 $M_\odot$
Radius	**Model 3**	**Model 3A**	**Model 3B**	**Model 3C**
5 kpc	0.38 $M_\odot$	0.80 $M_\odot$	1.55 $M_\odot$	2.73 $M_\odot$
8 kpc	0.97 $M_\odot$	2.07 $M_\odot$	4.02 $M_\odot$	7.11 $M_\odot$
18 kpc	1.72 $M_\odot$	3.60 $M_\odot$	6.95 $M_\odot$	12.24 $M_\odot$
Radius	**Model 5**	**Model 5A**	**Model 5B**	**Model 5C**
5 kpc	0.05 $M_\odot$	0.46 $M_\odot$	1.17 $M_\odot$	2.29 $M_\odot$
8 kpc	0.19 $M_\odot$	1.22 $M_\odot$	3.03 $M_\odot$	5.91 $M_\odot$
18 kpc	0.34 $M_\odot$	2.01 $M_\odot$	4.98 $M_\odot$	9.67 $M_\odot$

than the other three, due probably to their metallicity dependence of the yields. Model 2, Model 3 and Model 4 differ for the input prescriptions but the results they offer are similar.

To identify the best model I consider the flux ratio ^{60}Fe/^{26}Al observed by INTEGRAL. INTEGRAL measured a ratio in the range 0.2 – 0.4 which corresponds to a mass ratio that lies in the range 0.46 – 0.92. Therefore, by assuming that the best ^{26}Al mass observation is 2 $M_\odot$, ^{60}Fe mass should lie in the range 0.9 – 1.8 $M_\odot$. I stress that Model 3 is extremely noteworthy from this point of view: it is the only compatible model among those tested, since it produces 1.05 $M_\odot$ of ^{60}Fe within 5 kpc form the Galactic centre. Given that, I can consider Model 3 (Limongi et al. 2006 with Schwarzschild production criterion) as the best model for ^{60}Fe.

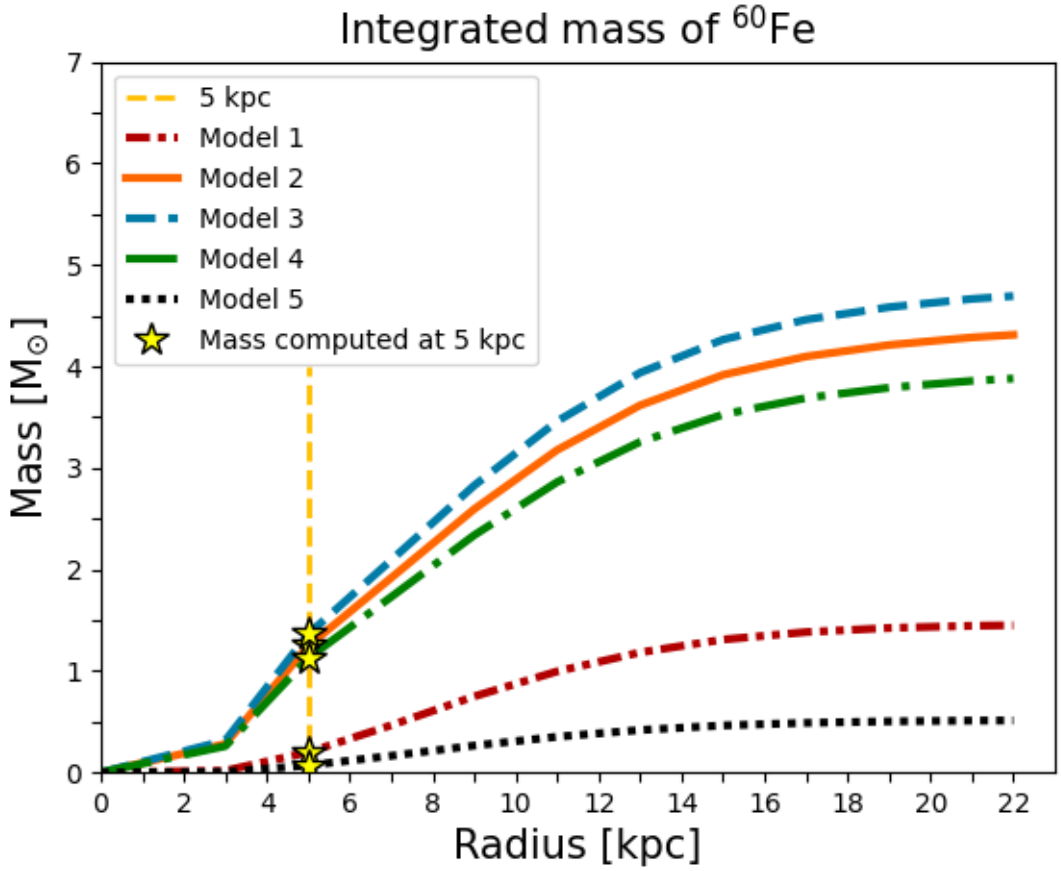

Figure 4.4: *Integrated mass of ^{60}Fe as a function of Galactocentric radius obtained with the five models tested. It is evident that Model* 1 *(dash-dot-dotted red line) and Model* 5 *(dotted black line), which are the two metallicity dependent ones, produce the lowest ^{60}Fe masses, whereas Model* 2*, Model* 3 *and Model* 4 *produce higher masses of ^{60}Fe. According to the conversion between flux ratio and abundance ratio, ^{60}Fe should lie in the range* $0.9 - 1.8\ M_\odot$*. My best model is Model* 3 *with* $1.05\ M_\odot$ *produced within* 5 *kpc from the Galactic centre.*

4.3.3 Injection rates

By means of Model 2, I also compute the present time integrated injection rates (measured in $M_\odot$ pc^{-1} Gyr^{-1}), for both ^{26}Al and ^{60}Fe: they represent the present rate at which these elements are injected into the ISM and are integrated assuming that they are constant in each Galactocentric ring. In Fig. 4.5, I show the comparison between the injection rates computed here and those of Timmes et al. (1995). The solid red line and the dashed blue line represent the integrated injection rates I obtain for ^{26}Al and ^{60}Fe, respectively. In Model 2, I assume the same yields and the same IMF (Salpeter 1955, normalized from 0.08 $M_\odot$ to 40 $M_\odot$) as in Timmes et al. 1995, in order to make a comparison with their results. In Fig. 4.5, also the results of Timmes et al. (1995) are reported: the dotted red line and dash-dotted

Table 4.4: *Integrated mass of ^{60}Fe within 5 kpc, 8 kpc and 18 kpc for the five massive star models tested. It is not possible to perform a comparison with the γ observations because no mass estimates are available for ^{60}Fe. The results listed here are a prediction of the ^{60}Fe mass at different Galactocentric distances, and can be used as constraints for future γ-ray surveys.*

	^{60}Fe results				
Radius	**Model 1**	**Model 2**	**Model 3**	**Model 4**	**Model 5**
5 kpc	0.20 $M_\odot$	0.87 $M_\odot$	1.05 $M_\odot$	0.82 $M_\odot$	0.07 $M_\odot$
8 kpc	0.71 $M_\odot$	2.17 $M_\odot$	2.59 $M_\odot$	2.09 $M_\odot$	0.26 $M_\odot$
18 kpc	1.28 $M_\odot$	3.64 $M_\odot$	4.52 $M_\odot$	3.69 $M_\odot$	0.45 $M_\odot$

blue line are the integrated injection rates for ^{26}Al and ^{60}Fe, respectively.
The plot shows clearly that in both cases the injection rate of ^{26}Al is higher than that of ^{60}Fe, but the trends are different in the two papers. The differences between my results and the previous ones, can be ascribed to different assumptions in the models adopted for the chemical evolution of the MW. In particular, in Timmes et al. (1995), they consider only one infall episode with a time scale constant with Galactocentric distance, and they assume that the Galactic bulge evolves as the innermost thin-disc. These two hypothesis are different from those used in this present study, where I assume an inside-out formation of the thin disc and a separate model for the bulge. These differences are probably responsible for the disagreement among the plots. In particular, my results show a maximum located at around 5 – 7 kpc which corresponds roughly to the maximum in the present time SFR, exactly as it is expected. In the bulge, where the current SFR is around $\sim 0.2\ M_\odot\ pc^{-2}\ Gyr^{-1}$, the injection rates are negligible. In the same way, at larger radii the injection rates decrease due to the assumed exponential Galactic disc and inside-out formation which lower the SFR, as shown in Fig. 4.6, where I report the predicted present time SFR gradient along the thin disc.

4.4 Discussion on the model parameters

It is worth noting that in this paper I vary only the stellar yields for the two radionuclides, ^{26}Al and ^{60}Fe. The reason is that I adopt a state-of-the-art chemical evolution model containing SFR, IMF and infall laws already tested in previous papers. In particular, the model for the bulge assumes a very intense SFR leading to a quick gas consumption, a hypothesis that is required to reproduce the stellar metallicity distribution as well as the [X/Fe] vs [Fe/H] diagrams for a large number

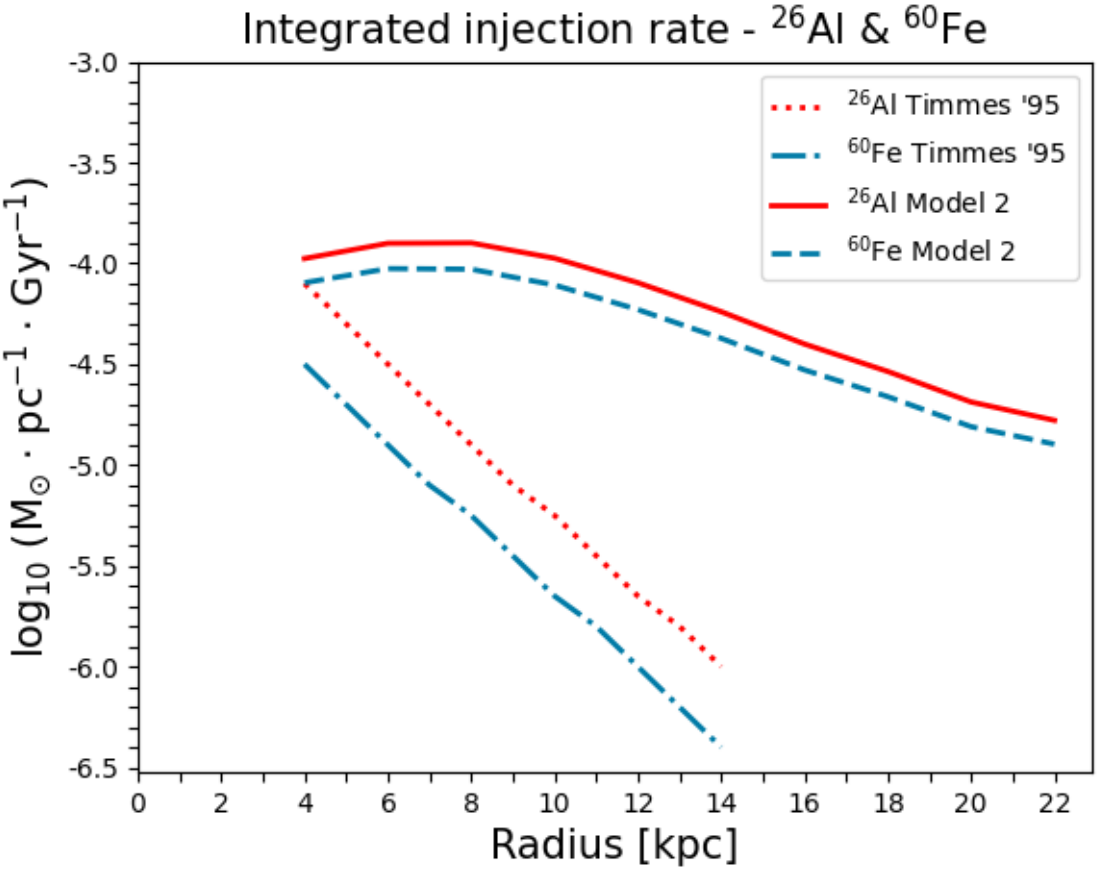

Figure 4.5: *Present time integrated injection rates computed with Model 2 for ^{26}Al (solid red line) and ^{60}Fe (dashed blue line), compared with those by Timmes et al. (1995) for ^{26}Al (dotted red line) and for ^{60}Fe (dash-dotted blue line) only for the disc ($R \geq 4$ kpc).*
***Timmes et al. (1995)**: the results are computed assuming that the time scale of the second infall τ_D is constant (no "inside-out"scenario assumed) and that the IMF is that by Salpeter (1955).*
***This study**: in this case I assumed the "inside-out"scenario for the disc and a Salpeter (1955) IMF. The results I get show that the highest contribution comes from the $6-8$ kpc region. The differences between the two studies do not lay in the IMF but in other model prescriptions such as the inside-out scenario.*

of chemical elements, such as α-elements (Cescutti et al., 2011; Matteucci et al., 2019), as well as s- and r-process elements (Grisoni et al., 2020). The model for thick and thin discs with the two-infall framework has also been tested in several previous papers (e.g. Grisoni et al. 2017; Spitoni et al. 2019b; Palla et al. 2020). This model reproduces the [X/Fe] vs. [Fe/H] diagrams for the same elements as those quoted before plus the SS abundances, namely the abundances of the ISM at the time of formation of the Sun (Asplund et al. 2009; Lodders 2010), as well as several present time observational constraints. In Tab. 4.5, I show a comparison between some observational constraints and the predictions of my model for the solar

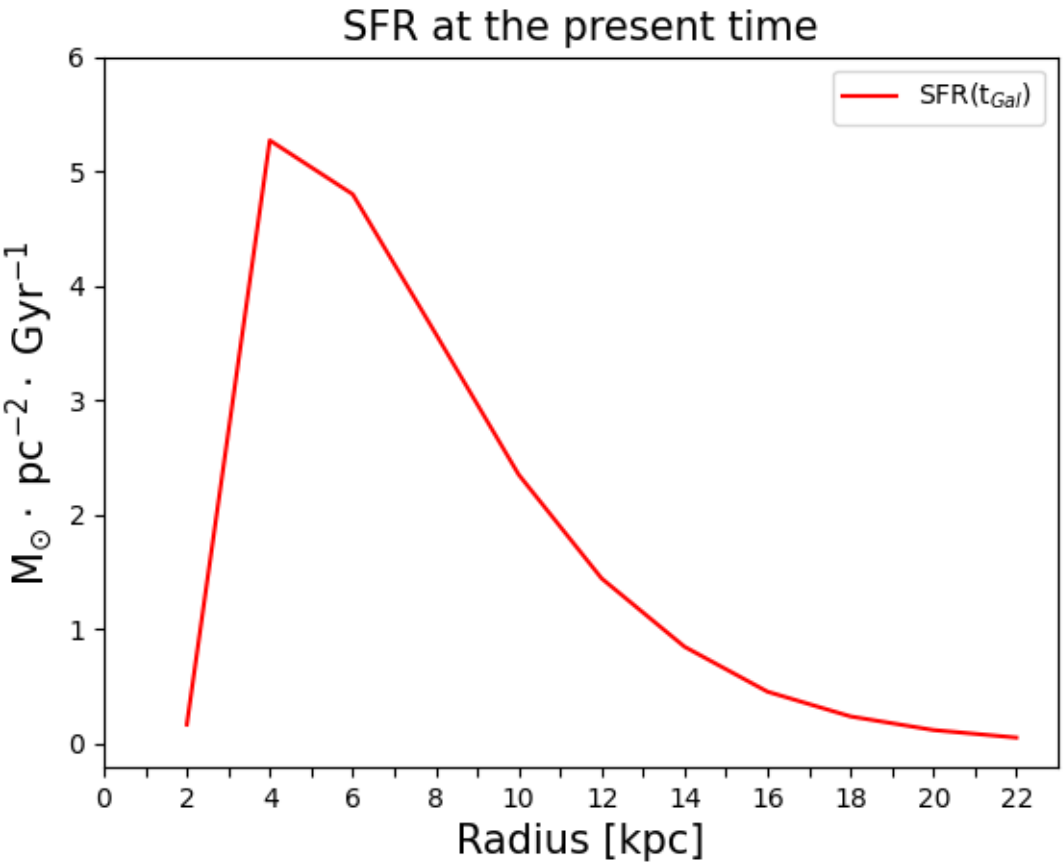

Figure 4.6: *SFR at the present time as a function of Galactocentric distance I assume in the model. The maximum is located at* 4 *kpc from the Galactic centre, whereas in the bulge and in the outer Galaxy it decreases.*

vicinity (SFR, surface gas density, surface stellar density, total surface mass density) and for the whole disc (gas infall rate, SN rates, nova rate). The first column lists the physical quantity considered, the second shows the value predicted by my model, the third contains the observed value and in the fourth column I list the references for the observed values. It is possible to see that the values I obtain for the physical quantities in Tab. 4.5 are all in reasonable agreement with the observations, and this reinforces the initial choice of the parameters.

4.5 Discussion on the yields

The differences between the yields of Woosley et al. (1995) and Limongi et al. (2006) that I adopt in this paper do not rely on the nucleosynthesis assumptions but rather on the dependence on metallicity. As shown in Fig. 4.3, the highest production of ^{26}Al is obtained when the $Z_\odot$-only sets are adopted (Model 2C and Model 3C),

Table 4.5: *Values of the most important observational constraint predicted by my model. Some quantities refer to the solar vicinity (surface density of gas, alive stars, total surface mass density and SF rate) and others are averaged over the whole disc (SNIa rate, SNII rate, nova rate and gas infall rate). The first column specifies the physical quantity considered, the second contains the prediction given by my model, the third contains the observed present day value and the last one lists the reference of the observation.*

Observable	Predicted value	Observed value	References
Surface density	8.5 $M_\odot$ pc^{-2}	13 ± 3 $M_\odot$ pc^{-2}	Kulkarni et al. (1987)
of gas		7 $M_\odot$ pc^{-2}	Dickey (1993)
Stars (alive)	~ 36 $M_\odot$ pc^{-2}	35 ± 5 $M_\odot$ pc^{-2}	Gilmore et al. (1995)
		33.4 ± 3 M$_\odot$ pc^{-2}	McKee et al. (2015)
total (discs)	~54 $M_\odot$ pc^{-2}	48± 9 $M_\odot$ pc^{-2}	Kuijken et al. (1991)
		52± 13 $M_\odot$ pc^{-2}	C. Flynn et al. (1994)
		50-60 $M_\odot$ pc^{-2}	Creze et al. (1998)
SF rate	~ 3 $M_\odot$ pc^{-2} Gyr^{-1}	2-10 $M_\odot$ pc^{-2} Gyr^{-1}	Guesten et al. (1982)
		~ 5 M$_\odot$ pc^{-2} Gyr^{-1}	Prantzos et al. (2018)
SNIa rate	0.43 century^{-1}	0.3±0.2 century^{-1}	Cappellaro et al. (1997)
SNII rate	1.93 century^{-1}	1.2±0.8 century^{-1}	Cappellaro et al. (1997)
Novae rate	~ 43 yr^{-1}	27-81 yr^{-1}	Shafter (2017)
		22-49 yr^{-1}	Darnley et al. (2006)
		35±11 yr^{-1}	Shafter (2017)
		20-40 yr^{-1}	Della Valle et al. (2020)
Infall rate	~ 1.5 $M_\odot$ pc^{-2} Gyr^{-1}	0.3-1.5 $M_\odot$ pc^{-2} Gyr^{-1}	Portinari et al. (1998)

whereas a lower production comes from the metallicity dependent one (Model 1C). Moreover, the yields by Limongi et al. (2018) with rotation included (Model 5C) offer a lower production of ^{26}Al, due both to the dependence on metallicity and the effects of rotation.

Other sets of yields for ^{26}Al and ^{60}Fe, both for massive stars and for novae, have been provided in the last years. Here, I do not test them but some qualitative considerations to understand their main differences relative to those adopted here can be done. For massive stars, Woosley et al. (2007) predicts a mass ratio ^{60}Fe/^{26}Al almost equal to that by Woosley et al. (1995), therefore I expect similar results. On the other hand, Sukhbold et al. (2016) predicts the mass ratio ^{60}Fe/^{26}Al to be lower than that of Woosley et al. (1995) by a factor of 2. As a consequence, I expect that this set of yields would produce proportionately around half of the ^{60}Fe I

produce with Woosley et al. (1995). Regarding the yields by novae, Starrfield et al. (2016) predict a higher ejecta of ^{26}Al with respect to José et al. (1998) (my Model B). Obviously, from this set I expect to have a higher contribution than Model A and Model B, thus reinforcing my conclusion about the importance of ^{26}Al production by novae.

4.6 Conclusions

In this study I present the chemical evolution of two unstable nuclei, ^{26}Al and ^{60}Fe, throughout the MW, including the radioactive decay in the chemical evolution equations of models already tested for the thick and thin discs and bulge. To account for the production of ^{26}Al and ^{60}Fe I consider yields from massive stars, AGB stars, Super-AGB stars, SNIa, and for the first time, only for ^{26}Al, also the contribution from novae.
For ^{26}Al, I test sixteen sets of yields, combining four different massive star yields with four different nova yields. For massive stars I use two yield sets by Woosley et al. (1995) (metallicity dependent and at $Z_{\odot}$), one by Limongi et al. (2006) and one by Limongi et al. (2018). To account for nova production, I test two models by José et al. (2007) and one by José et al. (1998). For each model I compute the mass of ^{26}Al within three different Galactic radii: 5 kpc (the scale radius of the observations), 8 kpc (the solar neighbourhood) and 18 kpc (the outer border of the Galaxy). Then, I compare these values with the γ-ray observations performed by COMPTEL and INTEGRAL suggesting that the observed mass of ^{26}Al within 5 kpc lies in the range 1.8 – 3.6 $M_{\odot}$. My results can be summarized as follows:

- among the models I test here, only four are compatible with the observed ^{26}Al mass interval: Model 1C (2.12 $M_{\odot}$), Model 2C (2.69 $M_{\odot}$), Model 3C (2.73 $M_{\odot}$) and Model 5C (2.29 $M_{\odot}$). In addition, the observations indicate that the best ^{26}Al mass value should be $\sim$ 2 $M_{\odot}$. I select as best models, Model 1C and Model 5C: the first assumes metallicity dependent yields for massive stars by Woosley et al. (1995) and high production by nova systems, the second adopts yields from rotating massive stars from Limongi et al. (2018) and high production from nova systems;

- regarding the production of ^{26}Al by novae, I stress that none of the models without nova production, low nova production (models A) or moderate nova production (models B) is compatible with the observations. This means that in order to reproduce ^{26}Al observations, the nova contribution is necessary;

- the effects of AGB and Super-AGB stars together with SNIa on the production of ^{26}Al at the present time are negligible;

- for ^{60}Fe five massive star sets of yields are tested: two by Woosley et al. (1995) (metallicity dependent and $Z_{\odot}$-only), two by Limongi et al. (2006) (which differ for the convection criterion adopted) and one by Limongi et al. (2018). In this case, no comparison with data can be performed due to the absence of ^{60}Fe mass observations. The only available observational constraint is the flux ratio ^{60}Fe/^{26}Al, which ranges in the interval $0.2 - 0.4$. According to this, ^{60}Fe mass should be within $0.9 - 1.8$ $M_{\odot}$. Model 3 is the only compatible model: I consider it as best model for ^{60}Fe with 1.05 $M_{\odot}$ produced (yields by Limongi et al. 2006 with Schwarzschild convection criterion);

- finally, I also compute the present time injection rates for both ^{26}Al and ^{60}Fe, assuming the yields used in Model 2, which contain similar prescriptions to those of Timmes et al. (1995). This is done to compare my rates with those of that previous work. In particular, I adopt the same set of yields for massive stars (e.g. Woosley et al. 1995 at $Z_{\odot}$ only) and same IMF (Salpeter, 1955) but a different Galactic model. This comparison shows that the maximum of my injection rate is located around $5 - 7$ kpc whereas that by Timmes et al. (1995) is located at 4 kpc. The differences among the results are probably caused by the different model prescriptions, such as the inside-out scenario in the thin disc versus a constant timescale for infall.

5

^{26}Al in the Milky Way: the role of novae in a 2D chemical evolution model

In this Chapter I am going to present a revision of the results already presented in Chap. 4, obtained by using a 2D chemical evolution model. The introduction of a second geometrical dimension, namely the azimuth, allows the reproduction of the behaviour of the ^{26}Al in more detail. In particular, such a model can account for the non-homogeneous mixing of the ^{26}Al with the ISM due to its short life-time.

I start by adopting the same prescriptions as those already presented in Chap. 4 and the yields I assume for the ^{26}Al are those identified as best yields in Chap. 4 as well. By introducing the dependence on the azimuth I can follow the evolution of the ^{26}Al and trace its variations along a ring at a fixed Galactocentric distance, to analyse how much its distribution resembles the SFR pattern.

This Chapter is organized as follows. In Sect. 5.2 I present the chemical evolution model adopted starting from the original 1D version for thick and thin discs and the bulge, and then I move to the nucleosynthesis considered with the description of the two models tested. In Sect. 5.3 I show how to extend the 1D model by adding the azimuthal dependency to the SFR, then I present my results about novae and ^{26}Al in Sect. 5.4 and, finally, I summarize my main conclusions in Sect. 5.5.

The results presented here are currently under peer-review in the paper Vasini et al. (2024b).

5.1 Introduction

Generally, massive stars have been considered as the main source of ^{26}Al, as was supposed after the first observations presented in Chap. 3, therefore this isotope is restored into the ISM shortly after the birth of its stellar progenitor. Moreover, its short decay timescale prevents ^{26}Al from moving too far away from the location of the progenitor. As a consequence, since massive stars are located in the active SF regions of the Galaxy, this isotope will also be detected in the proximity of these areas. Hence, ^{26}Al is considered a good tracer of SF regions (Limongi et al., 2006).

Chemical evolution studies relative to SLRs already tried to reproduce the observations provided in the last decades by the γ-ray astronomy community (see Chap. 4 and Wehmeyer et al. 2023) but many of these results were obtained by means of 1D chemical evolution models which assume that every observable (such as the SFR, the infall rate, the gas and stellar masses and the abundance gradients) depends only on the radial coordinate. Hence, the MW is modelled by assuming a concentric ring structure, where the gas in each ring instantaneously and homogeneously mixes (instantaneous mixing approximation).

The picture becomes more complex when dealing with SLRs since an additional timescale is introduced, namely the timescale of their radioactive decay, and in this particular case that of ^{26}Al ($\sim$ 1 Myr, see Chap. 1). ^{26}Al, after being re-injected into the ISM, starts spreading in the surrounding regions as stable isotopes also do but, simultaneously, it also decays into ^{26}Mg. As a consequence, the ^{26}Al atoms will not mix homogeneously, because the mixing timescale is very likely longer than the ^{26}Al decay timescale. Therefore, for ^{26}Al, such as for other SLRs, the assumption of homogeneous mixing does not hold anymore. This fact would not be a problem if the SFR in the Galaxy was homogeneous but, as observations confirm, the SFR is concentrated in the spiral arms of the MW. Therefore a 1D chemical evolution model that assumes homogeneous mixing is not suitable for dealing with SLRs in the Galaxy. The solution is introducing a second dimension, namely the azimuth, in order to trace inhomogeneities in each ring.

Moreover, the scenario is further complicated by the part played by the nova systems, that represent a second but non negligible source of ^{26}Al (Nofar et al., 1991; José et al., 2007) as also confirmed in Chap. 4. The chemical enrichment from novae is characterized by a long time delay due to the combination of the time necessary to form a WD and the additional cooling time requested to trigger the nova explosion (D'Antona et al., 1991). The direct consequence of this is that novae, unlike massive stars, do not trace the SFR. Given that a fraction of the ^{26}Al in the Galaxy has a nova origin, the ^{26}Al-SFR correlation is necessarily reduced,

even though it is not yet clear how much. To determine the damping due to the nova contribution, a 2D chemical evolution model is needed.

Spitoni et al. (2019a) and Spitoni et al. (2023) proposed a 2D chemical evolution model where azimuth and radial coordinates were considered. Azimutal perturbations of the SFR are introduced in order to take into account the effects of spiral arms on chemical evolution of the MW. In these papers, every ring is divided into smaller cells, and the homogeneity is not imposed over the whole ring but rather over the single cells. This updated scenario allows the authors to show clearly that for stable isotopes the 1D models represent a valid alternative almost everywhere in the Galaxy, except when dealing with the co-rotational radii regions (where the rotational velocity of the spiral arms relative to the disc is null) where oscillations in chemical abundances over cells in the same ring arise and only the 2D model can trace them.

From the observational side, the theoretical results that a 2D chemical evolution model will produce can still be compared to the integrated ^{26}Al mass value provided by COMPTEL and INTEGRAL, namely around 2 $M_{\odot}$ within 5 kpc from the Galactic centre. However, in addition to that, a 2D chemical evolution model opens to many more possibilities as, for example, the 2D distribution maps of the ^{26}Al mass and the nova outbursts, even though to make them suitable for an observational comparison some post-processing is needed (see discussion in Chap. 8).

With this work I want to provide a 2D chemical evolution model to follow the evolution in space (as a function of radial distance and azimuth) and time of ^{26}Al in the MW by adding an azimuth-dependent perturbation to the SFR that resembles the spiral arm pattern observed. My aim is to showcase the impact of the nova population on the present day distribution of this isotope. Moreover, with my model I can hopefully have deeper insights on the differences between the novae in the bulge and in the disc, by modelling these two regions separately.

5.2 The reference 1D chemical evolution model

In this Section, I present the reference 1D chemical evolution model that I use as starting point for this work. The 2D extension will be described later in Sec. 5.3.

I use as reference model the one adopted in Chap. 4 where the Galaxy is composed of two separated regions, the bulge (up to 2 kpc from the Galactic centre) and the disc (from 2 kpc to 15 kpc from the MW centre), itself composed of two chemically distinct substructures, the thick disc and the thin disc.

The thin disc is divided in 1 kpc wide concentric rings, that are isolated from

each other since I neglect every radial gas flow. The bulge as well is modelled by assuming a central region until 1 kpc from the centre and a surrounding ring, from 1 kpc to 2 kpc. Moreover, in the 1D model each ring is chemically homogeneous.

5.2.1 Galactic thick and thin discs

The thick and thin discs are assumed to be formed by a two infall episodes according to Eq. 2.9, assuming once more the "inside-out" scenario (see Eq. 2.10). All the parameters, such as the formation timescale of the thick disc (τ_T), the delay of the second infall ($t_{\max}$) and the total surface mass densities, ($a(R)$ and $b(R)$), are set to the values adopted in Chap. 4.

The SFR is expressed as the Kennicutt (1998) law (see Eq. 2.2) with SFE set to 1.0 Gyr^{-1} everywhere.

I assume a Kroupa et al. (1993) IMF with three slopes, defined in a mass interval up to 100 M$_\odot$, as presented in Eq. 2.6.

Regarding the stellar contribution to the ISM chemical composition, the model accounts for CCSN, SNIa (see Eq. 2.14) and novae (see Eq. 2.15), as already introduced in Chap. 2.

5.2.2 The bulge

Assuming that the Galactic bulge resides in the innermost region, within 2 kpc from the Galactic centre, I model it separately, following the prescriptions from Matteucci et al. (2019) (already adopted in Chap. 4). I divide it into a disc, from the centre up to 1 kpc, and an external ring, from 1 kpc to 2 kpc, so that the concentric rings throughout the entire Galaxy are all equally thick.

The gas forming the bulge is all accreted from a single infall (see Eq. 2.8) and the parameters are all taken from Chap. 4. Concerning the SFR, I adopt the same Kennicutt law as in Eq. 2.2 with SFEs equal to 25.0 Gyr^{-1} and 35.0 Gyr^{-1} for the ring and the inner region, respectively. These high SFEs, together with the short timescale of the SFR, reproduces the rapid increase in the metallicity and the average old stellar population observed in the bulge nowadays (Barbuy et al., 2018).

The assumed IMF is the one of Salpeter (1955) (see Eq. 2.4) as in the previous Chapter. The rates of the different stellar types, SNIa, SNII, SNIb, SNIc and novae are computed as done in the disc.

Model	Massive stars	Novae	AGBs	SNIa
Model 1	✓	✓	✓	✓
Model 2	✓	X	✓	✓

Table 5.1: *Descriptions of the nucleosynthesis of the two models tested. The check-marks mark the ^{26}Al sources included in the models. For the reference to the yields adopted for each astrophysical source see Sec. 5.2.3.*

5.2.3 Nucleosynthesis prescriptions

For the nucleosynthesis prescriptions I rely on the yields selected in Chap. 4. For massive stars I assume yields from Kobayashi et al. (2006), to which I add those for ^{26}Al from Woosley et al. (1995) adopting the whole metallicity grid provided. To be consistent with the prescriptions adopted in Chap. 4 where the chemical evolution model for ^{26}Al has originally been tested, I adopt the José et al. (2007) yields. For SNIa I assume yields from Iwamoto et al. (1999) and for ^{26}Al I adopt the prescriptions from Nomoto et al. (1984). Moreover, for AGBs ($M \leq 6\ M_{\odot}$) I adopt the yields from Karakas (2010).

In this work I test two different models that differ only for the nucleosynthesis prescriptions summarized in Table 5.1: Model 1 , where I consider the production of ^{26}Al from all the sources listed (massive stars and novae with minor contribution coming from SNIa and AGBs), and Model 2, where I exclude the contribution from novae, keeping massive star, AGBs and SNIa.

5.3 The 2D chemical evolution model

To extend the model from 1D to 2D, I include the azimuthal dimension by adopting the same mechanism proposed by Spitoni et al. (2019a) and Spitoni et al. (2023), where SFR perturbations are implemented in order to reproduce the spiral arm pattern observed in the MW. In this Section I show how the spiral patterns are modelled and then how are introduced in the SFR.

5.3.1 Multiple spiral patterns of Spitoni et al. (2023)

Spitoni et al. (2023) present the chemical evolution of several elements in the Galactic disc, considering the effects of multiple spiral patterns on the evolution of elements synthesized over different time scales, such as oxygen, iron, europium,

and barium. The presence of multiple spiral patterns was already predicted by N-body simulations (Quillen et al., 2011; Minchev et al., 2012; Sellwood et al., 2014) and shown by observations (Meidt et al., 2009).

The expression for the time evolution of the density perturbation, created by multiple pattern spiral arms is:

$$\Sigma_{MS}(R,\phi,t) = \chi(R,t)\sum_{j=1}^{N} M_j(\gamma_j)\cdot \mathbb{1}\left[R_{j,\min},\ R_{j,\max}\right], \tag{5.1}$$

where the quantity $\chi(R,t)$ if computed at the present time t_G, represents the present-day amplitude of the spiral density and can be expressed as:

$$\chi(R,t_G) = \Sigma_{S,0} e^{-\frac{R-R_0}{R_S}}. \tag{5.2}$$

In the previous expression, R_S is the radial scale-length of the drop-off in density amplitude of the arms, Σ_0 is the surface arm density at fiducial radius R_0 fixed to values of $\Sigma_{S,0} = 20\ \mathrm{M_\odot\ pc^{-2}}$, $R_0 = 8$ kpc, and $R_S = 7$ kpc as in Spitoni et al. (2023) and Cox et al. (2002). In eq. 5.1, N is the total number of spiral clumps and the $M_j\,(\gamma_j)$ term is the modulation function for concentrated spiral arms of Cox et al. (2002) defined for the j^{th} spiral mode clump associated with the angular velocity $\Omega_{s,j}$ and can be expressed as follows:

$$M_j\,(\gamma_j) = \left(\frac{8}{3\pi}\cos(\gamma_j) + \frac{1}{2}\cos(2\gamma_j) + \frac{8}{15\pi}\cos(3\gamma_j)\right), \tag{5.3}$$

where γ_j stands for

$$\gamma_j(R,\phi,t) = m_j\left[\phi + \Omega_{s,j}\cdot t - \phi_p(R_0) - \frac{\ln(R/R_0)}{\tan(\alpha)}\right]. \tag{5.4}$$

In Eq. 5.4, m_j refers to the multiplicity (e.g. the number of spiral arms) associated to the j^{th} clump, α is the pitch angle [1], $\Omega_{s,j}$ is the angular velocity of the pattern, $\phi_p(R_0)$ is the coordinate ϕ computed at t=0 Gyr and R_0.

Finally, in Eq. 5.1, the value of the indicator function $\mathbb{1}$ delimits the radial extension of the considered spiral arm mode enclosed between the Galactocentric distances $R_{j,\min}$ and $R_{j,\max}$: it is one if the argument is within the radial interval and zero otherwise.

In Fig. 5.1, I show the pattern speeds $\Omega_{s,j}(R)$ of the spiral arms of Model A in Spitoni et al. (2023), which I adopt in this work. The spiral structure is composed of three segments with multiplicity $m = 2$, each moving at different pattern speeds $\Omega_{s,j}(R)$. The j^{th} spiral structure is confined to the region $R \in \left[R_{j,,\min},\ R_{j,,\max}\right]$. The

[1] In this model all the spiral arms have the same pitch angle α.

velocity of the central spiral structure is fixed at $\Omega_{s,2} = 20$ km s^{-1} kpc^{-1}, consistent with the Roca-Fàbrega et al. (2014) model. A similar value was first estimated from moving groups in the U-V plane by Quillen et al. (2005, $\Omega = 18.1 \pm 0.8$ km s^{-1} kpc^{-1}). The innermost and outermost segments rotate at velocities of $\Omega_{s,1} = 30$ km s^{-1} kpc^{-1} and $\Omega_{s,3} = 15$ km s^{-1} kpc^{-1}, respectively.

It is interesting to note that one of the co-rotational radii is located at 8.75 kpc, which is close to the solar Galactocentric distance $(R, Z)_\odot = (8.249, 0.0208)$ kpc (GRAVITY Collaboration et al., 2021; M. Bennett et al., 2019).

5.3.2 SFR and perturbations

I first present the assumptions adopted for the SFR and for the spiral arms in the disc ($R > 2$ kpc), since the other chemical evolution prescriptions depend on those.

My starting point is the 1D Schmidt-Kennicutt SFR (see Sect. 5.2). This relation is still mono-dimensional, meaning that I have not introduced a dependency on the azimuthal angle yet.

I define the adimensional perturbation δ_{MS} as:

$$\delta_{MS}(R, \phi, t) \equiv \frac{\Sigma_D(R, t) + \Sigma_{MS}(R, \phi, t)}{\Sigma_D(R, t)}, \tag{5.5}$$

where Σ_D is the total surface mass density. Imposing as in Spitoni et al. (2023) that the ratio $\chi(R, t)/\Sigma_D(R, t)$ is constant in time, the adimensional perturbation δ_{MS} defined above becomes:

$$\delta_{MS}(R, \phi, t) = 1 + \frac{\chi(R, t_G)}{\Sigma_D(R, t_G)} \sum_{j=1}^{N} M_j(\gamma_j) \cdot \mathbb{1}\left[R_{j,\min},\ R_{j,\max}\right], \tag{5.6}$$

Finally, the new SFR in presence of the effect of spiral arms is computed as:

$$\psi(R, t, \phi) \propto \nu(R) \Sigma^k_{gas}(R, t) \cdot \delta^k_{MS}(R, \phi, t). \tag{5.7}$$

I apply the perturbation after 3 Gyr of evolution and then I let the MW evolve up to 13.7 Gyr, the assumed age of the Universe. I make this choice in order to mimic what is done in Spitoni et al. (2019a). There, the authors simulate the 2D evolution of the thin disc only, assuming a one-infall episode lasting for 11 Gyr. In my case, where I model both the thin and the thick discs in the framework of a two-infall scenario for 13.7 Gyr, I delay the rising of the perturbation by 3 Gyr so that also in my case the evolution of the perturbation lasts for roughly 11 Gyr.

I show my perturbed SFR in Fig. 5.2. I represent both the bulge (R≤ 2 kpc) and the disc at six different times using the same color coding so as to appreciate the SFR variations in time and space. In the top row, starting from the left panel, the

snapshots shown are those corresponding to the peak of the bulge SFR (T_1=0.066 Gyr), the peak of the disc SFR (T_2=2.25 Gyr), and the rising of the SFR perturbations (T_3=3.2 Gyr). Regarding the bottom panels, when dealing with SLRs as ^{26}Al the observations can recover only the recent history which is related to the recent SFR, therefore I show three recent times (T_4=13.5 Gyr, T_5=13.6 Gyr and T_6=13.7 Gyr) to hopefully trace their SFR when analyzing the ^{26}Al distribution. The white edge star shows the locations of the the solar neighbourhood.

In the T_1 panel I show that when the bulge SFR reaches a maximum, the disc SFR is still very low, roughly four order of magnitudes lower. Then, at T_2, the bulge SFR has already decreased since it is characterized by an extremely efficient and short burst whereas the disc SFR shows a spike, whose value is smaller and smaller as I go towards the outskirts. At T_3 the perturbations arise and are clearly visible in the disc since this is the moment when they are at their peak. After this moment the SFR perturbations will monotonically decrease. In the three bottom panels (T_4, T_5 and T_6) the perturbations are still evident, although quite weaker, and the different segments that compose the single arms are not aligned due to their different rotational velocities. The result is that the arms look broadened as it is particularly evident in the last panel.

5.4 Results

In this Section I show the results regarding the nova and ^{26}Al 2D distribution in the MW, from the bulge up to the outermost region of the Galaxy.

5.4.1 Nova systems

In this Section I show the results related to the nova outbursts in the MW.

In Fig. 5.3 I report the 2D map of the novae for four of the six times shown in Fig. 5.2. The four panels refer to times T_3, T_4, T_5 and T_6 as defined in Sec. 5.3.2. I do not show the snapshots at T_1 and T_2 since at such early epochs novae have not started to explode yet. The maps are colour coded according to the logarithm of the nova outburst rate, and the position of the Sun is marked by the white-edge star in the left side of each panel.

The difference between the early epoch (T_3) and the recent ones (T_4, T_5 and T_6) is evident. The reason, as anticipated, lies in the delay of the nova formation relative to the birth of its progenitor.

Because of this delay, novae do not trace the SFR, and no correspondence can be found between the 2D SFR map and the 2D nova map computed at the same epoch. Therefore, at T_3 the nova distribution is still uniform, even though the SFR

is already perturbed, and at late epochs novae do not show the spiral arm pattern which is shown by the SFR.

The same time delay affects the bulge novae but the result in this region is slightly different, since the SFR in the bulge is more efficient. Hence, the majority of the bulge novae is produced earlier, at T_1 when the bulge SFR peaks, and therefore they explode earlier. Hence, at T_3 the nova outburst rate in the bulge is already high.

5.4.2 ^{26}Al mass 2D distribution

In this Section, I show the results related to the 2D distribution of ^{26}Al in the MW within 15 kpc from the galactic centre.

In Fig. 5.4 I report the results from Model 1, where massive stars and nova systems both contribute to the synthesis of ^{26}Al. In this figure I show the snapshots at the same six times as in Fig. 5.2. The plots are colour coded according to the logarithm of the ^{26}Al mass in each cell. The location of the solar neighbourhood is suggested by the white-edge star in the left side of each snapshot.

A comparison between Fig. 5.4 and the SFR in Fig.5.2 is quite noteworthy. In Fig. 5.4 the first three panels (T_1, T_2 and T_3) reproduce perfectly the SFR pattern:

- at T_1=0.066 Gyr the only contribution to ^{26}Al in the MW comes from the bulge (R < 2 kpc) where the SFR is high, whereas ^{26}Al in the disc is still very low (as the SFR is);

- at T_2=2.25 Gyr the SFR in the bulge has already reached a maximum and decreased and the ^{26}Al shown in the plot has originated from the nova explosions. On the other hand, the SFR in the disc reached the peak, thus causing an increment in the amount of ^{26}Al produced. Nevertheless, the peak of the ^{26}Al production in the disc will occur slightly later, due to the delayed contribution from nova systems;

- At T_3=3.2 Gyr, the SFR perturbations have just kicked in and the spiral pattern is accurately reproduced by the ^{26}Al 2D distribution.

These first three panels perfectly mimic the SFR behaviour because after few billion years of evolution, the only significant contribution to the ^{26}Al comes from the massive stars. The nova contribution will arise at later times, therefore in the first stages of the evolution it is still negligible.

On the other hand, at T_4, T_5 and T_6 the scenario is different: in every snapshot the SFR pattern is reproduced with less accuracy and the spiral pattern is recognisable only in the outermost rings. Regarding the present time bulge, the massive stars are almost totally absent and the ^{26}Al predicted there comes exclusively from recent nova outbursts.

In Fig. 5.5, where the results from Model 2 are plotted, the scenario is rather different, since novae have been excluded from the ^{26}Al nucleosynthesis. The snapshots are taken at the same times, the colour coding is the same and the white-edge star still represents the indicative position of the solar neighbourhood.

The first three panels resemble Fig. 5.4. The only difference is the overall depletion of ^{26}Al mass over the entire Galaxy due to the removal of the nova systems. The bulge is much less enriched in ^{26}Al (see T_2 panel) with respect to Fig. 5.4, since the only contribution in this region was coming from nova systems, that are now excluded. On the other side, the three recent snapshots (T_4, T_5 and T_6) show a rather good tracing of the SFR since no smoothing from novae is involved. The bulge looks extremely poor in ^{26}Al since the massive stars are completely absent. The only recent production in the region R < 2 kpc is that coming from AGBs and SNIa.

5.4.3 ^{26}Al mass azimuthal oscillations

To quantify how much the novae contribute to the scenario I present Fig. 5.6:

- panel **a**: I show the SFR at the present time, in the solar ring as a function of the azimuth. The vertical dashed lines mark the peaks of the SFR and are reported in all the panels below. The oscillations are symmetric as was already shown in Fig. 5.2;

- panel **b**: I represent the ^{26}Al mass for Model 1 and Model 2 (pink and green lines respectively). The vertical dashed lines refer to the peaks of the SFR. The oscillations have the same amplitude in the two cases, but, as shown in Fig. 5.4 and 5.5, they are far smoother in Model 1 where the spiral pattern at the present time is almost lost. The relative enhancement of the peaks with respect to the minima: for Model 1 the peak is the 28% higher than the minima, whereas in the case of Model 2 the peak is the 150% higher than the minima. The peaks in Model 2 stand out against the background by a factor of ~5 more than in Model 1, hence the loss of the spiral pattern;

Model	0 - 1 kpc	1 - 2 kpc	2 - 3 kpc	3 - 4 kpc	4 - 5 kpc	Total (0 - 5 kpc)
Model 1	0.056 $M_\odot$	0.150 $M_\odot$	0.229 $M_\odot$	0.283 $M_\odot$	0.312 $M_\odot$	1.028 $M_\odot$
Model 2	0.006 $M_\odot$	0.014 $M_\odot$	0.057 $M_\odot$	0.083 $M_\odot$	0.105 $M_\odot$	0.265 $M_\odot$

Table 5.2: *^{26}Al integrated over the five innermost annuli (0 - 5 kpc) at the present time for both models. Columns 2-6 report the ^{26}Al for every single ring (each 1 kpc wide) and column 7 show the total ^{26}Al within 5 kpc.*

- panel **c**: I plot the difference between the ^{26}Al produced by Model 1 and Model 2. Here I show clearly that the mass of ^{26}Al produced by novae is dependent on the azimuth but not on the SFR. This value oscillates between 0.004 and 0.006 $M_\odot$ and is largest in the minima of the SFR, demonstrating why novae blunt the spiral pattern;

- panel **d**: here I show the nova distribution in the solar ring, that resembles that of the ^{26}Al in the previous panel.

5.4.4 ^{26}Al: predictions versus observations

Regarding the comparison with observational data in Tab. 5.2, I report the values of ^{26}Al within 5 kpc from the Galactic centre. Columns from 2-6 report the values in the 1 kpc wide annuli and their sum is listed in column 7. Up to now, the observations performed with COMPTEL and INTEGRAL agreed on the amount of ^{26}Al present in the MW. Adopting the COMPTEL data Prantzos et al. (1996) estimated an ^{26}Al mass in the range 1.5 - 2.0 $M_\odot$ within 5 kpc from the Galactic centre (see also Diehl et al. 1995). Later, Diehl (2016) estimated 2.0 ± 0.3 $M_\odot$ of ^{26}Al in the same region after the INTEGRAL data were released.

Within 5 kpc from the Galactic centre my Model 1 predicts 1.028 $M_\odot$ of ^{26}Al, whereas Model 2 predicts 0.265 $M_\odot$. In neither of the two cases I am able to recover the exact amount of the ^{26}Al observed, but a potential solution was proposed by Della Valle et al. (2020). The authors report that the nucleosynthesis of the novae in the bulge could be significantly different from that of the disc novae. Bulge novae typically evolve on timescales longer than the disc ones, since the progenitor WDs are on average less massive and therefore need to accrete more material to trigger the explosion. Observations of bulge novae support this hypothesis: the ejecta observed are up to ten times more massive than the disc nova ones, that evolve more rapidly. Hence, it follows that their nucleosynthesis products are enhanced

by the same factor as well. However, the observed rate of novae in the MW and in the LG is expected to increase with the imminent advent of LSST (Large Synoptic Survey Telescope), that will hopefully be able to clarify this issue.

By including this additional factor in the calculations, I can reproduce up to 2.882 $M_\odot$ of ^{26}Al with Model 1, therefore with a slightly smaller factor I can reproduce the ~2 $M_\odot$ observed.

Another possible scenario to reproduce the observations could be related to the present day SFR. The SFR adopted in my model is a typical Kennicutt (1998) law (see Eq. 2.2), which peaks at early times and constantly decreases up to the present day. A recent SF burst would give rise to a young stellar population with massive stars contributing to ^{26}Al. Even though there are evidences of recent bursts, around 2-3 Gyr ago (as shown for example by Isern 2019 and Mor et al. 2019), it occurred too long ago to produce an effect on the present day abundance of ^{26}Al, that decays on a timescale of 1 Myr. However, a present day burst was hypothesised by Ruiz-Lara et al. (2020) in the solar neighbourhood. Nevertheless, this impacts on the 2 kpc bubble around the Sun only, whereas my comparison is performed within the 5 innermost kpc of the Galaxy.

5.4.5 Galactic observational constraints

	Observations	Predictions
SFR [$M_\odot$ yr^{-1}]	0.65 - 3 (1)	2.24
Gas mass [10^9 $M_\odot$]	8.1 - 4.5 (2)	6.4
Stellar mass [10^{10} $M_\odot$]	3. - 4. (3)	3.7
Infall rate [$M_\odot$ yr^{-1}]	0.6 - 1.6 (4)	0.65
SNII [events century^{-1}]	0.4 - 2.0 (5)	0.88
SNIa [events century^{-1}]	0.1 - 0.5 (5)	0.2

Table 5.3: *MW disc (R>2 kpc) constraints: in column 2 the observed quantities, in column 3 the predictions from my models. Models 1 and 2 predict the same observables since they differ only on the nucleosynthesis side.* ***References:*** *(1) Prantzos et al. (2011), Chomiuk et al. (2011), (2) Kubryk et al. (2015a), (3) Chris Flynn et al. (2006), (4) Marasco et al. (2012), Lehner et al. (2011), (5) Cappellaro et al. (1997).*

With my choice of input parameters I am able to reproduce the main observational features of the MW disc (R>2 kpc). I highlight in particular that I can reproduce the current SFR, gas mass, stellar mass, infall rate and both SNIa and SNII rates.

I report in Tab. 5.3 the most important observational constraints in the Galactic disc: in column 2 I show the observed value with the reference, in column 3 the predicted value by my models. I compare my results with the observations from different authors. Regarding the SFR, I refer to the values proposed by Prantzos et al. (2011) and Chomiuk et al. (2011), for the gas mass I rely on Kubryk et al. (2015b), for the stellar mass I compare my results to Chris Flynn et al. (2006), for the infall rate I use the observations by Marasco et al. (2012) and Lehner et al. (2011) and for the SNII and SNIa rates I refer to Cappellaro et al. (1997). I highlight that the two models tested, Model 1 and Model 2, differ only for the nucleosynthesis, therefore the predictions of all the unrelated quantities (such as those listed here) are the same.

5.5 Conclusions

In this paper I model the temporal ad spatial evolution of ^{26}Al in the MW by adopting a 2D chemical evolution model to perform a comparison with the already existing data and a prediction for the upcoming ones.The introduction of a second dimension in the chemical evolution model allows me to investigate how much the approximation of homogeneous mixing affects the production of ^{26}Al, and which is the relative contribution of novae and massive stars to its mass in the MW. Moreover, I can also probe how good the tracing of the SFR is when considering nova systems as ^{26}Al producers. I assume the Galaxy to be divided into two main regions: the bulge ($R \leq 2$ kpc), that is described adopting a homogeneous 1D model, and the disc ($R > 2$ kpc) where I consider a 2D model, with the SFR being dependent not only on the Galactocentric distance and time but also on the azimuth. The dependency on the azimuth is introduced by applying a perturbation to the 1D SFR, resembling the rotating spiral arm pattern observed in the Galaxy. My main focus is ^{26}Al, a SLR with a ~1 Myr decay time-scale, generally assumed to be produced by massive stars. These two facts suggest that ^{26}Al can be a good tracer of active SF, therefore its current location in the MW is dependent on the shape of the recent SFR.

With this model I aim at reproducing the observed mass of ^{26}Al in the Galaxy to investigate the importance of nova contribution to the mass of this element, and studying the effects that novae can produce on ^{26}Al as tracer of SF. To do that, I compare two models considering different ^{26}Al sources: Model 1, where massive stars and nova systems are both responsible for the ^{26}Al production, and Model 2 where nova systems are excluded. Regarding the yields for both the production sites I adopt the prescriptions of Vasini et al. (2022). By means of my

chemical evolution model, I am able to produce 2D maps for the mass of ^{26}Al, the distribution of massive stars and nova systems in the MW. My main conclusions can be summarised as follows:

- the nova systems eject nucleosynthesis products with a large time delay due to the initial masses of the binary components and to the time necessary for a WD to cool. Due to this delay, novae are not tracers of the SFR. The maps that I produce show that that the peaks of the present time nova distribution at the solar neighbourhood are located in the minima of the present time SFR;

- the two hypotheses about the producers of ^{26}Al that I test, predict different distributions of the mass of this element. I highlight that when including the production by novae (Model 1), the spiral pattern at the present time is hardly visible, at variance with the case of production from massive stars only (Model 2). In particular, in the case of ^{26}Al from both production sites, the peaks of the ^{26}Al distribution are $\sim$ 28% higher that the minima, whereas in the case of ^{26}Al from massive stars only the peaks are $\sim$ 150% higher. Therefore, in the case without novae, the peaks of the distribution stand out from the background five times more than in the case with novae included, thus tracing better the spiral arm pattern;

- I compare the ^{26}Al predicted by the two models with the available observational data, which refer to the innermost 5 kpc of the Galaxy. I integrate the ^{26}Al within each ring from the centre up to 5 kpc and I obtain 1.028 $M_\odot$ if novae are included (Model 1) and 0.265 $M_\odot$ if novae are excluded (Model 2). Therefore, the relative contribution of novae to the total amount of ^{26}Al is $\sim$75% and the other $\sim$25% comes from massive stars. The observations report $\sim$ 2 $M_\odot$ of ^{26}Al, hence both my models underestimate the mass of ^{26}Al. The missing ^{26}Al mass can be recovered if I consider that bulge novae can eject up to 10 times more matter than disc novae. Considering a factor of ten, my Model 1 predicts 2.882 $M_\odot$ of ^{26}Al within 5 kpc from the Galactic centre, therefore by adopting a factor of $\sim$6 I can very well reproduce the observations.

In conclusion, since the tracing of the SFR by ^{26}Al is lowered by a factor of $\sim$5, if novae are considered, this element is a pure tracer of the SFR. Therefore, other SLRs not produced by novae, such as ^{60}Fe, are more reliable tracers of the SFR.

From the nucleosynthesis side, my 2D chemical evolution model confirms that the nova contribution to ^{26}Al is fundamental to reproduce the observations

especially in the bulge, where they should eject a larger amount of chemical elements as compared to those produced by the disc novae.

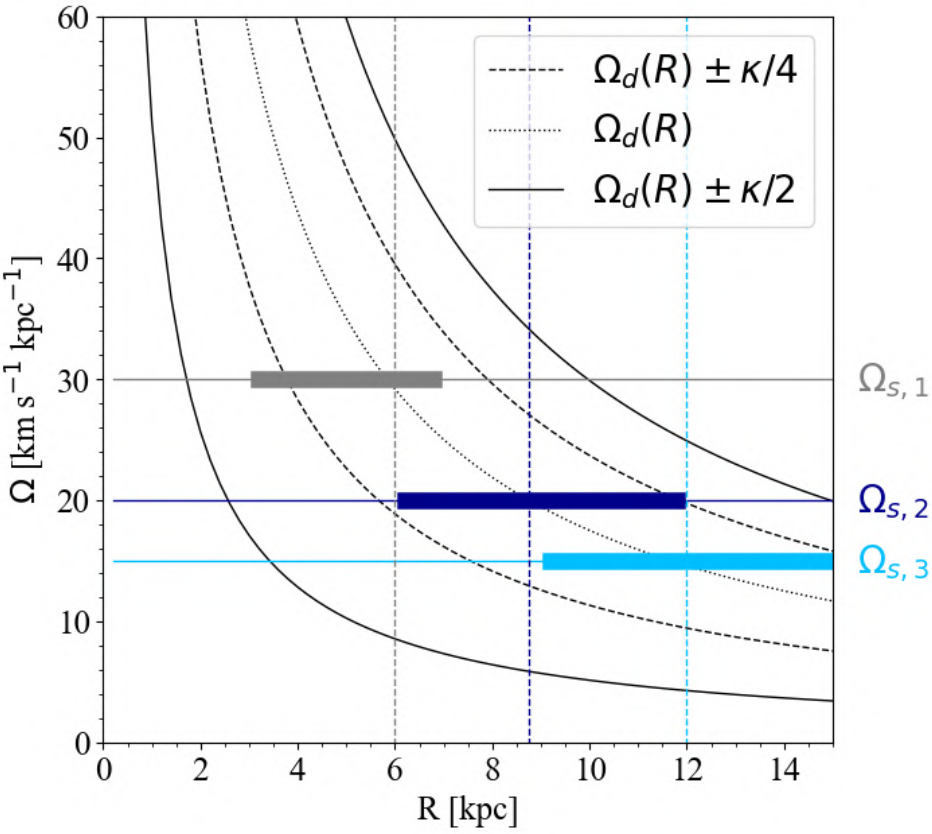

Figure 5.1: *Spiral pattern speeds $\Omega_{s,1}(R)$, $\Omega_{s,2}(R)$ and $\Omega_{s,3}(R)$ of the multiple spiral modes moving at different pattern speeds of Model A in Spitoni et al. (2023) are indicated by the three coloured horizontal lines. Inner and outer spiral structures (moving with the above-mentioned pattern speeds) are also indicated by the thicker grey and light-blue, respectively. The disc angular velocity $\Omega_d(R)$ computed by Roca-Fàbrega et al. (2014) is indicated with the dotted line. The 2:1 and 4:1 outer and inner Lindblad resonances (OLR and ILR) occur along the solid and dashed black curves, respectively. Resonances have been computed as $\Omega_{p2}(R) = \Omega_d(R) \pm \kappa/2$ and $\Omega_{p4}(R) = \Omega_d(R) \pm \kappa/4$, respectively where κ is the local radial epicyclic frequency. The long vertical dashed lines show the positions of the co-rotation radii assuming the three different Ω_S values.*

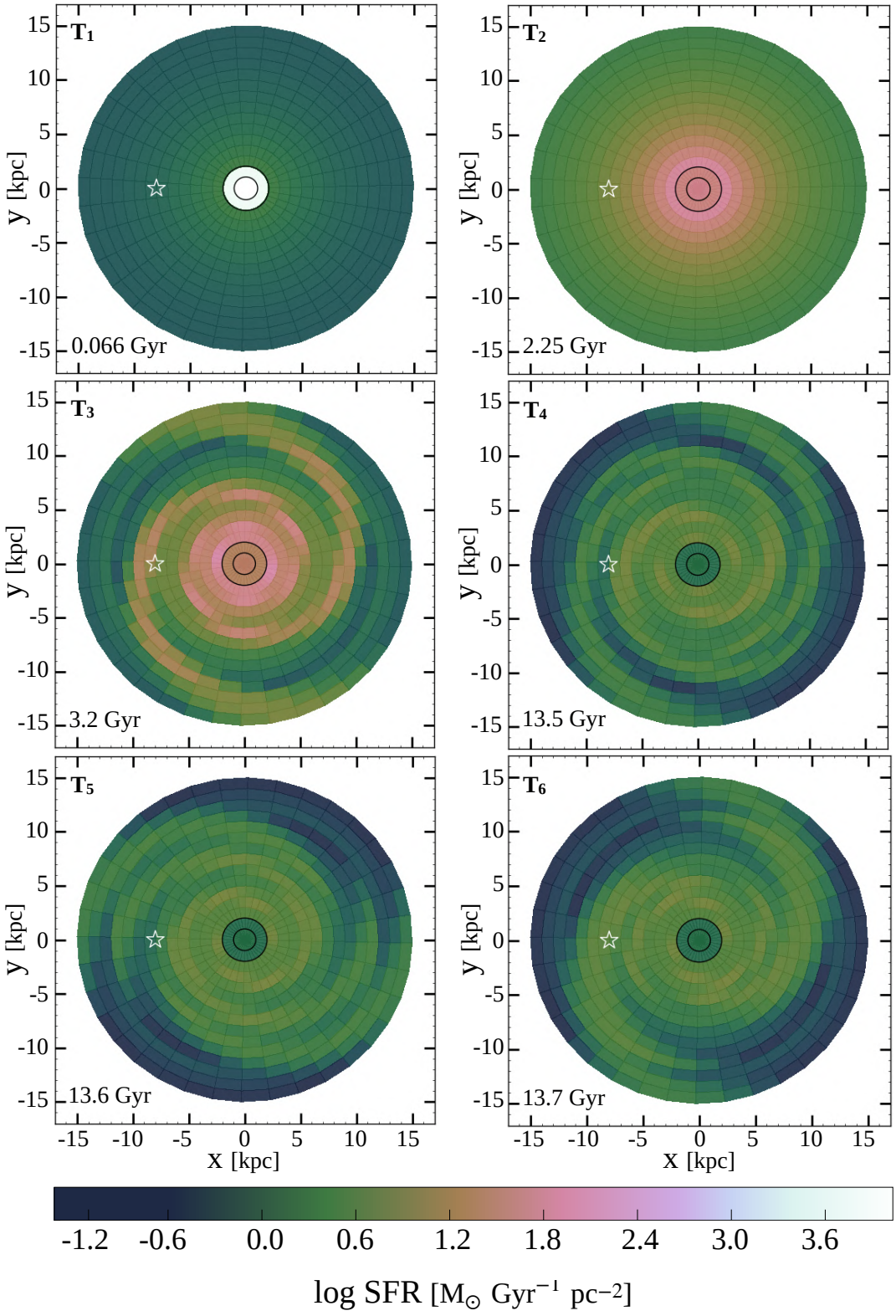

Figure 5.2: *2D SFR from the bulge to the outskirts of the MW. Six snapshots at different time steps: T_1=0.066 Gyr, T_2=2.25 Gyr, T_3=3.2 Gyr, two recent times T_4=13.5 Gyr and T_5=13.6 Gyr, and the present day time, T_6=13.7 Gyr. The position of the sun is represented by the white-edge star.*

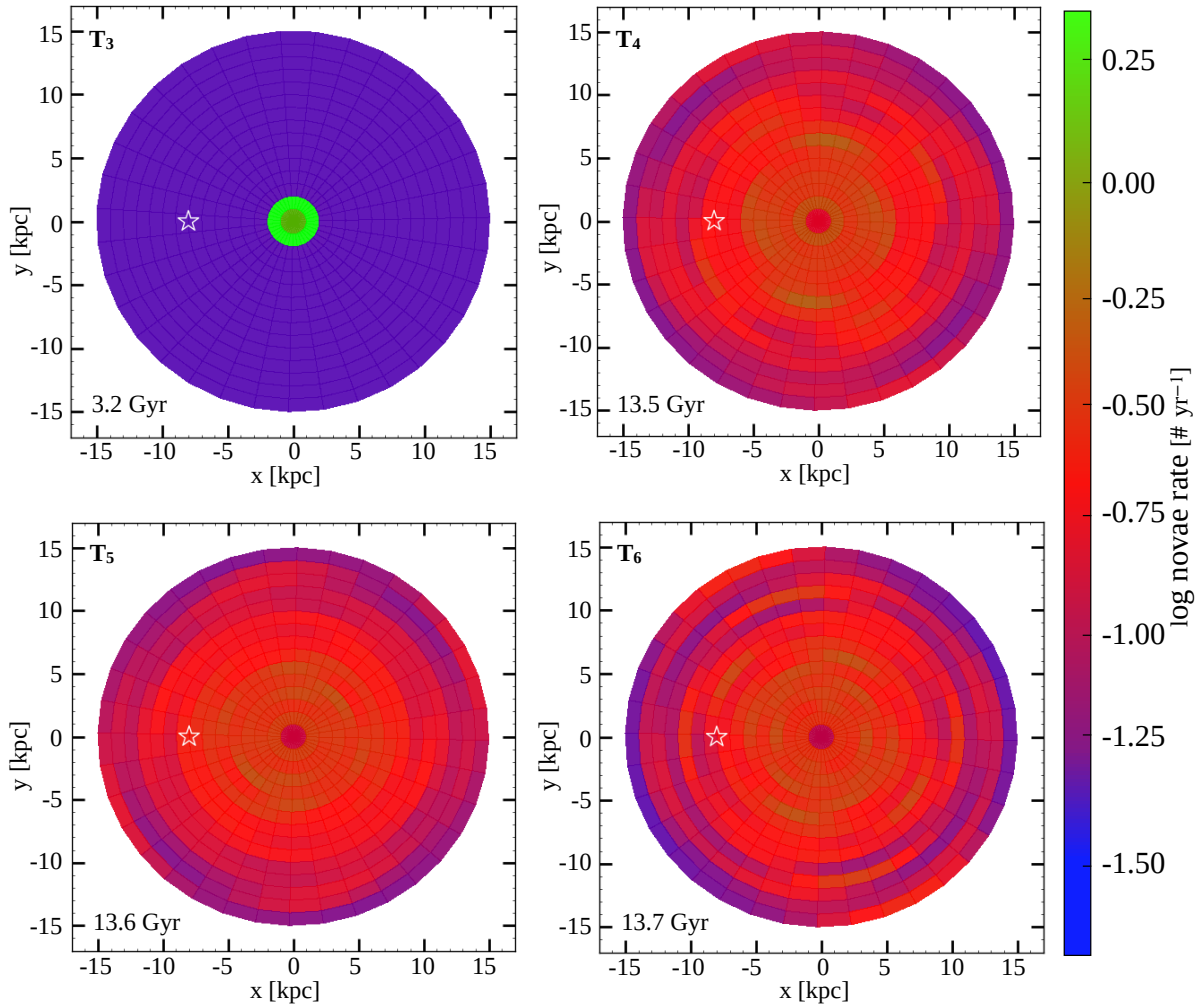

Figure 5.3: *2D map of nova outburst rate in the MW at four different times, T_3, T_4, T_5 and T_6.*

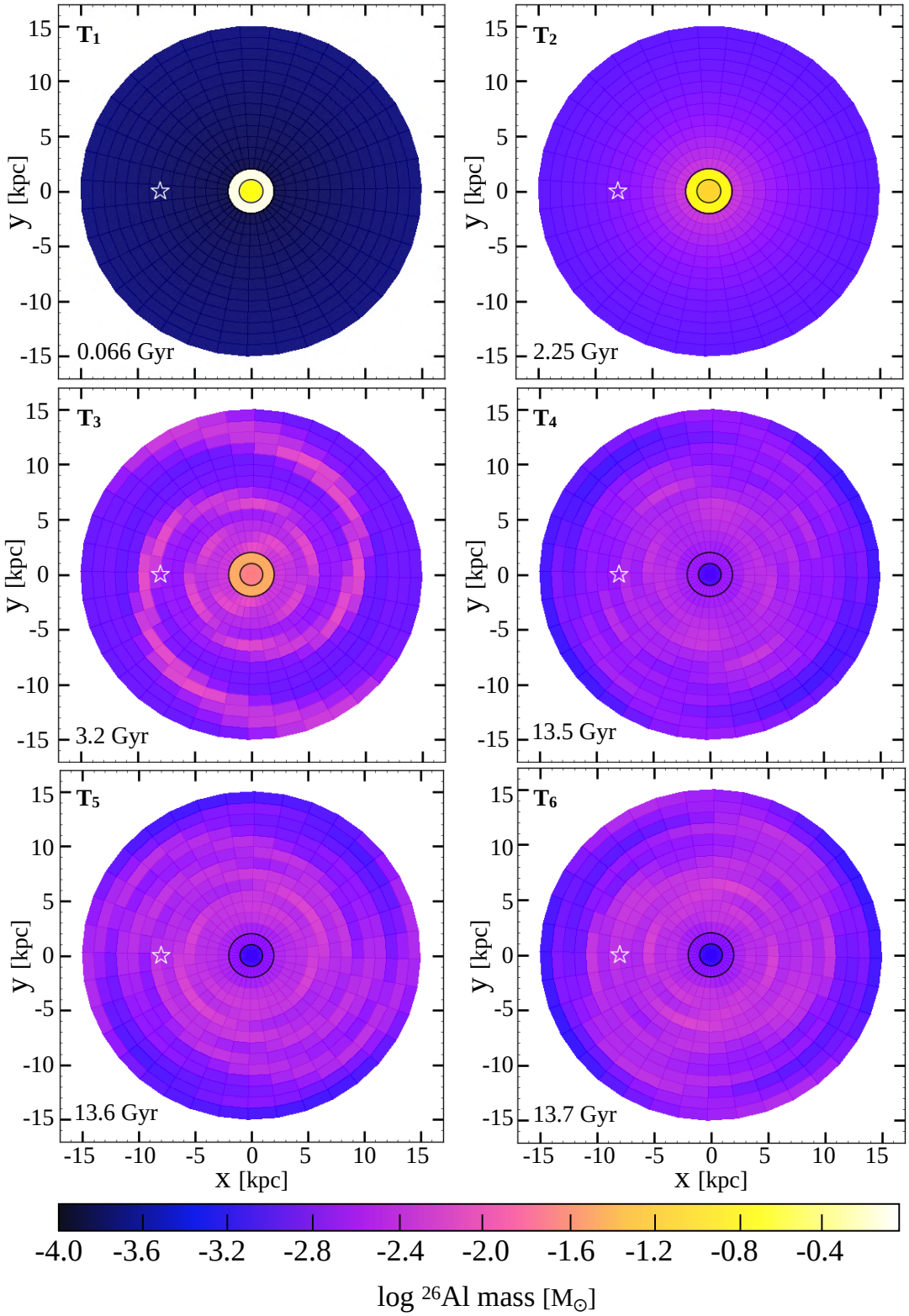

Figure 5.4: *2D distribution of ^{26}Al mass at the six time steps where I have previously analysed the SFR. The ^{26}Al producers here are massive stars and novae. Each cell is colour coded according to the ^{26}Al mass contained as in Fig. 5.2 the sun is indicated by the white-edge star.*

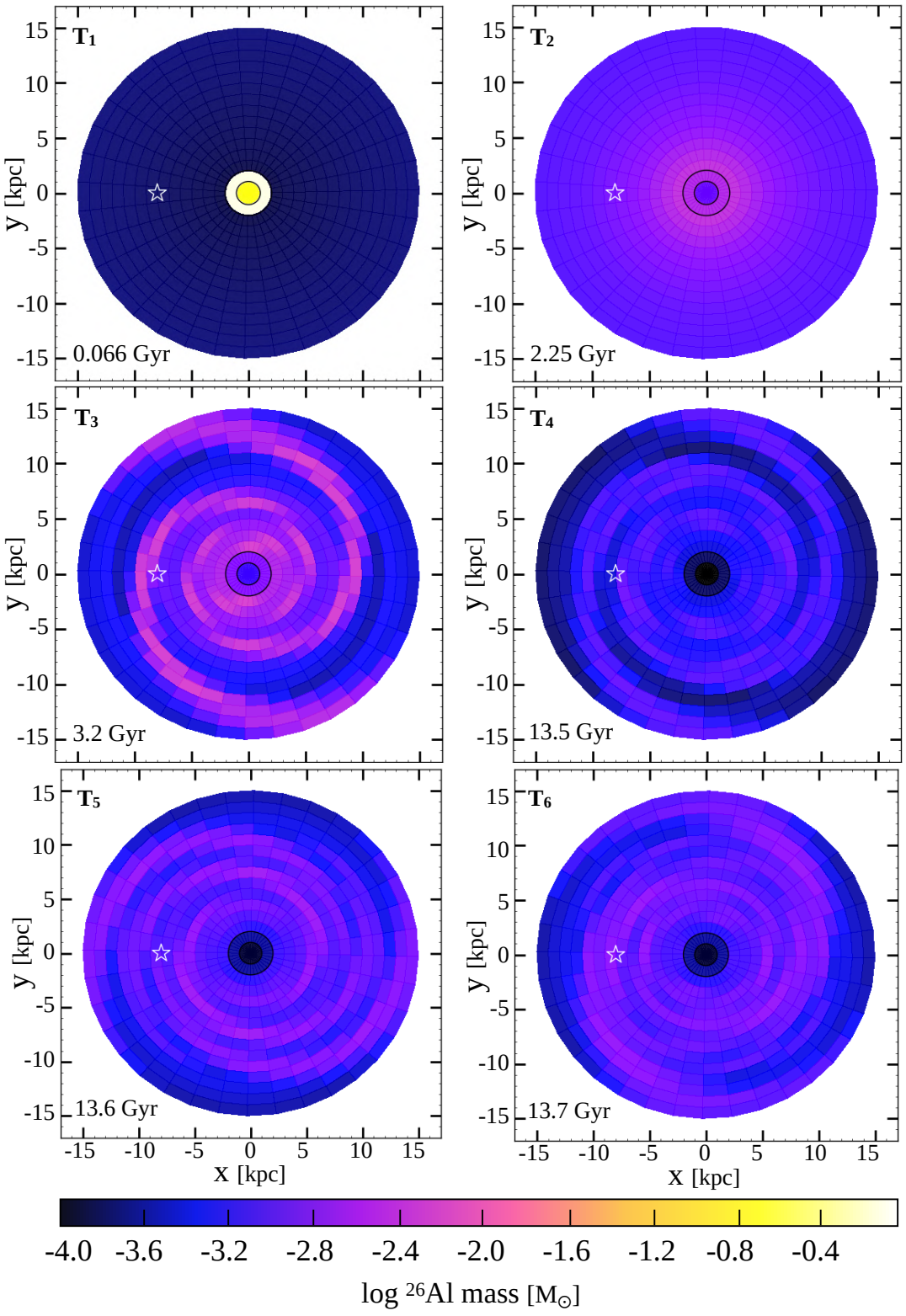

Figure 5.5: *Same as Fig. 5.4 but without any contribution from nova systems.*

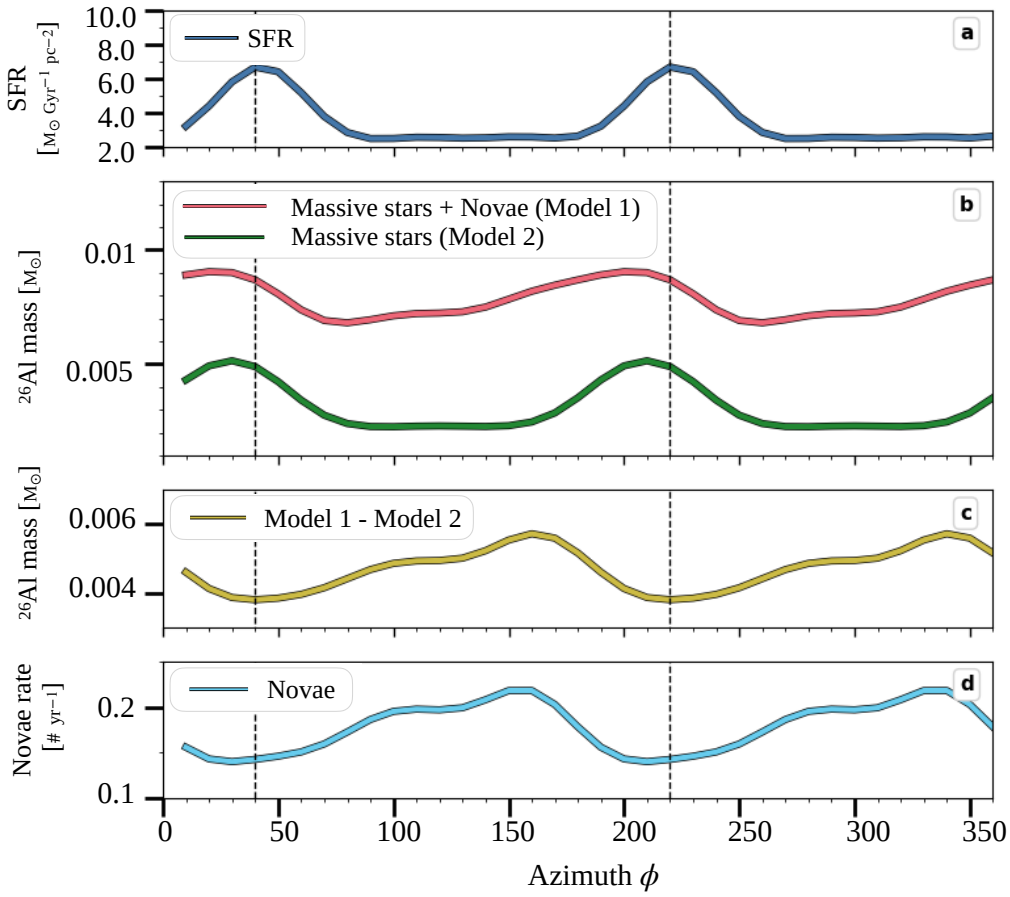

Figure 5.6: *Panel **a**: SFR as a function of the azimuth at the present time and the solar neighbourhood. The black dashed lines, in this plot and in those below, mark the peaks of the SFR. Panel **b**: ^{26}Al distribution in the solar ring and present time. In pink, ^{26}Al predicted by Model 1 and in green that from Model 2. Panel **c**: difference between the ^{26}Al production in the two cases. Panel **c**: novae distribution in the solar ring at the present time.*

6

Evolution of SLRs in the LMC: predictions for future γ-ray surveys

In this Chapter I present the chemical evolution of ^{26}Al and ^{60}Fe in the LMC to provide the first prediction of the ^{26}Al and ^{60}Fe masses and fluxes in view of the upcoming γ-ray survey, COSI, presented in Chap. 3.

Here, I start from the stellar yields constrained in Chap. 4 and test four different combinations of SFR and IMF proposed in the literature. By comparing these four models to the present day observational constraints I can identify the best one, which I adopt to predict the ^{26}Al and ^{60}Fe fluxes.

This Chapter is organised as follows. In Sect. 6.2 I present the chemical evolution model together with all the adopted parameters, in Sect. 6.3 I show the results relative to ^{26}Al and ^{60}Fe masses as well as the α-element patterns. In Sect. 6.4 I discuss the results and the constraints that I derive on the evolution of the LMC and on the predicted γ-ray line fluxes, and finally in Sect. 6.5 I summarise the work and I draw the main conclusions.

The results which I show here are published in the paper Vasini et al. (2023).

6.1 Introduction

The only galaxy that has been observed in the 0.1 - 10 MeV band up to now is the MW (Diehl et al., 1995; Diehl, 2013b; Kretschmer et al., 2013; Pleintinger et al., 2022). It is for this exact reason that in Chaps. 4 and 5 the attention was devoted to the ^{26}Al and ^{60}Fe in our Galaxy, being the only location that could be adopted to perform an actual comparison, thus constraining the nucleosynthesis.

The lack of data is partly due to the techniques needed for the detection, that are completely different from those applied to observe the stable element abundances (see Chap. 3) and therefore dedicated instruments must be built, targeting specifically these two nuclei. Things could change in the future since NASA is working on a new γ survey that could also target the LMC, crossing the boundaries of the Galaxy for the first time. The currently best γ-ray spectrometer telescope, SPI onboard ESA's INTEGRAL satellite (see Chap. 3) revolutionised our understanding of radioactive isotopes, SF (Diehl et al., 2006b), and superbubble structure of the ISM (Krause et al., 2015) through its unprecedented spectral resolution. Due to the large instrumental background in the MeV photon range, strongly limiting the sensitivity, SPI cannot [1] observe the LMC in the light of decaying nuclei. NASA's new instrument, COSI (see Chap. 3), slated for launch in 2027, will have an improved sensitivity over SPI and will be working as a survey instrument for γ-ray lines and continuum sources. The LMC could then be the first extragalactic source for which radioactive isotopes could be measured directly through their γ-ray signatures.

In parallel with the observations it is thus necessary to develop suitable chemical evolution models to provide theoretical constraints to the upcoming observations. This paper is aimed at computing a model for the chemical evolution of the LMC that reproduces the main observational features of this galaxy, including the [α/Fe] versus [Fe/H] relations, as well as to provide the first theoretical estimates of ^{26}Al and ^{60}Fe masses and fluxes. My main purpose is to offer predictions about the mass of ^{26}Al and ^{60}Fe in the framework of a good model for LMC, thus offering theoretical constraints in terms of γ-ray line fluxes to the future γ-ray survey mission COSI (J. Tomsick et al., 2019).

[1] It would require on the order of 6 years of dead-time corrected observation time to observe the LMC with SPI.

6.2 The Model

In this Section I recall the main prescriptions of the chemical evolution adopted that was already presented in Chap. 2. The parameters are fine-tuned so as to reproduce the main present day observations available for the LMC. Since I perform four tests with different Star Formation Histories (SFHs), I show all the common assumptions in Sect. 6.2.2 and separately each SFR with its IMF in Sect. 6.2.3. Regarding the nucleosynthesis prescriptions, the best stellar yields identified in Chap. 4 are adopted.

6.2.1 Chemical Evolution Equation

The chemical evolution model adopted is already described in Chap. 2 and is based on Eq. 2.19 where all the terms, included the wind one, is considered. The LMC in fact, being characterised by a small total mass experiences gas outflows that contribute to its chemical evolution. The wind term is regulated by the wind efficiency which is set to ω=0.25 Gyr^{-1} (see Bradamante et al. 1998).

When solving the Eq. 2.19 the stellar polluters included are SNII, SNIb, SNIc and SNIa according to Eq. 2.14 and the nova systems as explained by Eq. 2.15. The decay timescales adopted for ^{26}Al and ^{60}Fe are those presented in Sect. 1.2.1, namely $\tau_{^{26}\mathrm{Al}}$=1.05 Myr and $\tau_{^{60}\mathrm{Fe}}$=3.75 Myr.

The four SFR and IMF I test in this Chapter are presented in the following sections.

6.2.2 Model assumptions

The chemical evolution model I use is a one-zone model, which means that I assume the LMC to be a structure with a homogeneous chemical composition, and adopt a one-infall process for galaxy formation according to Eq. 2.8. The timescale of formation of the LMC τ_{inf} is set to 5 Gyr, and the parameter a is obtained by reproducing the present time total mass of the LMC. a is derived by imposing an infall mass that should be reached at the end of the accretion process. Here I assume for all models $M_{\mathrm{inf}} = 6 \cdot 10^9 M_\odot$.

Regarding the SFR, as default prescription I adopt the Kennicutt (1998) law in Eq. 2.3. In this study I test four different SFRs that differ for the value of ν. I adopt both values of ν constant in time and time-dependent, which will be presented in detail in Sect. 6.2.3.

6.2.3 Star Formation History

The SFH is given by the combination of the adopted SFR and IMF. The gas depletion induced by the galactic wind, as explained in Sect. 6.2.1, affects the SFH. As already anticipated, I test four cases that differ for the SFH adopted. The assumed SFRs follow always Eq. 2.3 but with a variable SFE ν in order to reproduce the SFRs proposed in the literature. Regarding the IMF, I adopt the one suggested by the various SFH studies. The SFHs tested are taken from Kennicutt (1998) (see Eq. 2.3), Hasselquist et al. (2021), Harris et al. (2009) and Calura et al. (2003) and are described in the next subsections. It is necessary to specify that more recent SFHs have been proposed but they are compatible with the four just listed. The choice of testing more than one SFH is due to the fact that in the literature many SFHs have been proposed but none of them can firmly exclude the others. Tab. 6.1 summarises the parameters of each SFH case. The first column lists the parameters of the model and the columns from the second to the fifth report the value of the parameters for the four different cases explored. In particular, the adopted parameters are: the SFR, IMF, the fraction of binary systems becoming SNIa (A in Eq. 2.14), the wind efficiency (ω in Eq. 2.11), the infall timescale ($\tau_{\rm inf}$ in Eq. 2.8), the infall mass ($M_{\rm inf}$) and the SFE (ν).

Model 1 - Kennicutt et al. (1998) SFR with Kroupa et al (1993) IMF

As a first case I test the classical Schmidt-Kennicutt law, proposed by Kennicutt (1998). The mathematical form of this SFR is shown in Eq. 2.3. The adopted SFE is ν=0.4 Gyr^{-1}. In the top right panel of Fig. 6.1 I compare this theoretical SFR with the present time observed value and the observed average SFR in the last 4.5 Gyrs, both from Harris et al. (2009). They propose a present time SFR in the LMC of 0.38 M$_\odot$ yr^{-1} and an average value in the last 4.5 Gyrs of 0.2 M$_\odot$ yr^{-1}. The model predicts a lower value, but given the large uncertainties that affect the observations, I can consider the model acceptable since it agrees within a factor of 2 with the observations. It is worth noting that the following models are developed starting from the same Schmidt-Kennicutt law, but with a time-dependent SFE in order to reproduce the bursts of SF. In this way I can preserve the dependence from the gas mass while changing the actual shape of the SFR.

The IMF adopted in this case is from Kroupa et al. (1993) (see Eq. 2.6) that I assume as a default choice since it is derived to reproduce the features of the solar neighbourhood.

Parameter	Model 1	Model 2	Model 3	Model 4
SFR	**Ken98**	**Has21**	**HZ09**	**Cal03**
IMF	**Kro93**	**Kro01**	**Sal55**	**Sal55**
fraction of SNIa	0.035	0.035	0.09	0.09
ω [Gyr^{-1}] (wind efficiency)	0.25	0.25	0.25	0.25
τ_{LMC} [Gyr] (infall time)	5.0	5.0	5.0	5.0
M_{inf} [$M_\odot$]	$6{\cdot}10^9$	$6{\cdot}10^9$	$6{\cdot}10^9$	$6{\cdot}10^9$
ν [Gyr^{-1}] (SFE)	0.4	0.05 (t < 11) 0.7 (t>11)	0.03 (t<10.8) 0.25 (10.8 < t < 11.8) 0.1 (11.8 < t < 13.2) 0.4 (13.2 < t < 13.4) 0.35 (13.4 < t < 13.5) 0.8 (t > 13.5)	0.05 (t<2) 0.6 (2 < t < 4) 0.05 (4 < t < 12) 0.5 (t > 12)

Table 6.1: *List of parameters adopted for the four models tested. The first column contains the parameters and each of the following four columns is representative of a specific model. Notice that the differences among the models lay in the SFR adopted (first row) which is obtained fine tuning the SFE ν, which is variable as well (last row). In the first and second row the short version of the references are reported: Ken98 for Kennicutt (1998), Has21 for Hasselquist et al. (2021), HZ09 for Harris et al. (2009), Cal03 for Calura et al. (2003), Kro93 for Kroupa et al. (1993), Kro01 for Kroupa (2001) and Sal55 for Salpeter (1955).*

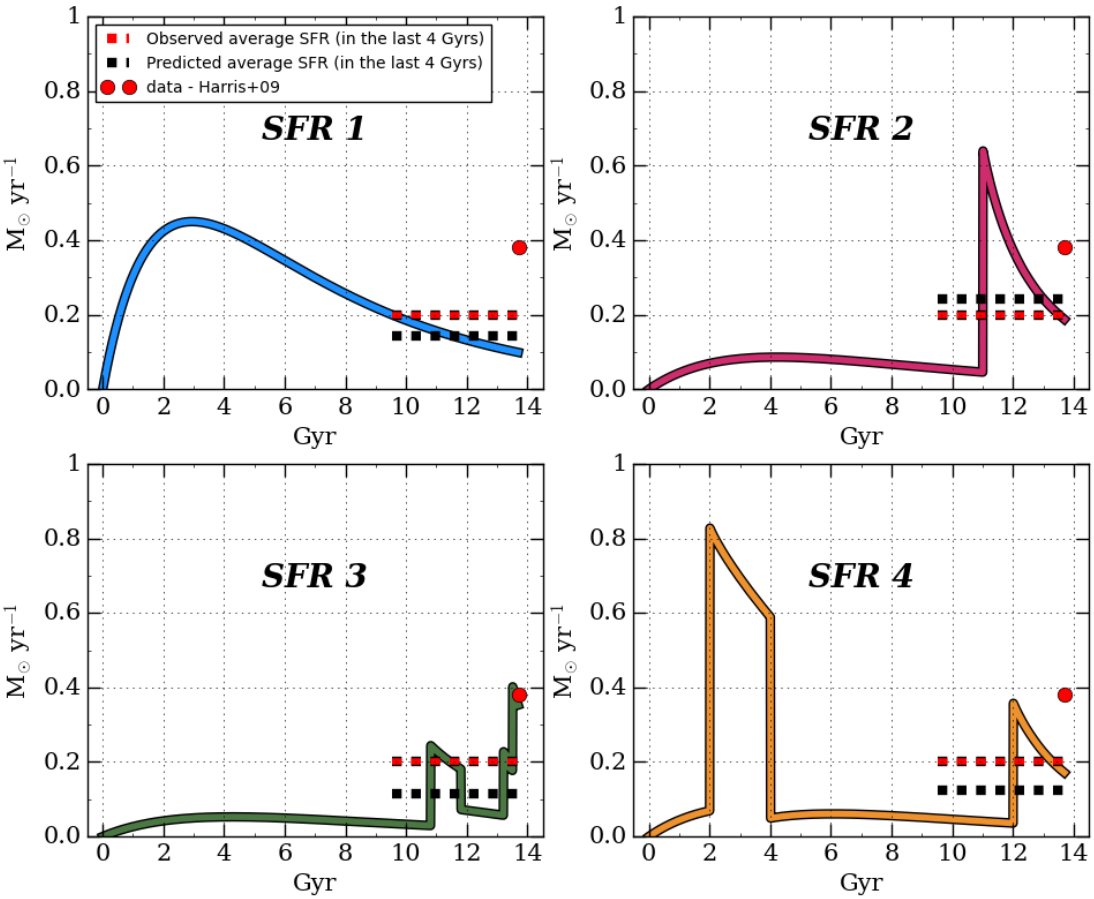

Figure 6.1: *The four SFHs tested in this study. Top right panel: Model 1 with a Schmidt-Kennicutt law taken from Kennicutt (1998) with constant SFE ν. The red point is the present time observed SFR, 0.38 $M_\odot$ yr^{-1}, taken from Harris et al. (2009). The dashed red line is the average SFR in the last 4.5 Gyrs, again by Harris et al. (2009) and the dashed black line is the average SFR in the last 4.5 Gyrs that I obtain. Top left panel: Model 2 with Hasselquist-like SFH inspired by Hasselquist et al. (2021). Bottom left: SFH by Harris et al. (2009) used for Model 3. The authors propose a SFH very low for the first 10 Gyr followed by four bursts, whereas I adopt just three bursts, since the two most recent ones are very close in time and the SF in between is not too low. With this SFH I reproduce the observed value. Bottom right panel: SFH by Calura et al. (2003) tested in Model 4. This SFH is inspired by Bradamante et al. (1998) and is derived on purely theoretical basis but it is suitable to fit the data available at the time. Notice that only Model 3 can reproduce the present time value and also the average SFR is consistent with the observation, given the uncertainties.*

Model 2 - step function and Kroupa 2001 IMF

The second SFR I test is a step function that is modelled following the theoretical one by Hasselquist et al. (2021). This SFH suggests a low and almost constant value for the SFR until 2 Gyr ago, followed by a burst. The present time predicted SFR fits nicely the observed value proposed by Harris et al. (2009).

The IMF I assume in this case is the one that also Hasselquist et al. (2021) used, namely the two-slope IMF from Kroupa (2001) (see Eq. 2.7), very similar in shape to a Salpeter (1955) law for masses $M > 0.5 M_{\odot}$. From this IMF I expect a larger metal production because the contribution by massive stars is higher than in the Kroupa et al. (1993) previously adopted.

Model 3 - Harris & Zaritsky (2009) SFR with Salpeter (1995) IMF

The third model I adopt is that by Harris et al. (2009) where a more complex SFR is suggested. The shape they propose, presented in their Fig. 11, is obtained by collecting the Colour-Magnitude Diagram (CMD) of the LMC divided in a sub-grid. For each portion of the grid many synthetic CMDs are produced assuming different SFHs and then the best one is selected. Lastly, they perform a convolution between the SFHs around the grid and obtain the final one. Their SFH is quite similar to the Hasselquist et al. (2021) one since also in this case it is flat for the first $\sim$ 11 Gyr. Then, there are four peaks very close in time which are consistently higher than the early SFR. In the bottom right panel of Fig. 6.1 I show how I model this third SFH, again by means of the Schmidt-Kennicutt law with a non-constant SFE. I highlight that I merge the two most recent bursts in one single burst due to the fact that they occur very close to each other.

The IMF I adopt for Model 3 is the one by Salpeter (1955) as adopted by Harris et al. (2009) (see Eq. 2.4):

Model 4 - Calura et al. (2003) and Salpeter (1955) IMF

The last model I test is the SFH proposed by Calura et al. (2003). In that paper a double burst scenario is proposed, with the first one between 2 and 4 Gyr after the LMC formation and the second one, less intense, which started after around 12 Gyr of evolution and is still on-going with a present time value that reproduces quite well the observations, as shown in the bottom left panel of Fig. 6.1.

The assumed IMF is the Salpeter (1955) one (see Eq. 2.4).

6.2.4 Nucleosynthesis and yields

Concerning the nucleosynthesis, my model accounts for the contribution by different types of stars as massive stars, AGB stars, SNIa and nova systems. The stellar yields adopted both for stable and unstable isotopes are those used also in Chap. 5.

6.3 Results

In this Section I show the results I obtain with the four SFH cases explored. I discuss the observational constraint used to select the best model and then the results obtained with that one.

6.3.1 Observational constraints

In order to chose my best model, I have to ensure that as many observational constraints as possible are reproduced within their error bars, also considering that the chemical evolution model itself has several sources of uncertainties. Among these, the most important is related to the uncertainties in the nucleosynthesis yields. The observational constraints are shown in Tab. 6.2. The first column indicates the observable quantity considered, the second indicates the label of the model, the third shows the predicted value, the fourth lists the observed value taken from the literature and the fifth reports the reference in the literature from which the observed value is taken. The observed and theoretical quantities reported in Tab. 6.2 are: present time SFR, present time SN rates (CCSN+SNIa), nova rate, gas mass, stellar mass and average metallicity in the LMC. It is worth noting that in the third column, about the present time nova rate, two values are reported. In Eq. 2.15 indeed the factor α is a free parameter of the model and its value can change from galaxy to galaxy. In this case I consider two possible values of α, 0.0115 and 0.024, and the two values in the table are obtained using these two prescriptions. The best α is chosen in order to reproduce the present time nova outburst rate.

According to this table, the two best models are Model 3 and Model 4. It is worth noting that the final total mass (gas plus stars dead and alive) agrees with the assumed infall mass for all the models. Looking at all the other quantities, some considerations regarding the predictions from every single model can be made. Model 1 can be excluded quite easily because the SN rate, nova rate, gas mass and metallicity Z values are not in good agreement with the observations. Regarding Model 2, it can be noted that the predictions about the nova rate and

the metallicity Z are higher than the expectations. These two quantities are rather important for the study I am carrying on, so I can rule out also Model 2 since it does not fit these two observables.

Regarding Model 3 and Model 4 (Harris et al. 2009 and Calura et al. 2003 respectively) a deeper discussion is needed. Looking at Tab. 6.2, the present time SFR and stellar mass are more in agreement in Model 4, whereas the SN rate, present time gas mass and metallicity Z favours Model 3.

Interesting considerations to unravel this ambiguity can come from the analysis of the abundances of the α-elements, namely O, Mg, Si and Ca. The nucleosynthesis of these chemical species is known quite well and the stellar yields either have a relatively small uncertainties or, if not, it is known how to correct for them. Moreover, the α-elements show a very clear behaviour when analysed as a function of [Fe/H]. They generally show a plateau at low [Fe/H] followed by a decrease when [Fe/H] becomes larger. Such a change in slope, that identifies the so called α-knee, is important since it allows to infer information regarding the morphological type of the host galaxy and its SFR just based on its position on the [α/Fe]-[Fe/H] plane. In fact, on the basis of the time-delay model (see Matteucci 2021), the behaviour of the[α/Fe]-[Fe/H] relation and in particular the location of the α-knee, depends on the SFH of the specific galaxy taken into exam. The explanation of that lies in the lifetime of the progenitors of the α-elements and of Fe.The α-elements are mainly produced by SNII, whereas SNIa are the most important contributors to Fe abundance. According to stellar physics, SNII eject their nucleosynthesis products into the ISM on short timescales, on the contrary, SNIa are characterised by much longer lifetimes. Therefore, at the early stages of galaxy evolution the ISM is polluted mainly by SNII, which enrich the gas mainly in α-elements. They also produce small quantities of Fe, hence [Fe/H] increases slowly. When the first SNIa start to explode, injecting large quantities of Fe, the [α/Fe] ratio starts decreasing. If a galaxy underwent a very mild or gasping SF, such as irregulars, then the knee is located at very low [Fe/H], whereas in galaxies with more intense SF such as spirals and spheroids (where the SF was an intense and short burst) the knee occurs at larger [Fe/H] values. The α-element behaviour makes it a reliable constraint to chose among different models. In Fig. 6.2 I show the trend of O, Mg, Si and Ca predicted by Model 3 (Harris & Zaritsky SFR, green line) and by Model 4 (Calura SFR, yellow line) compared to several sets of data from the literature. In particular I use the LMC globular cluster data from Hill et al. (2000), Mucciarelli et al. (2008) and Asa'd et al. (2022), and the LMC bar stars data by Van der Swaelmen et al. (2013). I can see that the trend is well reproduced by both models and at low [Fe/H] both models are acceptable. Regarding the α-knee discussed above, nor the two models neither the data show it in the [Fe/H]

Observable	Model	Prediction	Observation	References
Present time	# 1	0.1	$0.2^{+0.6}_{-0.05}$	Harris et al. (2009)
SFR	# 2	0.2		
$[M_\odot\ yr^{-1}]$	# 3	0.35		
	# 4	0.17		
CCSN rate +	# 1	0.064	$0.67^{+0.49}_{-0.35}$	Mannucci et al. (2005)
SNIa rate	# 2	0.24		
$[SN\ century^{-1}]$	# 3	0.28	0.86±0.25	Maoz et al. (2010)
	# 4	0.15		
Nova	# 1	5.66-11.82	2.4±0.8	Mróz et al. (2016)
rate	# 2	3.9-8.2		
$[novae\ yr^{-1}]$	# 3	1.27-2.7		
	# 4	2.1-4.3		
Present time	# 1	$2.5{\cdot}10^8$	$5{\cdot}10^8$	van der Marel (2006)
gas mass	# 2	$2.7{\cdot}10^8$	(neutral gas)	
$[M_\odot]$	# 3	$4.4{\cdot}10^8$	$7{\cdot}10^8$	Matteucci et al. (1983)
	# 4	$3.4{\cdot}10^8$		
Present time	# 1	$2.28{\cdot}10^9$	$2.7{\cdot}10^9$	van der Marel (2006)
stellar mass	# 2	$0.9{\cdot}10^9$		
$[M_\odot]$	# 3	$0.6{\cdot}10^9$		
	# 4	$1.5{\cdot}10^9$		
Present time	# 1	$5.2{\cdot}10^9$	$3.6{\cdot}10^9$	van der Marel (2006)
total mass	# 2	$5.2{\cdot}10^9$		
$[M_\odot]$	# 3	$5.2{\cdot}10^9$		
	# 4	$5.2{\cdot}10^9$		
Present time	# 1	Z = 0.019	Z= 0.006 - 0.01	Nosowitz et al. (2022)
metallicity Z	# 2	Z = 0.05	Z = 0.01	Tchernyshyov et al. (2015)
	# 3	Z = 0.015		
	# 4	Z = 0.024		
Present time	# 1	[Fe/H] = 0.18	[Fe/H]=-0.3 dex	Hasselquist et al. (2021)
metallicity	# 2	[Fe/H] = 0.38	(upper limit)	
[Fe/H]	# 3	[Fe/H] = 0.016	[Fe/H]=-0.2 dex	Nidever et al. (2020)
	# 4	[Fe/H] = 0.29	(upper limit)	

Table 6.2: *Observational quantities used to constrain the chemical evolution model. The columns from 1 to 5 indicate, in order, the observable quantity considered, the model, the theoretical prediction from that model, the observation and the reference. It is highlighted that Model 3 and Model 4 reproduce these observables better than Model 1 and Model 2 do, but, relying only on this table, is not possible to prefer one over the other.*

range plotted, since it happens earlier given the LMC low level of SF. The only discriminant factor between Model 3 and Model 4 is the maximum [Fe/H] value reached at the present time. All the four plots show that Model 3 reproduces the data up to the solar [Fe/H] value whereas Model 4 goes further towards a higher Fe content, more similar to the MW one, whereas the data stops earlier. In conclusion, these four plots indicate Model 3, with SFR by Harris et al. (2009), as the best model.

The last important consideration about Model 3 and Model 4 concerns the way in which the SFRs were derived. Calura et al. (2003) proposed a chemical evolution study of purely theoretical nature, where the SFR was assumed and compared to the data available at the time (those that I am also showing by Hill et al. 2000). The origin of this SFR comes from a previous work by Bradamante et al. (1998) regarding the SFR of dwarf irregulars (and not specifically of the LMC). In that work, they concluded that irregular galaxies should have a SFR characterised by one ore more bursts, for a maximum of 10 bursts, with a SFE for each burst from 0.1 Gyr^{-1} to 7 Gyr^{-1}. The SFR by Harris et al. (2009) itself falls within the range proposed by Bradamante et al. (1998), the only difference is that this one is also supported by observations. As already mentioned in Sect. 6.2.3, the authors derived this SFH carrying out a very detailed observational study.

The last aspect to clarify about my models is the fraction of systems that can form novae, represented by the factor α in Eq. 2.15. Since my best model is Model 3, the value of the parameter α that can best reproduce the observations is 0.024.

6.3.2 ^{26}Al and ^{60}Fe masses

In this Section I present the results about the masses of ^{26}Al and ^{60}Fe in the LMC, as predicted by Model 3.

As mentioned in Sect. 6.2.4 I test two different nova contribution to ^{26}Al, assuming, at first, no nova production and then testing the yield by José et al. (2007), whereas for ^{60}Fe I only have production by massive stars. I report in Tab. 6.3 the results predicted by the four SFHs studied. The first two rows are dedicated to the references where the yields come from, whereas the other four rows list the results about ^{26}Al and ^{60}Fe masses. The first column reports the value of the mass of ^{26}Al obtained excluding the production by nova systems and assuming only a production by massive stars, AGBs and SNIa. The second column contains the mass of ^{26}Al in the case where also novae are considered among the ^{26}Al producers. Finally, the third column contains the obtained mass of ^{60}Fe. Since for this element there is no contribution coming from novae, there are no multiple cases to discuss.

The values obtained using Model 3 are, as stated since the beginning, predictions

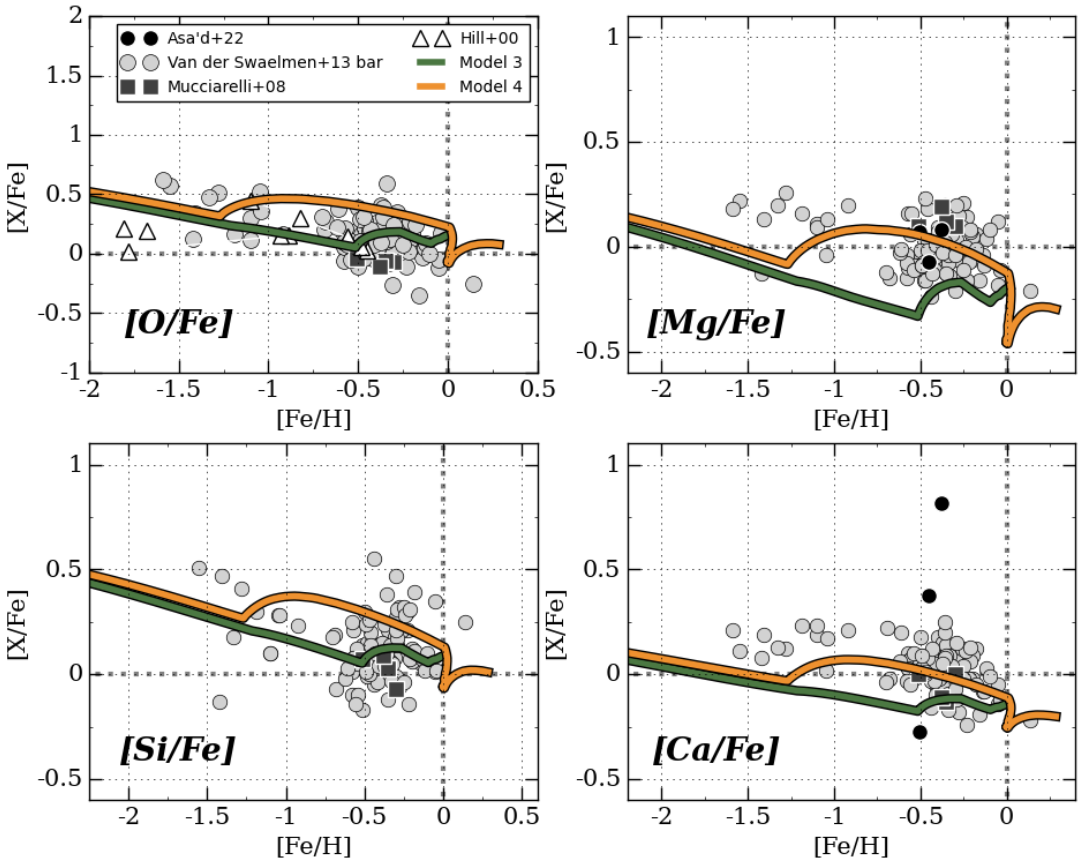

Figure 6.2: *Abundances of four α-elements, namely, O, Mg, Si and Ca. The models shown are Model 3 with Harris et al. (2009) SFH (green solid line) and Model 4 with Calura et al. (2003) SFH (orange solid line). The data taken from Asa'd et al. (2022) (black circles), Mucciarelli et al. (2008) (dark grey squares) and Hill et al. (2000) (white triangles) refer to LMC globular clusters whereas those by Van der Swaelmen et al. (2013) (light grey circles) regard the LMC bar stars. Since, by means of Tab. 6.2 I already excluded Model 1 and Model 2, here I show just the two remaining ones to clarify if I can rule out another one. It can be seen that Model 4 predicts too much Fe abundance, therefore I select Model 3 as my best model.*

for future γ-observations, thus no comparison with any data can be provided, yet. Some considerations can nevertheless be made, the most important one being the ratio between the mass of the two isotopes. From the observational point of view, I only have data about the MW (Martin et al., 2009; Diehl et al., 2010; Diehl, 2016). I know that the instruments detected a much higher flux of ^{26}Al than that of ^{60}Fe, and specifically the ratio ^{60}Fe/^{26}Al of the fluxes is around ~15%. In Vasini et al. (2022), where a similar calculation of the masses of ^{26}Al and ^{60}Fe was done for the MW, the mass of ^{26}Al was higher than that of ^{60}Fe. On the contrary, in the case of

	^{26}Al (Case #1)	**^{26}Al** (Case #2)	**^{60}Fe**
massive stars yield	Woosley et al. (1995)	Woosley et al. (1995)	Woosley et al. (1995)
nova systems yield	no contribution	José et al. (2007)	no contribution
Model 1	0.04 $M_\odot$	0.33 $M_\odot$	0.13 $M_\odot$
Model 2	0.17 $M_\odot$	0.57 $M_\odot$	0.49 $M_\odot$
Model 3	0.20 $M_\odot$	0.33 $M_\odot$	0.44 $M_\odot$
Model 4	0.11 $M_\odot$	0.20 $M_\odot$	0.29 $M_\odot$

Table 6.3: *In the first two rows the references to the yields are listed, whereas from the third to the sixth row I show the results for all my models, with the best one being Model 3. The first column shows the mass of ^{26}Al produced by massive stars, the second one lists the total mass of ^{26}Al produced by massive stars together with nova systems and the third column contains the results about ^{60}Fe.*

LMC I obtain the opposite result, predicting an ^{60}Fe mass of 0.44 $M_\odot$, larger than all the ^{26}Al values predicted by the four models.

6.4 Discussion

Together with the four models proposed, while carrying out this study I test some other options. In particular I check what happens if I assume the same IMF for all the models, namely the Kroupa et al. (1993) one. Adopting this IMF and combining it with the SFRs by Hasselquist et al. (2021), Harris et al. (2009) and Calura et al. (2003) is not totally correct since, as argued in the previous paragraphs, these works assumed specific IMFs, and in order to reproduce those studies I have to make the same assumptions. The results I obtain in these cases do not reproduce the observational constraints of the LMC, thus suggesting that in this galaxy a Salpeter-like IMF should be preferred.

In Sect. 6.3.2 I present the masses of these two isotopes predicted only by my best model. I already pointed out that Model 3 predicts more ^{60}Fe than ^{26}Al unlike the MW, but more interesting considerations can be made analysing what the other models predicted. In Tab. 6.3 it is noteworthy the fact that both Model 3 and Model 4, namely the two best models, predict more ^{60}Fe than ^{26}Al. The reason behind this difference of the LMC with respect to the MW lies probably in the IMF. Both Model 3 and Model 4 adopt a Salpeter IMF whereas Model 1 and Model 2 adopt a Kroupa et al. (1993) and a Kroupa (2001) IMF respectively. The main

	^{26}Al (massive stars) [ph cm^{-2} s^{-1}]	^{26}Al (massive stars + novae) [ph cm^{-2} s^{-1}]	^{60}Fe (massive stars) [ph cm^{-2} s^{-1}]	^{60}Fe/^{26}Al (^{26}Al by massive stars and novae)
Model 1	0.19×10^{-6}	1.56×10^{-6}	0.07×10^{-6}	0.047
Model 2	0.8×10^{-6}	2.7×10^{-6}	0.28×10^{-6}	0.10
Model 3	0.9×10^{-6}	1.56×10^{-6}	0.25×10^{-6}	0.16
Model 4	0.5×10^{-6}	0.9×10^{-6}	0.16×10^{-6}	0.18

Table 6.4: *Fluxes of ^{26}Al and ^{60}Fe for all the models computed using Eq. 6.1. In the first column I present the flux of ^{26}Al in the case of production only by massive stars, in the second the flux of ^{26}Al considering also the contribution by novae, in the third I list the flux of ^{60}Fe. In the fourth i show the flux ratio ^{60}Fe/^{26}Al using the the values from columns 3 and 2.*

producers of both ^{26}Al and ^{60}Fe are massive stars, and going to higher and higher masses the yield of ^{60}Fe is larger than that of ^{26}Al. The Salpeter IMF predicts a fraction of high mass stars larger than the other two laws, therefore, when adopting a Salpeter IMF I obtain more ^{60}Fe than ^{26}Al.

Regarding the production by nova systems of the ^{26}Al, I can emphasise that, depending on the considered model, they contribute to the total fraction in different proportions. For the best model (Model 3) the contribution from novae is $\sim 1/3$ of the total ^{26}Al mass. For Model 1, 2 and 4, on the contrary, the fractions are much higher, ~87%, ~70% and ~45% respectively. This percentage can be compared with those obtained in Chap. 4 for the MW. For the two best models identified in there, the novae contribute for more than 95% of the total ^{26}Al abundance, much more than what they do in the LMC. This is again due to the IMF adopted: since the Salpeter (1955) IMF produces more massive stars than the Kroupa et al. (1993) adopted for the MW, the nova systems will contribute less. This explains the discrepancy between the results obtained for the MW and for the LMC.

By adopting the best model (Model 3) I perform two other tests, about different nova yields and ECSN. Regarding nova yields, I compute the ^{26}Al mass making use of one of the most recent set of yields by Starrfield et al. (2020). I adopt the three models proposed there, that differ from each other in the chemical composition of the progenitor WD. For each model, they propose yields for different WD masses, that I average to obtain one single value for each of the three models. The results show that the contribution by novae with Starrfield yields is much lower, since the yields are lower than those by José et al. (2007). In the three cases, I obtain 0.205,

0.207 and 0.209 $M_\odot$ of ^{26}Al, which is only slightly more than what I obtain without novae (0.20 $M_\odot$). The second aspect I investigate is the inclusion of the yields of ECSN by Wanajo et al. (2013) relative to ^{60}Fe. In particular, I include this class of progenitors assuming three different yields proposed by Wanajo et al. (2013), 3.61×10^{-5}, 7.61×10^{-5} and 13×10^{-5} $M_\odot$. In these three cases I obtain 0.45, 0.48 and 0.50 $M_\odot$ respectively, whereas without the ECSN contribution the mass is 0.44 $M_\odot$. I can see that ECSNe increase only slightly the mass of ^{60}Fe and can be considered negligible.

The last aspect I would like to discuss is related to the uncertainty associated to my results. Concerning the production of ^{26}Al I can consider the uncertainties in the observed present day nova and SFRs. By adopting the observed uncertainties listed in Tab. 6.2 I obtain a minimum mass of ^{26}Al of $0.20^{+0.09}_{-0.07}$ $M_\odot$ and a maximum mass of $0.33^{+0.27}_{-0.04}$ $M_\odot$. Given these values I predict a mass of ^{26}Al in the range 0.13 – 0.60 $M_\odot$. By repeating the same procedure for ^{60}Fe, I predict its mass to be $0.44^{+0.76}_{-0.18}$ $M_\odot$.

In the light of the upcoming COSI mission in 2027, these predicted radioactive masses can be converted to quasi-steady-state γ-ray line fluxes. Assuming a point-like distribution at a distance $d_{\rm LMC} = 49.6$ kpc to the LMC as a first order estimate, the γ-ray line flux F_i from a radioactive element i can be calculated as:

$$F_i = \frac{M_i p_i}{m_i \tau_i} \frac{1}{4\pi d^2_{\rm LMC}}, \tag{6.1}$$

where M_i is the mass of element i that I predict, m_i its isotopic mass, τ_i its lifetime, and p_i the probability to emit a γ-ray photon after the decay. For $p \approx 1$ for both isotopes, the flux at 1.809 MeV from the decay of ^{26}Al is 1.6×10^{-6} ph cm^{-2} s^{-1}, and at 1.173 and 1.332 MeV from the decay of ^{60}Fe is 2.5×10^{-7} ph cm^{-2} s^{-1}, respectively, for Model 3. I summarise the flux estimated from my models in Tab. **??**. The first column contains the predicted flux of ^{26}Al in case of production only by massive stars, the second one refers to the case of ^{26}Al produced by massive stars together with novae, the third shows the ^{60}Fe flux and the fourth lists the flux ratio between column 3 and column 2. If the fluxes are distributed across the actual size of the LMC on the sky of about $4^\circ \times 5^\circ$, the extended emission lowers the expected total fluxes by less than 5 %, but the flux per resolution element (J. Tomsick et al., 2019) is then about 4–6 times smaller, requiring a somewhat longer integration time than the nominal two-year mission. The exact exposure time required to detect the 1.809 MeV signal from the LMC then depends on the actual morphology of the galaxy, that is, where the emission could be found. Given the HI measurements of (Dawson et al., 2013) of the LMC, a superbubble structure is evident which may concentrate more ^{26}Al in fewer cavities than being spread out across the entire

galaxy. In the MW, ^{26}Al is also found inside superbubbles (e.g. Diehl et al. 2010; Siegert et al. 2017b; Krause et al. 2015), so that the same idea for the LMC is not unreasonable. For my best model, then, the LMC could be detectable in ^{26}Al γ-rays within 2–4 years with COSI.

In the case of ^{60}Fe, albeit having a larger persistent mass, the lifetime is longer and the nuclei masses larger, so that the fluxes for each of the two decay lines at 1.173 and 1.332 MeV, respectively, are about a factor of 8 smaller than the ^{26}Al line. This means that even with COSI, ^{60}Fe γ-rays will not be detected from the LMC unless additional contributions from, as of yet unknown ^{60}Fe producers, would be enhanced in this galaxy.

6.5 Conclusions

In this work I develop a model to study the chemical evolution of ^{26}Al and ^{60}Fe in the LMC. I test four different cases with different SFHs taken from the literature and I select as best model the one that could reproduce at best the present time LMC observations and α-elements abundance patterns. My results can be summarised as follows:

- according to the tests I perform here, the model that can best reproduce the present time features of the LMC is Model 3, that adopts a SFH by Harris et al. (2009) and an IMF by Salpeter (1955). These assumptions allow me to reproduce the present time SFR, SN rate, nova rate, gas mass and metallicity. Moreover, they also fit the abundances of the most important α-elements such as O, Mg, Si, and Ca. In general, this indicates that the LMC underwent a very low SF at the beginning of its history, followed by a recent burst that is still active. This behaviour agrees with the characteristics of an irregular galaxy, as the LMC is;

- my best model, Model 3, predicts ~0.44 $M_\odot$ of ^{60}Fe and a ^{26}Al mass in the range 0.20 – 0.33 $M_\odot$, depending on the presence or absence of the nova contribution. However, considering the uncertainties observed in nova and in SFRs, I predict a ^{26}Al mass in the range 0.13 – 0.60 $M_\odot$ and a ^{60}Fe mass of $0.44^{+0.76}_{-0.18}$ $M_\odot$. Even though the intervals partially overlap, the models always predict more ^{60}Fe than ^{26}Al. This is in contrast with what I find with a similar modelling approach for the MW, where the mass of ^{60}Fe is smaller than that of ^{26}Al. This result is reinforced by the fact that also Model 4, that is the second most reliable model from this study, predicts more ^{60}Fe than ^{26}Al. The reason for this lies in the Salpeter IMF adopted by these two models: in

fact, this IMF predicts more massive stars than the IMF suitable for the MW disk. Since these stars are the main producers of ^{60}Fe, then ^{60}Fe abundance is larger than ^{26}Al abundance. It is important to highlight that the uncertainties in the model and in the input parameters, such as the yields, are not the main cause of the discrepancy between LMC and MW, simply because I adopt the same chemical evolution model with the same yields for the two galaxies. Therefore, this can be interpreted as an evidence to prefer a Salpeter-like IMF when describing the LMC;

- according to my best model, the contribution to ^{26}Al coming from nova systems should not exceed 1/3 of the total abundance. This percentage is much lower than what obtained in Chap. 4 for the MW, where it was ~95% of the total ^{26}Al abundance. Again, this is mainly due to the larger fraction of massive stars in the Salpeter (1955) IMF relative to the Kroupa et al. (1993) one;

- given the estimated sensitivity of the upcoming COSI mission in 2027, 1.809 MeV γ-rays from the decay of ^{26}Al at a flux level of (1–2)$\times10^{-6}$ ph cm^{-2} s^{-1} is within reach. The γ-ray lines from the decay of ^{60}Fe at 1.173 and 1.332 MeV are probably too faint to be detectable from the LMC, even with improved instrumentation.

7

Galactic archaeology with the [Mg/Mn] vs. [Al/Fe] plane: Uncertainties and caveats

In this Chapter I am going to analyse the diagram [Mg/Mn] versus [Al/Fe] which has gained significant attention in recent literature as a valuable tool to distinguish between accreted and in situ stars in the MW and the nearby dwarf galaxies. In particular, this combination of elements is supposed to be highly sensitive to the SFH, unveiled by the imprints left on those abundances. However, a complete discussion on the uncertainties associated with these nuclei is still missing, making it difficult to know how reliable the associated results are. In this work, I aim to analyse, by means of detailed chemical evolution models, the uncertainties related to the nucleosynthesis of Mg, Al, Mn, and Fe to show how different yield prescriptions can substantially affect the trends in the [Mg/Mn] versus [Al/Fe] plane. I adopt different nucleosynthesis prescriptions both for the MW and for the LMC and analyse how the trends for these two galaxies change on the [Mg/Mn] versus [Al/Fe] diagram.

In Sect. 7.2, I present chemical evolution models for the MW and for the LMC. In Sect. 7.3, the observational samples used in my analysis are described. In Sect. 7.4, I show my results. Finally, in Sect. 7.5, I critically discuss my results and draw conclusions. In particular, I discuss the role of the IMF and the stellar yields on the results.

The results presented in this Chapter are published in the paper Vasini et al. (2024a).

7.1 Introduction

In a recent paper, Fernandes et al. (2023) compared the [Mg/Mn] versus [Al/Fe] relation for the stars of Gaia-Enceladus with those of several dwarf satellite galaxies of the MW, including the LMC and the SMC (Small Magellanic Cloud), in order to establish if the stars in the Galactic halo were accreted or formed in situ. The above relation, in fact, is different for different SFHs, typical of different galactic systems that could have been the building blocks of the halo.

Galaxy mergers were common in the early Universe, and in recent years remnants of merging activity of the MW have been identified in several stellar streams. Moreover, the discovery of Gaia-Enceladus (Helmi et al., 2018) has suggested that a major merger occurred roughly 10 Gyr ago (Helmi et al., 2018; Montalbán et al., 2021) in the Galactic halo. The proposed [Mg/Mn] versus [Al/Fe] relation (Hawkins et al., 2015) can in principle discriminate between different SFRs. This is due to the different production timescales of the elements involved: Mn is produced with long time delays by SNIa, which also contribute to the bulk of the Fe production, whereas massive stars (CCSN) produce Mg, Al and a small fraction of Fe. The data adopted by Fernandes et al. (2023) belong to the DR17 of the APOGEE Survey-2 (Majewski et al., 2017; Ahumada et al., 2020; Abdurro'uf et al., 2022). In the observational diagram, the stellar systems formed by means of an intense burst of SF are expected to occupy a particular region with high [Mg/Mn] at high [Al/Fe], while objects that evolved with a mild SFR, such as dwarf spheroidals, show a lower [Mg/Mn] at low [Al/Fe]. Several observational investigations have indeed revealed a significant number of kinematically identified accreted stellar populations in the MW clumps, in the same region of the above-mentioned chemical plane (i.e. Feuillet et al., 2021; Perottoni et al., 2022; Horta et al., 2023; Feltzing et al., 2023). Therefore, this diagram allows to better distinguish the stars formed in situ from those accreted than using the classical [α/Fe] versus [Fe/H] ratios, which are very similar in all systems at low metallicity ([Fe/H]), due to the dominance of the enrichment by CCSN at early times (Spitoni et al., 2016). In fact, these [α/Fe] ratios observed in dwarf spheroidal galaxies (dSphs) and ultra-faint dwarf galaxies (UfDs) can coincide with those of halo stars at extremely low metallicities, while they diverge towards higher metallicities (Das et al., 2020). The choice of the [Mg/Mn] ratio is to highlight the α-poor population better than [Mg/Fe] does, since Mn is a better tracer of SNIa. It should be noted that Spitoni et al. (2016) suggested adopting the [Ba/Fe] ratio as a discriminant of accreted stars instead of the [α/Fe] one, since Ba is mainly an s-process element produced by low-mass stars, and this ratio can be quite different in different SF environments,

especially at low metallicities. The same technique was also proposed from the observational point of view by Tolstoy et al. (2009) and references therein, where the ratio [Be/Fe] is presented in the case of four different dwarf spheroidals that show different behaviour due to the SFH of the environment under analysis.

In this Chapter, I show that the theoretical [Mg/Mn] versus [Al/Fe] relation is strongly model dependent, and I highlight how different chemical evolution models can provide different solutions, thus suggesting a cautios approach to this tool. In any case, this should be combined with dynamical information, such as eccentricity, an energy-angular momentum relation, radial action-angular momentum, and action diamond (i.e. Myeong et al., 2019; Recio-Blanco et al., 2023; Carrillo et al., 2023), before drawing firm conclusions.

Model	**Star formation efficiency [Gyr^{-1}]**	**IMF**	**Infall rate timescale [Gyr]**	**Mass loading factor [Gyr^{-1}]** ω_i
REF MW	2.0 (t<1 Gyr) 1.0 (t≥1 Gyr)	Kro93	$\tau_T = 0.7$ $\tau_D(8\ \mathrm{kpc}) = 7.0$	no wind
NEW MW	"	"	"	"
MIX MW	"	"	"	"
CL04 MW	"	"	"	"
K01 MW	"	Kro01	"	"
WIND MW	"	Kro93	"	2.5
REF LMC	0.03 (t<10.8 Gyr) 0.25 (10.8 < t/Gyr < 11.8) 0.1 (11.8 < t/Gyr < 13.2) 0.4 (13.2 < t/Gyr < 13.4) 0.35 (13.4 < t/Gyr < 13.5) 0.8 (t/Gyr > 13.5)	Sal55	$\tau = 5.0$	0.25
NEW LMC	"	"	"	"
MIX LMC	"	"	"	"

Table 7.1: *Parameters of the five MW and two LMC models tested (indicated in the first column). The following columns list, in order, the SFE (time dependent in both cases), the IMF adopted, the timescale of the infall, the wind efficiency (if included in the model) and the fraction of SNIa. In column three the short reference is reported: Kro93 for Kroupa et al. (1993), Kro91 for Kroupa (2001) and Sal55 for Salpeter (1955).*

7.2 Chemical evolution models for the MW and LMC

In this work, I consider the models of Chap. 4 and Chap. 6 (Model 3) as reference models for the MW and for the LMC, and I label them as REF MW and REF LMC models. I also introduce NEW MW and NEW LMC models where I consider additional corrective factors on the nucleosynthesis yields, while keeping the other parameters the same. In addition, I combine some reference yields with some corrected ones in the MIX MW and MIX LMC models (see Sect. 7.4.2). Moreover, I also test three additional MW models with different IMF, nucleosynthesis, and wind prescriptions.

7.2.1 The MW discs

I adopt the model of Vasini et al. (2022) (presented in Chap. 4) as a reference for studying the evolution of [Mg/Mn] versus [Al/Fe] abundance ratios in the MW disc components in the solar neighbourhood. This model is based on the chemical evolution equation (see Eq. 2.19) where the wind term is excluded. The the pollution comes from SNII, SNIb and SNIc, SNIa and novae (see Eq. 2.15). The formation of the MW is described by the two-infall law (see Eq. 2.9) where the first accretion event is assumed to occur on a timescale of τ_T = 0.7 Gyr and the second one develops on the Galactocentric distance dependent timescale presented in Eq. 2.10. It should be noted that in this paper I perform all the calculations in the solar neighbourhood (the annular area centred at 8 kpc from the Galactic centre). The SFR is the Kennicutt (1998) law presented in Eq. 2.2 where the SFE ν is set to 2 Gyr^{-1} and 1 Gyr^{-1} for the thick and thin disc phases, respectively. In Fig. 7.1, I show the SFH of the MW for the solar neighbourhood (red line) compared to the measured present day as suggested by Prantzos et al. (2018) (in the range 0.2 – 0.5 $M_\odot$ yr^{-1}, vertical orange line). In particular, I predict a present day value in the solar neighbourhood of ~ 0.3 $M_\odot$ yr^{-1}. For the IMF, I use the Kroupa et al. (1993) (Eq. 2.6), constant in time. The model accounts for the chemical contribution by SNII, SNIb, SNIc, SNIa, as well as novae. The rate for the explosions of these stars are the same as those adopted in Chap. 4.

7.2.2 The LMC

To study the chemical evolution of the LMC, I adopt the prescriptions of Model 3 presented in Vasini et al. (2023) (see Chap. 6). The evolution of the abundances in the gas is again described by Eq. 2.19 including the wind term. This accounts for the depletion of gas due to the galactic wind. The wind depends on the SFR $\psi(t)$

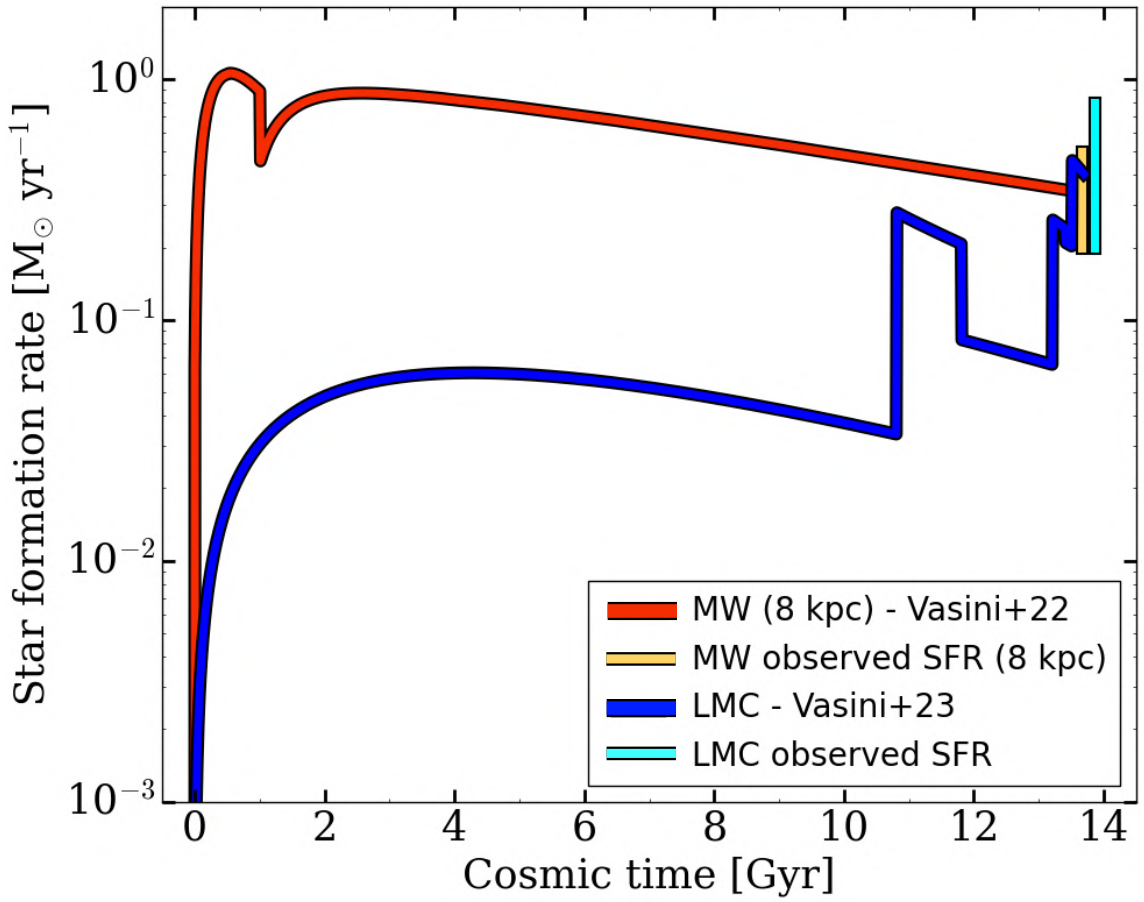

Figure 7.1: *SFHs predicted in Chaps. 4 and 6 and used in the paper. For the MW (red line), the Kennicutt (1998) law with exponent $k = 1.5$ is adopted, and the temporal evolution of the SF at the solar ring (8 kpc) is compared with the present-day observed SFR (vertical yellow line, data taken from Prantzos et al. 2018). For the LMC (blue line) I assume a linear Kennicutt (1998) law with a variable SFE to reproduce the Harris et al. (2009) SFR. I compare it with the observation at the present time by Harris et al. (2009) itself (vertical cyan line).*

through the mass loading factor ω_i, whose value is reported in Tab. 7.1.

The chemical evolution model of the LMC is a one-zone model based on the single infall law (see Eq. 2.8), a SFR with a linear Kennicutt (1998) law presented in Eq. 2.3 (k=1), and a variable SFE ν so as to reproduce the recent bursts studied by Harris et al. (2009) (that was identified as the most suitable SFR in Chap. 6). This irregular behaviour of the SFR is typical of the structures identified as dwarf irregular galaxies, as the LMC is traditionally classified. This SFH is shown in Fig. 7.1 (blue line) compared to the measurements by Harris et al. (2009) at the present time (within the interval 0.2 – 0.8 M$_\odot$ yr^{-1}, vertical cyan line). I predict a present time SFR of $\sim$ 0.4 M$_\odot$ yr^{-1}, which is compatible with the observed range.

7.2.3 Nucleosynthesis prescriptions

Prescriptions of NEW and NEW LMC models			
Element	LIMS (Karakas, 2010)	Massive stars (Kobayashi et al., 2006)	SNIa (Iwamoto et al., 1999)
Fe	✓	× 0.7	✓
Mg	✓	$Z \in (3\text{-}8)\times10^{-3} \longrightarrow \times1.2$ $Z > 8\times10^{-3} \longrightarrow \times (Z/0.004)^{0.4}$	✓
Al	$Z > 8\times10^{-3} \longrightarrow \times0.8$	×1.5	✓
Mn	✓	✓	$\times(Z/Z_{\odot})^{0.65}$ (from Cescutti et al. 2008)

Table 7.2: *Modified nucleosynthesis yields. Correction factors adopted in the NEW MW and NEW LMC models for Fe, Mg, Al, and Mn considering the same stellar sources as in Vasini et al. (2022) and Vasini et al. (2023). These same prescriptions are also used in the WIND MW model.*

Prescriptions of MIX MW and MIX LMC models			
Element	LIMS (Karakas, 2010)	Massive stars (Kobayashi et al., 2006)	SNIa (Iwamoto et al., 1999)
Fe	✓	× 0.7	✓
Mg	✓	$Z \in (3\text{-}8)\times10^{-3} \longrightarrow \times1.2$ $Z > 8\times10^{-3} \longrightarrow \times (Z/0.004)^{0.4}$	✓
Al	$Z > 8\times10^{-3} \longrightarrow \times0.8$	×1.5	✓
Mn	✓	✓	✓

Table 7.3: *Yield correction adopted in MIX MW model and MIX LMC model. In these two models, I adopt the corrections already introduced in Tab. 7.2 for Mg, Fe, and Al. Regarding Mn, I adopt the original prescriptions since, as displayed in the right panel of Fig.* **??**, *they are the best at reproducing the observed abundance ratio.*

From now on, I refer to models REF MW and REF LMC when the nucleosynthesis prescription from Vasini et al. (2022) (see Chap. 4) and Vasini et al. (2023) (see Chap. 6) have been considered, which in turn were taken from Model 15 by Romano et al. (2010). In particular, I adopt Karakas (2010) for the nucleosynthesis in AGB stars, Kobayashi et al. (2006) for massive stars, Iwamoto et al. (1999) for SNIa, and José et al. (1998) for nova systems.

On the other hand, models NEW MW and NEW LMC are based on the same yields, but with additional correction factors tailored to fit the abundance patterns of Mg, Al, and Mn in the MW, as explained in Sect. 7.4.1. I also compute a MIX MW model and a MIX LMC model with the combined prescriptions from the other models. The corrections are all listed in Tab. 7.2, where the first column indicates the element analysed, whereas the second, the third and the fourth are dedicated to LIMS, massive stars and SNIa, respectively. The corrections listed are chosen to fit the MW APOGEE DR17 data and are applied to the yields adopted (whose reference is indicated in the first row as a reminder). The only exception is the Mn case, that I correct as suggested by Cescutti et al. (2008), who introduced a metal dependency on the yields of this element. Then, in the model MW CL04 I perform a test using nucleosynthesis prescriptions identical to those employed by the chemical evolution models proposed by Andrews et al. (2017). In the same way, I perform two more tests with the K01 MW and WIND MW models, assuming the IMF and the wind prescriptions proposed by Andrews et al. (2017), respectively. These prescriptions are chosen since they are the reference ones in the paper by Fernandes et al. (2023).

7.3 Observational data

I compare my model predictions in the [Mg/Mn] versus [Al/Fe] abundance space for the MW and LMC with APOGEE DR17 data as selected by Fernandes et al. (2023). The samples discard unreliable parameters using the STARFLAG or ASPCAPFLAG=**BAD** indicators (see Holtzman et al. 2015 for definitions). Only red giant stars are considered by imposing the following conditions: stellar effective temperatures ($T_{\rm eff}$) ranging from 3750 to 5500 K and surface gravity log(g)< 3.0 dex.

The APOGEE stars of the MW are selected using orbital parameters in the integral of motion considering circular and prograde orbits: $L_z > 0$, eccentricity < 0.3, $S/N > 70$. As in Fernandes et al. (2023), I do not impose any condition on the Galactocentric distances. In fact, model predictions in the solar vicinity (see Sect. 7.2.1) should represent the average behaviour of the whole MW disc well. They consider bright and faint Red Giant Branch (RGB) stellar populations. In their Tab. 2, they summarise the LMC member selection indicating the sky position, projected distance on the sky, Gaia proper motions, radial velocities, and magnitudes. This selection mimics that proposed by Nidever et al. (2020), where Tab. 1 lists the APOGEE MC Fields.

7.4 Results

In this Section, I present model results obtained for the MW and the LMC. First, in Sect. 7.4.1, I show the plots for the single abundances ([Mg/Fe], [Al/Fe], and [Mn/Fe]) for the MW and then the trends in the [Mg/Mn] versus [Al/Fe] plane in Sect. 7.4.2. In Sect. 7.4.3 and 7.4.4, I show the abundances and the [Mg/Mn] versus [Al/Fe] trends for the LMC, respectively. Finally, in Sect. 7.4.5, I describe how I test the effects of adopting the nucleosynthesis prescriptions by Andrews et al. (2017) on the chemical evolution of the MW discs.

7.4.1 MW: [Mg/Fe], [Al/Fe], and [Mn/Fe]

In Fig. 7.2, I compare the abundances of Mg, Al, and Mn for the MW that I predict adopting the REF MW model (black lines) and the NEW MW model (white lines), with the APOGEE DR17 data. In the left panel, I note that the REF MW model underestimates Mg throughout the whole [Fe/H] range, which is a quite common feature among many sets of yields for this element (e.g. François et al., 2004; Romano et al., 2010; Prantzos et al., 2018; Lian et al., 2020). The underestimation is particularly pronounced for [Fe/H] $\gtrsim -0.5$ dex, and it becomes larger towards the solar metallicity. To fix this behaviour, I can add corrections to slightly increase the Mg production, especially at the latest stages of the MW evolution. In the middle panel, REF MW model also shows an underestimation for Al. The data show a trend that is quite high at low metallicities ([Al/Fe] ~ 0.25 dex) and then decreases as long as I go towards the solar value. Therefore, the Al yield should be increased at low [Fe/H] and then decreased. In the right panel, I present the Mn abundance. The REF MW model is quite compatible with the range of [Mn/Fe] across the [Fe/H] range spanned by the observations, although the shape of the trend is not that of the running median. In this case, the NEW MW model adopts a yield correction that was introduced by Cescutti et al. (2008) with a metallicity dependence, as shown in Tab. 7.2. This correction actually does not work as well as the original prescriptions, but it is worth also investigating the [Mg/Mn] versus [Al/Fe] plane.

Moreover, since the abundances of Mg, Mn, and Al seem to be underestimated by the models through the whole [Fe/H] range, together with the corrections to each element already explained, I choose to slightly decrease the yield of Fe from massive stars. The corrections I apply to the adopted yields are shown in Tab. 7.2. In the first column, I indicate the element analysed, in the second one I present the correction adopted for the LIMS, in the third one I give those for massive stars, and in the fourth column I list the corrections for the SNIa yield. The tick marks

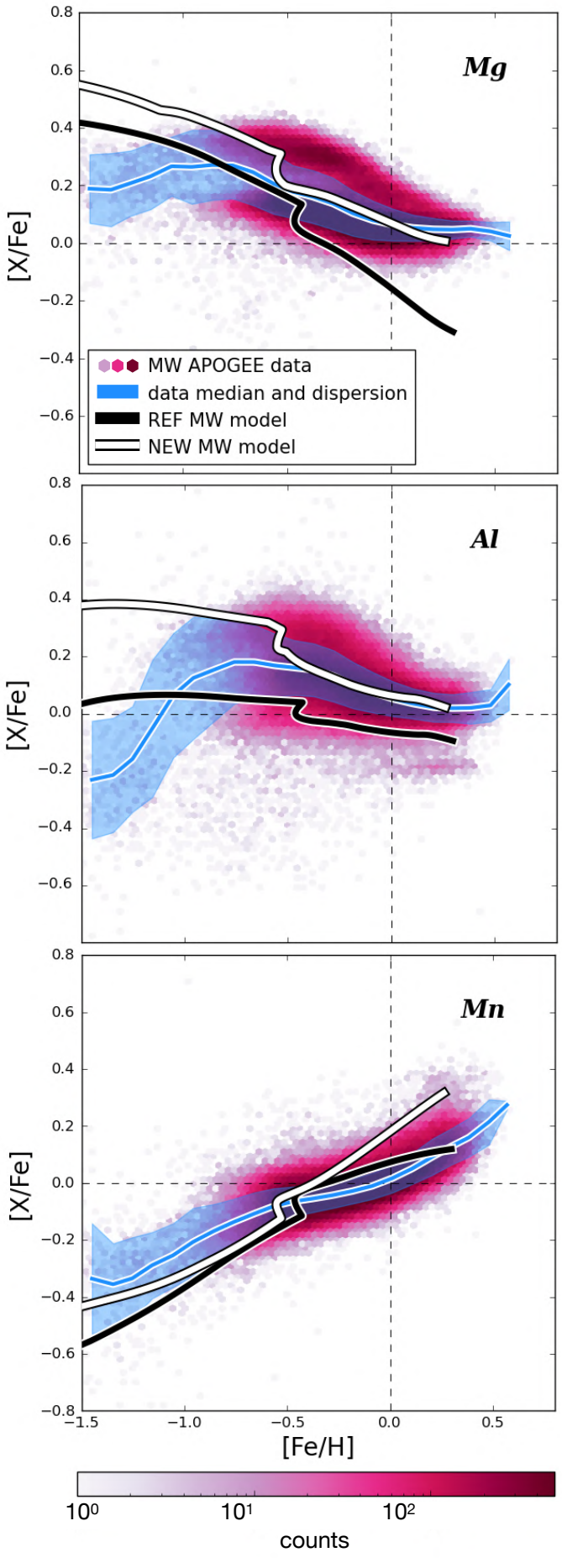

Figure 7.2: *Abundance ratios of the three elements involved. The data are from APOGEE DR17 and are binned and colour-coded according to the data density in each bin. The blue line represents the running median, computed assuming a bin size of 0.1 dex and an overlap of 0.025 dex, and the blue shaded area represents the related standard deviation. Left panel: [Mg/Fe] in the MW as predicted by REF MW model (black line) and by NEW MW model (white line) compared to APOGEE data. Middle panel: [Al/Fe] MW abundance for both models (same colour-coding as left panel). Right panel: [Mn/Fe] abundance for REF MW and NEW MW models (same colour-coding).*

represent those cases where no corrections were added.

For the MIX MW model, I assume the NEW MW model prescriptions for Mg, Al, and Fe and the REF MW model ones for Mn. I therefore highlight that I do not plot the [Mg/Fe], [Al/Fe], and [Mn/Fe] ratios predicted by the MIX MW model since they are just a combination of the other two models.

Since the MW data set is the largest available, I consider it as the benchmark of my work. I also test the corrections presented in Tab. 7.2 with the LMC model to check if they still represent an improvement also for other systems (see Sect. 7.4.3).

7.4.2 MW: [Mg/Mn] versus [Al/Fe]

In the two panels of Fig. 7.3, I show the behaviour of my models in the [Mg/Mn] versus [Al/Fe] plane compared to the APOGEE DR17 data and to the results by Fernandes et al. (2023) obtained with the prescriptions by Andrews et al. (2017). Their model is a one-zone model that assumes a Kroupa (2001) IMF, a single infall Schmidt-Kennicutt SF law according to Kennicutt (1998) (as shown in Fig. 6, lower panel of Fernandes et al. 2023), and yields from Chieffi et al. (2004) for CCSNe, Iwamoto et al. (1999) model W70 yields for SNIa, and Karakas (2010) for AGBs. All my models and the data are colour-coded according to the [Fe/H] range to show the evolution in metallicity. The data are binned so that the colour of each data point actually represents the median [Fe/H] of the data lying in that bin. The three circles mark the abundance ratios of the chemical evolution model at 0.3 Gyr, 1 Gyr, and 5 Gyr evolutionary times, respectively.

The plane is divided into three regions, according to what is usually done in the literature (see Fernandes et al. 2023 and references therein), by the horizontal and the diagonal black lines. This subdivision helps in identifying different populations of stars. The upper left sector has been interpreted as the locus of the unevolved stars, the upper right one as the location of the high-α in situ population, and the lower region as the low-α in situ population locus.

In both the panels I show the data, my REF MW model predictions (colour-coded black-edge line) and the results by Fernandes et al. (2023) (black thin line). As the REF MW model did not reproduce the trends of Mg and Al, it does not even reproduce the trend shown by the data in this plane and, in particular, it shows a large underproduction of Al at low [Fe/H], which was also evident in the [Al/Fe] versus [Fe/H] plot. On the contrary, the obtained [Fe/H] range is in good agreement with the data, meaning that my choice of applying a small-effect correction on the Fe yield is quite reasonable.

In the left panel, I also show the NEW MW model with the yields corrected as in Tab. 7.2 (colour-coded white-edge model). It is evident that this second model

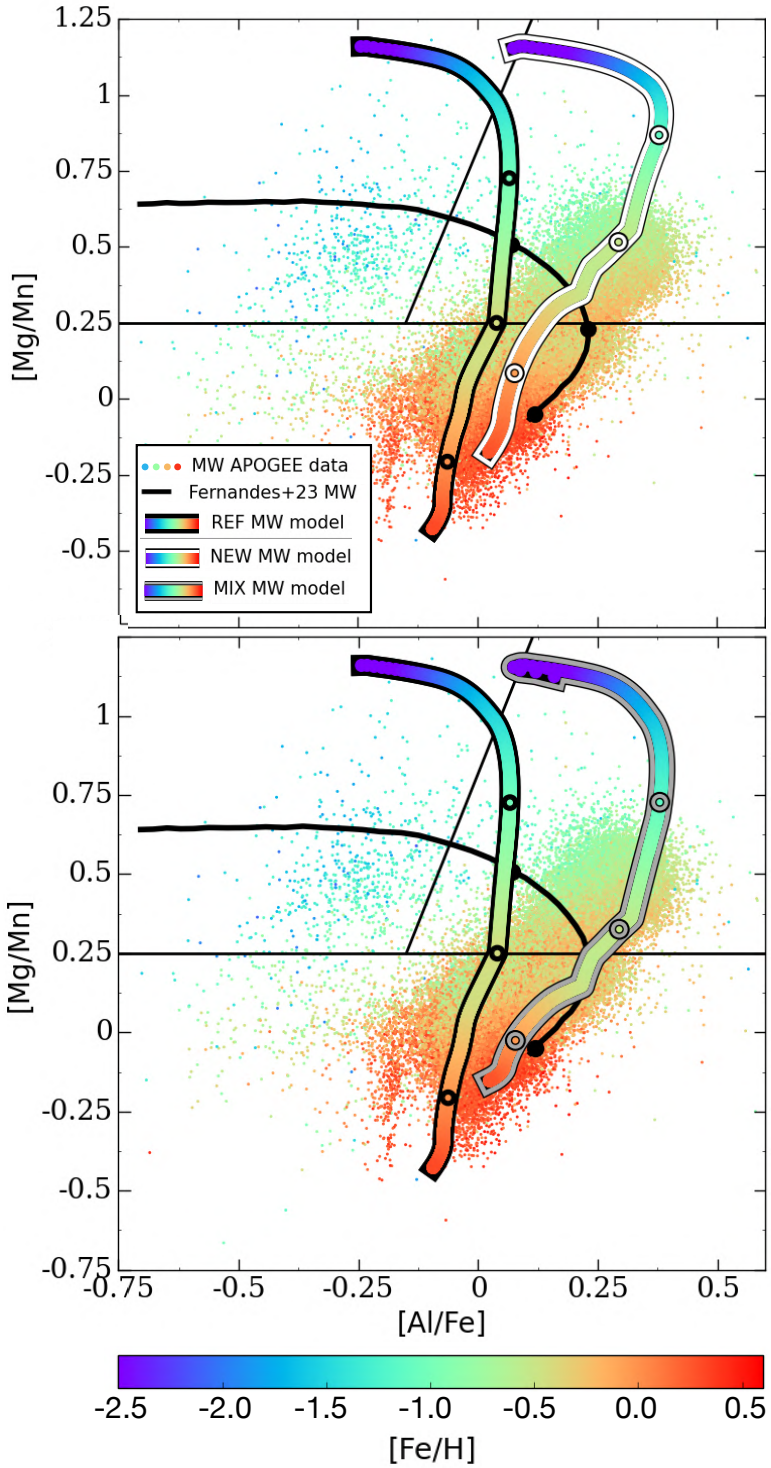

Figure 7.3: *Data compared to models (REF MW and NEW MW models in the upper panel, REF MW and MIX MW models in the lower panel) and previous results from the literature. The colour-coding shows the [Fe/H] content (see the colour bar). The data are binned so as to show the mean value of [Fe/H] in each bin. The three circles plotted on the models mark the ages 0.3 Gyr, 1 Gyr, and 5 Gyr. The horizontal and diagonal black lines separate three different plane regions as denoted by Fernandes et al. (2023); the unevolved populations lie in the upper left region, the MW high-α in situ population lies in the upper right region; and the MW low-α in situ population lies in the lower region.*

better reproduces the data, matching the [Fe/H] range at the same time. The corrections that have the larger effect on this plane are those on Al and Fe, because their global effect is increasing the [Al/Fe] abundance. The corrections on Mg and Mn yields, on the other side, are less evident in this plane because they increase the production of both Mg and Mn; hence, the effect is smoothed out when I study the ratio between them.

In the right panel I show, together with the REF MW model, the MIX MW model. As presented in Tab. 7.2 this model is the combination of the prescription of the REF MW and the NEW MW models. It adopts the corrections for Mg and Al and the original prescriptions for Mn so that I am able to reproduce all the abundances. As is evident from the right panel, I can also fit the [Mg/Mn] versus [Al/Fe] trend; therefore, I can consider this combination of yields as the best one to reproduce the MW abundance features.

7.4.3 LMC: [Mg/Fe], [Al/Fe], and [Mn/Fe]

In this Section I show the results I obtain with the LMC models regarding the abundances of Mg, Al, and Mn. For this dwarf galaxy I test the REF LMC model (black line) and the NEW LMC model (white line), which contains the same yield corrections applied to the MW. Again, I do not show the MIX LMC model since it is just a combination of the other two. I show the abundance ratio predicted compared to the observed ones in Fig. 7.4. In this case, I see that although none of the two models is able to properly reproduce the abundance patterns observed, the NEW LMC models show a slight improvement. The case of Mn is noteworthy; the corrective factor that in the MW increases the Mn predicted by the model, when applied to the LMC decreases the Mn production substantially. This is easily understood by looking at the Mn corrective factor itself listed in Tab. 7.2. Since the factor is metallicity dependent, its effect on the abundance depends on the environment.

7.4.4 LMC: [Mg/Mn] versus [Al/Fe]

In this Section, I show Fig. 7.5 with the results for the LMC in the plane [Mg/Mn] versus [Al/Fe] compared to the APOGEE DR17 data for LMC and the previous results presented by Fernandes et al. (2023). The models and the data follow the same colour-coding as in Fig. 7.3 as well as the division of the plane into three regions and the circles. In this case, the data are not binned since the data set is smaller than for the MW.

The interesting aspect of this plot is the location of the data and the model

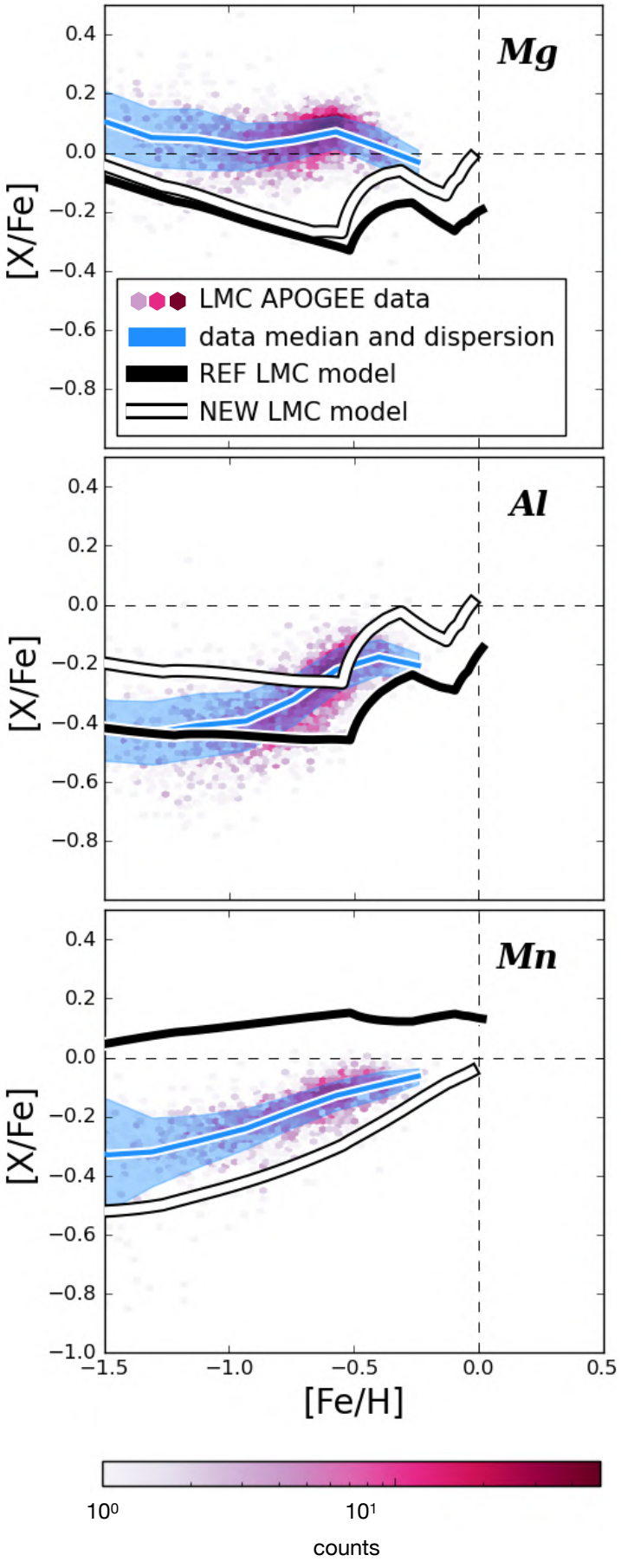

Figure 7.4: *LMC abundance ratios of Mg, Al, and Mn. The data are from APOGEE DR17 and are binned and colour-coded as in Fig. 7.2. Again, the blue line represents the running median computed with the same bin size and overlap, and the blue area is the standard deviation. The black and the white lines are the REF LMC model and the NEW LMC model, respectively.*

results on the plane. As already explained, the upper left part of the diagram is the locus of the unevolved populations, where around half of the LMC data points are located. The other half occupies the evolved region closer to the centre of the plot. In this context, the comparison between the LMC and the other nearby dwarf systems is noteworthy. As shown in Fernandes et al. (2023), the smallest satellites (e.g. Sculptor, Carina, Fornax, Draco, Sextans, and Ursa Minor), which are those with an SFR that was quenched at early times, tend to occupy the leftmost region of the plane, whereas the LMC is located more towards the centre of the diagram (with coordinates [Mg/Mn] ~ 0.25 dex and [Al/Fe] ~ -0.10 dex). This difference could be a consequence of the SFH of the LMC, which presents active SF at the present time, at variance with the other dwarf spheroidal galaxies. In my models, I adopt this kind of SFR and I am able to reproduce the observed evolution towards the centre of the plot. On the contrary, the MW has a present day SF lower than the initial peak, and this produces an opposite evolution, from the right to the left of the plot.

As in Fig. 7.3, I show two panels displaying the models adopted. In both panels I show the data compared to the REF LMC model (colour-coded black-edge line) and to the results by Fernandes et al. (2023) (thin black line) based on the LMC prescriptions by Andrews et al. (2017). It is evident that this model cannot reproduce the observations due to a too small Mg abundance and a too large Mn abundance. In the left panel, I compare these two trends with the NEW LMC model. This model does not reproduce the data either, but it represents an improvement with respect to the reference one. In particular, as shown in Fig. 7.5, the [Mg/Mn] predicted is substantially improved. In the right panel, I compare the REF LMC model to the MIX LMC model, which for the MW resulted to be the best one.

To highlight the best model among the three tested from a quantitative point of view, I compute the average [Mg/Mn] weighted on the stars formed in each time step and compare it to the average [Mg/Mn] obtained from the data. The REF MW model has an average [Mg/Mn] of ~ – 0.32 dex, for the NEW LMC model the average [Mg/Mn] is ~ 0.16 dex, and for the MIX LMC model it is ~ – 0.29. The data on the other side show an average [Mg/Mn] of ~ 0.23, which is in much better agreement with the result from the NEW LMC model.

The reason for the behaviour of the different models lies in the Mn yield. In the case of the MW, the original Mn prescription is the best one to reproduce the data, whereas for the LMC, even though none of the models overlap the running median, the new prescriptions work slightly better. Therefore, the NEW LMC model is the best one to describe the LMC.

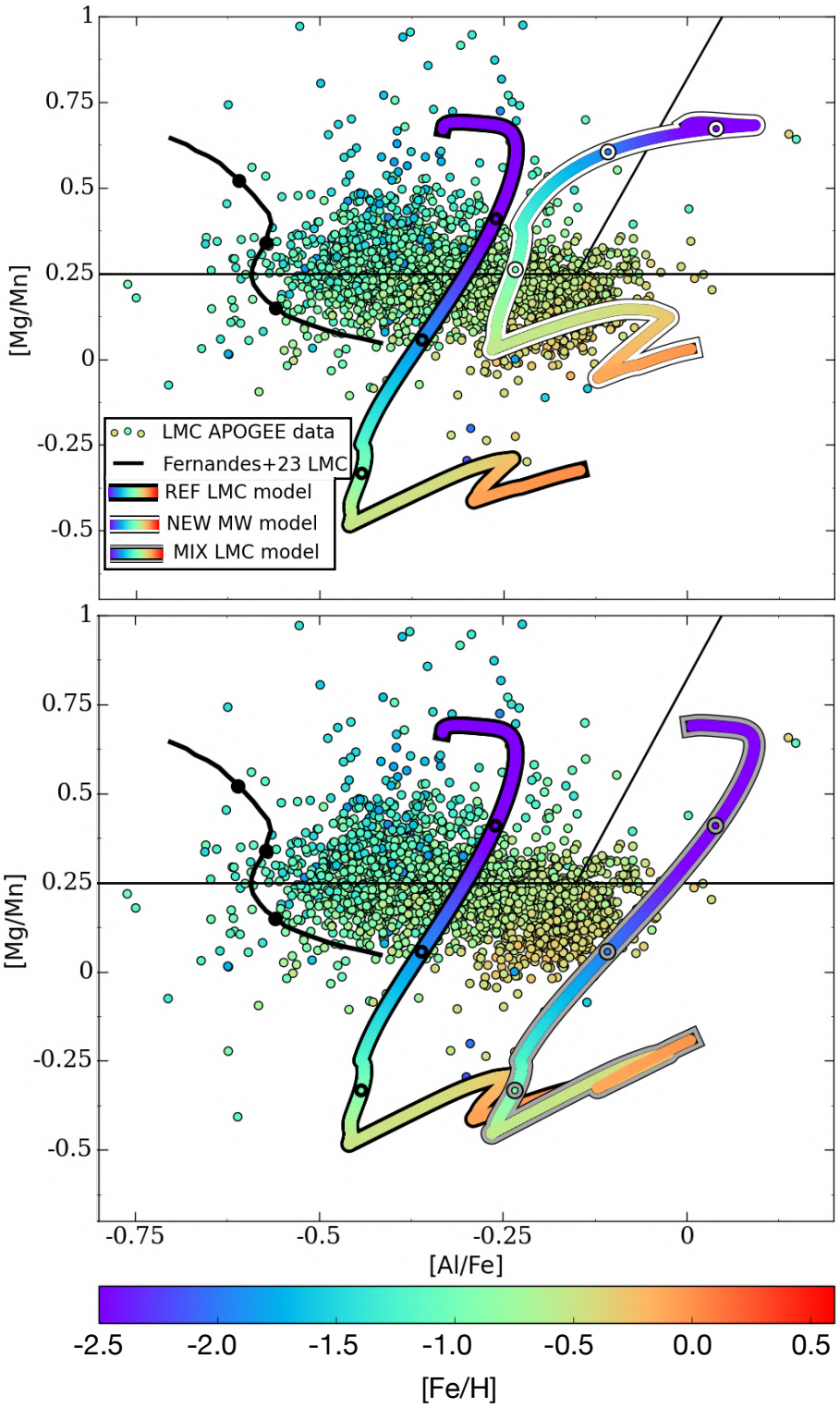

Figure 7.5: *LMC in [Mg/Mn] versus [Fe/H] plane. My models are plotted against the APOGEE DR17 data and the model from Fernandes et al. (2023). As in Fig. 7.3 the colour-coding represents the [Fe/H] content. Again, the circles on the models mark three ages, 0.3 Gyr, 1 Gyr, and 5 Gyr. Here, unlike Fig. 7.3, the data are not binned. Left panel: REF LMC model (colour-coded black-edge line) and NEW LMC (with yields corrections, colour-coded white-edge line) are compared to data and to the results of Fernandes et al. (2023). Right panel: REF LMC model (colour-coded black-edge line) and MIX LMC model (colour-coded grey-edge line) together with the data and the results of Fernandes et al. (2023).*

7.4.5 Testing different nucleosynthesis and IMF prescriptions

Fernandes et al. (2023) compared APOGEE DR17 data with the predictions obtained by the chemical evolution models of Andrews et al. (2017). Therefore, in addition to my models, I also test their nucleosynthesis prescriptions: they used the same sets of yields except for massive stars, where they adopted Chieffi et al. (2004). I test this combination of yields for the MW in order to show how sensitive the [Mg/Mn] versus [Al/Fe] plane is to the nucleosynthesis prescriptions. I label this test model as the CL04 MW model, and I show the results compared to the data and to the REF MW model in Fig. 7.6. Here, I can see that by changing only the yields for the massive stars and no other parameters, I obtain a behaviour substantially different from the reference case shown in Fig. 7.3. Since I modify the production from massive stars, the differences concern the first part of the evolution of the Galaxy due to the massive star explosion timescales. Nevertheless, it is evident that I cannot reproduce the abundance pattern or the [Fe/H] range.

The reason for this is that the nucleosynthesis of the elements considered in this plot is quite uncertain. Mg is known to be underestimated by many different sets of yields, the nucleosynthesis of Mn is quite uncertain (Mn being a Fe-peak element), and that of Al has a dependence on the metallicity that introduces a further level of complexity. Hence, the adoption of the ratios of the above elements makes it quite difficult to draw firm conclusions. By changing the yields of these elements within their uncertainties one can obtain trends on the [Mg/Mn] versus [Al/Fe] plot with different behaviours, slopes, and [Fe/H] ranges.

In principle, the combination of these elements would allow us to disentangle some properties of the galaxies analysed, such as the SFR. However, given the state-of-the-art yields available in the literature, the nuclear uncertainties prevent this plane from being a strong diagnostic for the SFH of a galaxy.

I perform a second comparison with Fernandes et al. (2023) adopting all the parameters of REF MW model except the IMF, for which I adopt the one they used, namely Kroupa (2001). I show this model in Fig. 7.6. The Kroupa (2001) IMF is a top-heavy IMF that produces more massive stars than the Kroupa et al. (1993) that I adopt in the REF MW model and that was derived for the MW. The Kroupa (2001) IMF produces a more rapid increase of the metallicity than the Kroupa et al. (1993) one, and the net result is an increase of the [Al/Fe] ratios and the range in [Fe/H], relatively to the other models, as highlighted by the colour-coding in the figure.

The reason for choosing the Kroupa et al. (1993) IMF instead of the more recent Kroupa (2001) one is that the former was specifically derived for the solar vicinity, while the latter is a sort of universal IMF. Many previous papers on the MW have

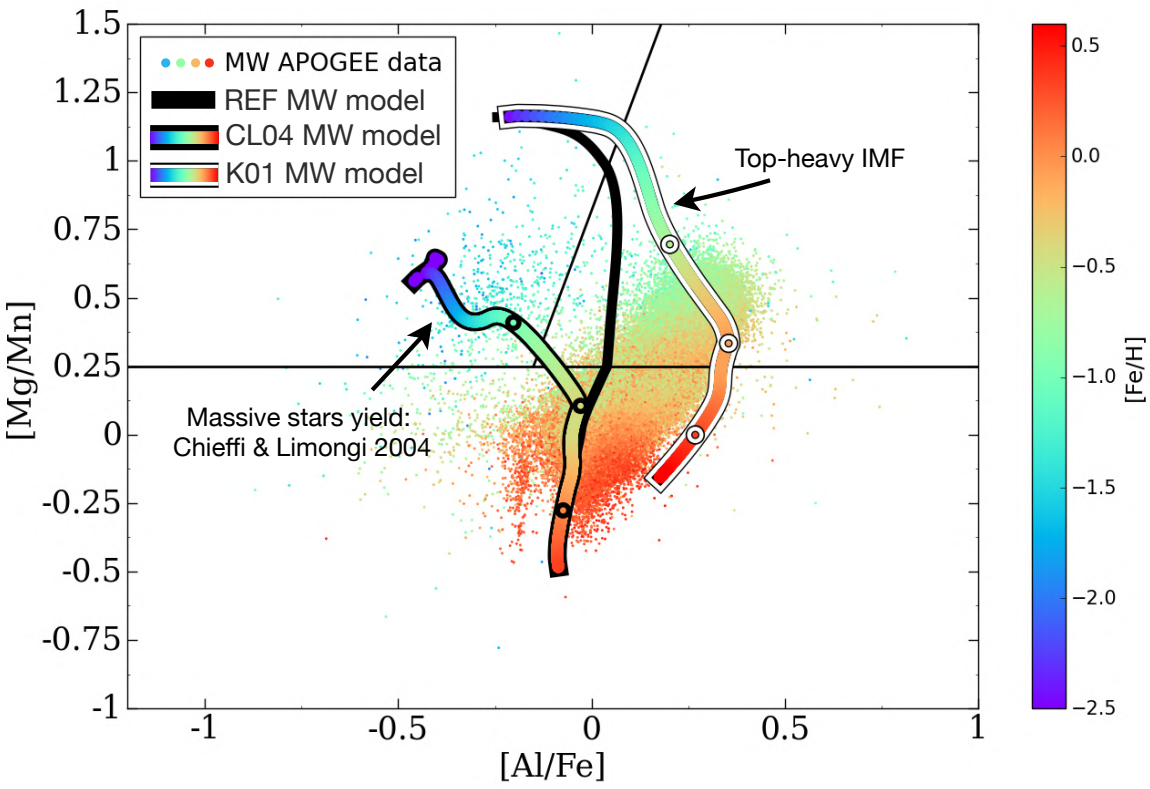

Figure 7.6: *[Mg/Mn] versus [Al/Fe] for CL04 MW model (colour-coded line, black edge) and K01 MW model (colour-coded line, white edge) compared to APOGEE DR17 data and REF MW model (black line). The colour-coding of the data, the CL04 MW model, and the K01 MW model is the same as Fig. 7.3, as are the binning of the data and the three circles plotted on the model.*

suggested the Kroupa et al. (1993) IMF as the best one to reproduce the main features of the Galactic disc (see e.g. Romano et al. 2010). For external galaxies, such as the satellites of the MW, the situation is different because no observational derivation of the IMF exists. In these cases, a Salpeter IMF is usually used, and this IMF is similar to the Kroupa (2001) one.

7.4.6 The effects of Galactic wind

Fernandes et al. (2023) compared APOGEE data with the predictions of the chemical evolution model proposed by Andrews et al. (2017), where a Galactic wind is assumed for the MW. In my REF MW and NEW MW models, I do not include any outflow since, for a potential well such as that of the MW, only Galactic fountains are allowed (Melioli et al., 2008; Melioli et al., 2009; Spitoni et al., 2008; Spitoni et al., 2009). Therefore, for comparison with the Andrews et al. (2017) model, I compute a model for the MW with Galactic wind (WIND MW model; see

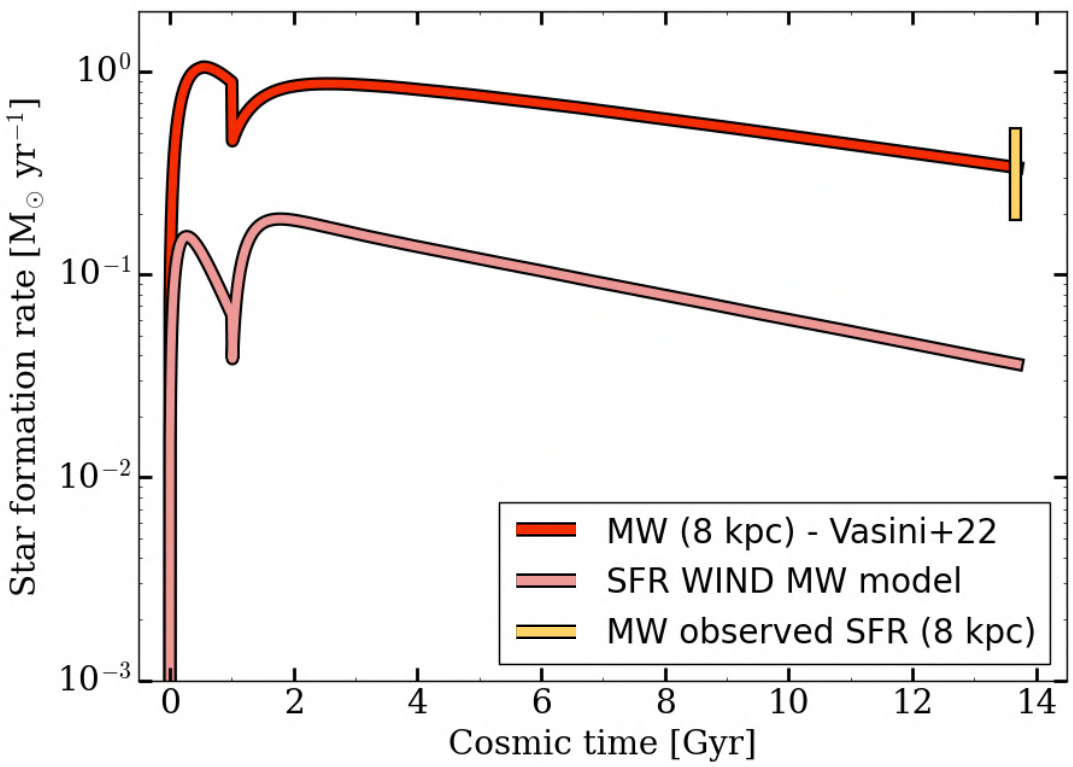

Figure 7.7: *SFHs for MW models without wind contribution (red line) and for WIND MW model (pink line) at 8 kpc from Galactic centre, compared to observed data (see reference in Fig. 7.1).*

Tab. 7.1). The introduction of the wind term into the chemical evolution equation works as a depletion term that decreases the gas available for the SF. The net effect is that of a decline in the SFR (see Fig. 7.7), with fewer stars formed and therefore a lower abundance of metals restored into the interstellar medium. The wind affects the abundances in a very clear way, since the abundance ratios of elements produced on different timescales, for example [Mg/Mn] (in the case of a wind independent of the chemical species), drop drastically, because the effect of the gas loss is immediate on the elements produced on short timescales (e.g. Mg) and therefore related to the SFR. Mathematically, the intensity of the wind depends on the mass loading factor ω_i, as shown in Sect. 7.2.2. In my case, I require it to be equal to 2.5, as was done by Andrews et al. (2017). Regarding the other prescriptions the WIND MW model follows the NEW MW model. In Fig. 7.8, I show that the WIND MW model, which is in the [Mg/Mn] versus [Al/Fe] plane, is shifted towards smaller values of both the abundance ratios. In addition, the range of [Fe/H] spanned by the WIND MW model is consistently lower than that spanned by the data, as shown by the colour-coding. In conclusion, once I add the wind to my models I am no longer able to properly reproduce the data trend or

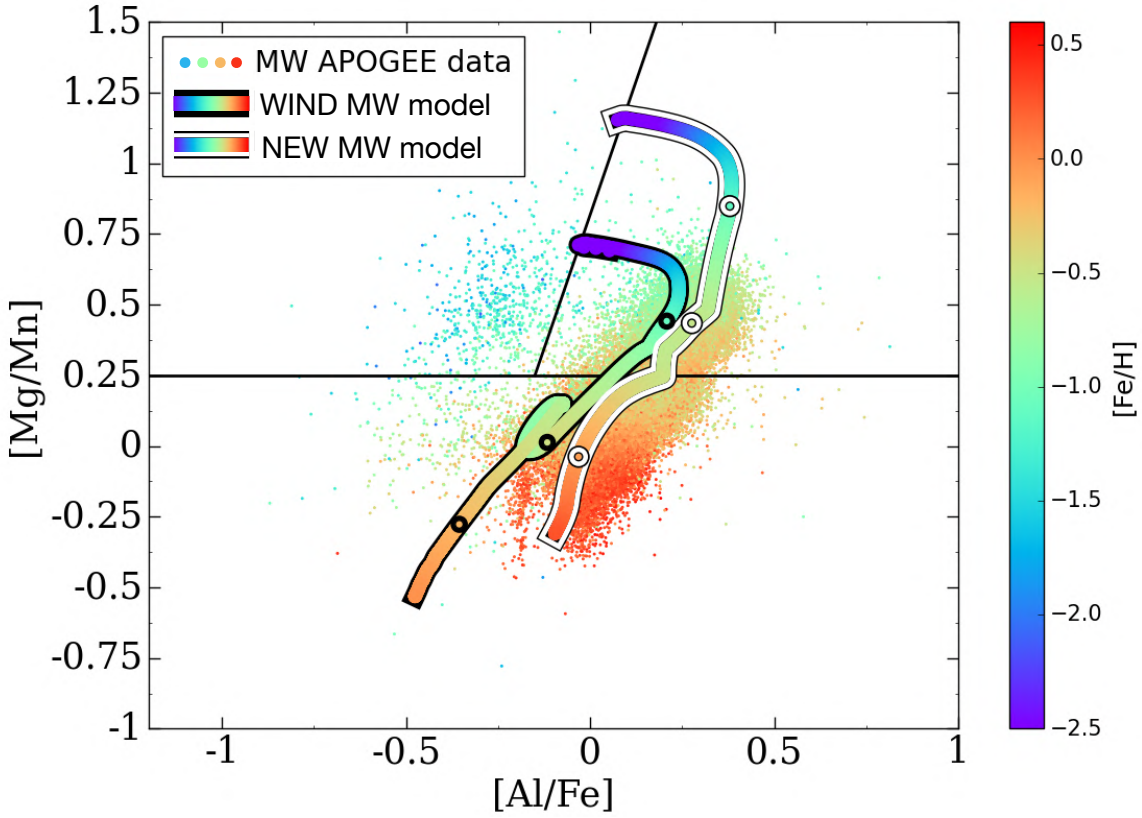

Figure 7.8: *[Mg/Mn] versus [Al/Fe] for WIND MW model (colour-coded line, black edge) and NEW MW model (colour-coded line, white edge) compared to APOGEE DR17 data. The colour-coding is the same as Fig. 7.3, as are the binning of the data and the circles plotted on the model.*

the range in [Fe/H].

7.5 Conclusions

In this work, I study the chemical evolution of the MW and of the LMC in order to understand the role of the [Mg/Mn] versus [Al/Fe] plane in unveiling the SFH of galaxies. According to the observational data, different stellar populations belonging to the same galaxy lie in different regions of the plane (as explained in Sect. 7.4.2). Hence, the galaxy pattern in this diagram is the result of the imprints left on those abundances by the SFH of that specific galaxy. In principle, this element combination is ideal for extracting information about the SFH, since they have different sites and timescales of production, but a discussion on the related uncertainties was still missing from the literature. My aim was to analyse the uncertainties, in particular those related to the nucleosynthesis of these elements.

I do that by means of three already tested models for the MW and three for the LMC, where I vary the nucleosynthesis prescriptions. I also introduce a fourth

model for the MW adopting the same yields from massive stars as in Andrews et al. (2017), with the aim of showing how the trends on the [Mg/Mn] versus [Al/Fe] plane depend on the assumed stellar nucleosynthesis.

The results that I obtain can be summarized as follows:

- To reproduce the abundance patterns of Mg, Al, and Mn in the MW as shown by APOGEE DR17 data, it is necessary to add corrective factors to the yields adopted in Vasini et al. (2022) (see Chap. 4). In particular, as shown in Tab. 7.2, I modify the massive stars contributions for Fe, Mg, and Al; the LIMS contribution for Al; and the SNIa production for Mn.

- Regarding the LMC [Mg/Mn] versus [Al/Fe] diagram, the corrected yields also improve the agreement with the APOGEE data for this galaxy. This means that, even if the corrective factors were tailored to the MW, they also work for the LMC. At the same time, the recent SFR bursts, assumed for the LMC, account for those stars found on the evolved star region.

- Changing the yields for massive stars only, as shown in Fig. 7.6, produces completely different results. By assuming different sets of yields one can obtain very different behaviours of the [Mg/Mn] versus [Al/Fe], as well as the predicted range of [Fe/H]. In the same way, also changing the IMF by adopting a top-heavy one modifies the behaviour on the [Mg/Mn] versus [Al/Fe] plane, predicting larger [Al/Fe] ratios, since the fraction of massive stars, which produce Al, is larger. In the work of Andrews et al. (2017), which computed the same diagram for the MW and satellite galaxies, the yields of CL04, the Kroupa (2001) IMF, and the presence of galactic winds in the MW are adopted. Their predicted trends marginally fit the data, and in some cases they are different from mine. In my standard model, I do not adopt the galactic winds in the MW, since it is more probable that in our Galaxy the gas produces Galactic fountains rather than winds, due to the deep potential well. However, I also compute a model including the Galactic wind with the same parameters as in Andrews et al. (2017), and the results produce a worse agreement with data than my standard model without wind.

- Unfortunately, no firm conclusions are possible on the basis of theoretical models, mainly because of the uncertainties still present in the stellar yields and the IMF in our Galaxy and its satellites, the two quantities that most influence the abundance ratios.

In conclusion, this work focused on an issue that is not only related to the

[Mg/Mn] versus [Al/Fe] plane, but also to all the other chemical elements. Many sets of stellar yields are available in the literature, but they differ from one another due to different nucleosynthesis and stellar evolution prescriptions and the presence or absence of mass loss and rotation. In addition, there are some elements whose nucleosynthesis is very poorly known, and among those elements are, indeed, Mn and Al. Therefore, it is risky to rely only on one diagram, such as that discussed in this paper. Other chemical clocks should be adopted at the same time, such as s-process elements and alpha elements relative to Fe, coupled with the kinematic properties.

8

Closing remarks

In this Thesis I investigated the chemical evolution of two SLRs, namely ^{26}Al and ^{60}Fe in the MW and in the LMC.

The analysis performed allowed me to constrain their nucleosynthesis from massive stars and from novae (see Chap. 4), to perform the first ^{60}Fe mass estimate in the MW (see Chap. 4) and to predict their expected flux from the LMC (see Chap. 6). Other related results were also obtained, such as the first 2D map of the ^{26}Al mass distribution and nova outburst distribution (see Chap. 5) and the chemical evolution confirmation of the dichotomy in the nova population (see Chap. 5). Moreover, also the [Mg/Mn] vs [Al/Fe] was investigating, highlighting its limitations in the discrimination between accreted and in-situ formed populations (see Chap. 7). However, several aspects still need an investigation and the work that I presented here contribute to opening new questions on this topic.

In this closing Chapter I present the main conclusions: in Sect. 8.1.1 I discuss the results obtained on the MW chemical evolution obtained in Chaps. 4 and 5, in Sect. 8.1.2 I present the results relative to the SLRs in the LMC obtained in Chap. 6 and in Sect. 8.1.3 the conclusions relative to the [Mg/Mn] vs [Al/Fe] plane obtained in Chap. 7 are discussed. Finally, in Sect. 8.2 I present the aspects that are worth investigating in the future, how could be implemented in the model adopted in this Thesis and how could affect the results obtained up to now.

8.1 Discussion and conclusions

8.1.1 SLRs in the Milky Way

In Chap. 4 the chemical evolution of ^{26}Al and ^{60}Fe was performed in order to clarify the nucleosynthesis, still uncertain, of these two isotopes by comparing

the theoretical results to the observations available. In the chemical evolution model adopted, the MW experiences two infall episodes that are responsible for the formation of the thick and thin discs, respectively. The SFR follows the prescriptions by Kennicutt (1989) (see Eq. 2.2) and the IMF is that suggested by Kroupa et al. (1993) (Eq. 2.6). By the means of these two parameters it is possible to reproduce the main present day Galactic observational constraints, such as the SN rate, the nova rate, the surface gas mass density, and the α-element abundance patterns.

Regarding ^{26}Al, the most important open question concerns its production in nova systems. The observations of ^{26}Al performed by the two γ-ray satellites COMPTEL and INTEGRAL agreed on the ^{26}Al mass located within 5 kpc from the Galactic centre. The nominal ^{26}Al mass value provided is around 2 $M_{\odot}$ which, however, does not give enough information nor to confirm neither to discard the novae as ^{26}Al producers.

Chemical evolution can, in principle, solve the nova issue but the only chemical evolution work on ^{26}Al that can be found in the literature (Timmes et al., 1995) did not include novae and therefore no conclusions on their ^{26}Al production could be drawn.

Therefore, I aim at providing the first theoretical estimate of the ^{26}Al mass in the MW by the means of a chemical evolution model that includes SNII, SNIb, SNIc, SNIa and novae. In this framework, the nucleosynthesis is explored by testing several stellar yields presented in the literature, both for massive stars and for nova systems. The purpose is finding the combination of yields that could better reproduce the 2 $M_{\odot}$ of ^{26}Al observed. Four different yields for massive stars are tested together with four different nova yields, for a total of sixteen different nucleosynthesis models.

After the comparison with the observations it is possible to conclude that:

- the best estimate of the ^{26}Al mass is provided by adopting the yields from Woosley et al. (1995) (including all the sets provided, each of them depending on the initial stellar metallicity) for massive stars and from José et al. (2007) for novae. These yields provide 2.12 $M_{\odot}$ of ^{26}Al within 5 kpc from the Galactic centre. This means that in following works these nucleosynthesis prescriptions can be adopted as the most reliable ones to study the abundance of this isotope both in the MW and in other galaxies;

- according to my model, the production from novae is necessary to reproduce the observations of ^{26}Al. Without the nova contribution the theoretical results provided by my model underestimate the ^{26}Al mass in the Galaxy.

- the reason why Timmes et al. (1995) could reproduce the ^{26}Al mass in the Galaxy without including the novae lies in the yields for massive stars adopted. Timmes et al. (1995) in fact, adopted the yields by Woosley et al. (1995) for massive stars. However, only the set computed with progenitors of initial metallicity equal to the solar value ($Z_{\odot}$=0.02) was included. With the choice of a metallicity independent production, without the novae, they reproduced the 2 $M_{\odot}$ observed. Woosley et al. (1995) actually proposed not only the set at solar metallicity but also several sets computed at lower initial metallicities, that give indications on the production of ^{26}Al by the previous stellar generations. When the whole range of metallicity is included, the final amount of ^{26}Al mass is lowered because, since ^{26}Al is a secondary element, its production decreases when the metallicity of the progenitor decreases. In this case, massive stars alone cannot explain any more the ^{26}Al mass, and the contribution from novae becomes necessary. My results suggest that Woosley et al. (1995) is the best set of yields for massive stars but only if the dependency on the initial metallicity of the progenitors is included.

In Chap. 5 I revise the results related to ^{26}Al obtained in Chap. 4 by the means of a 2D chemical evolution model. The decay of ^{26}Al occurs on a shorter timescales with respect to the mixing of the newly ejected gas with the pre-existing one. Hence, the assumption of homogeneous mixing usually adopted in a 1D chemical evolution model does not hold any more and should be relaxed to properly analyse the distribution of ^{26}Al in the MW, which is expected to be concentrated in the peaks of the SF. However, it is necessary to remind that my results are always compared to integrated observations, therefore in principle a 1D chemical evolution model is anyway a valid option.

The immediate purpose in adopting a 2D chemical evolution model is mainly that of understanding if the introduction of a second dimension, namely the azimuth, influences the ^{26}Al integrated mass value. Nevertheless, it is also worth noticing that the implementation of a second dimension opens to several future perspectives that could exploit the full potential of the information provided by COMPTEL and INTEGRAL. This aspect will be later discussed in Sect. 8.2.

By adopting the 2D chemical evolution model without changing any other prescription I can draw the following conclusions:

- the implementation of the azimuthal dimension influences the total amount of ^{26}Al that I predict in the MW. In fact, in the 1D case my best model is predicting 2.12 $M_{\odot}$ of ^{26}Al, whereas with the same prescriptions the 2D model predicts 1.03 $M_{\odot}$. The reason is related to the fact that the proportionality

between the surface gas mass density and the SFR is not linear (see Eq. 2.2), and therefore, since I reshape the surface gas mass density distribution to simulate the second dimension, the SFR changes in a non linear way, and so all the chemical abundances do;

- the novae turn out to be even more important that they were in the 1D case. In fact, when the 1D model showed that they were necessary to reproduce the observations, in the 2D model not even with their contribution the ^{26}Al mass can be reproduced. However, the observations of novae in the Galactic bulge suggest an enhancement in their nucleosynthesis relative to the disc novae up to a factor of ten, because of their smaller WD progenitors (Della Valle et al., 2020). By including this enhancement in the bulge novae, I am able to reproduce the observations. Therefore, by the means of the 2D model I am able to confirm also from the chemical evolution point of view the presence of two different nova population in the MW.

- the contribution from novae worsen the capability of ^{26}Al to trace the SFR. At the present time, for a fixed Galactocentric distance I compare the ^{26}Al maxima relative to the ^{26}Al minima. In the case without the novae contribution the maxima are $\sim$ 150% larger than the minima, whereas when including novae the maxima are only $\sim$ 28% larger. This is due to the distribution of the novae that is almost homogeneous and azimuth independent. For this reason, I suggest that a better SFR tracer is ^{60}Fe, which is produced only by massive stars;

- by the means of my 2D chemical evolution model I provide the first 2D maps of the nova outbursts distribution and of the ^{26}Al mass in the MW. This aspect is particularly important for the future prospects related to this topic, that will be discussed later in Sect. 8.2.

Regarding ^{60}Fe, there is general agreement on its production site, namely massive stars. Nevertheless, the best set of yields among those proposed in the literature, as was for ^{26}Al, had not been identified yet. In principle, the same procedure that is adopted to select the best nucleosynthesis prescriptions for ^{26}Al can be applied also to ^{60}Fe. However, the observations did not provide any constraint on the mass of ^{60}Fe in the MW, and only an indirect rough estimate is available. According to that, the ^{60}Fe mass within 5 kpc from the Galactic centre should be in the range 0.8 $M_{\odot}$ - 1.9 $M_{\odot}$.

For ^{60}Fe I test five different sets of yields for massive stars. From my results I

can conclude that:

- the only set of yields that predicts a ^{60}Fe mass value compatible with the observations is the set by Limongi et al. (2006) (in the version with Schwarzschild convection criterion). Adopting these prescriptions I obtain 1.05 $M_{\odot}$ of ^{60}Fe within 5 kpc from the Galactic centre;

- after the publication of this result, the observations of ^{60}Fe were revised obtaining a larger uncertainty but adopting a more reliable technique. According to this re-evaluation the ^{60}Fe mass should be in the range 1 $M_{\odot}$ - 6 $M_{\odot}$ (Siegert et al., 2023), which reinforces my first theoretical estimate of 1.05 $M_{\odot}$.

8.1.2 SLRs in the Large Magellanic Cloud

In Chap. 6 I compute the chemical evolution of ^{26}Al and ^{60}Fe in the LMC. I adopt the same 1D chemical evolution model as that in Chap. 4 but with different parameters, suitable to reproduce the LMC features.

The satellite INTEGRAL, that has provided ^{26}Al flux and ^{60}Fe flux observations since 2002, will be decommissioned at the end of 2024. In view of this, a new γ-ray instrument, COSI, is in its developing phase and its launch is scheduled for 2027. The improved sensitivity of the satellite relative to the previous ones could allow COSI to observe beyond the MW borders, hopefully as far as the LMC. However, no theoretical estimates of the expected ^{26}Al and ^{60}Fe flux from the LMC have been computed yet, hence it is not possible to know if the LMC lies within the detection limits of COSI.

The main purpose in this work is that of providing the first estimate of the ^{26}Al and ^{60}Fe masses and fluxes in the LMC and verify their compatibility with the detection limits of COSI. To do that I start from the best set of yields for massive stars and novae that I constrained in Chap. 4 and test four different SFRs and IMFs, all reported in the literature. By comparing the results of these four models with several present day observational quantities, such as SN rates, nova rate, gas mass, stellar mass and α-element abundance patterns, I identify the best combination of SFR + IMF. Assuming that, I compute the ^{26}Al and ^{60}Fe masses and fluxes in the LMC and conclude that:

- the best SFR + IMF combination to reproduce the present day features of the LMC is that obtained by combining the SFR by Harris et al. (2009), that shows a present day burst, and the IMF by Salpeter (1955). Adopting these assumptions I am able to reproduce the present time SFR, SN rate, nova rate,

gas mass, metallicity and the abundance patterns of O, Mg, Si and Ca;

- by adopting the Harris et al. (2009) SFR I predict $\sim 0.44\ M_{\odot}$ of ^{60}Fe and $\sim 0.33\ M_{\odot}$ of ^{26}Al. This result is in contrast with what I find in the MW, where I obtain more ^{26}Al than ^{60}Fe. This can be explained considering that for the MW the IMF adopted is the Kroupa et al. (1993) one, which produces less massive stars than the Salpeter (1955) adopted for the LMC. Since the more massive a star is, the more ^{60}Fe it produces, in the LMC ^{60}Fe results to be higher than ^{26}Al. It is important to highlight that even though the prescription adopted are affected by uncertainties these cannot be the cause of the discrepancy between LMC and MW since I adopt the same chemical evolution model and the same yields in the two cases. This can be interpreted as an evidence to prefer a Salpeter-like IMF when modelling the LMC;

- according to my best model, the contribution to ^{26}Al coming from nova systems should not exceed 1/3 of the total abundance. This percentage is much lower than what obtained in Chap. 4 for the MW, where it is ~95% of the total ^{26}Al abundance. Again, this is mainly due to the larger fraction of massive stars in the Salpeter (1955) IMF relative to the Kroupa et al. (1993) one. Moreover, the Harris et al. (2009) SFR adopted for the LMC is very low in the first part of its history with a recent burst still active. Since novae are a delayed source the bulk of them, whose progenitors were formed during this recent burst, has not started to pollute the ISM yet. On the contrary, the MW has a SFR peak in the first part of its evolution, hence the novae have been contributing since several billion years ago;

- from the ^{26}Al and ^{60}Fe masses I compute the fluxes expected from the LMC, knowing its distance. I obtaine a ^{26}Al flux of $1.56 \times 10^{-6}\,\mathrm{ph\,cm^{-2}\,s^{-1}}$ that given the estimated sensitivity of the upcoming COSI mission in 2027, is within reach. On the other side, the mass of ^{60}Fe produces a flux of $0.25 \times 10^{-6}\,\mathrm{ph\,cm^{-2}\,s^{-1}}$ that is probably too faint to be detectable from the LMC, even with improved instrumentation.

8.1.3 The [Mg/Mn] versus [Al/Fe] plane

In Chap. 7 I analyse a newly proposed chemical diagnostic which involves four stable isotopes: ^{24}Mg, ^{55}Mn, ^{27}Al and ^{56}Fe. The combination of this four chemical species, specifically the ratio [Mg/Mn] versus [Al/Fe], was pointed out as particularly sensitive to the SFH of the host galaxy. The reason is related to their

production timescales: ^{24}Mg is a primary element produced on short timescales by SNII, ^{27}Al is still produced by SNII but it is a secondary element, ^{55}Mn is purely produced by SNIa on long timescales and ^{56}Fe is produced for 1/3 by SNII and for 2/3 by SNIa. By comparing their ratio it should be possible to disentangle the accreted stellar populations to the *in-situ* formed ones, therefore in the last decade it has been used with this purpose. However, a complete analysis of the uncertainties affecting the [Mg/Mn] versus [Al/Fe] plane is still missing, hence it is not clear which is the error affecting the conclusion drawn adopting this diagnostic.

In Chap. 7 I aim at studying the uncertainties behind the [Mg/Mn] versus [Al/Fe] plane in order to identify its limitations and clarify the limits within which this diagnostic is reliable. I explore the uncertainties related to the choice of the yields, the IMF and the wind prescriptions both for the MW and the LMC. The other prescriptions are the same adopted in Chap. 4 and Chap. 6 for the MW and LMC respectively.

I study the abundance of ^{24}Mg, ^{27}Al, and ^{55}Mn separately in order to identify the issues related to every single element, and after that I analyse their combination. By comparing the different models to the APOGEE-2 DR17 data I concluded that:

- the yields adopted in Chap. 4 have to be revised in order to reproduce the abundance patterns of ^{24}Mg, ^{27}Al, and ^{55}Mn both in the MW and in the LMC. It is worth noticing that I add corrective factors tailored on the MW abundance patterns but when testing them on the LMC abundance patterns they produce an improvement in the fitting as well. This points towards the universality of the yields since they are expected to be independent of the galactic environment;

- by completely substituting the yields for massive stars adopted, the results change completely. The same conclusion is obtained by changing the IMF with a top-heavier one as well as by adding a Galactic outflow (as suggested by Andrews et al. (2017)). The meaning behind these tests and their results is related to quantify the intrinsic uncertainties in the [Mg/Mn] vs [Al/Fe] plane. The tests performed on the yields and the IMF are made by changing these parameters within the uncertainties that still affect them. For a diagram to be a good chemical diagnostic means being sensitive only to one parameter, that in this case is claimed to be the SFR. But if this same diagram is very sensitive also to other parameters, such as the yields and the IMF, then its reliability decreases;

- the uncertainties affecting the stellar yields are still too large to make this chemical combination suitable for the identification of accreted populations. The reliability of this diagnostic can be improved by coupling it with other chemical clocks, such as the s-process and α-element abundance patterns and the kinematic properties.

8.2 Future perspectives

The work that has been presented in this Thesis answers some of the open questions related to unstable and stable isotopes. Nevertheless, the aspects which need deeper examination are numerous and the analysis presented here itself opens to future investigations.

The nucleosynthesis of ^{26}Al, for example, is still far from being fully understood. First of all, the nova yields that are tested do not represent the totality of the nova models computed up to now. More recent yields have been proposed, such as Deibel et al. (2007), M. B. Bennett et al. (2014), Bardayan (2021), and Starrfield et al. (2023), and additional tests including them should be performed, in order to reinforce or update the conclusions I present above.

Another important aspect related to novae systems is the dependency on the metallicity. In my model the novae are implemented assuming that a fraction of the binary systems that can form SNIa actually evolves to become novae. This fraction is constant over the whole evolution of the galaxy and is fine-tuned to reproduce the current observed nova rate. Moreover, the WD from which the nova originates can have different progenitors (producing a carbon-oxygen or an oxygen-neon nova), but my model does not differentiate them. Nevertheless, since the nova yields are computed for the two types of WDs, I account for this aspect by assuming that the 70% of the nova population is formed by CO novae and the rest is composed of ONe novae (as done in Romano et al. 2010). Under this assumption I adopt a single value for the nova yield which is the weighted average of the CO nova and ONe nova yields. The delay of the explosion with respect to the formation of the system is obtained considering the time needed to form a WD plus an additional delay of 1 Gyr to cool the system down.

To properly simulate the nova population, several additional aspects should be included, among which the metallicity dependence is one of the most important. The metallicity in fact, influences the evolutionary path of the WD progenitor which necessarily alters the behaviour of the resulting nova, in particular the

delay of the explosion with respect to the formation of the progenitor. Kemp et al. (2022) proposed a detailed study of how the metallicity affects the nova population, differentiating both between the accretor types (CO WD or ONe WD) and among the donor types (low mass main sequence stars, main sequence stars, Hertzsprung gap, first giant branch, core He burning, early AGB or thermally pulsing AGBs). The general conclusion is that at lower metallicities ($Z = 0.0001$) the nova formation rate is consistently larger (the double) than it is at higher metallicities ($Z = 0.03$). In my model I do not consider such effect, but it can be easily introduced by varying in time the fraction of binary systems that can evolve as novae. However, even though the introduction of this time-dependence would produce a more realistic scenario, I do not expect large differences in the present day ^{26}Al mass. In fact, the largest variations are expected at low metallicities, but the ^{26}Al produced by those novae has already almost completely decayed. Another interesting result by Kemp et al. (2022) is the ratio between CO novae and ONe novae in different Galactic environments, such as thin and thick discs, bulge and halo. Even though in my model the ratio CO/ONe novae is fixed to 7:3 everywhere and at every time, in reality it depends on the SFH that the region in exam experienced. A region whose SF peaked several billion years ago hosts only very low mass stars, that can now host only CO novae. On the contrary, in regions where the SF is still active also a non negligible fraction of ONe is found. Kemp et al. (2022) computed these ratios and found that in the thin disc and in the bulge the ONe novae are the 66% and the 61% of the total respectively, whereas in the thick disc and in the halo they represent only the 32% and 16% of the nova population respectively. The ratio CO/ONe novae is computed by Kemp et al. (2022) for two different metallicities ($Z = 0.03$ and $Z = 0.0001$) for 15 Gyrs with a resolution of 500 Myr. These values can be implemented in the chemical evolution code used in the previous Chapters so that the ^{26}Al yield adopted follows the evolution of the CO/ONe nova ratio. However, as it is for the fraction of binary systems, by including the CO/ONe nova ratio temporal evolution I do not expect any large variation in the present day result because the ratio that I adopt (7:3) is very close to the one suggested by Kemp et al. (2022) (6.6:3.4) for the thin disc now.

Another point that has not been taken into account in the previous Chapters is the influence of the binary systems. Recently, the three papers by Brinkman et al. (2019), Brinkman et al. (2021), and Brinkman et al. (2023) explored the effects on the ^{26}Al mass ejection of non-rotating binary systems and rotating single stars. Even though the main focus is the nucleosynthesis occurring in these systems, they anyway make considerations on the impact that such nucleosynthesis could have on a Galactic chemical evolution model. Their first order approximation

conclusions are that the enhancement in the ^{26}Al ejected mass due to the binary systems should not exceed the 5%-10% and that the rotation of single stars also has minimal effects on the ^{26}Al yields that are noticeable only around the WR limit.

Nevertheless, these conclusions are based on several assumptions that affects the results by far. The chemical evolution model adopted and presented in this Thesis could represent the perfect tool to explore the effects of binaries and rotation on the present mass of ^{26}Al in the Galaxy. Moreover, by including the yields presented in Brinkman et al. (2019), Brinkman et al. (2021), and Brinkman et al. (2023) I would be able to constrain even more the role played by other ^{26}Al producers, such as the largely discussed novae.

Regarding the massive stars nucleosynthesis, another aspect that is worth the investigation is the possible contribution by the stellar winds experienced by the so called *Very Massive Stars* (VMSs), with initial masses > 100 $M_{\odot}$, shown by Higgins et al. (2023). Their nucleosynthesis has been computed by adopting an enhanced mass-loss rate, suggested by the optically thick winds observed in these stars. This wind prescription enhances of a factor of 10-100 the ^{26}Al production relative to the standard O stars or evolved WR. However, such a high production from a single VMS does not necessarily imply a large contribution to the present ^{26}Al mass over the whole Galactic scale. The reason is simply that such massive stars are extremely rare, therefore their net contribution could be comparable to that of less massive but more numerous stars. For this reason Higgins et al. (2023) also estimated the IMF-weighted contribution of VMSs and, by adopting a Salpeter (1955) IMF, they confirmed that a VMS can contribute up to 10 times more than a 50 $M_{\odot}$.

This VMS population can in principle be introduced in the chemical evolution model presented in this Thesis, especially after the observations reported by Crowther et al. (2010), that confirmed the presence of a few stars in the globular clusters 30 Doradus and NGC 3603 (in the LMC and the MW, respectively) exceeding the 150 $M_{\odot}$. Anyway, the results by Higgins et al. (2023) cannot be incorporated into my model straightforwardly, and some points should be clarified. The first issue is related to the assumptions on the IMF. Higgins et al. (2023), when IMF-weighting the VMSs contribution, adopted a Salpeter (1955) which is top-heavier than the Kroupa et al. (1993) that I adopted for the MW. Therefore, I expect a lower contribution from VMSs to the ^{26}Al mass in the MW relative to the factor of 10 that Higgins et al. (2023) suggested. It is noticeable, however, that this is not true for the LMC, where I adopted a Salpeter (1955) IMF as well and therefore no differences with Higgins et al. (2023) are expected. More important than these considerations is the fact that neither the Salpeter (1955) IMF nor the

Kroupa et al. (1993) IMF are defined beyond 100 $M_\odot$, therefore the yield weighting that Higgins et al. (2023) performed is carried out extrapolating the IMF for a wider mass range and without making any whatsoever consideration concerning that. A more correct treatment could be performed assuming an IMF that was defined for masses over 100 $M_\odot$, such as the Schneider et al. (2006) for Pop III stars. Nonetheless, the Pop III IMFs are valid up to a critical metallicity, which represents the transition from a Pop III dominated epoch to a Pop II/I dominated one. The Schneider et al. (2006) IMF, for example, is defined for $Z < Z_{\rm cr} = 10^{-5\pm1}\, Z_\odot$, which can be reached in some cases by a single Pop III star dying. The stars observed by Crowther et al. (2010) belong to a much metal richer environment, therefore a suitable IMF should be considered.

In conclusion, VMSs can be included among the ^{26}Al producers in the chemical evolution model presented here provided that an appropriate IMF is adopted. Alternatively, if a regular IMF is chosen, some considerations regarding how to correct for the effects related to the mass and the metallicity should be made. What is expected however, is that the contribution of these stars should be minor given that the number of stars which have been observed to be that massive is very small, therefore the integrated contribution over the VMS population is almost negligible.

Bibliography

Abdurro'uf et al. (Apr. 2022). "The Seventeenth Data Release of the Sloan Digital Sky Surveys: Complete Release of MaNGA, MaStar, and APOGEE-2 Data". In: 259.2, 35, p. 35. DOI: 10.3847/1538-4365/ac4414. arXiv: 2112.02026 [astro-ph.GA].

Ahumada, Romina et al. (July 2020). "The 16th Data Release of the Sloan Digital Sky Surveys: First Release from the APOGEE-2 Southern Survey and Full Release of eBOSS Spectra". In: 249.1, 3, p. 3. DOI: 10.3847/1538-4365/ab929e. arXiv: 1912.02905 [astro-ph.GA].

Andrews, Brett H. et al. (Feb. 2017). "Inflow, Outflow, Yields, and Stellar Population Mixing in Chemical Evolution Models". In: 835.2, 224, p. 224. DOI: 10.3847/1538-4357/835/2/224. arXiv: 1604.08613 [astro-ph.GA].

Arcones, Almudena and Friedrich-Karl Thielemann (Dec. 2023). "Origin of the elements". In: 31.1, 1, p. 1. DOI: 10.1007/s00159-022-00146-x.

Arnett, W. David (Sept. 1969). "Explosive Nucleosynthesis in Stars". In: 157, p. 1369. DOI: 10.1086/150157.

Arnould, M., S. Goriely, and A. Jorissen (July 1999). "Non-explosive hydrogen and helium burnings: abundance predictions from the NACRE reaction rate compilation". In: 347, pp. 572–582. DOI: 10.48550/arXiv.astro-ph/9904407. arXiv: astro-ph/9904407 [astro-ph].

Arnould, M., W. Hillebrandt, and F. K. Thielemann (Jan. 1979). "Al-26 production in explosive burning of hydrogen-helium layers". In: *Liege International Astrophysical Colloquia*. Ed. by A. Boury, N. Grevesse, and L. Remy-Battiau. Vol. 22. Liege International Astrophysical Colloquia, pp. 71–76.

Arnould, M. et al. (May 1980). "Synthesis of Al-26 in explosive hydrogen burning". In: 237, pp. 931–950. DOI: 10.1086/157940.

Asa'd, Randa et al. (Apr. 2022). "Detailed Chemical Abundances of Star Clusters in the Large Magellanic Cloud". In: 929.2, 174, p. 174. DOI: 10.3847/1538-4357/ac5f3e. arXiv: 2203.11868 [astro-ph.GA].

Asplund, Martin et al. (Sept. 2009). "The Chemical Composition of the Sun". In: 47.1, pp. 481–522. DOI: 10.1146/annurev.astro.46.060407.145222. arXiv: 0909.0948 [astro-ph.SR].

Banerjee, Projjwal et al. (June 2018). "Effective stellar β -decay rates of nuclei with long-lived isomers: ^{26}Al and ^{34}Cl". In: 97.6, 065807, p. 065807. DOI: 10.1103/PhysRevC.97.065807. arXiv: 1804.05657 [astro-ph.HE].

Barbuy, Beatriz, Cristina Chiappini, and Ortwin Gerhard (Sept. 2018). "Chemodynamical History of the Galactic Bulge". In: 56, pp. 223–276. DOI: 10.1146/annurev-astro-081817-051826. arXiv: 1805.01142 [astro-ph.GA].

Bardayan, Dan (Jan. 2021). "Reanalysis of ^{28}Si(p,t)^{26}Si data to constrain nova ^{26}Al production". In: *APS Division of Nuclear Physics Meeting Abstracts*. Vol. 2021. APS Meeting Abstracts, ED.009, ED.009.

Bennett, K. et al. (Dec. 1993). "COMPTEL Observations of AGN". In: *American Astronomical Society Meeting Abstracts*. Vol. 183. American Astronomical Society Meeting Abstracts, 64.07, p. 64.07.

Bennett, M. B. et al. (Jan. 2014). "Measurement of the Beta Decay of 26P to Determine Classical Nova 26Al Production in the Milky Way". In: *XIII Nuclei in the Cosmos (NIC XIII)*, 40, p. 40. DOI: 10.22323/1.204.0040.

Bennett, Morgan and Jo Bovy (Jan. 2019). "Vertical waves in the solar neighbourhood in Gaia DR2". In: 482.1, pp. 1417–1425. DOI: 10.1093/mnras/sty2813. arXiv: 1809.03507 [astro-ph.GA].

Bernard, Edouard J. et al. (July 2018). "Star formation history of the Galactic bulge from deep HST imaging of low reddening windows". In: 477.3, pp. 3507–3519. DOI: 10.1093/mnras/sty902. arXiv: 1801.01426 [astro-ph.GA].

Bouchet, Laurent, Elisabeth Jourdain, and Jean-Pierre Roques (Mar. 2015). "The Galactic ^{26}Al Emission Map as Revealed by INTEGRAL SPI". In: 801.2, 142, p. 142. DOI: 10.1088/0004-637X/801/2/142. arXiv: 1501.05247 [astro-ph.HE].

Bradamante, F., F. Matteucci, and A. D'Ercole (Sept. 1998). "The influence of stellar energetics and dark matter on the chemical evolution of dwarf irregulars". In: 337, pp. 338–348. DOI: 10.48550/arXiv.astro-ph/9801131. arXiv: astro-ph/9801131 [astro-ph].

Brinkman, H. et al. (Oct. 2019). "Aluminium-26 from Massive Binary Stars. I. Nonrotating Models". In: 884.1, 38, p. 38. DOI: 10.3847/1538-4357/ab40ae. arXiv: 1909.04433 [astro-ph.SR].

Brinkman, H. et al. (Dec. 2021). "^{26}Aluminum from Massive Binary Stars. II. Rotating Single Stars Up to Core Collapse and Their Impact on the Early Solar System". In: 923.1, 47, p. 47. DOI: 10.3847/1538-4357/ac25ea. arXiv: 2109.05842 [astro-ph.SR].

Brinkman, H. et al. (July 2023). "Aluminium-26 from Massive Binary Stars. III. Binary Stars up to Core Collapse and Their Impact on the Early Solar System". In: 951.2, 110, p. 110. DOI: 10.3847/1538-4357/acd7ea. arXiv: 2305.16787 [astro-ph.SR].

Burbidge, E. Margaret et al. (Jan. 1957). "Synthesis of the Elements in Stars". In: *Reviews of Modern Physics* 29.4, pp. 547–650. DOI: 10.1103/RevModPhys.29.547.

Calamida, A. et al. (Sept. 2015). "New Insights on the Galactic Bulge Initial Mass Function". In: 810.1, 8, p. 8. DOI: 10.1088/0004-637X/810/1/8. arXiv: 1505.07128 [astro-ph.SR].

Calura, F., F. Matteucci, and G. Vladilo (Mar. 2003). "Chemical evolution and nature of damped Lyman α systems". In: 340.1, pp. 59–72. DOI: 10.1046/j.1365-8711.2003.06197.x. arXiv: astro-ph/0211153 [astro-ph].

Cappellaro, E. and M. Turatto (Jan. 1997). "The rate of supernovae: biases and uncertainties". In: *Thermonuclear Supernovae*. Ed. by P. Ruiz-Lapuente, R. Canal, and J. Isern. Vol. 486. NATO Advanced Study Institute (ASI) Series C, p. 77. DOI: 10.1007/978-94-011-5710-0_5. arXiv: astro-ph/9511129 [astro-ph].

Carrillo, Andreia et al. (June 2023). "Can we really pick and choose? Benchmarking various selections of Gaia Enceladus/Sausage stars in observations with simulations". In: *arXiv e-prints*, arXiv:2306.00770, arXiv:2306.00770. DOI: 10.48550/arXiv.2306.00770. arXiv: 2306.00770 [astro-ph.GA].

Cescutti, G. and F. Matteucci (Jan. 2011). "Galactic astroarchaeology: reconstructing the bulge history by means of the newest data". In: 525, A126, A126. DOI: 10.1051/0004-6361/201015665. arXiv: 1010.1469 [astro-ph.GA].

Cescutti, G. and P. Molaro (Feb. 2019). "^{7}Li evolution in the thin and thick discs of the Milky Way". In: 482.4, pp. 4372–4382. DOI: 10.1093/mnras/sty2967. arXiv: 1810.12215 [astro-ph.SR].

Cescutti, G. et al. (Nov. 2008). "The chemical evolution of manganese in different stellar systems". In: 491.2, pp. 401–405. DOI: 10.1051/0004-6361:200810537. arXiv: 0807.1463 [astro-ph].

Chiappini, C., F. Matteucci, and R. Gratton (Mar. 1997). "The Chemical Evolution of the Galaxy: The Two-Infall Model". In: 477.2, pp. 765–780. DOI: 10.1086/303726. arXiv: astro-ph/9609199 [astro-ph].

Chiappini, C., F. Matteucci, and D. Romano (June 2001). "Abundance Gradients and the Formation of the Milky Way". In: 554.2, pp. 1044–1058. DOI: 10.1086/321427. arXiv: astro-ph/0102134 [astro-ph].

Chieffi, Alessandro and M. Limongi (June 2004). "Explosive Yields of Massive Stars from Z = 0 to Z = Z_{solar}". In: 608.1, pp. 405–410. DOI: 10.1086/392523. arXiv: astro-ph/0402625 [astro-ph].

Chiosi, C. (Mar. 1980). "Chemical evolution of the galactic disk: the inflow problem." In: 83, pp. 206–216.

Chomiuk, Laura and Matthew S. Povich (Dec. 2011). "Toward a Unification of Star Formation Rate Determinations in the Milky Way and Other Galaxies". In: 142.6, 197, p. 197. DOI: 10.1088/0004-6256/142/6/197. arXiv: 1110.4105 [astro-ph.GA].

Clayton, D. (May 1984a). "Al-26 in the interstellar medium". In: 280, pp. 144–149. DOI: 10.1086/161978.

Clayton, D. (Oct. 1984b). "Galactic chemical evolution and nucleocosmochronology - Standard model with terminated infall". In: 285, pp. 411–425. DOI: 10.1086/162518.

Clayton, D. (Sept. 1988). "Nuclear cosmochronology within analytic models of the chemical evolution of the solar neighbourhood." In: 234, pp. 1–36. DOI: 10.1093/mnras/234.1.1.

Clayton, D. (Mar. 1994). "Production of ^{26}A1 and other extinct radionuclides by low-energy heavy cosmic rays in molecular clouds". In: 368.6468, pp. 222–224. DOI: 10.1038/368222a0.

Coc, A. et al. (July 1995). "ONeMg novae: nuclear uncertainties on the Ĵ26Âl and Ĵ22Na yields." In: 299, p. 479.

Coc, Alain, Marie-Geneviève Porquet, and Frédéric Nowacki (Dec. 1999). "Lifetimes of ^{26}Al and ^{34}Cl in an astrophysical plasma". In: 61.1, 015801, p. 015801. DOI: 10.1103/PhysRevC.61.015801. arXiv: astro-ph/9910186 [astro-ph].

Côté, Benoit et al. (June 2019a). "Galactic Chemical Evolution of Radioactive Isotopes". In: 878.2, 156, p. 156. DOI: 10.3847/1538-4357/ab21d1. arXiv: 1905.07828 [astro-ph.GA].

Côté, Benoit et al. (Dec. 2019b). "Stochastic Chemical Evolution of Radioactive Isotopes with a Monte Carlo Approach". In: 887.2, 213, p. 213. DOI: 10.3847/1538-4357/ab5a88. arXiv: 1911.01457 [astro-ph.GA].

Cowan, John J. et al. (Jan. 2021). "Origin of the heaviest elements: The rapid neutron-capture process". In: *Reviews of Modern Physics* 93.1, 015002, p. 015002. DOI: 10.1103/RevModPhys.93.015002. arXiv: 1901.01410 [astro-ph.HE].

Cox, Donald P. and Gilberto C. Gómez (Oct. 2002). "Analytical Expressions for Spiral Arm Gravitational Potential and Density". In: 142.2, pp. 261–267. DOI: 10.1086/341946. arXiv: astro-ph/0207635 [astro-ph].

Creze, M. et al. (Jan. 1998). "The distribution of nearby stars in phase space mapped by Hipparcos. I. The potential well and local dynamical mass". In: 329, pp. 920–936. DOI: 10.48550/arXiv.astro-ph/9709022. arXiv: astro-ph/9709022 [astro-ph].

Crowther, Paul A. et al. (Oct. 2010). "The R136 star cluster hosts several stars whose individual masses greatly exceed the accepted 150M$_{solar}$ stellar mass limit". In: 408.2, pp. 731–751. DOI: 10.1111/j.1365-2966.2010.17167.x. arXiv: 1007.3284 [astro-ph.SR].

D'Antona, F. and F. Matteucci (Aug. 1991). "Galactic evolution of lithium." In: 248, p. 62.

Darnley, M. J. et al. (June 2006). "Classical novae from the POINT-AGAPE microlensing survey of M31 - II. Rate and statistical characteristics of the nova population". In: 369.1, pp. 257–271. DOI: 10.1111/j.1365-2966.2006.10297.x. arXiv: astro-ph/0509493 [astro-ph].

Das, Payel, Keith Hawkins, and Paula Jofré (Apr. 2020). "Ages and kinematics of chemically selected, accreted Milky Way halo stars". In: 493.4, pp. 5195–5207. DOI: 10.1093/mnras/stz3537. arXiv: 1903.09320 [astro-ph.GA].

Dawson, J. R. et al. (Jan. 2013). "Supergiant Shells and Molecular Cloud Formation in the Large Magellanic Cloud". In: 763.1, 56, p. 56. DOI: 10.1088/0004-637X/763/1/56. arXiv: 1211.7119 [astro-ph.GA].

de Jager, O. C. et al. (Jan. 1996). "Gamma-Ray Observations of the Crab Nebula: A Study of the Synchro-Compton Spectrum". In: 457, p. 253. DOI: 10.1086/176726.

Dearborn, D. S. P. and J. B. Blake (Jan. 1985). "On the source of the Al-26 observed in the interstellar medium". In: 288, pp. L21–L24. DOI: 10.1086/184413.

Deibel, Catherine et al. (Oct. 2007). "The impact of the $\hat{2}$6Alm(p,γ)$\hat{2}$7Si reaction rate on the destruction of $\hat{2}$6Al in ONe novae". In: *APS Division of Nuclear Physics Meeting Abstracts*. APS Meeting Abstracts, HD.005, HD.005.

del Rio, E. et al. (Nov. 1996). "1.8 MeV line emission from the Cygnus region." In: 315, pp. 237–242.

Della Valle, Massimo and Luca Izzo (July 2020). "Observations of galactic and extragalactic novae". In: 28.1, 3, p. 3. DOI: 10.1007/s00159-020-0124-6. arXiv: 2004.06540 [astro-ph.SR].

Dickey, John M. (Jan. 1993). "Gas as a Tracer of Galactic Structure". In: *The Minnesota Lectures on the Structure and Dynamics of the Milky Way*. Ed. by Roberta M. Humphreys. Vol. 39. Astronomical Society of the Pacific Conference Series, p. 93.

Diehl, R. (Dec. 1995). "Imaging Diffuse Emission with COMPTEL". In: *Experimental Astronomy* 6.4, pp. 103–108. DOI: 10.1007/BF00419264.

Diehl, R. (July 2002). "^{26}Al production in the Vela and Orion regions". In: 46.8-10, pp. 547–552. DOI: 10.1016/S1387-6473(02)00199-9.

Diehl, R. (July 2013a). "Cosmic Gamma-Ray Spectroscopy". In: *The Astronomical Review* 8.3, pp. 19–65. DOI: 10.1080/21672857.2013.11519722. arXiv: 1307.4198 [astro-ph.HE].

Diehl, R. (Feb. 2013b). "Nuclear astrophysics lessons from INTEGRAL". In: *Reports on Progress in Physics* 76.2, 026301, p. 026301. DOI: 10.1088/0034-4885/76/2/026301. arXiv: 1302.3441 [astro-ph.HE].

Diehl, R. (Jan. 2016). "Gamma-Rays from Nucleosynthesis Ejecta". In: *Journal of Physics Conference Series*. Vol. 665. Journal of Physics Conference Series, 012011, p. 012011. DOI: 10.1088/1742-6596/665/1/012011.

Diehl, R. and F. X. Timmes (June 1998). "Gamma-Ray Line Emission from Radioactive Isotopes in Stars and Galaxies". In: 110.748, pp. 637–659. DOI: 10.1086/316169.

Diehl, R. et al. (Feb. 1992). "Data analysis of the COMPTEL instrument on the NASA Gamma Ray Observatory." In: *NASA Conference Publication*. Vol. 3137. NASA Conference Publication, pp. 95–101.

Diehl, R. et al. (Jan. 1993). "COMPTEL Observations of the 1.809 MeV Gamma-Ray Line from Galactic ^{26}Al". In: *23rd International Cosmic Ray Conference (ICRC23), Volume 1*. Vol. 1. International Cosmic Ray Conference, p. 136.

Diehl, R. et al. (June 1995). "COMPTEL observations of Galactic 26Al emission." In: 298, p. 445.

Diehl, R. et al. (Jan. 2003a). "Gamma-rays from massive stars in Cygnus and Orion". In: *A Massive Star Odyssey: From Main Sequence to Supernova*. Ed. by Karel van der Hucht, Artemio Herrero, and César Esteban. Vol. 212. IAU Symposium, p. 706.

Diehl, R. et al. (Nov. 2003b). "SPI measurements of Galactic ^{26}Al". In: 411, pp. L451–L455. DOI: 10.1051/0004-6361:20031347. arXiv: astro-ph/0309097 [astro-ph].

Diehl, R. et al. (Apr. 2006a). "^{26}Al in the inner Galaxy. Large-scale spectral characteristics derived with SPI/INTEGRAL". In: 449.3, pp. 1025–1031. DOI: 10.1051/0004-6361:20054301. arXiv: astro-ph/0512334 [astro-ph].

Diehl, R. et al. (Jan. 2006b). "Radioactive ^{26}Al from massive stars in the Galaxy". In: 439.7072, pp. 45–47. DOI: 10.1038/nature04364. arXiv: astro-ph/0601015 [astro-ph].

Diehl, R. et al. (Jan. 2007). "^{26}Al Gamma-Ray Line Observations of the Galaxy". In: *The Obscured Universe. Proceedings of the VI INTEGRAL Workshop*. Vol. 622. ESA Special Publication, p. 71.

Diehl, R. et al. (Nov. 2010). "Radioactive ^{26}Al from the Scorpius-Centaurus association". In: 522, A51, A51. DOI: 10.1051/0004-6361/201014302. arXiv: 1007.4462 [astro-ph.HE].

Diehl, R. et al. (June 2021a). "Steady-state nucleosynthesis throughout the Galaxy". In: 92, 101608, p. 101608. DOI: 10.1016/j.newar.2020.101608. arXiv: 2011.06369 [astro-ph.IM].

Diehl, R. et al. (Dec. 2021b). "The radioactive nuclei ({26}) Al and ({60}) Fe in the Cosmos and in the solar system". In: 38, e062, e062. DOI: 10.1017/pasa.2021.48. arXiv: 2109.08558 [astro-ph.HE].

Diehl, R. et al. (Nov. 2022). "Cosmic nucleosynthesis: A multi-messenger challenge". In: *Progress in Particle and Nuclear Physics* 127, 103983, p. 103983. DOI: 10.1016/j.ppnp.2022.103983. arXiv: 2206.12246 [astro-ph.HE].

Doherty, Carolyn L. et al. (Jan. 2014a). "Super and massive AGB stars - II. Nucleosynthesis and yields - Z = 0.02, 0.008 and 0.004". In: 437.1, pp. 195–214. DOI: 10.1093/mnras/stt1877. arXiv: 1310.2614 [astro-ph.SR].

Doherty, Carolyn L. et al. (June 2014b). "Super and massive AGB stars - III. Nucleosynthesis in metal-poor and very metal-poor stars - Z = 0.001 and 0.0001". In: 441.1, pp. 582–598. DOI: 10.1093/mnras/stu571. arXiv: 1403.5054 [astro-ph.SR].

Eddington, A. S. (Oct. 1919). "The sources of stellar energy". In: *The Observatory* 42, pp. 371–376.

Ellis, John, Brian D. Fields, and David N. Schramm (Oct. 1996). "Geological Isotope Anomalies as Signatures of Nearby Supernovae". In: 470, p. 1227. DOI: 10.1086/177945. arXiv: astro-ph/9605128 [astro-ph].

Feltzing, Sofia and Diane Feuillet (Feb. 2023). "The metal-weak Milky Way stellar disk hidden in the Gaia-Sausage-Enceladus debris: the APOGEE DR17 view". In: *arXiv e-prints*, arXiv:2303.00016, arXiv:2303.00016. DOI: 10.48550/arXiv.2303.00016. arXiv: 2303.00016 [astro-ph.GA].

Fernandes, Laura et al. (Mar. 2023). "A comparative analysis of the chemical compositions of Gaia-Enceladus/Sausage and Milky Way satellites using APOGEE". In: 519.3, pp. 3611–3622. DOI: 10.1093/mnras/stac3543. arXiv: 2301.01302 [astro-ph.GA].

Feuillet, Diane K. et al. (Nov. 2021). "Selecting accreted populations: metallicity, elemental abundances, and ages of the Gaia-Sausage-Enceladus and Sequoia populations". In: 508.1, pp. 1489–1508. DOI: 10.1093/mnras/stab2614. arXiv: 2105.12141 [astro-ph.GA].

Fields, P. R. et al. (Jan. 1970). "Isotopic Abundances of Actinide Elements in Lunar Material:" in: *Science* 167.3918, p. 499. DOI: 10.1126/science.167.3918.499.

Flynn, C. and B. Fuchs (Oct. 1994). "Density of dark matter in the Galactic disk". In: 270, pp. 471–479. DOI: 10.1093/mnras/270.3.471.

Flynn, Chris et al. (Nov. 2006). "On the mass-to-light ratio of the local Galactic disc and the optical luminosity of the Galaxy". In: 372.3, pp. 1149–1160. DOI: 10.1111/j.1365-2966.2006.10911.x. arXiv: astro-ph/0608193 [astro-ph].

Ford, H. C. (Jan. 1978). "The number of outbursts of a classical nova." In: 219, p. 595. DOI: 10.1086/155819.

Forestini, M., M. Arnould, and G. Paulus (Dec. 1991). "On the production of Al-26 in AGB stars". In: 252.2, pp. 597–604.

Forestini, M. and C. Charbonnel (June 1997). "Nucleosynthesis of light elements inside thermally pulsing AGB stars: I. The case of intermediate-mass stars". In: 123, pp. 241–272. DOI: 10.1051/aas:1997348. arXiv: astro-ph/9608153 [astro-ph].

Forrest, D. J. et al. (Feb. 1980). "The gamma ray spectrometer for the Solar Maximum Mission." In: 65.1, pp. 15–23. DOI: 10.1007/BF00151381.

François, P. et al. (July 2004). "The evolution of the Milky Way from its earliest phases: Constraints on stellar nucleosynthesis". In: 421, pp. 613–621. DOI: 10.1051/0004-6361:20034140. arXiv: astro-ph/0401499 [astro-ph].

Gallagher, J. S. and S. Starrfield (Jan. 1978). "Theory and observations of classical novae." In: 16, pp. 171–214. DOI: 10.1146/annurev.aa.16.090178.001131.

Gilmore, Gerard, Rosemary F. G. Wyse, and J. Bryn Jones (Mar. 1995). "A Determination of the Thick Disk Chemical Abundance Distribution: Implications for Galaxy Evolution". In: 109, p. 1095. DOI: 10.1086/117344. arXiv: astro-ph/9411116 [astro-ph].

Graser, U. and V. Schoenfelder (Mar. 1977). "Theoretical zenith angle distribution of atmospheric MeV gamma radiation at high balloon altitudes". In: 82.7, p. 1055. DOI: 10.1029/JA082i007p01055.

GRAVITY Collaboration et al. (Oct. 2021). "Constraining particle acceleration in Sgr A* with simultaneous GRAVITY, Spitzer, NuSTAR, and Chandra observations". In: 654, A22, A22. DOI: 10.1051/0004-6361/202140981. arXiv: 2107.01096 [astro-ph.HE].

Grisoni, V. et al. (Dec. 2017). "The AMBRE project: chemical evolution models for the Milky Way thick and thin discs". In: 472.3, pp. 3637–3647. DOI: 10.1093/mnras/stx2201. arXiv: 1706.02614 [astro-ph.GA].

Grisoni, V. et al. (Feb. 2020). "Modelling the chemical evolution of Zr, La, Ce, and Eu in the Galactic discs and bulge". In: 492.2, pp. 2828–2834. DOI: 10.1093/mnras/staa051. arXiv: 1911.04271 [astro-ph.GA].

Guesten, R. and P. G. Mezger (Jan. 1982). "Star formation and abundance gradients in the galaxy". In: *Vistas in Astronomy* 26.3, pp. 159–224. DOI: 10.1016/0083-6656(82)90005-8.

Gupta, Sanjib S. and Bradley S. Meyer (Aug. 2001). "Internal equilibration of a nucleus with metastable states: ^{26}Al as an example". In: 64.2, 025805, p. 025805. DOI: 10.1103/PhysRevC.64.025805.

Harris, Jason and Dennis Zaritsky (Nov. 2009). "The Star Formation History of the Large Magellanic Cloud". In: 138.5, pp. 1243–1260. DOI: 10.1088/0004-6256/138/5/1243. arXiv: 0908.1422 [astro-ph.CO].

Hasselquist, Sten et al. (Dec. 2021). "APOGEE Chemical Abundance Patterns of the Massive Milky Way Satellites". In: 923.2, 172, p. 172. DOI: 10.3847/1538-4357/ac25f9. arXiv: 2109.05130 [astro-ph.GA].

Hawkins, K. et al. (Oct. 2015). "Using chemical tagging to redefine the interface of the Galactic disc and halo". In: 453.1, pp. 758–774. DOI: 10.1093/mnras/stv1586. arXiv: 1507.03604 [astro-ph.GA].

Helmi, Amina et al. (Oct. 2018). "The merger that led to the formation of the Milky Way's inner stellar halo and thick disk". In: 563.7729, pp. 85–88. DOI: 10.1038/s41586-018-0625-x. arXiv: 1806.06038 [astro-ph.GA].

Hermsen, W. et al. (Jan. 1993). "COMPTEL detections of the quasars 3C 273 and 3C 279." In: 97, pp. 97–100.

Higdon, J. C. and William A. Fowler (Apr. 1989). "Angular Distribution of 1.809 MeV Gamma Rays Generated in the Decay of 26Al Produced by Galactic Novae". In: 339, p. 956. DOI: 10.1086/167350.

Higgins, Erin R. et al. (Nov. 2023). "Stellar wind yields of very massive stars". In: 526.1, pp. 534–547. DOI: 10.1093/mnras/stad2537. arXiv: 2308.10941 [astro-ph.SR].

Hill, V. et al. (Dec. 2000). "Age-metallicity relation and chemical evolution of the LMC from UVES spectra of Globular Cluster giants". In: 364, pp. L19–L25. DOI: 10.48550/arXiv.astro-ph/0009273. arXiv: astro-ph/0009273 [astro-ph].

Holmbeck, E. M., T. M. Sprouse, and M. R. Mumpower (Feb. 2023). "Nucleosynthesis and observation of the heaviest elements". In: *European Physical Journal A* 59.2, 28, p. 28. DOI: 10.1140/epja/s10050-023-00927-7. arXiv: 2304.01850 [nucl-th].

Holtzman, Jon A. et al. (Nov. 2015). "Abundances, Stellar Parameters, and Spectra from the SDSS-III/APOGEE Survey". In: 150.5, 148, p. 148. DOI: 10.1088/0004-6256/150/5/148. arXiv: 1501.04110 [astro-ph.GA].

Horta, Danny et al. (Apr. 2023). "The chemical characterization of halo substructure in the Milky Way based on APOGEE". In: 520.4, pp. 5671–5711. DOI: 10.1093/mnras/stac3179. arXiv: 2204.04233 [astro-ph.GA].

Iben Icko, Jr. (Jan. 1967). "Stellar Evolution Within and off the Main Sequence". In: 5, p. 571. DOI: 10.1146/annurev.aa.05.090167.003035.

Isern, Jordi (June 2019). "The Star Formation History in the Solar Neighborhood as Told by Massive White Dwarfs". In: 878.1, L11, p. L11. DOI: 10.3847/2041-8213/ab238e. arXiv: 1905.10779 [astro-ph.GA].

Iwamoto, Koichi et al. (Dec. 1999). "Nucleosynthesis in Chandrasekhar Mass Models for Type IA Supernovae and Constraints on Progenitor Systems and Burning-Front Propagation". In: 125.2, pp. 439–462. DOI: 10.1086/313278. arXiv: astro-ph/0002337 [astro-ph].

Jensen, P. L. et al. (Nov. 2003). "The INTEGRAL spacecraft - in-orbit performance". In: 411, pp. L7–L17. DOI: 10.1051/0004-6361:20031173.

José, Jordi and Margarita Hernanz (Feb. 1998). "Nucleosynthesis in Classical Novae: CO versus ONe White Dwarfs". In: 494.2, pp. 680–690. DOI: 10.1086/305244. arXiv: astro-ph/9709153 [astro-ph].

José, Jordi and Margarita Hernanz (Dec. 2007). "TOPICAL REVIEW: Nucleosynthesis in classical nova explosions". In: *Journal of Physics G Nuclear Physics* 34.12, R431–R458. DOI: 10.1088/0954-3899/34/12/R01.

José, Jordi, Margarita Hernanz, and Alain Coc (Apr. 1997). "New Results on ^{26}Al Production in Classical Novae". In: 479.1, pp. L55–L58. DOI: 10.1086/310575. arXiv: astro-ph/9701181 [astro-ph].

Karakas, A. I. (Apr. 2010). "Updated stellar yields from asymptotic giant branch models". In: 403.3, pp. 1413–1425. DOI: 10.1111/j.1365-2966.2009.16198.x. arXiv: 0912.2142 [astro-ph.SR].

Kemp, Alex J. et al. (Jan. 2022). "The impact of metallicity on nova populations". In: 509.1, pp. 1175–1193. DOI: 10.1093/mnras/stab3103. arXiv: 2110.13396 [astro-ph.SR].

Kennicutt Robert C., Jr. (Sept. 1989). "The Star Formation Law in Galactic Disks". In: 344, p. 685. DOI: 10.1086/167834.

Kennicutt Robert C., Jr. (May 1998). "The Global Schmidt Law in Star-forming Galaxies". In: 498.2, pp. 541–552. DOI: 10.1086/305588. arXiv: astro-ph/9712213 [astro-ph].

Knödlseder, J. et al. (Oct. 2004). "SPI/INTEGRAL Observation of 1809 keV Gamma-Ray Line Emission from the CYGNUS X Region". In: *5th INTEGRAL Workshop on the INTEGRAL Universe*. Ed. by V. Schoenfelder, G. Lichti, and C. Winkler. Vol. 552. ESA Special Publication, p. 33.

Kobayashi, Chiaki et al. (Dec. 2006). "Galactic Chemical Evolution: Carbon through Zinc". In: 653.2, pp. 1145–1171. DOI: 10.1086/508914. arXiv: astro-ph/0608688 [astro-ph].

Krause, Martin G. H. et al. (June 2015). "^{26}Al kinematics: superbubbles following the spiral arms?. Constraints from the statistics of star clusters and HI supershells". In: 578, A113, A113. DOI: 10.1051/0004-6361/201525847. arXiv: 1504.03120 [astro-ph.GA].

Kretschmer, Karsten et al. (Nov. 2013). "Kinematics of massive star ejecta in the Milky Way as traced by ^{26}Al". In: 559, A99, A99. DOI: 10.1051/0004-6361/201322563. arXiv: 1309.4980 [astro-ph.HE].

Kroupa, Pavel (Apr. 2001). "On the variation of the initial mass function". In: 322.2, pp. 231–246. DOI: 10.1046/j.1365-8711.2001.04022.x. arXiv: astro-ph/0009005 [astro-ph].

Kroupa, Pavel, Christopher A. Tout, and Gerard Gilmore (June 1993). "The Distribution of Low-Mass Stars in the Galactic Disc". In: 262, pp. 545–587. DOI: 10.1093/mnras/262.3.545.

Kubryk, M., N. Prantzos, and E. Athanassoula (Aug. 2015a). "Evolution of the Milky Way with radial motions of stars and gas. I. The solar neighbourhood and the thin and thick disks". In: 580, A126, A126. DOI: 10.1051/0004-6361/201424171. arXiv: 1412.0585 [astro-ph.GA].

Kubryk, M., N. Prantzos, and E. Athanassoula (Aug. 2015b). "Evolution of the Milky Way with radial motions of stars and gas. I. The solar neighbourhood and the thin and thick disks". In: 580, A126, A126. DOI: 10.1051/0004-6361/201424171. arXiv: 1412.0585 [astro-ph.GA].

Kuijken, Konrad and Gerard Gilmore (Jan. 1991). "The Galactic Disk Surface Mass Density and the Galactic Force K Z at Z = 1.1 Kiloparsecs". In: 367, p. L9. DOI: 10.1086/185920.

Kulkarni, Shrinivas R. and Carl Heiles (Jan. 1987). "The Atomic Component". In: *Interstellar Processes*. Ed. by David J. Hollenbach and Jr. Thronson Harley A. Vol. 134, p. 87. DOI: 10.1007/978-94-009-3861-8_5.

Kutschera, Walter et al. (Nov. 1984). "Half-life of ^{60}Fe". In: *Nuclear Instruments and Methods in Physics Research B* 5.2, pp. 430–435. DOI: 10.1016/0168-583X(84)90555-X.

Larson, Richard (Jan. 1992). "Galaxy Formation and Evolution". In: *Star Formation in Stellar Systems*. Ed. by G. Tenorio-Tagle, M. Prieto, and F. Sanchez, p. 125.

Lee, T., D. A. Papanastassiou, and G. J. Wasserburg (Jan. 1977). "Aluminum-26 in the early solar system: fossil or fuel?" In: 211, pp. L107–L110. DOI: 10.1086/182351.

Lehner, Nicolas and J. Christopher Howk (Nov. 2011). "A Reservoir of Ionized Gas in the Galactic Halo to Sustain Star Formation in the Milky Way". In: *Science* 334.6058, p. 955. DOI: 10.1126/science.1209069. arXiv: 1111.3981 [astro-ph.GA].

Leising, M. D. and D. Clayton (July 1985). "Angular distribution of interstellar Al-26". In: 294, pp. 591–598. DOI: 10.1086/163326.

Lian, Jianhui et al. (Sept. 2020). "The age-chemical abundance structure of the Galactic disc - II. α-dichotomy and thick disc formation". In: 497.2, pp. 2371–2384. DOI: 10.1093/mnras/staa2078. arXiv: 2007.03687 [astro-ph.GA].

Limongi, M. and A. Chieffi (Jan. 2013). "Presupernova Evolution and Explosion of Rotating Massive Stars at Different Metallicities". In: *GRBs and their Hosts as Tracers of the High Redshift Universe*, 15, p. 15.

Limongi, M. and Alessandro Chieffi (Aug. 2006). "The Nucleosynthesis of ^{26}Al and ^{60}Fe in Solar Metallicity Stars Extending in Mass from 11 to 120 M_{solar}: The Hydrostatic and Explosive Contributions". In: 647.1, pp. 483–500. DOI: 10.1086/505164. arXiv: astro-ph/0604297 [astro-ph].

Limongi, M. and Alessandro Chieffi (July 2018). "Presupernova Evolution and Explosive Nucleosynthesis of Rotating Massive Stars in the Metallicity Range -3 ≤ [Fe/H] ≤ 0". In: 237.1, 13, p. 13. DOI: 10.3847/1538-4365/aacb24. arXiv: 1805.09640 [astro-ph.SR].

Ling, J. C. (Aug. 1975). "A semiempirical model for atmospheric γ rays from 0.3 to 10 MeV at $\lambda = 40°$". In: 80.22, p. 3241. DOI: 10.1029/JA080i022p03241.

Lockwood, J. A. et al. (Apr. 1979). "Atomspheric neutron and gamma ray fluxes and energy spectra". In: 84.A4, pp. 1402–1408. DOI: 10.1029/JA084iA04p01402.

Lodders, Katharina (Jan. 2010). "Solar System Abundances of the Elements". In: *Principles and Perspectives in Cosmochemistry*. Vol. 16. Astrophysics and Space Science Proceedings, p. 379. DOI: 10.1007/978-3-642-10352-0_8. arXiv: 1010.2746 [astro-ph.SR].

Lodders, Katharina (Apr. 2021). "Relative Atomic Solar System Abundances, Mass Fractions, and Atomic Masses of the Elements and Their Isotopes, Composition of the Solar Photosphere, and Compositions of the Major Chondritic Meteorite Groups". In: 217.3, 44, p. 44. DOI: 10.1007/s11214-021-00825-8.

Lugaro, Maria et al. (June 2022). "Origin of Plutonium-244 in the Early Solar System". In: *Universe* 8.7, 343, p. 343. DOI: 10.3390/universe8070343. arXiv: 2208.02074 [astro-ph.SR].

Mahoney, W. A. et al. (Nov. 1982). "Diffuse galactic gamma-ray line emission from nucleosynthetic Fe-60, Al-26, and Na-22 - Preliminary limits from HEAO 3." In: 262, pp. 742–748. DOI: 10.1086/160469.

Mahoney, W. A. et al. (Nov. 1984). "HEAO 3 discovery of Al-26 in the interstellar medium". In: 286, pp. 578–585. DOI: 10.1086/162632.

Majewski, Steven R et al. (Aug. 2017). "The Apache Point Observatory Galactic Evolution Experiment". In: *The Astronomical Journal* 154.3, pp. 0–0.

Mannucci, F. et al. (Apr. 2005). "The supernova rate per unit mass". In: 433.3, pp. 807–814. DOI: 10.1051/0004-6361:20041411. arXiv: astro-ph/0411450 [astro-ph].

Maoz, Dan and Carles Badenes (Sept. 2010). "The supernova rate and delay time distribution in the Magellanic Clouds". In: 407.2, pp. 1314–1327. DOI: 10.1111/j.1365-2966.2010.16988.x. arXiv: 1003.3031 [astro-ph.GA].

Marasco, A., F. Fraternali, and J. J. Binney (Jan. 2012). "Supernova-driven gas accretion in the Milky Way". In: 419.2, pp. 1107–1120. DOI: 10.1111/j.1365-2966.2011.19771.x. arXiv: 1109.1010 [astro-ph.GA].

Martin, P. et al. (July 2009). "Constraints on the kinematics of the ^{44}Ti ejecta of Cassiopeia A from INTEGRAL/SPI". In: 502.1, pp. 131–137. DOI: 10.1051/0004-6361/200809735. arXiv: 1001.0898 [astro-ph.HE].

Matteucci, F. (2003). *The Chemical Evolution of the Galaxy*. Vol. 253.

Matteucci, F. (2012). *Chemical Evolution of Galaxies*. DOI: 10.1007/978-3-642-22491-1.

Matteucci, F. (Dec. 2021). "Modelling the chemical evolution of the Milky Way". In: 29.1, 5, p. 5. DOI: 10.1007/s00159-021-00133-8. arXiv: 2106.13145 [astro-ph.GA].

Matteucci, F. and C. Chiosi (July 1983). "Stochastic star formation and chemical evolution of dwarf irregular galaxies." In: 123, pp. 121–134.

Matteucci, F. and P. Francois (Aug. 1989). "Galactic chemical evolution : abundance gradients of individual elements." In: 239, pp. 885–904. DOI: 10.1093/mnras/239.3.885.

Matteucci, F. and L. Greggio (Jan. 1986). "Relative roles of type I and II supernovae in the chemical enrichment of the interstellar gas". In: 154.1-2, pp. 279–287.

Matteucci, F. and S. Recchi (Sept. 2001). "On the Typical Timescale for the Chemical Enrichment from Type Ia Supernovae in Galaxies". In: 558.1, pp. 351–358. DOI: 10.1086/322472. arXiv: astro-ph/0105074 [astro-ph].

Matteucci, F. et al. (Aug. 2019). "The origin of stellar populations in the Galactic bulge from chemical abundances". In: 487.4, pp. 5363–5371. DOI: 10.1093/mnras/stz1647. arXiv: 1903.12440 [astro-ph.GA].

Maurin, D. et al. (Oct. 2004). "Search for ^{26}Al Emission in the Vela Region with INTEGRAL/SPI". In: *5th INTEGRAL Workshop on the INTEGRAL Universe*. Ed. by V. Schoenfelder, G. Lichti, and C. Winkler. Vol. 552. ESA Special Publication, p. 107.

Mayer, M. G. (Oct. 1952). "Radioactivity and Nuclear Theory". In: *Annual Review of Physical Chemistry* 3, pp. 19–38. DOI: 10.1146/annurev.pc.03.100152.000315.

McKee, Christopher F., Antonio Parravano, and David J. Hollenbach (Nov. 2015). "Stars, Gas, and Dark Matter in the Solar Neighborhood". In: 814.1, 13, p. 13. DOI: 10.1088/0004-637X/814/1/13. arXiv: 1509.05334 [astro-ph.GA].

Meidt, Sharon E., Richard J. Rand, and Michael R. Merrifield (Sept. 2009). "Uncovering the Origins of Spiral Structure by Measuring Radial Variation in Pattern Speeds". In: 702.1, pp. 277–290. DOI: 10.1088/0004-637X/702/1/277. arXiv: 0907.3443 [astro-ph.GA].

Melioli, C. et al. (Aug. 2008). "Hydrodynamical simulations of Galactic fountains - I. Evolution of single fountains". In: 388, pp. 573–586. DOI: 10.1111/j.1365-2966.2008.13446.x. arXiv: 0805.1138.

Melioli, C. et al. (Nov. 2009). "Hydrodynamical simulations of Galactic fountains - II. Evolution of multiple fountains". In: 399, pp. 1089–1105. DOI: 10.1111/j.1365-2966.2009.14725.x. arXiv: 0903.0720.

Minchev, I. et al. (Dec. 2012). "Evolution of galactic discs: multiple patterns, radial migration, and disc outskirts". In: 548, A126, A126. DOI: 10.1051/0004-6361/201219198. arXiv: 1203.2621 [astro-ph.GA].

Montalbán, Josefina et al. (Jan. 2021). "Chronologically dating the early assembly of the Milky Way". In: *Nature Astronomy* 5, pp. 640–647. DOI: 10.1038/s41550-021-01347-7. arXiv: 2006.01783 [astro-ph.GA].

Mor, R. et al. (Apr. 2019). "Gaia DR2 reveals a star formation burst in the disc 2-3 Gyr ago". In: 624, L1, p. L1. DOI: 10.1051/0004-6361/201935105. arXiv: 1901.07564 [astro-ph.GA].

Morris, D. J. et al. (Jan. 1993). "Neutron Flux Measurements in Near-Earth Orbit with COMPTEL". In: *23rd International Cosmic Ray Conference (ICRC23), Volume 3*. Vol. 3. International Cosmic Ray Conference, p. 809.

Mowlavi, N. and G. Meynet (Sept. 2000). "Aluminum 26 production in asymptotic giant branch stars". In: 361, pp. 959–976.

Mróz, P. et al. (Jan. 2016). "OGLE Atlas of Classical Novae. II. Magellanic Clouds". In: 222.1, 9, p. 9. DOI: 10.3847/0067-0049/222/1/9. arXiv: 1511.06355 [astro-ph.SR].

Mucciarelli, Alessio et al. (July 2008). "The Chemical Composition of Red Giant Stars in Four Intermediate-Age Clusters of the Large Magellanic Cloud". In: 136.1, pp. 375–388. DOI: 10.1088/0004-6256/136/1/375. arXiv: 0804.4061 [astro-ph].

Myeong, G. C. et al. (Sept. 2019). "Evidence for two early accretion events that built the Milky Way stellar halo". In: 488.1, pp. 1235–1247. DOI: 10.1093/mnras/stz1770. arXiv: 1904.03185 [astro-ph.GA].

Nidever, David L. et al. (June 2020). "The Lazy Giants: APOGEE Abundances Reveal Low Star Formation Efficiencies in the Magellanic Clouds". In: 895.2, 88, p. 88. DOI: 10.3847/1538-4357/ab7305. arXiv: 1901.03448 [astro-ph.GA].

Nofar, Irit, Giora Shaviv, and S. Starrfield (Mar. 1991). "The Formation of 26Al Nova Explosions". In: 369, p. 440. DOI: 10.1086/169772.

Nomoto, K., F. -K. Thielemann, and K. Yokoi (Nov. 1984). "Accreting white dwarf models for type I supernovae. III. Carbon deflagration supernovae." In: 286, pp. 644–658. DOI: 10.1086/162639.

Norgaard, H. (Mar. 1980). "Al-26 from red giants". In: 236, pp. 895–898. DOI: 10.1086/157815.

Nosowitz, Jonathon et al. (June 2022). "Physical and Chemical Conditions in the N113 Star-Forming Region in the Low-Metallicity Large Magellanic Cloud". In: *American Astronomical Society Meeting Abstracts*. Vol. 54. American Astronomical Society Meeting Abstracts, 103.02, p. 103.02.

O'Flaherty, K. S. et al. (May 1995). "COMPTEL upper limits to MeV emission from the globular cluster 47 Tucanae." In: 297, p. L29.

Oberlack, U. et al. (Dec. 1996). "The COMPTEL 1.809MeV all-sky image." In: 120, pp. 311–314.

Ostdiek, Karen M. et al. (May 2017). "Activity measurement of ^{60}Fe through the decay of $^{Co}m_{60}$ and confirmation of its half-life". In: 95.5, 055809, p. 055809. DOI: 10.1103/PhysRevC.95.055809.

Palacios, A. et al. (Jan. 2005). "New estimates of the contribution of Wolf-Rayet stellar winds to the Galactic ^{26}Al". In: 429, pp. 613–624. DOI: 10.1051/0004-6361:20041757. arXiv: astro-ph/0409580 [astro-ph].

Palla, M. et al. (Oct. 2020). "Chemical evolution of the Milky Way: constraints on the formation of the thick and thin discs". In: 498.2, pp. 1710–1725. DOI: 10.1093/mnras/staa2437. arXiv: 2008.07484 [astro-ph.GA].

Paul, M. et al. (Sept. 2001). "Experimental Limit to Interstellar ^{244}Pu Abundance". In: 558.2, pp. L133–L135. DOI: 10.1086/323617. arXiv: astro-ph/0106205 [astro-ph].

Perottoni, Hélio D. et al. (Sept. 2022). "The Unmixed Debris of Gaia-Sausage/Enceladus in the Form of a Pair of Halo Stellar Overdensities". In: 936.1, L2, p. L2. DOI: 10.3847/2041-8213/ac88d6. arXiv: 2207.11869 [astro-ph.GA].

Pleintinger, Moritz M. M. et al. (Dec. 2022). "^{26}Al gamma rays from the Galaxy with INTEGRAL/SPI". In: *arXiv e-prints*, arXiv:2212.11228, arXiv:2212.11228. DOI: 10.48550/arXiv.2212.11228. arXiv: 2212.11228 [astro-ph.HE].

Plüschke, S. et al. (Sept. 2001). "The COMPTEL 1.809 MeV survey". In: *Exploring the Gamma-Ray Universe*. Ed. by A. Gimenez, V. Reglero, and C. Winkler. Vol. 459. ESA Special Publication, pp. 55–58. DOI: 10.48550/arXiv.astro-ph/0104047. arXiv: astro-ph/0104047 [astro-ph].

Politano, M. et al. (Aug. 1995). "Hydrodynamic Studies of Accretion onto Massive White Dwarfs: ONeMg-enriched Nova Outbursts. I. Dependence on White Dwarf Mass". In: 448, p. 807. DOI: 10.1086/176009.

Portinari, L., C. Chiosi, and A. Bressan (June 1998). "Galactic chemical enrichment with new metallicity dependent stellar yields". In: 334, pp. 505–539. DOI: 10.48550/arXiv.astro-ph/9711337. arXiv: astro-ph/9711337 [astro-ph].

Prantzos, N. and M. Casse (Aug. 1986a). "On the Production of 26Al by Wolf-Rayet Stars: Galactic Yield and Gamma-Ray Line Emissivity". In: 307, p. 324. DOI: 10.1086/164419.

Prantzos, N. and R. Diehl (Mar. 1996). "Radioactive 26Al in the galaxy: observations versus theory". In: 267, pp. 1–69. DOI: 10.1016/0370-1573(95)00055-0.

Prantzos, N. et al. (May 1986b). "Nucleosynthesis and Evolution of Massive Stars with Mass Loss and Overshooting". In: 304, p. 695. DOI: 10.1086/164208.

Prantzos, N. et al. (July 2011). "The 511 keV emission from positron annihilation in the Galaxy". In: *Reviews of Modern Physics* 83.3, pp. 1001–1056. DOI: 10.1103/RevModPhys.83.1001. arXiv: 1009.4620 [astro-ph.HE].

Prantzos, N. et al. (May 2018). "Chemical evolution with rotating massive star yields - I. The solar neighbourhood and the s-process elements". In: 476.3, pp. 3432–3459. DOI: 10.1093/mnras/sty316. arXiv: 1802.02824 [astro-ph.GA].

Quillen, A. C. and Ivan Minchev (Aug. 2005). "The Effect of Spiral Structure on the Stellar Velocity Distribution in the Solar Neighborhood". In: 130.2, pp. 576–585. DOI: 10.1086/430885. arXiv: astro-ph/0502205 [astro-ph].

Quillen, A. C. et al. (Oct. 2011). "Structure in phase space associated with spiral and bar density waves in an N-body hybrid galactic disc". In: 417.1, pp. 762–784. DOI: 10.1111/j.1365-2966.2011.19349.x. arXiv: 1010.5745 [astro-ph.GA].

Quirk, William J. (Aug. 1972). "On the Gas Content of Galaxies". In: 176, p. L9. DOI: 10.1086/181009.

Ramaty, R. and R. E. Lingenfelter (Apr. 1977). "^{26}Al: a galactic source of gamma-ray line emission." In: 213, pp. L5–L7. DOI: 10.1086/182397.

Recio-Blanco, A. et al. (June 2023). "Gaia Data Release 3. Analysis of RVS spectra using the General Stellar Parametriser from spectroscopy". In: 674, A29, A29. DOI: 10.1051/0004-6361/202243750. arXiv: 2206.05541 [astro-ph.GA].

Reipurth, B. and N. Schneider (2008). "Star Formation and Young Clusters in Cygnus". In: *Handbook of Star Forming Regions, Volume I*. Ed. by B. Reipurth. Vol. 4, p. 36.

Roca-Fàbrega, Santi et al. (May 2014). "A novel method to bracket the corotation radius in galaxy discs: vertex deviation maps". In: 440.3, pp. 1950–1963. DOI: 10.1093/mnras/stu437. arXiv: 1401.4191 [astro-ph.GA].

Romano, D. and F. Matteucci (June 2003). "Nova nucleosynthesis and Galactic evolution of the CNO isotopes". In: 342.1, pp. 185–198. DOI: 10.1046/j.1365-8711.2003.06526.x. arXiv: astro-ph/0302233 [astro-ph].

Romano, D. et al. (Aug. 2000). "The Mass Surface Density in the Local Disk and the Chemical Evolution of the Galaxy". In: 539.1, pp. 235–240. DOI: 10.1086/309223. arXiv: astro-ph/0003130 [astro-ph].

Romano, D. et al. (Nov. 2010). "Quantifying the uncertainties of chemical evolution studies. II. Stellar yields". In: 522, A32, A32. DOI: 10.1051/0004-6361/201014483. arXiv: 1006.5863 [astro-ph.GA].

Romano, D. et al. (Feb. 2015). "Chemical enrichment in very low metallicity environments: Boötes I". In: 446.4, pp. 4220–4231. DOI: 10.1093/mnras/stu2427. arXiv: 1411.4508 [astro-ph.GA].

Romano, D. et al. (Dec. 2019). "The evolution of CNO isotopes: the impact of massive stellar rotators". In: 490.2, pp. 2838–2854. DOI: 10.1093/mnras/stz2741. arXiv: 1907.09476 [astro-ph.GA].

Romano, D. et al. (July 2020). "The variation of carbon abundance in galaxies and its implications". In: 639, A37, A37. DOI: 10.1051/0004-6361/202037972. arXiv: 2005.05717 [astro-ph.GA].

Rugel, G. et al. (Aug. 2009). "New Measurement of the Fe60 Half-Life". In: 103.7, 072502, p. 072502. DOI: 10.1103/PhysRevLett.103.072502.

Ruiz-Lara, Tomás et al. (May 2020). "The recurrent impact of the Sagittarius dwarf on the star formation history of the Milky Way". In: *Nature Astronomy* 4, pp. 965–973. DOI: 10.1038/s41550-020-1097-0. arXiv: 2003.12577 [astro-ph.GA].

Runkle, R. C., A. E. Champagne, and J. Engel (Aug. 2001). "Thermal Equilibration of ^{26}Al". In: 556.2, pp. 970–978. DOI: 10.1086/321594.

Russell, Henry Norris (July 1919). "On the Sources of Stellar Energy". In: 31.182, p. 205. DOI: 10.1086/122855.

Ryan, J. et al. (Sept. 1993). "Comptel measurements of solar flare neutrons". In: *Advances in Space Research* 13.9, pp. 255–258. DOI: 10.1016/0273-1177(93)90487-V.

Salpeter, Edwin E. (Jan. 1955). "The Luminosity Function and Stellar Evolution." In: 121, p. 161. DOI: 10.1086/145971.

Schatzman, Evry (Jan. 1951). "Remarques sur le phénomène de Nova: IV. L'onde de détonation due à l'isotope ^{3}He". In: *Annales d'Astrophysique* 14, p. 294.

Schmidt, Maarten (Mar. 1959). "The Rate of Star Formation." In: 129, p. 243. DOI: 10.1086/146614.

Schneider, Raffaella et al. (June 2006). "Constraints on the initial mass function of the first stars". In: 369.2, pp. 825–834. DOI: 10.1111/j.1365-2966.2006.10331.x. arXiv: astro-ph/0510685 [astro-ph].

Schoenfelder, V. et al. (June 1993). "Instrument Description and Performance of the Imaging Gamma-Ray Telescope COMPTEL aboard the Compton Gamma-Ray Observatory". In: 86, p. 657. DOI: 10.1086/191794.

Schoenfelder, V. et al. (Nov. 1996). "COMPTEL overview: Achievements and expectations." In: 120, pp. 13–21.

Schönfelder, V. et al. (Jan. 1984). "The imaging Compton telescope COMPTEL on the Gamma Ray Observatory." In: *IEEE Transactions on Nuclear Science* 1, pp. 766–770. DOI: 10.1109/TNS.1984.4333363.

Schulreich, M. M., J. Feige, and D. Breitschwerdt (Dec. 2023). "Numerical studies on the link between radioisotopic signatures on Earth and the formation of the Local Bubble. II. Advanced modelling of interstellar ^{26}Al, ^{53}Mn, ^{60}Fe, and ^{244}Pu influxes as traces of past supernova activity in the solar neighbourhood". In: 680, A39, A39. DOI: 10.1051/0004-6361/202347532. arXiv: 2309.13983 [astro-ph.SR].

Sellwood, J. A. and R. G. Carlberg (Apr. 2014). "Transient Spirals as Superposed Instabilities". In: 785.2, 137, p. 137. DOI: 10.1088/0004-637X/785/2/137. arXiv: 1403.1135 [astro-ph.GA].

Shafter, A. W. (Jan. 2017). "The Galactic Nova Rate Revisited". In: 834.2, 196, p. 196. DOI: 10.3847/1538-4357/834/2/196. arXiv: 1606.02358 [astro-ph.SR].

Share, G. H. et al. (May 1985). "Detection of galactic Al-26 gamma radiation by the SMM spectrometer". In: 292, pp. L61–L65. DOI: 10.1086/184473.

Siegert, Thomas and R. Diehl (Jan. 2017a). "The ^{26}Al Gamma-ray Line from Massive-Star Regions". In: *14th International Symposium on Nuclei in the Cosmos (NIC2016)*. Ed. by Shigeru Kubono et al., 020305, p. 020305. DOI: 10.7566/JPSCP.14.020305.

Siegert, Thomas and R. Diehl (Jan. 2017b). "The ^{26}Al Gamma-ray Line from Massive-Star Regions". In: *14th International Symposium on Nuclei in the Cosmos (NIC2016)*. Ed. by Shigeru Kubono et al., 020305, p. 020305. DOI: 10.7566/JPSCP.14.020305. arXiv: 1609.08817 [astro-ph.HE].

Siegert, Thomas et al. (Apr. 2023). "Galactic population synthesis of radioactive nucleosynthesis ejecta". In: 672, A54, A54. DOI: 10.1051/0004-6361/202244457. arXiv: 2301.10192 [astro-ph.GA].

Spitoni, E. and F. Matteucci (July 2011). "Effects of the radial flows on the chemical evolution of the Milky Way disk". In: 531, A72, A72. DOI: 10.1051/0004-6361/201015749. arXiv: 1104.4881 [astro-ph.GA].

Spitoni, E., S. Recchi, and F. Matteucci (June 2008). "Galactic fountains and their connection with high and intermediate velocity clouds". In: 484, pp. 743–753. DOI: 10.1051/0004-6361:200809403. arXiv: 0803.3032.

Spitoni, E. et al. (Sept. 2009). "Effects of galactic fountains and delayed mixing in the chemical evolution of the Milky Way". In: 504, pp. 87–96. DOI: 10.1051/0004-6361/200911768. arXiv: 0906.3400.

Spitoni, E. et al. (May 2016). "Are ancient dwarf satellites the building blocks of the Galactic halo?" In: 458.3, pp. 2541–2552. DOI: 10.1093/mnras/stw519. arXiv: 1603.00344 [astro-ph.GA].

Spitoni, E. et al. (Aug. 2019a). "2D chemical evolution model: The impact of Galactic disc asymmetries on azimuthal chemical abundance variations". In: 628, A38, A38. DOI: 10.1051/0004-6361/201834665. arXiv: 1811.11196 [astro-ph.GA].

Spitoni, E. et al. (Mar. 2019b). "Galactic Archaeology with asteroseismic ages: Evidence for delayed gas infall in the formation of the Milky Way disc". In: 623, A60, A60. DOI: 10.1051/0004-6361/201834188. arXiv: 1809.00914 [astro-ph.GA].

Spitoni, E. et al. (Dec. 2023). "2D chemical evolution models. II. Effects of multiple spiral arm patterns on O, Eu, Fe, and Ba abundance gradients". In: 680, A85, A85. DOI: 10.1051/0004-6361/202347325. arXiv: 2310.11504 [astro-ph.GA].

Starrfield, S., C. Iliadis, and W. R. Hix (May 2016). "The Thermonuclear Runaway and the Classical Nova Outburst". In: 128.963, p. 051001. DOI: 10.1088/1538-3873/128/963/051001. arXiv: 1605.04294 [astro-ph.SR].

Starrfield, S. et al. (May 2020). "Carbon-Oxygen Classical Novae Are Galactic ^{7}Li Producers as well as Potential Supernova Ia Progenitors". In: 895.1, 70, p. 70. DOI: 10.3847/1538-4357/ab8d23. arXiv: 1910.00575 [astro-ph.SR].

Starrfield, S. et al. (June 2023). "^{7}Li, ^{22}Na, ^{26}Al, and ^{31}P ejected in Carbon-Oxygen and Oxygen-Neon Classical Nova Outbursts". In: *American Astronomical Society Meeting Abstracts*. Vol. 242. American Astronomical Society Meeting Abstracts, 400.05, p. 400.05.

Sukhbold, Tuguldur et al. (Apr. 2016). "Core-collapse Supernovae from 9 to 120 Solar Masses Based on Neutrino-powered Explosions". In: 821.1, 38, p. 38. DOI: 10.3847/0004-637X/821/1/38. arXiv: 1510.04643 [astro-ph.HE].

Talbot Raymond J., Jr. and W. David Arnett (Nov. 1973). "The Evolution of Galaxies. III. Metal-Enhanced Star Formation". In: 186, pp. 69–90. DOI: 10.1086/152478.

Tchernyshyov, Kirill et al. (Oct. 2015). "Elemental Depletions in the Magellanic Clouds and the Evolution of Depletions with Metallicity". In: 811.2, 78, p. 78. DOI: 10.1088/0004-637X/811/2/78. arXiv: 1503.08852 [astro-ph.GA].

Thielemann, F. -K. et al. (2011). "Massive Stars and Their Supernovae". In: *Lecture Notes in Physics, Berlin Springer Verlag*. Ed. by R. Diehl, Dieter H. Hartmann, and Nikos Prantzos. Vol. 812, pp. 153–232. DOI: 10.1007/978-3-642-12698-7_4.

Timmes, F. X. et al. (Aug. 1995). "26Al and 60Fe from Supernova Explosions". In: 449, p. 204. DOI: 10.1086/176046. arXiv: astro-ph/9503120 [astro-ph].

Timmes, F. X. et al. (May 2019). "Catching Element Formation In The Act ; The Case for a New MeV Gamma-Ray Mission: Radionuclide Astronomy in the 2020s". In: 51.3, 2, p. 2. DOI: 10.48550/arXiv.1902.02915. arXiv: 1902.02915 [astro-ph.HE].

Tolstoy, Eline, Vanessa Hill, and Monica Tosi (Sept. 2009). "Star-Formation Histories, Abundances, and Kinematics of Dwarf Galaxies in the Local Group". In: 47.1, pp. 371–425. DOI: 10.1146/annurev-astro-082708-101650. arXiv: 0904.4505 [astro-ph.CO].

Tomsick, J. et al. (Sept. 2019). "The Compton Spectrometer and Imager". In: *Bulletin of the American Astronomical Society*. Vol. 51, 98, p. 98. DOI: 10.48550/arXiv.1908.04334. arXiv: 1908.04334 [astro-ph.IM].

Tomsick, J. A. (Jan. 2016). "GRB 160530A: discovery with the Compton Spectrometer and Imager." In: *GRB Coordinates Network* 19473, p. 1.

Trueman, Thomas C. L. et al. (Jan. 2022). "Galactic Chemical Evolution of Radioactive Isotopes with an s-process Contribution". In: 924.1, 10, p. 10. DOI: 10.3847/1538-4357/ac31b0. arXiv: 2110.11126 [astro-ph.GA].

Tueller, J. et al. (Sept. 1991). "GRIS Observations of the Galactic Center and the Gamma-Ray Galactic Diffuse Continuum". In: *Bulletin of the American Astronomical Society*. Vol. 23, p. 1393.

Ubertini, P. et al. (Nov. 2003). "IBIS: The Imager on-board INTEGRAL". In: 411, pp. L131–L139. DOI: 10.1051/0004-6361:20031224.

Van der Swaelmen, M. et al. (Dec. 2013). "Chemical abundances in LMC stellar populations. II. The bar sample". In: 560, A44, A44. DOI: 10.1051/0004-6361/201321109. arXiv: 1306.4224 [astro-ph.GA].

Vasini, A., F. Matteucci, and E. Spitoni (Dec. 2022). "Chemical evolution of ^{26}Al and ^{60}Fe in the Milky Way". In: 517.3, pp. 4256–4264. DOI: 10.1093/mnras/stac2981. arXiv: 2204.00510 [astro-ph.GA].

Vasini, A., E. Spitoni, and F. Matteucci (Mar. 2024a). "Galactic archaeology with [Mg/Mn] versus [Al/Fe] abundance ratios. Uncertainties and caveats". In: 683, A121, A121. DOI: 10.1051/0004-6361/202347603. arXiv: 2310.04530 [astro-ph.GA].

Vasini, A. et al. (July 2023). "Evolution of radioactive elements in the LMC: predictions for future γ-ray surveys". In: 523.1, pp. 1153–1162. DOI: 10.1093/mnras/stad1440. arXiv: 2305.04753 [astro-ph.GA].

Vasini, A. et al. (July 2024b). "Tracing the Milky Way spiral arms with 26Al – The role of nova systems in the 2D distribution of 26Al". In: *arXiv e-prints*, arXiv:2407.16765, arXiv:2407.16765. DOI: 10.48550/arXiv.2407.16765. arXiv: 2407.16765 [astro-ph.GA].

Vedrenne, G. et al. (Nov. 2003). "SPI: The spectrometer aboard INTEGRAL". In: 411, pp. L63–L70. DOI: 10.1051/0004-6361:20031482.

Voss, R. et al. (Sept. 2010). "Probing the evolving massive star population in Orion with kinematic and radioactive tracers". In: 520, A51, A51. DOI: 10.1051/0004-6361/201014408.

Voss, R. et al. (Mar. 2012). "Energetic feedback and ^{26}Al from massive stars and their supernovae in the Carina region". In: 539, A66, A66. DOI: 10.1051/0004-6361/201118209.

Wallner, A. et al. (Jan. 2015). "Settling the Half-Life of ^{60}Fe: Fundamental for a Versatile Astrophysical Chronometer". In: 114.4, 041101, p. 041101. DOI: 10.1103/PhysRevLett.114.041101.

Walter, R. and A. Maeder (July 1989). "The synthesis of 26Al in massive stars." In: 218, pp. 123–130.

Wanajo, Shinya, Hans-Thomas Janka, and Bernhard Müller (Sept. 2013). "Electron-capture Supernovae as Sources of ^{60}Fe". In: 774.1, L6, p. L6. DOI: 10.1088/2041-8205/774/1/L6. arXiv: 1307.3319 [astro-ph.SR].

Wang, W. et al. (July 2007). "SPI observations of the diffuse ^{60}Fe emission in the Galaxy". In: 469.3, pp. 1005–1012. DOI: 10.1051/0004-6361:20066982.

Wang, W. et al. (Feb. 2020). "Gamma-Ray Emission of ^{60}Fe and ^{26}Al Radioactivity in Our Galaxy". In: 889.2, 169, p. 169. DOI: 10.3847/1538-4357/ab6336.

Wehmeyer, Benjamin et al. (Feb. 2023). "Inhomogeneous Enrichment of Radioactive Nuclei in the Galaxy: Deposition of Live ^{53}Mn, ^{60}Fe, ^{182}Hf, and ^{244}Pu into Deep-sea Archives. Surfing the Wave?" In: 944.2, 121, p. 121. DOI: 10.3847/1538-4357/acafec. arXiv: 2301.04593 [astro-ph.GA].

Winkler, C. et al. (Nov. 2003). "The INTEGRAL mission". In: 411, pp. L1–L6. DOI: 10.1051/0004-6361:20031288.

Winkler, Christoph (June 1994). "INTEGRAL: Overview and Mission Concept". In: 92, p. 327. DOI: 10.1086/191973.

Woosley, S. E. and A. Heger (Apr. 2007). "Nucleosynthesis and remnants in massive stars of solar metallicity". In: 442.1-6, pp. 269–283. DOI: 10.1016/j.physrep.2007.02.009. arXiv: astro-ph/0702176 [astro-ph].

Woosley, S. E. and T. A. Weaver (June 1980). "Explosive neon burning and Al-26 gamma-ray astronomy". In: 238, pp. 1017–1025. DOI: 10.1086/158067.

Woosley, S. E. and Thomas A. Weaver (Nov. 1995). "The Evolution and Explosion of Massive Stars. II. Explosive Hydrodynamics and Nucleosynthesis". In: 101, p. 181. DOI: 10.1086/192237.

Yagüe López, A., B. Côté, and M. Lugaro (May 2021). "Monte Carlo Investigation of the Ratios of Short-Lived Radioactive Isotopes in the Interstellar Medium". In: *arXiv e-prints*, arXiv:2105.09210, arXiv:2105.09210. DOI: 10.48550/arXiv.2105.09210. arXiv: 2105.09210 [astro-ph.GA].